Understanding how Molecular Interactions Control the Stability of Concentrated Surfactant Formulations and their Interactions with Lipid Membranes

Mohammed Haris Khan

Institute of Chemical Biology & Department of Chemistry

Imperial College London

A Thesis Submitted for a Degree of Doctor of Philosophy

September 2020

Abstract

Surfactants are one of the most versatile chemical compounds as it is utilised in a wide range of products and processes such as pharmaceuticals, oil extractions, agrochemicals, food industry, personal care industry and household cleaning products. The use of high levels of surfactants in some of these applications, e.g. detergents, bring about several challenges including, product stability (shelf-life) and physiological safety. Countering these challenges leads to extensive research and development time, enduring high cost, which does not always result in a commercially viable product. The broad aim of this thesis is to address these challenges through understanding the molecular interactions within surfactant formulations involving low temperature stability and also understanding the interactions between these concentrated surfactant solutions with lipid membranes, in the context of ocular irritancy.

The effect of changing organic solvent content on the Krafft point of the model surfactant sodium dodecyl sulfate (SDS) was determined through the surface tension pendant drop technique, which proved to be a robust method, and together with the sensitivity and accuracy of X-ray scattering and DSC techniques, the transitions near the solubility boundary of hydrated crystals to lyotropic liquid crystals (and vice-versa) were explored. This enabled SDS phase diagrams to be established for a series of water-glycerol mixtures, identifying and distinguishing between the numerous phases and the conditions under which they form. This knowledge base now provides a platform for understanding the performance of structured, surfactant-based systems, as well as controlling and fine-tuning the route of negative transformations in future studies.

Concentrated surfactant formulations also have to comply with health hazard and safety regulations, particularly regarding ocular irritancy. There is a lack of ethical and reproducible eye irritancy test and a need for a better understanding of how surfactant systems interact with lipid membranes. Here, this understanding was gained through examining the permeation and solubility of model membrane, liposomes, by actual detergent formulations and later by surfactant(s) only systems. Through developing a liposome-calcein release assay (LCRA), a meaningful, negative correlation was

established between the calcein release (liposome permeation) and corneal swelling, a parameter from the ICE test, suggesting that slow and incomplete solubilisation of lipid membranes leads to higher corneal swelling in the epithelial membrane. To gain a better insight, the three surfactants used in the detergent were tested in various ratios to analyse exclusively their interactions with the lipid bilayer, with the aid of the LCRA and real-time DLS analysis. It was gathered that NI follows the conventional three-stage solubilisation mechanism due to its structure consisting of a large headgroup to tail ratio, while the two anionic surfactants involved interact via a time-limiting flip-flop mechanism. It is proposed that the negative correlation between permeation and ICE test corneal swelling measurements, is due to this prolonged flip-flop mechanism. The LCRA developed provides a high-throughput and a less expensive framework, which shows great promise in developing novel, complimentary assays for predicting ocular irritancy.

Acknowledgements

This thesis would not have been possible without the people who have supported, guided and encouraged me over the last 4 years and I would therefore like to express my deepest appreciation to you all.

First and foremost, I would like to express my deepest gratitude to Oscar Ces, my research supervisor, for his valuable guidance, constant encouragement and infectious passion for the research we do. I would also like to thank him for his time and patience in proof-reading my entire thesis, it is very much appreciated. I would like to extend my thanks to all my supervisors; To João Cabral (Dept. of Chemical Engineering) for his constructive guidance during the planning and development of this research project. To Nick Brooks, Rob Law and John Seddon for their expert advice and useful critique, allowing me to advance my research. To my supervisors at Procter & Gamble, Eric Robles for an enlightening collaboration and sharing his years of experience and knowledge on the research topic, and to Oreste Todini for his valuable insight on the product formulations. My thanks are also extended to Daniela Holland, Pauline Mcnamee and Jeanpol Boutique, my collaborators at P&G for generously giving their time, advice and encouragement.

Many thanks to the EPSRA and P&G for their financial support, to the Institute of Chemical Biology- CDT programme for providing this excellent opportunity, and Imperial College of London for a stimulating environment, allowing me to develop as a scientist.

I would like to thank all past and present members of the Membrane Biophysics group. In particular, to Yuval Elani, Mark Friddin and Nathan Barlow for always willing to help, to Ruhina Miller, Norman Chan, James Hindley and Mohit Devgan for their friendship and support in numerous ways and to Jenny Liu for positively taking this research forward. And to the rest of the group, for making my PhD journey enjoyable and enlightening. It has been a real pleasure working alongside you all.

My special gratitude is extended all my friends and family, including my grandparents for their constant prayers and wisdom, to my sister for always guiding and encouraging me and to my brother & his wife for their generosity and support during my Ph.D. I wish to acknowledge my late grandfathers, Prof. A.T Khan, whose academic pursuit has inspired me to embark on my own doctoral journey and Dr Ilyas Khan for imparting his calm temperament in handling pressure. Most importantly, I want to convey my profound gratitude to my parents for their continuing guidance and love, for instilling the value of hard work and always encouraging me to pursue academic and professional endeavours.

Lastly, my unconditional thanks to my wife for her constant love and support, for being very understanding and for keeping me sane during the final stages of my PhD.

Publications

Haris Khan et al, Effect of glycerol with sodium chloride on the Krafft point of sodium dodecyl sulfate using surface tension, *Journal of Colloid and Interface Science* (2019), **538**, 75-82.

Originality and Copyright Declaration

I, M. Haris Khan, declare that all the material presented in this thesis is my own work except where noted.

The copyright of this thesis rests with the author and is made available under a Creative Commons Attribution Non-Commercial No Derivatives licence. Researchers are free to copy, distribute or transmit the thesis on the condition that they attribute it, that they do not use it for commercial purposes and that they do not alter, transform or build upon it. For any reuse or redistribution, researchers must make clear to others the licence terms of this work.

Abbreviations

AES – Alcohol Ethoxysulfate

CHOL – Cholesterol

DIB– Droplet Interface Bilayer

DLS– Dynamic Light Scattering

DMPC – 1,2-dimyristoyl-sn-glycero-3-phosphocholine

DOPC – 1,2-dioleoyl-sn-glycero-3-phosphocholine

DOPE – 1,2-dioleoyl-sn-glycero-3-phosphoethanolamine

DOPS – 1,2-dioleoyl-sn-glycero-3-phospho-L-serine

DPhPC – 1,2-diphytanoyl-sn-glycero-3-phosphocholine

DSC – Differential Scanning Calorimetry

LAS – Linear Alkylbenzene Sulphonate

LCRA– Liposome Calcein Release Assay

LLC– Lyotropic Liquid Crystals

NI – Non-ionic Alcohol Ethoxylates

PBS– Phosphate Buffer Saline

SAXS – Small Angle X-ray Scattering

SDS – Sodium Dodecyl Sulfate

SM – Sphingomyelin

SUV– Small Unilamellar Vesicles

TLC– Thermotropic Liquid Crystals

TX-100 – Triton X-100

WAXS – Wide Angle X-ray Scattering

Table of Contents

Abstract 1
Acknowledgements 3
Publications 5
Originality and Copyright Declaration 6
Abbreviations 7

Chapter 1 - Introduction 13
1.1 Thesis Overview 13
1.1.1 Chapter Outline 14
1.2 Amphiphilic Systems 14
1.2.1 Surfactants 15
1.2.2 Surfactant Phase Behaviours 16
1.2.3 Temperature Instability 22
1.2.3.1 Precipitation Instability 23
1.2.4 Technique to determine Liquid Crystalline Phase 25
1.2.4.1 Structural Analysis 25
1.2.4.1.1 Small-Angle X-Ray Scattering 27
1.2.4.1.2 Wide-Angle X-Ray Scattering 27
1.2.4.2 Thermal Analysis 28
1.3 Concentrated Surfactant Systems 29
1.3.1 Liquid Detergents 29
1.3.2 Ocular Health and Safety Regulations 30
1.3.3 Eye Irritancy Test 32
1.3.3.1 In-Vivo Draize eye test 32
1.3.3.2 Other in-vitro alternatives 34
1.4 Membrane Biophysics 35
1.4.1 Biological Membranes 35
1.4.1.1 Membrane Compositions 36
1.4.2 Lipids 36
1.4.2.1 Lipids Flip-Flop and Bi-Layer Scrambling 37
1.4.3 Models Membrane 37
1.4.3.1 Droplet Interface Bilayers (DIBs) 38
1.4.3.2 Liposomes 39
1.5 Thesis Aims 40

Chapter 2 – Materials and Methods Overview 42
2.1 Surfactants 42
2.2 Organic Solvent 43
2.3 Lipids 43
2.4 Fluorescent Dye 45
2.5 Surface Tension Measurements 45
2.6 Conductivity Experiments 47
2.7 Dynamic Light Scattering Experiments 48
2.8 Differential Scanning Calorimetry 49
2.9 X-Ray Scattering 50
2.10 Droplet Interface Bilayer (DIBs) Experiments 51
2.10.1 DIBs Formations 51
2.10.2 PDMS well construction 51
2.11 Microscopy Experiments 52
2.12 Lipid Vesicle Preparation 53
2.13 Liposome-Calcein Release Assay 54
2.13.1 Calcein Encapsulated SUV Preparation 54
2.14 Fluorimeter Experiments 55

Chapter 3 - Effect of organic solvent and electrolytes on Krafft point of SDS 56
3.1 Overview 56
3.2 Introduction 56
3.2.1 SDS Phase Behaviour 57
3.2.2 Micellization 58
3.2.2.1 Solvophobic Interactions 59
3.2.2.2 Electrolyte Interactions 60
3.2.3 Surface Tension 62
3.2.3.1 Surface Tension Models 63
3.3 Experimental 64
3.3.1 Materials and Compositions 64
3.3.2 Surface Tension 64
3.3.2.1 Pendant drop method validation 64
3.3.3 Krafft temperature 66
3.3.4 Conductivity 67
3.3.5 DSC 67
3.4 Results and Discussion 68

3.4.1 CMC Determinations 68
3.4.1.1 Surface tension vs Conductivity 69
3.4.1.2 Solvophobic Effects 77
3.4.1.3 Effect of Electrolytes 80
3.4.2 Krafft Temperature Determination 82
3.4.2.1 DSC experiments 82
3.4.2.2 Surface tension vs Temperature 82
3.4.2.3 Effect of Glycerol and NaCl on T_K 84
3.4.3 Pendant Drop Method 88
3.4.4 Alterations to the Krafft point of SDS 88
3.5 Chapter Conclusions 91

Chapter 4 – SDS phase Behaviour in Organic Solvent 93
4.1 Overview 93
4.2 Introduction 93
4.2.1 SDS Hydrated Crystals 94
4.2.2 DSC 95
4.2.3 X-ray Scattering 97
4.2.3.1 SAXS 97
4.2.3.2 WAXS 98
4.3 Experimental 98
4.3.1 Materials and Compositions 99
4.3.2 DSC analysis 99
4.3.3 X-ray Scattering 99
4.4 Results and Discussion 100
4.4.1 DSC Analysis 100
4.4.1.1 SDS-water control system 100
4.4.1.2 Effect of glycerol 106
4.4.2 X-ray Scattering Analysis 113
4.4.2.1 Temperature Resolved 114
4.4.2.1.1 SDS-Water Systems 114
4.4.2.1.2 SDS-Glycerol Systems 119
4.4.2. Linkam Analysis 125
4.4.3 SDS Phase Diagrams 131
4.5 Chapter Conclusions 134

Chapter 5 - Eye irritation determination for complex surfactant formulations 136
5.1 Overview 136
5.2 Introduction 136
5.2.1 Liquid Detergent Formulations 137
5.2.2 Ocular Irritancy 138
5.2.2.1 Eye Structure 138
5.2.3 Current Methods 140
5.2.3.1 *Ex-vivo* – Isolated Chicken Eye test 141
5.2.4 Lipid membrane models 144
5.2.4.1 Droplets Interface Bilayers (DIBs) 144
5.2.4.2 Liposomes Leakage Assay 145
5.3 Experimental 147
5.3.1 Detergent Formulations 147
5.3.2 Surface Tension 148
5.3.3 DIBs 148
5.3.4 Liposome-Calcein Release Assay 148
5.3.4.1 Liposome composition 149
5.3.4.2 Fluorimeter experiments 149
5.4 Results and Discussion 150
5.4.1 Detergent samples CMC and ICE irritation correlation 150
5.4.1.1 Surface tension and CMC of detergents 150
5.4.1.2 CMC vs ICE irritation 153
5.4.1.3 ICE test data review 154
5.4.2 DIBs as Corneal Epithelium membrane model 156
5.4.2.1 DIBs formation and stability 157
5.4.2.2 Detergent interactions with DIBs 158
5.4.3 Liposomes as Corneal Epithelium membrane model 163
5.4.3.1 SUVs Characterisation 163
5.4.3.2 LCRA controls 164
5.4.3.3 Calcein release data analysis 166
5.4.3.4 Calcein release vs ICE test data 172
5.5 Chapter Conclusions 175

Chapter 6 – Interactions between Surfactants and Lipid membrane 177
6.1 Overview 177
6.2 Introduction 177
6.2.1 Surfactant Systems 178

6.2.1.1 Anionic Surfactants 178
6.2.1.2 Non-ionic Surfactants 179
6.2.2 Lipid bilayer- surfactant interaction 180
6.2.2.1 Triton X-100 mode of solubilisation 180
6.3 Experimental 183
6.3.1 Materials and Compositions 183
6.3.2 Surface Tension 183
6.3.3 LCRA 184
6.3.4 DLS- Particle size analysis 184
6.4 Results and Discussion 185
6.4.1 CMC of various surfactant systems 185
6.4.1.1 Single surfactant systems 186
6.4.1.2 Co-surfactants systems 189
6.4.2 LCRA 190
6.4.2.1 Individual surfactant systems 191
6.4.2.1.1 Temperature effect on liposome permeation 195
6.4.2.2 Binary systems 197
6.4.2.3 Ternary systems 199
6.4.3 DLS-particle size analysis 202
6.4.3.1 Individual surfactants 203
6.4.3.2 Binary system 211
6.4.3.3 Ternary system 213
6.4.4 Surfactant-lipid bilayer interactions 216
6.4.4.1 Solubilisation mechanism 218
6.4.4.2 Corneal swelling - % Calcein release relationship 221
6.5 Chapter Conclusions 223

Chapter 7 – Conclusions and Further Work 224
7.1 Summary of Findings 224
7.2 Further Work 227

References 229
Appendix 238

Chapter 1
Introduction

Parts of this introduction chapter has been published by me as; Haris Khan et al, Effect of glycerol with sodium chloride on the Krafft point of sodium dodecyl sulfate using surface tension, *Journal of Colloid and Interface Science* (2019), **538**, 75-82.[1]

1.1 THESIS OVERVIEW

Surfactants are used in a wide range of industries, including pharmaceutical, oil extraction, agrochemicals, food industry, household and personal care industry, in many applications such as medicines, food stabilisers, cosmetics, shampoos and laundry detergents.[2, 3] Formulated systems containing high concentration of surfactants e.g. liquid detergents, shampoos, involves temperature stability challenges and ocular hazard safety concerns.[4] Dealing with these concerns and resolving these challenges usually entails costly, time-consuming research, which may not translate in to robust, commercially successful product.[4, 5]

This thesis aims to provide an insight into some of the undesirable properties of, and the challenges associated with concentrated surfactant systems, in the context of low temperature stability (molecular interactions within surfactant formulations) and ocular irritancy (interactions between surfactants and lipid membranes). This thesis is divided into two broad sections. After this introduction chapter and chapter 2, which give an overview of the methods and materials, the first two data chapters, 3 and 4, look in to the molecular interactions of surfactants in organic solvents in order to determine and control the temperature instability of high surfactant formulations. Then chapter 5 and 6 provide further insights into how concentrated surfactant systems interact with lipid membranes, together with developing assays to determine the permeation of detergent surfactants through the lipid bilayer. Chapter 7 summarises the conclusions and discusses further potential projects which can build on the research from this thesis.

1.1.1 Chapter Outline

This chapter provides the readers with the relevant background information regarding the topics of interest as well as to provide a context to the significance of this work in the current scientific research. The first few sections of this chapter, from 1.2 to 1.2.4, gives a general overview of amphiphilic systems, particularly surfactants, their phase behaviour and interactions in liquid systems, various factors which effect these interactions, the stability challenges encountered in formulating with concentrated surfactant systems and the techniques used to study them.

Section 1.3 of this chapter outlines the safety aspects of these surfactant systems with regards to the ocular irritancy, highlighting the various irritancy categories and the limitations of current *in vitro* eye irritancy test methods. The use of lipid membrane models are also discussed in section 1.4, with a brief overview of the membrane biophysics and potential techniques which can be used as complimentary *in vitro* eye irritancy test.

1.2 AMPHIPHILIC SYSTEMS

Amphiphiles are complex organic molecules containing both hydrophilic and hydrophobic components.[6] The hydrophilic region forms the polar 'head' group which dissolves in water, while the hydrophobic region consists of hydrocarbon chain(s) forming the 'tail'.[6, 7] This structural property of amphiphiles enables them to self-assemble in polar and non-polar solvents to form a large variety of specific aggregates, depending on a number of conditions.[7, 8] Fig 1.1 illustrate this amphiphilic structure, using sodium dodecyl sulfate as an example. Surfactants and lipids are the most relevant groups of amphiphiles as they form part of fundamental biochemical and physiochemical processes.[8] Hence, there has been a vast global interest and intensive research being carried out for decades in studying these amphiphilic systems. The first part of the introduction mainly focuses on surfactants, but many of the principles and properties discussed are applicable to lipid systems as well.



Fig 1.1 – Chemical structure of an anionic surfactant (SDS), illustrating its amphiphilic nature with the polar headgroup region and the hydrophobic hydrocarbon tail.

1.2.1 Surfactants

Surfactants are surface active agents, which lowers the surface tension of liquids by diffusing at the solvent-air interface. In an aqueous solution, at low concentrations, the surfactant monomer would dissolve the hydrophilic headgroup in water while extending the hydrophobic tail in air.[2, 8] This arrangement satisfies the hydrophobic effect of the tails. The amphiphilic properties of surfactants allows water to solubilise dirt and oil/grease when used in detergents and also to act as emulsifying agents in systems which contain both hydrophilic and lipophilic ingredients.[9] Which surfactant to use for such applications is governed by the degree of hydrophilicity to hydrophobicity, which is identified through a hydrophilic-lipophilic balance scale.[10] A high HLB value specifies a more water soluble surfactant and vice-versa.[11, 12] The right choice of surfactant(s) effectively stabilises the system by forming a colloidal dispersion. The formation of these colloids and their physicochemical properties (their quality and ability to remain as a homogenous dispersion) is dependent on several factors such as temperature, additives (co-surfactants, electrolytes), surfactant polar headgroup charge, the length of hydrocarbon chain, linear or branched tail, thermodynamics formation, etc.[2, 8, 9]

Another criteria for choosing the type of surfactant, for a particular application, can based on the charge of the polar headgroup. Amphiphiles are commonly categorised into four headgroup types as shown in Fig 1.2, anionic, cationic, non-ionic and zwitterionic.[2, 3, 6, 8] Anionic surfactants mostly consist of sulphates or sulphonates and are widely used in detergent / washing formulation due to their economical

manufacturing.[13] Therefore anionics will be the main surfactant type of interest in this research. Cationics typically contain amines and are used as antiseptic or conditioning agents such as cethyltrimethlyammonium chloride (CTAC).[8, 9] A headgroup with no charge is called non-ionic, which are compatible with any of the other types of surfactants. They are commonly used as co-surfactant to help stabilise the system[13, 14] and are part of the detergent formulations used in this thesis. Zwitterionic surfactants have an overall neutral charge at neutral pH as it consist of two oppositely charged headgroup, with carboxylate group typically forming the negatively charge group and ammonium the positive group.[2, 15] These are ideal for cosmetic and personal care formulations as less irritating to the skin and eyes compared to the others.[8, 9]

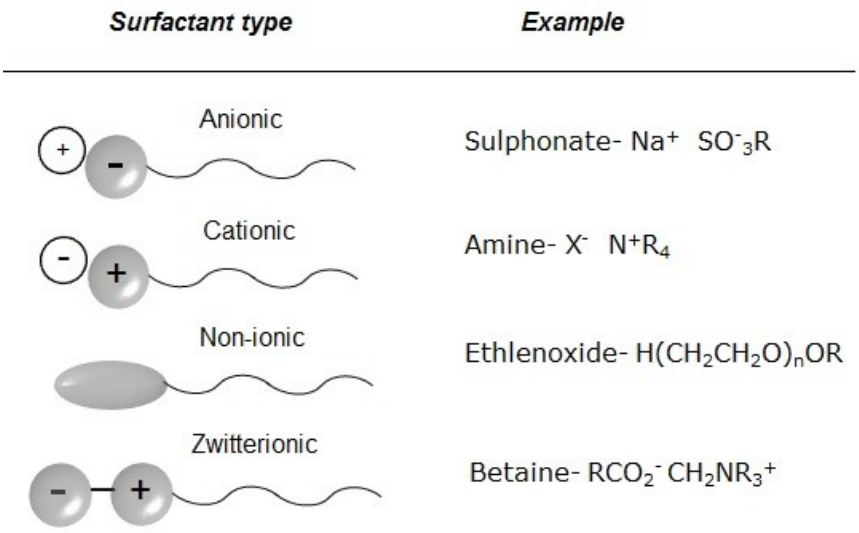


Fig 1.2 – Schematic structures of different type of surfactants.

1.2.2 Surfactant Phase Behaviours

As mentioned above, the surfactant monomers arrange themselves at the surface of an aqueous solution, at low concentrations, forming a complete monolayer. As the surfactant concentration increases, the monomers start to form structures within the bulk solution to conform to the hydrophobic effect. Therefore surfactant forms aggregates which drives the tails into a core, protected from the aqueous environment by the polar head groups, forming a structure known as micelles.[16, 17] This formation of micelles, called micellization is driven by an increase in entropy as the hydrocarbon

tail adopts a more favourable position (away from the aqueous solution) and the aqueous structure surrounding the tail becomes more disordered.[16, 17] The concentration at which these surfactants begin to form these micelle structures is called the critical micelle concentration (CMC).[18] Even above CMC levels, the surfactant monomers still exist, but are in equilibrium with the micelles and are exchanged between the two phases.[7, 18] The transformation of monomers into micelles induces certain physical changes to the bulk solution which allows for this concentration point to be determined. This point usually involved changes to the rate of change of a physical property like electrical conductivity, surface tension, self-diffusion and turbidity as showcased in Fig 1.3.[8, 19] Conductivity and surface tension are most commonly measured over increasing surfactant concentration to determine the CMC.

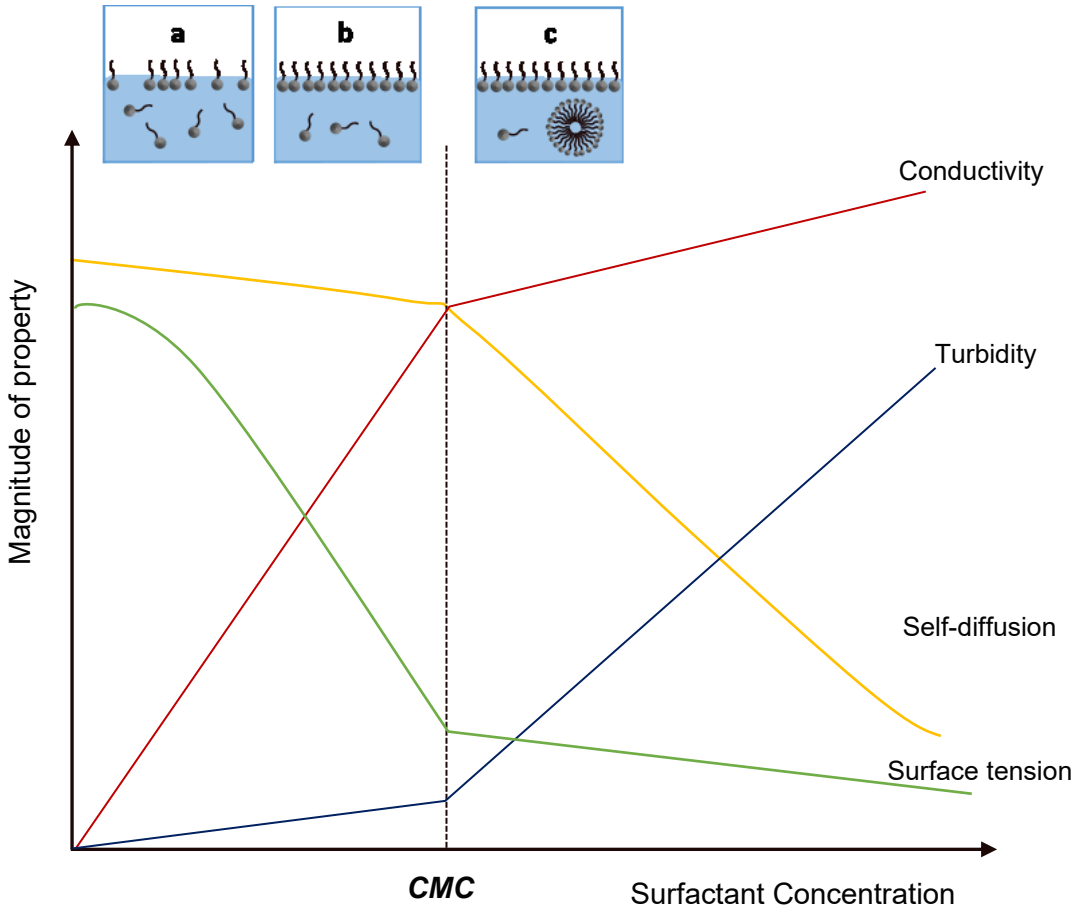


Fig 1.3 – Schematic of some physical properties of surfactants, which undergo a change/breaking point at concentrations above which micelles are form (CMC). **a** - Surfactants monomers at the surface of water-air interface, **b** - Surface saturated with monomers and **c** – Micelles forming. Adapted from given references.[8, 17, 19]

In order for this self-assembly of micelles to be favourable/ spontaneous, the aggregates has to have a lower entropy (higher order) and the surrounding to be more disordered (higher entropy).[20] Therefore the thermodynamics of micellization is driven by the competing hydrophobic interaction between the hydrocarbon chain and water, the interactions between the hydrophilic head-group and the surrounding solvent, the head-group electrostatic and/or steric repulsion and the order/disorder of the solvent system.[8, 17, 21] The shape and size of the micelles is highly dependent on molecular geometry of surfactant molecule and concentration, solution conditions (temperature, pH, electrolytes), as well as the interactions mentioned above which contribute to the packing parameter.[22] Close to the CMC level, micelles are near spherical in shape for surfactants. Upon increase in surfactant concentration, the size and number of micelles grows, from a globular to a rod-like/ worm-like shape to accommodate the extra monomers while preventing a void space at the core.[23] The molecular geometry (desired curvature) of the surfactant is governed by the size of the head-group and hydrocarbon tail.[16] The critical packing parameter (CPP) equates the head-group to tail size ratio to the curvature of the surfactant monomer, which in turn can be used to determine the aggregate structure.[17, 23] Equation 1 shows this association, where v is the hydrocarbon chain volume, a_0 is the surface area per head group and l_c the extended chain length.

$$CPP = \frac{v}{a_0\, l_c} \qquad (1.1)$$

The CPP can be categorised based on the aggregate morphology that is favourable to be produced as shown in Fig 1.4. A small CPP value (< 1/3) indicates a large head-group to tail ratio which results in highly curved micelles also denoted as ‘type 1’ curvature.[17, 22] For CPP values between 1/3 and 1/2, a cylindrical micelle is produced which leads to a spherical bilayer structures called vesicles or liposomes with a CPP above 1/2 and below 1. A ‘type 0’ curvature is produced when CPP is ~1, which gives a cylindrical surfactant morphology, creating a planar bilayer (lamellar) aggregate structure.[22, 24] CPP above 1 (curvature type 2) is commonly seen with surfactant (or lipid) containing a small head-group and two hydrocarbon chain which can produce inverse micelle/ hexagonal aggregates.[17, 22]

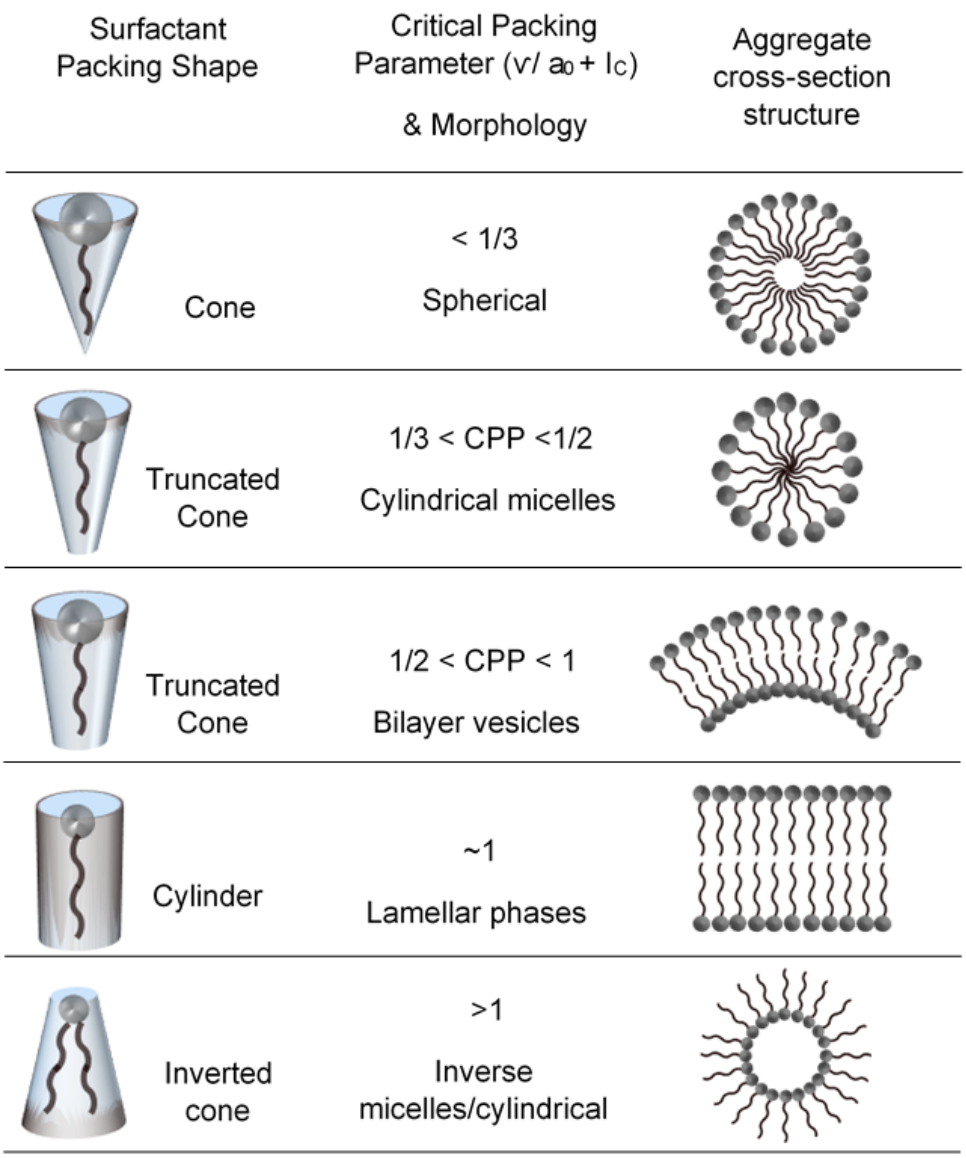


Fig 1.4 – Schematic of surfactant self-assembled structures in relation to the critical packing parameter. Adapted from given references [17, 22]

As previously mentioned above, the concentration of amphiphiles determines the structure of the self-assembling aggregates. Around the CMC, micelles and free monomers are dispersed randomly within the solution. When the surfactant concentration increases, the self-assembled micelles arrange in to a long range order, while the free monomers are in more of a short range order.[25] This arrangement of aggregates in the solution creates a physical state known as the lyotropic liquid crystals (LLC).[22, 26] There are a number of different LLC phases that can form, majorly depending on the intra and inter-micellar interactions as previously mentioned.[22, 27]

Fig 1.5 presents a schematic illustration of the various LLC phases formed as the concentration of amphiphiles increases, across both types of surfactant curvatures.

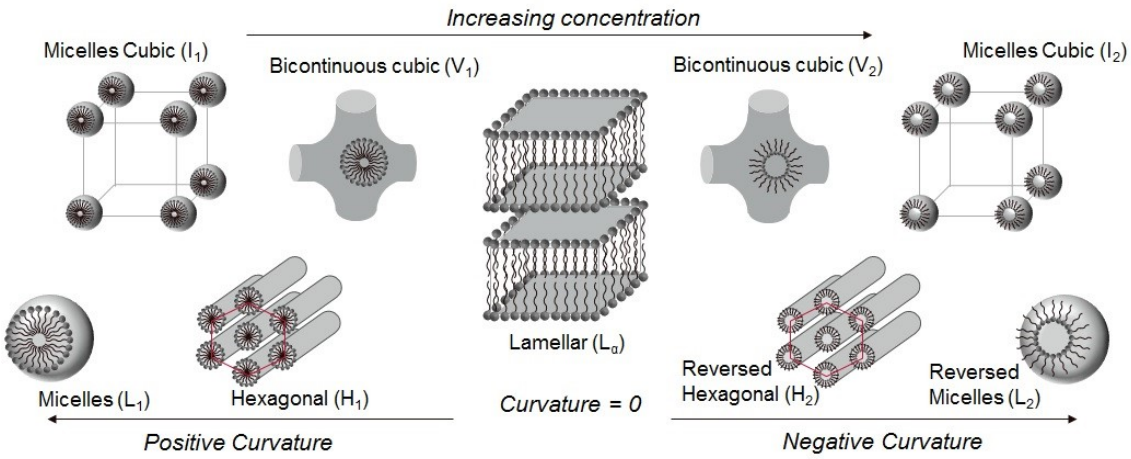


Fig 1.5 – Schematic of some lyotropic liquid crystals structure formed by self-assembling surfactants depending on the system composition, redrawn from[8, 22, 24]

The different LLC mesophases have been studied extensively, as a comprehensive understanding of these nanostructure enables them to be controlled, fabricated and developed into a wide range of technological applications, e.g. targeted drug delivery vesicles, membrane ion-channel mimic and stable / longer shelf-life products. Since these LLC phases are dependent on the surfactant type, concentration, temperature etc., a surfactant phase diagram is typically constructed to track its phase behaviour over concentration as a function of temperature.[23, 27] Amongst the many different amphiphiles studied for LLC learnings, ionic surfactants have been a prominent surfactant type since they can be modified according to the application needs.[28] Sodium dodecyl sulfate is one of the anionic surfactants which has been extensively studied, particularly with regards to its LLC phases in aqueous mixtures.[3, 20, 29-31] Since the focus of this project is detergent formulations, which mainly contain anionic surfactants, SDS will be used as a model surfactant for the first part of this thesis.

In an aqueous solution, the solubility of SDS decreases as the temperature decreases.[17, 30] Below a certain temperature, known as the Krafft temperature (T_K) boundary or solubility boundary, the SDS precipitates in the solution forming a hydrated crystalline phase (H_C), containing ordered and densely packed hydrocarbon chains.[32] A schematic phase diagram of SDS in water is provided in Fig 1.6, showing the main transition points / boundaries. For SDS micelles (L_1) to form in water, the level of surfactant has to be above the CMC and the temperature of the aqueous solution above the solubility boundary, which is typically reported to be between 6.9 – 8.3 mM and 14 – 16 °C respectively.[8, 9, 17, 18] This critical transition point where the CMC curves and the T_K intersect is known as the Krafft point.[17, 33] The Krafft point is an important characteristic of surfactants, as it establishes the parameters under which surfactants can carry out its intended role, e.g. emulsification, foaming, lipid solubilisation, etc., and therefore influence the composition of surfactant containing formulations.[3]

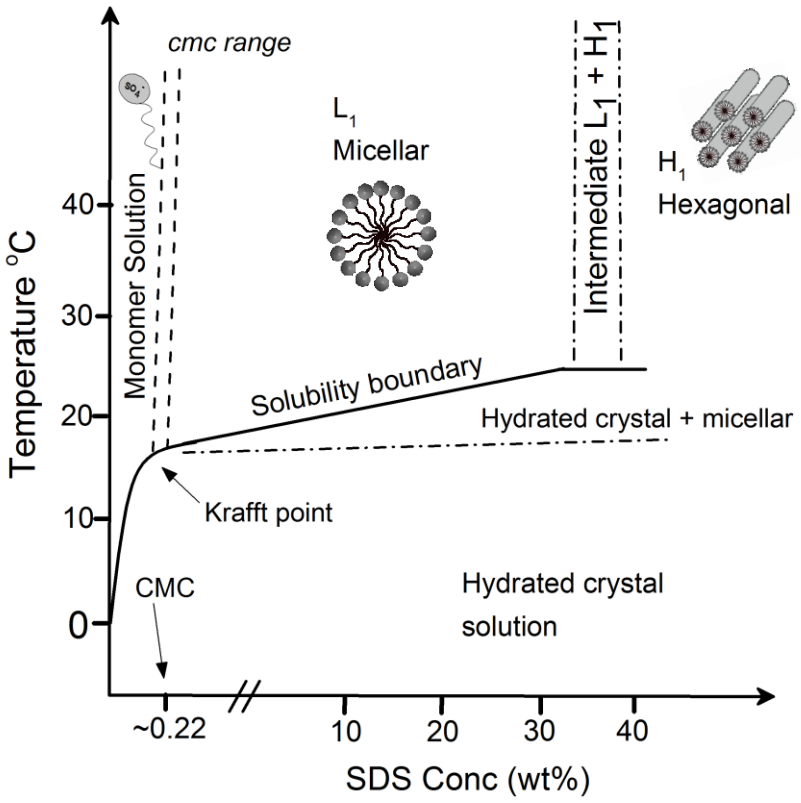


Fig 1.6 – Schematic of SDS phase diagram in water, showing aggregates in up to concentrations of 40 wt%, highlighting the Krafft point at the intersection between the solubility boundary (Krafft temperature) and CMC. Adapted from given references.[8, 34]

At low temperatures (below 15 °C) as the surfactant precipitates, forming partially rigid SDS hydrates (H_C) containing orientationally ordered chains creates a state known as the thermotropic liquid-crystalline phases (TLC).[35] A variety of SDS H_C morphologies can form as a function of temperature / hydration state, which will be discussed later in this chapter. At low SDS concentration (above the CMC level), as the temperature is increased close to 14 °C, the H_C hydrocarbon chain become less ordered and begin to transform in to L_1 phase.[35, 36] During this transition, there is a narrow region where the H_C and L_1 phases co-exist.[30] This region becomes wider as the surfactant concentration increases.

At surfactant concentrations of up to ~34 wt%, the SDS aggregates remain in the L_1 phase, with increasing, elongated micellar cylinders being formed.[30, 37] Above 35 wt% SDS, these cylindrical micelles begin to arrange themselves in to a hexagonal lattice, forming 'type 1' hexagonal (H_1) LLC phase. An intermediate is created between 35 to 38 wt% SDS concentration where the L_1 and H_1 phases co-exist, and above 38 wt% the H_1 transition is completed. The SDS phase behaviour will only be explored up to 40 wt% concentration in this thesis, as this study focuses on liquid detergent formulations, which usually contain a maximum of 40 wt% total surfactant level. A detailed SDS phase diagram has been established by Kékicheff, P et al (1989), which can be referred to for understanding the phase behaviour from 30 to 100 wt% SDS level.[30]

Although there has been a substantial amount of work carried out in understanding the phase transitions of SDS and the effect of co-solvents, co-surfactants, electrotypes etc., a comprehensive phase diagram has not been established for SDS in organic solvents, particular for precipitation transitions occurring at low temperatures.

1.2.3 Temperature Instability

Temperature is a major contributing factor towards colloidal / physical stability failures in surfactant-based formulations. Phase separation and precipitation are common instability issues seen in a range of product types, which directly affects the

shelf-life of a product.[9, 38] Phase separation at high temperatures is a common failure mode for emulsion-based formulations such as lotions, conditioners and mayonnaise, which can occur through a series of mechanism like flocculation and coalescence leading to sedimentation or creaming as shown in Fig 1.7.[39, 40] Precipitation commonly occurs in concentrated surfactant formulations at low temperature as the solubility limit is surpassed and there is an agglomeration of hydrates, as explained above for SDS phase behaviour.[38] Since the stability failure mode of interest in this thesis is precipitation, the main focus will be the TLC phases forming at low temperature for SDS systems.

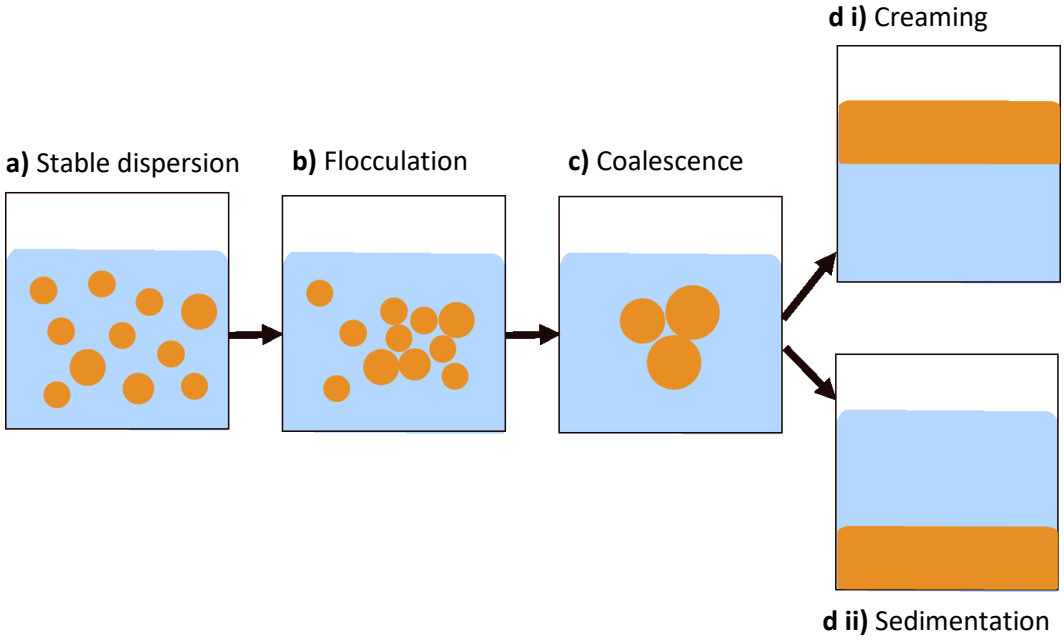


Fig 1.7 – Schematics of phase separation failure modes; a) stable colloidal system b) colloids clump together into a floc, c) the colloids coalesce forming large aggregates and either d i) float to the top- creaming or ii) sediment to the bottom. Adapted from given references.[9, 39, 40]

1.2.3.1 Precipitation instability

Precipitation, also called crystallisation for surfactant system, is a reversible change (depending on the rate of change), however it is considered a stability failure mode for

liquid formulations as it changes its appearance to a seemingly unstable and unappealing product. Crystallisation of surfactants not only occurs at low temperatures, but can be formed above room temperatures by changing the composition of the system, particular the solvent properties and the surfactant concentration.[41] Fig 1.8 shows the changing solubility of 20 wt% SDS in various water-glycerol mixtures, at 20 °C. As the level of glycerol is increased in the mixture, SDS become increasingly insoluble. The extent of precipitation and size of SDS H_C is known to grow with decreasing temperatures and aqueous levels for these systems.[36, 42]

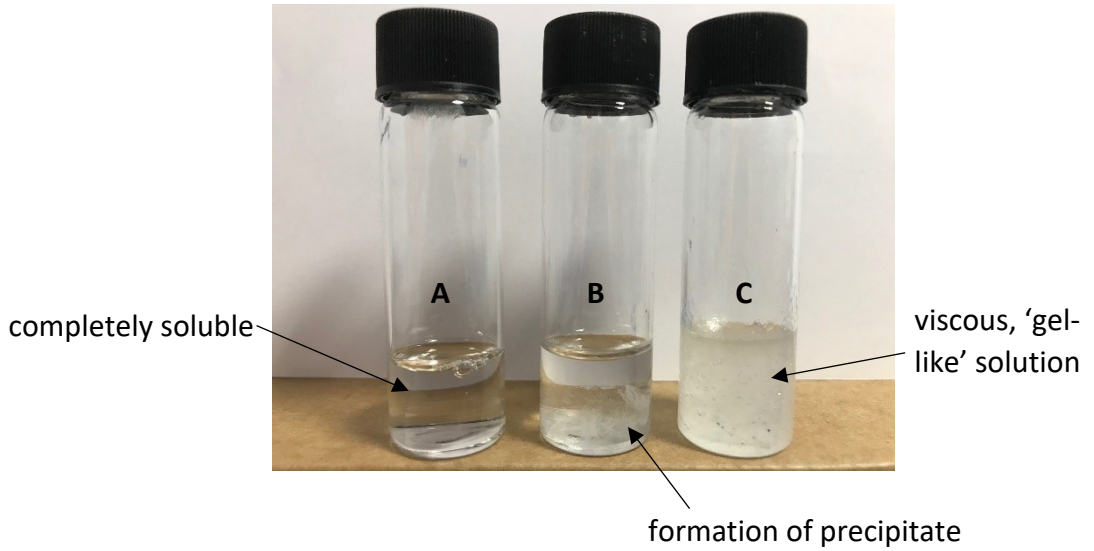


Fig 1.8 – Photograph showing the solubility of 20 wt% SDS in various water-glycerol mixtures: **A**- 80-20 wt%, **B**- 60-40 wt% and **C**- 40-60 wt%. at 20 °C.

A variety of SDS H_C morphologies can form as a function of temperature and more importantly, the cooling rate of the system.[42, 43] The crystallisation process of surfactant consists of two steps; nucleation and crystal growth.[44] All the SDS hydrate structures have been revealed to consist of a higher order lamellar structure, with varying levels of bilayer thickness and hydration levels.[32] These concepts are discussed in further details in chapter 4.

1.2.4 Techniques to determine Liquid Crystalline Phase

There are a number of techniques which can be used to determine the LLC and TLC phases of surfactants, which can provide some structural and phase transition temperature details, as well as thermodynamical knowledge of the various liquid crystals formed.[26] These techniques include, X-ray and neutron scattering methods, Nuclear Magnetic Resonance (NMR), Differential Scanning Calorimetry (DSC), polarising light and transmission electron microscopies.[26, 45] Scattering techniques are commonly used for studying translational order and analysing liquid crystalline structures with DSC as a complimentary method to detect phase transition temperatures of the various transformations of amphiphiles.[45-47] Since one of the focus of this thesis is to identify the various liquid crystal structures and their transition temperature across the precipitation boundary, only structural techniques like scattering and calorimetry principles for thermal analysis are discussed in this thesis. Below is an overview of these techniques, with a more detailed account given in the chapter 4.

1.2.4.1 Structural Analysis

X-ray scattering techniques are a power tool to determine the structural properties and physical characterises of liquid crystals.[48] X-ray scattering occurs when a radiation with a wavelength comparable to atomic spacing, interacts with an electron, the reflected waves travel in all directions.[49]

When these incident X-ray waves irradiate on a series of sequential atoms in a crystalline lattice, at certain angles and directions (vector), the diffraction peaks (maxima) are aligned and hence the scattered X-rays are ‘in phase’, which is known as constructive interference.[48, 50] The waves will only be ‘in phase’ when the phase shift is a multiple of 2π.[46] These ‘in phase’ scattered waves are detected accumulatively, revealing nanoscale information of the crystal particles present in the sample and hence providing a structural analysis.[48, 51] Crystalline lattices consist of parallel planes (denoted *hkl*), which are separated by an inter-planar distance ‘d’, so when the reflected X-ray waves from the various parallel planes are in phase, each consecutive wave is travelling further by a path length difference which is an integer multiple (n) of the wavelength (h).[46, 48, 49] Therefore, the path different between two

constructive interfering waves is given by the Bragg equation (1.2), where n is the order of reflection, λ is the wavelength of the incident X-ray, 2θ is the scattering angle and d_{hkl} is the inter-planar distance.[46, 48, 52] This principle is illustrated in Fig 1.9.

$$n\lambda = 2d_{hkl}\sin\theta \qquad (1.2)$$

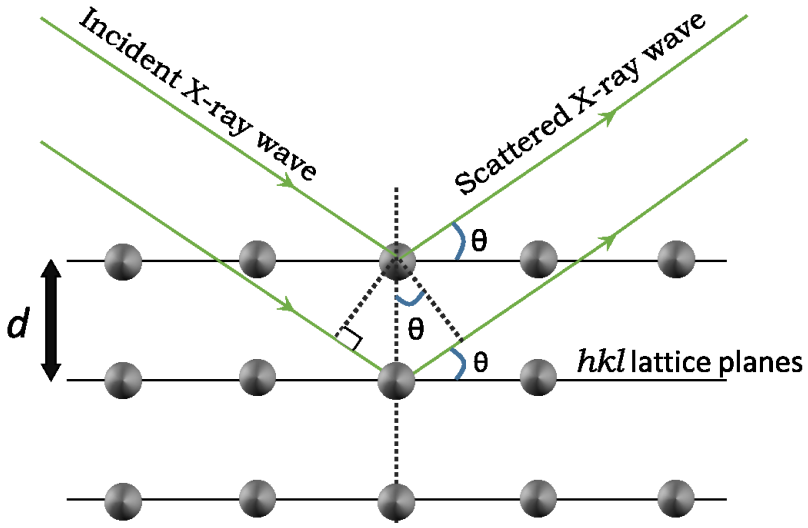


Fig 1.9 – Schematic showing the scattering of X-ray waves from parallel equidistant planes of a crystalline lattice (*hkl*), illustrating the inter-planer distance '*d*' and the angle '*θ*' of X-ray beams. Adapted from given references.[46, 49, 50]

The orientation of a crystal plane can be defined by how any parallel plane intersects the main crystallographic axes (i.e. passes through the origin). The integers hkl are known as the Miller Indices and are set of numbers which quantify the intercepts and therefore help identify the plane.[46, 48, 52] A diffraction pattern and Bragg peaks are obtained by measuring the scattering intensity *I(q)* against the scattering vector, *q*, which is a function of the incident angle (θ) and the wavelength of the incident radiation (λ), as define in equation 1.3.[46, 48] The Bragg peaks related to specific lattice

$$q = |q| = \frac{4\pi \sin\theta}{\lambda} \qquad (1.3)$$

planes as a results of reciprocal lattice points (end of the reciprocal lattice vector |q|) intersecting the Ewald sphere as shown in Fig 1.10, which is determined by the scattered X-ray beam angle, satisfying the Bragg's law.[48] Therefore the vector q is reduced to ; $q = 2\pi / d$ and hence $1/d = q / 2\pi$.[46, 48, 50]

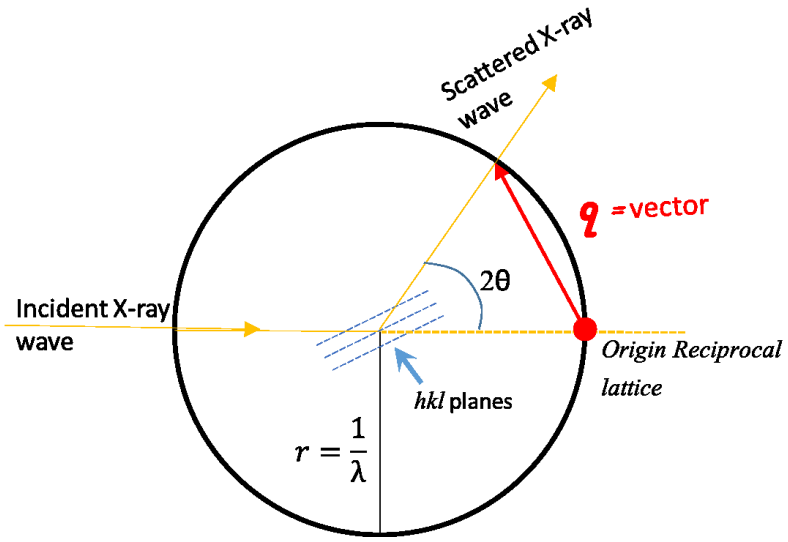


Fig 1.10 – Schematic of Ewald sphere. Adapted from given references.[48, 52]

1.2.4.1.1 Small-angle X-ray scattering

To determine structural information of long range ordered systems like micelles and lamellar phases, small-angle X-ray scattering (SAXS) is used as it analyses structures with a size range of 1 to over 100 nm.[51] SAXS uses a monochromatic X-ray beam to probe the crystal structures with scattering angle of less than 1°, resulting in Bragg peaks as function of the small scattering angle.[53] As previously illustrated (Fig 1.5), surfactants can transform into a range of different liquid crystal phases depending particularly on the system composition and temperature.[48] Each of these possible phases give a distinct scattering pattern and most of their corresponding Bragg peaks have been characterised.[46, 48, 54] Since there are a limited number of liquid crystals morphologies which can exist in a SDS systems, the crystal phases can be determined by comparing the detected scattering patterns with known model patterns.[48]

1.2.4.1.2 Wide-angle X-ray scattering

Wide-angle X-ray scattering (WAXS) is the same as SAXS, with the main difference being that the detector is placed at a longer distance from the sample.[48, 54] Therefore

WAXS covers a larger angular range (5-60°), which allows the structure to be probed at a much smaller length scale of interatomic distances of < 1 nm.[46, 48] From Bragg's law it is explained that as the scattering angle increases, smaller structural characterisation can be produced.[55] Hence WAXS analysis provides information about the state of the hydrocarbon chains of the surfactants. It can differentiate between the various SDS hydrates lamellar structures, however the high order TLC phases result in multiple sharp diffraction peaks in WAXS analysis which can be challenging to interpret.[56]

These X-ray scattering techniques are discussed in more detail, particularly regarding the structure analysis of surfactant aggregates and the SAXS diffraction patterns/ ratio of peak etc., in chapter 4.

1.2.4.2 Thermal Analysis

Differential scanning calorimetry (DSC) is used to detect changes in the physical properties of a sample.[57] These changes, such as phase transitions from a thermotropic to lyotropic liquid crystal, transitions between different liquid crystal phases and glass transitions, can be identified through the changes in the heat capacity of the system.[47] For example, as energy is required to change a liquid phase into a gas, the heat supplied to the system is measured, resulting in a peak representing the heat capacity.[58] The point of this thermal transition can be determine accurately by the DSC and hence phase transitions temperatures can be identified.[57, 58] Similarly for liquid crystals, as the various phase transitions occur it causes a difference in energy within the system, leading to the energy of the surrounding system to change.[59] The point and amount of these heat exchanges can differ depending on the rate of temperature change and whether the system is being cooled or heated.[30, 42] All this information can provide valuable insight into thermal behaviour of surfactant systems.

Further details regarding the workings of DSC is explained in the next chapter (section 2.8). For this project, the DSC was used in combination with X-ray scattering experiments to determine the effect of organic solvent on phase behaviour of SDS, identifying the impact on the various thermotropic crystal phases formed at low temperatures and to understand the changes occurring to the lyotropic liquid crystal phases.

1.3 CONCENTRATED SURFACTANT SYSTEMS

1.3.1 Liquid Detergents

A commercial liquid laundry detergent needs to satisfy a large number of requirements and therefore when developing the detergent samples, a number of factors and attributes need to be considered and specifications set.[5, 13] The main attributes include efficacy, stability and safety. An extensive evaluation on each of these features is carried out at the research & development stage, where the feasibility of the desired formulation and the commercial viability of the developed product is determined, based on the overall outcome of those evaluations.[5]

Liquid detergents are mainly concentrated surfactants in an aqueous-organic solvent mixture, with additional additives like enzymes and brighteners added to help solubilise specific dirt and improve whiteness respectively. Also polymers, binders and pH modifiers are added to enhance stability. The key active and bulk of the detergent formulation are surfactants, typically three or four. A list of common ingredients used in liquid detergents and a summary of their functions is provided in table 1.1.

A series of liquid detergent formulations manufactured by P&G were used as concentrated surfactant systems for the study carried out to develop lipid membrane models for eye irritation predictions.

Table 1.1 – Common types of ingredients used in liquid laundry detergents and their functions[13]

Ingredient	Function
Surfactants	Main active material in a liquid detergent as they allow for its primary function to be carried out of reducing the surface tension of water, emulsifying the soil/dirt for easy removal.
Polymers	E.g. PEGs. Used to provide structural strength to the formulation by acting as binders and/or rheology modifiers, allowing for desirable flowing properties.
Builders/ Chelating agents	E.g. EDTA and critic acid. Acts as stabiliser and water softeners by interacts with hard-water ions i.e. calcium, magnesium, etc.
Enzymes	Targets specific types of soils (e.g. protein based, fat based, cellulases) and breaks them down through catalytic action for easy removal.
pH modifiers	Balances the acids and bases in water to provide ideal pH conditions.
Optical brighteners	Improve the appearance of whiteness.
Preservatives	Used to prevent microbial growth
Perfume	Added for aesthetics/consumer appeal
Dyes	

1.3.2 Ocular Health & Safety Regulations.

The European Chemicals Agency (ECHA) was founded in June 2007, by the initiation of the Regulation, Evaluation, Authorisation and restriction of CHemicals (REACH), under the European Council.[60] The main purpose of REACH is to outline and communicate the information relating to the health and safety of chemical products/substances across the supply chain down to the customer/ end user.[61] Therefore ECHA has made it a legislative requirement and is responsible for the Classification, Labelling and Packaging (CLP) regulation that fall under the United Nations's Globally Harmonised System of Classification and Labelling of Chemicals (UN GHS rev.7, 2017).[62] The onus is on the manufacturers and distributers of chemical products/substances to identify, classify and communicate accurately the health hazards. One of the major health hazard groups is the *'serious eye damage/eye irritation'* classes established in the GHS.[63] The eye irritation hazard is categorised in to three broad levels; serious eye damage (category 1), irritants (category 2) and

non-irritants (no category).[62] Category 2 is further split in to two levels, 2A and 2B.[62, 64] Both category 2 sub-levels have a similar initial irritancy score, but substances can be classified as category 2B if the irritancy effect is reversed/ eye recovers within 7 days and are considered mildly irritating.[64] These categories are summarised in table 1.2.

Table 1.2 – UN GHS Classification Criteria for Eye Irritation Categorisation.[62]

Category	GHS Classification Criteria
Category 1 **Serious eye damage**	A substance that produces; a) in at least one animal, effects on the cornea, iris or conjunctiva that are not expected to reverse or have not fully reversed within an period of 21 days; and/or; b) in at least 2 of 3 tested animals a positive response of: corneal opacity ≥ 3 and/or iritis > 1.5, calculated as the mean scores, following grading at 24, 48, and 72 hours
Category 2/ 2A **Irritant**	Substances that have a potential to induce reversible eye irritation Substance that produces a positive response in at least 2 of 3 tested animals of: • corneal opacity ≥ 1; and/or • iritis ≥ 1; and/ or • conjunctival edema ≥ 2; and/or • conjunctival chemosis ≥ 2. calculated as the mean scores, following grading at 24, 48, and 72 hours; and such effects are usually reversible within 21 days.
Category 2/ 2B **Mild Irritant**	If a substance meets classification criteria for 2A and such effects can be reversible within 7 days, the substance can be considered mildly irritating to eyes and classified as 2B.
No Category **Non-irritant**	Minimal effect; clearing in less than 24 hours

Any sort of damage to the eyes can not only be painful but can lead to life altering incidents such as low vision or loss of eyesight completely. Therefore it is important to evaluate the potential risk substances can cause to the eye in order to have appropriate control measures and precautions in place. Hence it is vital that all substances are categorised accurately.

1.3.3 Eye Irritancy test

The main objective of any ocular irritancy test is to determine the potential damage that can be caused by a substance to the human eye. Since clinical trials using human subjects cannot be used for such vital and sensitive organ, the eye test ideally needs to be representative of the human eye and its responses. Therefore the assessment of eye irritation potential has traditionally involved the use of animal testing, which continues till date.[65] The overall assessment process involved as few steps before final hazard and its precautions are communicated (e.g. on the safety date sheets), which includes; testing maximum potential irritancy of a substance, consider the intended use of the substance and determine the probability of it entering the eye, from which an overall risk associated with the substance is calculated.[66]

The use of animals for testing has not only been controversial due to ethical concerns, but has also raised concerns regarding the lack of validity that the animal eye generates the same physiological response as the human eye.[66, 67] The Draize eye test, the most traditional animal test used, has been shown to give overestimation of human responses for most substances.[68] Due to these reasons, there has been a great push over the last decade or so to develop a more ethical, efficacious and cost-effect alternative test. There have been some promising *ex vivo* and *in vitro* alternative eye tests developed, but gaining approval for these tests to replace the Draize, animal eye test has been challenging.[63, 65]

An understanding the Draize test evaluation and other alternatives methods currently used is required to help recognise the subjective nature and the challenges involved respectively.

1.3.3.1 *In-vivo* Draize eye test

The Draize rabbit eye test,[69] initiated in 1944 by John H. Draize and his colleagues, has been evolved into an ocular irritancy test adopted globally by regulatory bodies. Although the Draize test has been modified over the decade to address certain concerns, majority of the issues still remain unresolved. The main controversy surrounding this method has been the ethical concerns of using live animals and

causing them suffering.[67, 70] Due to pre-screening methods, the testing of potentially severe eye irritants and damaging substances has been stopped, the number of animals used per substance significantly reduced, along with the exposure limit of the test substances, to reduce discomfort.[71] However this method is still used, particularly to distinguish and categorise the mild range eye irritants[63]. Other major concerns for this has been the subjectivity and reproducibility of the evaluations.[72]

A standardised guideline was issued to be used by the observers for the Draize eye test scoring system in order to help reduce the inconsistencies[73]. The crux of this *in-vivo* method, after applying the test substance, involves a visual assessment of the physiological responses to three part/tissues of the eye; the cornea, iris and conjunctiva.[69]

As shown in Table 1.3, this assessment is based on a numerical scoring scale through which an overall score is calculated and the ocular irritation is judged. Extra weighting is given to the cornea and iris assessment parameters in the scoring system as they play a vital role in protecting the vision.[66, 70] Even though the scoring is carried out by trained observers, it is subjective, which can be misleading particular for mid-level irritants (category 2A and 2B). This along with the animal to animal variability with regards to repeat experiments, causes poor reproducibility.[66, 70] Also it has found that the rabbit eye contains a few significant physiological differences to the human eye and is not as representative as previously thought.[66, 67]

Table 1.3 – Summarised Draize eye test weighted scoring for grading ocular irritation.[69]

Ocular tissue	Testing parameter	Scoring Scale	Total Score calculations	Max Score possible
Cornea	Degree of Opacity (O) Area involved (A)	0 – 4 0 – 4	O x A x 5	80
Iris	Congestion and haemorrhage (I)	0 – 2	I x 5	10
Conjuntiva	Redness (R) Chemosis (C) Discharge (D)	0 – 3 0 – 4 0 – 3	(R+C+D) x 2	20
		Final overall score =	Sum of total scores	110

1.3.3.2 Other *in-vitro* alternatives

There are several other established alternative *in-vitro* tests which have been developed other the years, with some gaining validation and approval for eye irritation testing under certain categories.[63] A basic understanding of some of these methods was gained, a summary of which is provided in Table 1.4, to help with method development for testing detergent samples.

Table 1.4 – Summary of alternative methods to the Draize eye test.

Model/Assay type	Characteristics / End point	Limitation	Validated Category / status
Organotypic models / Ex vivo			
Isolated eye (ICE,[74] BCOP[75])	Corneal swelling, opacity, permeability (fluorescein retention)	Subjective, no reversibility	Category 1 & No Category
Chorioallantoic membrane (CAM); Hen Egg Test (HEM-CAM),[76] Tryon Blue staining (CAM-TB)[65]	Haemorrhage, vasoconstriction, coagulation	Use of live embryo, no reversibility,	Ongoing validation
Cell based models / Assays			
Cytotoxicity methods; Neutral Re Uptake (NRU)[77]	Inhibition of update of neutral red	No reversibility, viscous material, non-soluble substances, extreme pH	Not Validated
Red Blood Cell (RBC) test[78]	Haemolysis, haemoglobin denaturation		Ongoing validation
Cell function based methods; Fluorescein Leakage (FL) test[79] Cytosensor Microphysiometer (CM)[65]	Permeability Cellular metabolism	No reversibility, limited testing substance	Category 1- Ongoing validation for others
Reconstructed Human Cornea Epithelium (RHCE) Model			
EpiOcular™ RHCE test[80]	Cell viability/ permeability	Oversensitive to alcohols, extreme pH	No Category
SkinEthic™ HCE test[81]	Tissue viability, quantification of cytokine release		Ongoing validation for Category 1

The ex-vivo models, the Bovine Corneal Opacity and Permeability (BCOP) and Isolated Chicken Eye (ICE) have shown some promise and have managed to gain

approval to classify category 1 and no category substances.[74, 75] The cell-based models and the Reconstructed Human Cornea Epithelium (RHCE) models are yet to find approval for more than one category.[63, 79] The table above also summarises the limitations of these methods and no reversibility is a common drawback, due to which no single in-vitro method has gained approval to completely replace the in vivo Draize eye test.[63, 64] The interactions and response to foreign substances entering the eye are likely to be different from *in-vivo* to *ex-vivo /in-vitro* and therefore the recovery response is extremely challenging to achieve with any *ex-vivo* /*in-vitro* testing.

Although no single method has been accepted to classify UN GHS category 2 (mild to moderate irritation), combining certain methods which serve different endpoints are being used to gain validation across all categories. The HET-CAM is recognised to be a promising model for predicting the conjunctival irritation, therefore combining this with a method which examines the corneal irritation, like the isolated eye method, can provide good link with the overall Draize test evaluation.[82]

Due to the approval of the ICE test for two irritation categories, this method was chosen as the 'reference' eye irritation test to develop an *in-vitro* method against. A sufficient amount of ICE testing had been carried out externally on P&G's liquid detergent samples and resulting data was made available for me to compare and correlate with the lipid membrane-based assay developed in this thesis.

1.4 MEMBRANE BIOPHYSICS

1.4.1 Biological membranes

A biological membrane defines the outer boundary of a biological cell and its internal cellular compartments i.e. organelles. These organelles such as the nucleus, mitochondria, golgi apparatus etc, play a key role in the functioning of the cell.[83] The biological membrane acts as a selectively permeable membrane, by only allowing specific solutes to pass through, separating and compartmentalising the organelles and their functions.[84] The primary roles of the semi-permeable membrane is to prevent foreign toxic substance from entering the cell and selectively allowing the required molecule to pass through (e.g. via receptors and channels).[83, 84] The mechanism of

transport across the membrane is categorised as either active, which is only mediated by carrier/receptor or passive, which can occur via simple diffusion, channelled diffusion and carriers.[83, 85, 86] Permeability through passive- simple diffusion mechanism is reflective of the structural packing of the membrane.[85] Therefore, the composition of the membrane has to be such that it supports its primary function.

1.4.1.1 Membrane compositions

The bulk of the membrane consist of lipids, which are assembled in a bilayer structure facilitated by their amphiphilic properties.[87] The nature of amphiphiles has been explained in the earlier sections of this chapter. The rest of the membrane is composed of integral and peripheral proteins and cholesterol.[83] Enriched regions of proteins and cholesterol within the bilayer form mircodomains which are of high order and rigidity, called lipid rafts.[88] The type of lipid can also influence the packing and hence the rigidity of the membrane.[84] Also the lipid membranes are known to be asymmetric, i.e. the lipid composition of the outer and inner monolayer of membrane is different, mostly to facilitate transmembrane transportation.[83] Fig 1.11 shows the schematic of a typical membrane.

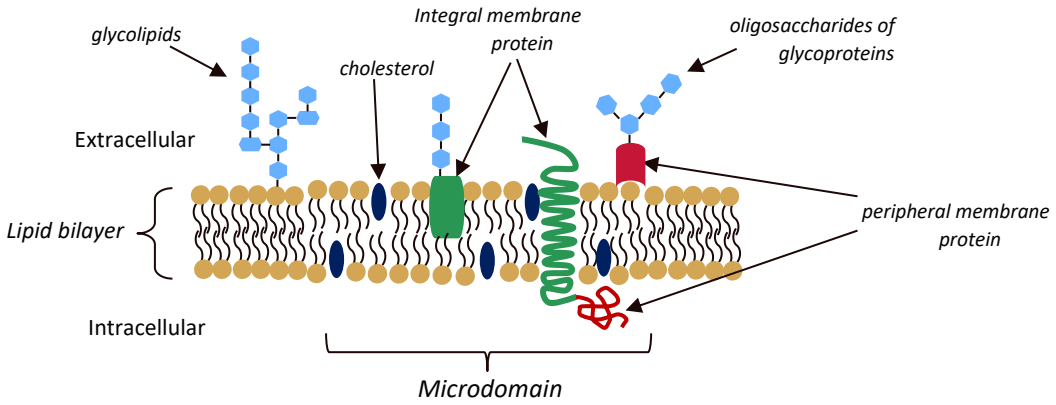


Fig 1.11 – Schematic representation of a cell membrane, showing the region of microdomains.

1.4.2 Lipids

There are numerous type of lipids present which can form membranes, which differ from each other base on their headgroup structure, length and number of hydrocarbon tail and whether or not the hydrocarbon chain is saturated.[83, 87] Like surfactants, lipids

are also categorised according to their headgroup types, which are divided in to three broad classes: Glycerophospholipids, Sphingolipids and glycolipids.[83, 84] Both glycerolphospholids and sphingolipids contain phosphorylate headgroups and therefore are grouped together as phospholipids. Glycolipids contains a sugar molecular as the headgroup.[83] Sterols, such as cholesterol are sometimes considered a sub-fourth category of lipids as they contain small, alcohol headgroup and a bulky fused ringed hydrocarbon tail, affecting the lipid bilayer mobility.[89]

Similar to surfactants, lipids also form different phases/ aggregates depending on the chemical structure of lipids and hence the curvature type, concentration of lipids in the system, temperature and solvent composition.[34, 87] The curvature types and phases explained previously in section 1.2.2 with regards to surfactants, are also applicable to lipids. Membrane lipids typically contain two fatty acid tails, whereas common surfactants contain only one, therefore the interactions between the two usually results in an altered monolayer curvature.[90]

1.4.2.1 Lipid Flip-Flop and Bilayer Scrambling

The mobility of the lipid membrane not only allows for movement of lipids within the bilayer plane, but also through the bilayer in a trans-bilayer motion commonly denoted as 'flip-flop'.[91, 92] These flip-flop mechanisms refers to the diffusion of single lipid molecules from one bilayer leaflet to the other, which are suggested to be either a slower spontaneous (several minutes to hours) or a more rapid enzyme-catalysed process (taking seconds) since it requires a hydrophilic headgroup to pass through the hydrophobic core of the bilayer. Another transmembrane mechanism, lipid scrambling, refers to the motion of a group of lipid molecules thought a passive transporters, usually induced by an impulsive defect in the bilayer leaflet.[92, 93] The addition of detergent to the lipid membrane is suggested to follow either of the mechanisms depending on the surfactant type and the membrane composition.[90, 92]

1.4.3 Models Membrane

The development of model/ artificial membranes has enabled researchers to study the behaviour and function of biological membranes. Although the complexity of the lipid

membrane structure, i.e. the different lipids and protein types present and asymmetry of the bilayer, is not fully matched in model membranes, the effect on the primary function of the membrane can be studied using these less complex models. The types of model membrane available include: droplet interface bilayers (DIBs)[94], liposomes /vesicles[95], supported lipid bilayer (SLB)[96] and planer lipid membrane (PLB).[97] DIBs and liposomes were explored in this thesis as potential models for corneal membrane and are discussed below in detail.

1.4.3.1 Droplet Interface Bilayers (DIBs)

Over the last decade, DIBs has been widely used to construct model membranes to study the physiological behaviour of biological membranes.[94] This concept initially developed by Bayley et al in 2008[94] and further advanced by Ces and co-workers,[98-101] allowed for more complex multi-component networks to be fabricated. As the name suggest, DIBs comprise of a lipid bilayer formed at the interface of two aqueous droplets.[94] These aqueous droplets are engulfed with lipid monolayers as they are submerged in a well of oil, enabled by the self-assembly of the lipids to the water-oil interface.[94, 98] As the two droplets are brought into contact with each other, they form a lipid bilayer membrane as illustrated in Fig. 1.12.

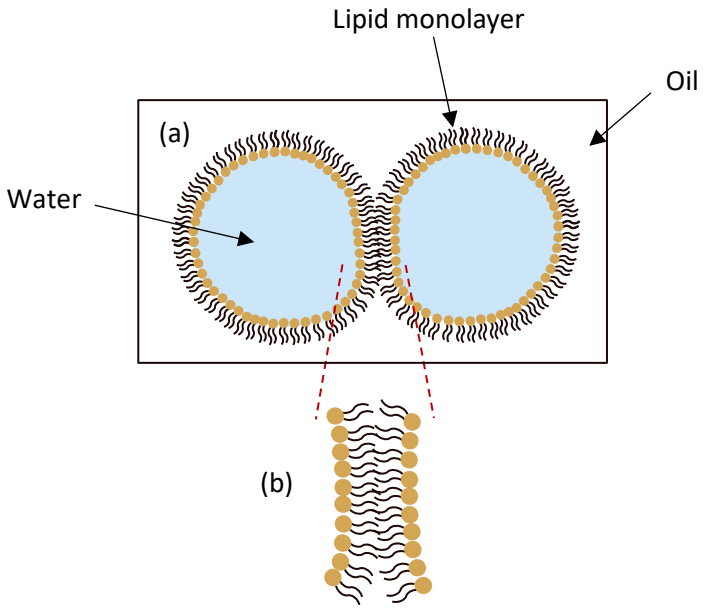


Fig 1.12 – Schematic showing (a) formation of DIBS with (b) a closer look at the lipid bilayer formed at the droplets interface. Adapted from.[94]

DIBs have been effectively used in studying membrane permeability, due to their high stability which allows for the incorporation of transmembrane pores.[102] This enabled cellular communication and translocation of substances across membrane to be explored.[100-102] Therefore the DIBs approach will be used as one of the model membranes to determine its potential for studying detergent-lipid bilayer interactions and whether it can be developed as a corneal epithelial membrane model.

1.4.3.2 Liposomes

Liposomes are microscopic spherical-shaped lipid vesicles containing a central aqueous compartment engulfed by one or more phospholipid bilayer.[103] Due to their unique structural properties with hydrophilic and hydrophobic compartmentalisation, they can be used as carrier for both water soluble and lipophilic biologically active molecules, enabling them to be used a range of application.[95] The most researched and developed application of liposomes has been regarding drug delivery systems, with applications including oral, ophthalmic and topical (related to cosmetics).[95, 104-107] They have also been extensively used as cell tissue and membrane models to study the mechanisms of bilayer action.[106, 108, 109] The advantages of using liposomes as nano-carrier systems and membrane models is that they can be fabricated and characterised into various vesicles types and sizes, giving them high stability and encapsulation efficiency.[95, 103] Liposome can be characterised by the number of bilayers they contain within an overall vesicle, providing multiple layers of compartments and encapsulation potentials.[103] The various types and sizes of liposomes are summarised in Fig 1.13, together with a schematic of their vesicle structure.

These various vesicle types are contrived through different preparation techniques, where the lipids are dried, re-dispersed in aqueous solution and put under a mechanical process by different means.[110] Common techniques included; hydration of thin lipid films, detergent dialysis and reverse phase evaporation.[103, 110] The most widespread method for SUVs and LUVs is the hydration of lipid films followed by sonication or extrusion techniques.[103, 110, 111] Liposome-based assay will be developed in the thesis to explore the lipid membrane - surfactant interactions with regards to membrane permeation.

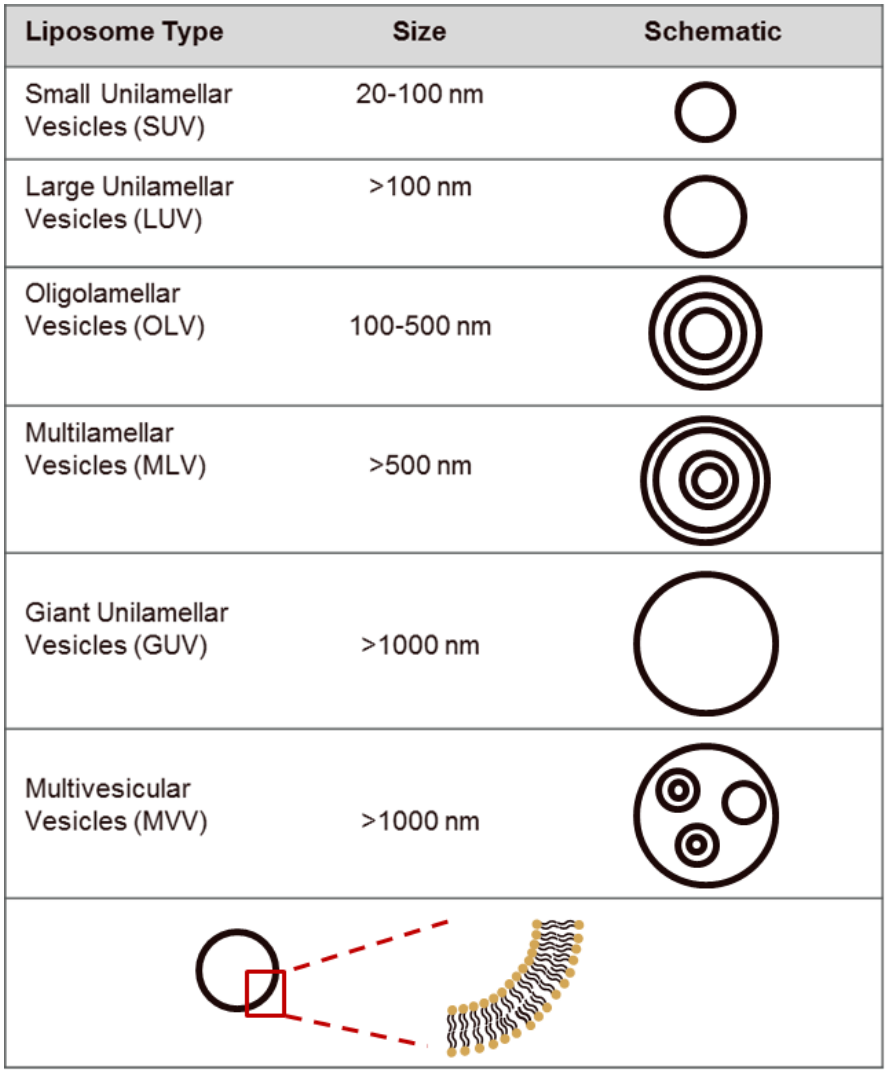


Fig 1.13 – Schematics of various types of liposomes, with their relative size ranges and number of lamellar layers/ vesicles. Redrawn and adapted from given reference.[103]

1.5 THESIS AIMS

The phase behaviour of common surfactants and the effect of various factors mentioned in this chapter are well known. However, there is still a lack of complete understanding on the effect of organic solvents on the Krafft point and precipitation boundary of surfactants. More insight is required in to the effect of organic solvent on the transformation of hydrated crystals (H_C) into micelles (L_1) and vice versa.

One of the aims of this thesis is to determine the various phases formed near the solubility boundary of surfactant systems containing the organic solvents. The objective is to establish phase diagrams of the model surfactant SDS, under various organic solvent levels, particularly focusing on the narrow phase transition at low temperatures. Understanding the effects of organic solvent on the surfactant phase behaviour will allow us to control the negative transformations encountered and hence the performance and stability of surfactant-based formulations.

The potential ocular hazard of surfactant-based formulations, like many other substances, has to be identified, categories and communicated to a global standard, as a legal requirement. Alternative in vitro eye irritancy tests developed have only found partial acceptance and therefore better representative eye test method is needed. The overall objective from the second part of this thesis, is to determine the potential of lipid membrane models for eye irritancy predictions, with the corroboration of irritancy results of liquid detergents obtained from the ICE test. The aim is to determine how concentrated surfactant systems interact with lipid membranes and gather an understanding of the mechanisms by which these liquid detergents (particularly the key surfactants it contains) solubilise the lipid membrane, which can aid in understanding how these substances cause irritation to the eyes.

Chapter 2
Materials and Methods Overview

In this chapter, an overview of the general materials, methods and procedures that were used during the course of this thesis are outlined and explained. Specific details regarding the individual experiments and procedures are reported in the relevant chapters.

2.1 SURFACTANTS

There were mainly 4 different surfactants used throughout this thesis. These surfactants along with their chemical structure and abbreviations are shown below in Fig 2.1

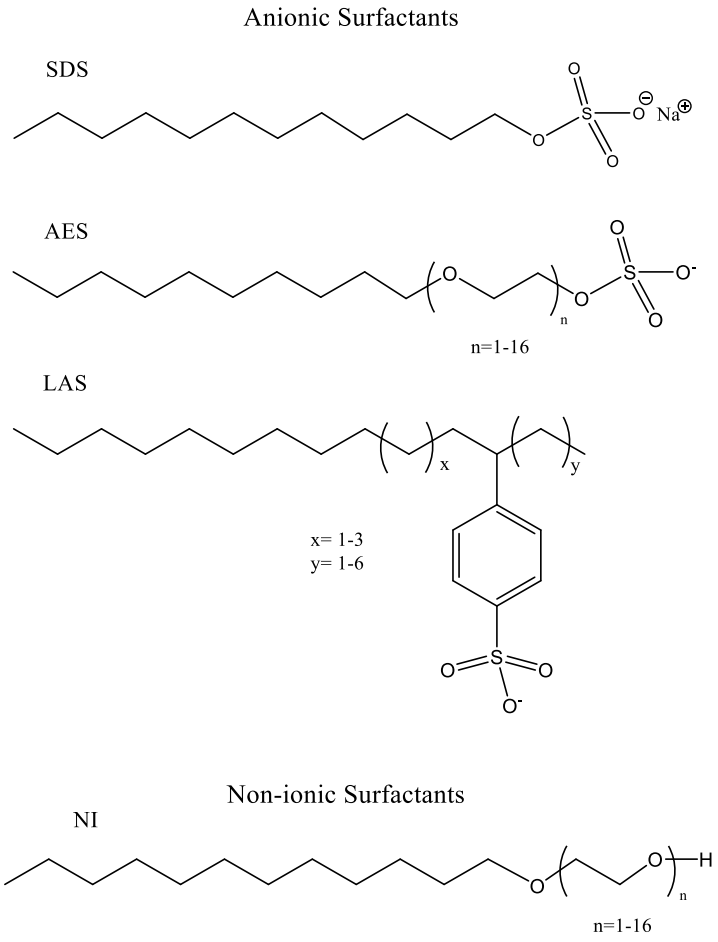


Fig. 2.1 – Chemical structures of relevant surfactants

SDS – Sodium Dodecyl Sulfate

AES – Alcohol Ethoxysulfate

LAS – Linear Alkylbenzene Sulphonate

NI – Non Ionic Alcohol Ethoxylates

SDS (99%) was purchased from Sigma Aldrich and used as received since it was analytical grade. Industrial grade AES, LAS and NI were obtained from Procter & Gamble (P&G), as used in their detergent formulations. AES and NI was used as received whereas LAS were neutralised with monoethanolamine (MEA) before use. The details regarding AES, LAS, NI and actual detergent formulation are given in the relevant chapters.

2.2 ORGANIC SOLVENT

Two main organic solvents were used, Glycerol and Propylene glycol, either as individual water-solvent mixtures or together as ternary solvent mixtures. Glycerol (>99.5%) was purchased from Sigma Aldrich and Propylene glycol (99%) was obtained from P&G.

The ternary solvent mixture was composed of 15 wt% Glycerol: 25 wt% Water: 60 wt% Propylene glycol. This ternary solvent composition was standardised, based on the detergent formulations provided by P&G.

2.3 LIPIDS

There were different lipid types used in this thesis for various experiments. These are shown below in Fig 2.2. All lipids were purchases from Sigma Aldrich.

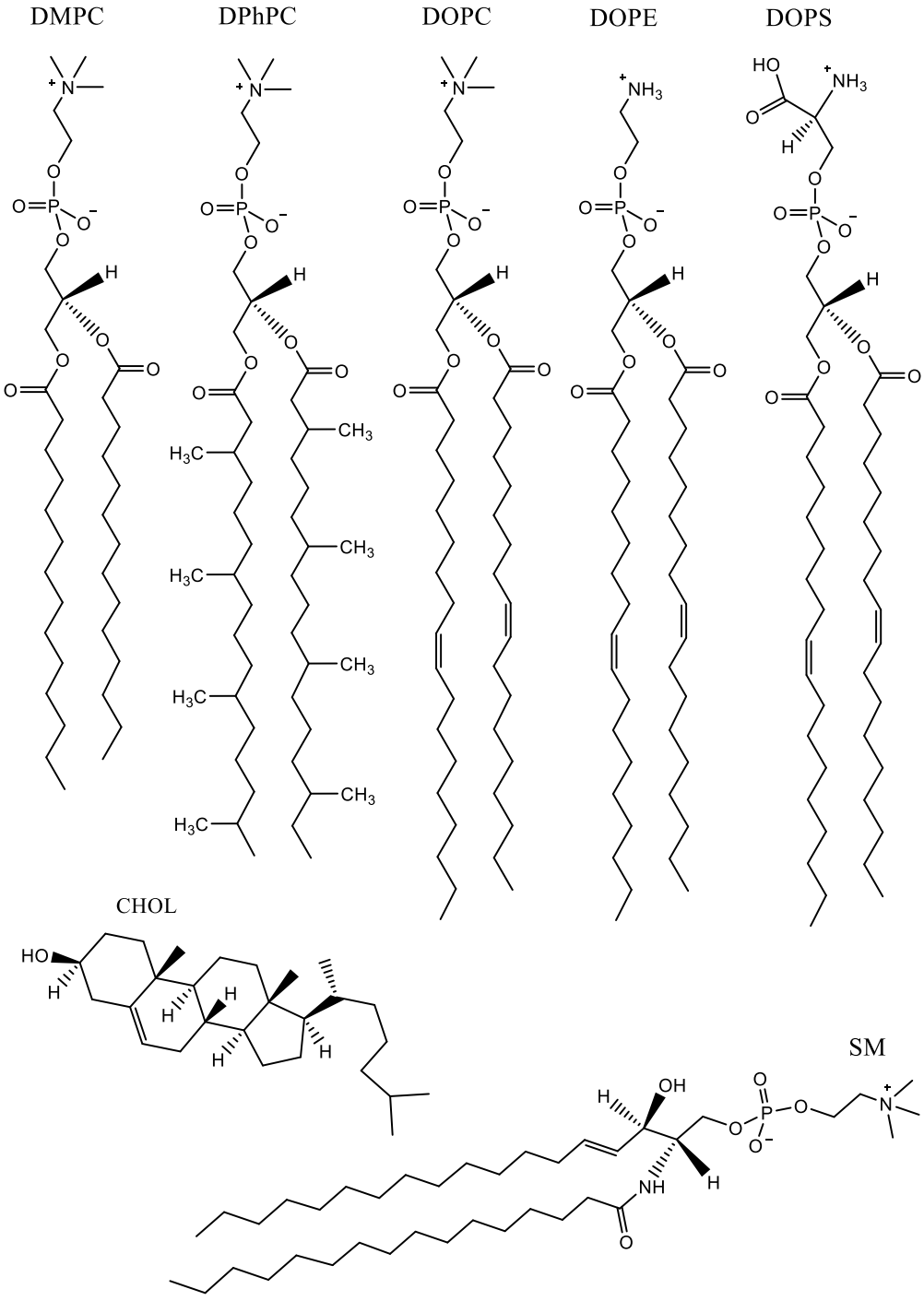


Fig. 2.2 – Chemical Structure of lipids used.

DMPC – 1,2-dimyristoyl-sn-glycero-3-phosphocholine

DPhPC – 1,2-diphytanoyl-sn-glycero-3-phosphocholine

DOPC – 1,2-dioleoyl-sn-glycero-3-phosphocholine

DOPE – 1,2-dioleoyl-sn-glycero-3-phosphoethanolamine

DOPS – 1,2-dioleoyl-sn-glycero-3-phospho-L-serine

SM – Sphingomyelin

CHOL – Cholesterol

2.4 FLUORESCENT DYE

Calcein was the fluorescent probe used in this thesis. The self-quenched and de-quenched structure of calcein is shown below in Fig 2.3

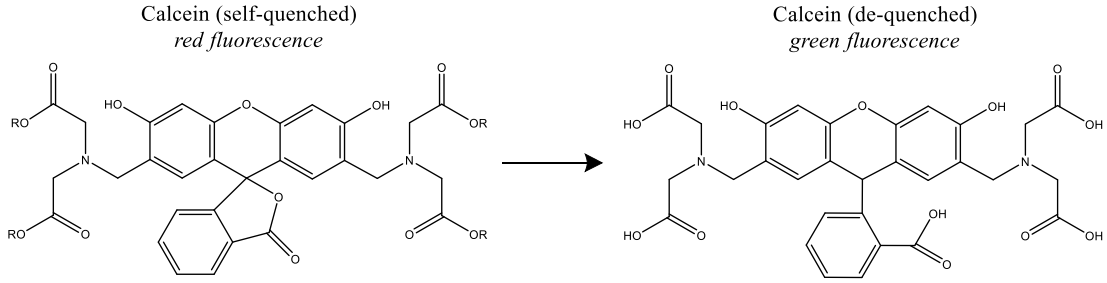


Figure 2.3 – Chemical Structure of calcein from a self-quenched state to a de-quenched state.

2.5 SURFACE TENSION MEASUREMENTS

The pendant drop method was used to measure the surface tension of all surfactant solutions using the Krüss EasyDrop Standard Tensiometer (DSA1) and the Drop Shape Analyzer (v 1.92) software for analysis. This instrument has a sensitivity of ±0.1 mN/m.

A droplet was suspended in air via a blunt needle of a known diameter (1.83 mm). The diameter of the needle is used to determine the magnification of the droplet image. The volume of the droplet was controlled and automated using the dispensing control panel. The outline of the droplet is extracted by the program and Young-Laplace fitted parameter is used to calculate the surface tension. A screenshot of the software is displayed in Fig 2.4 showing the droplet dispensing control panel, results table and a live image of a deionised water droplet with the outline (green line) used for parameter fittings. The Young-Laplace equation[112] (1) together with Fig 2.5 (a) illustrates the

principle behind the pendant drop method. For surface tension measurements against temperature, for Krafft temperature determination, a glass cuvette chamber (SC30) as shown in Fig 2.5 (b) was used and the temperature was controlled using a water bath (Haake DC50).

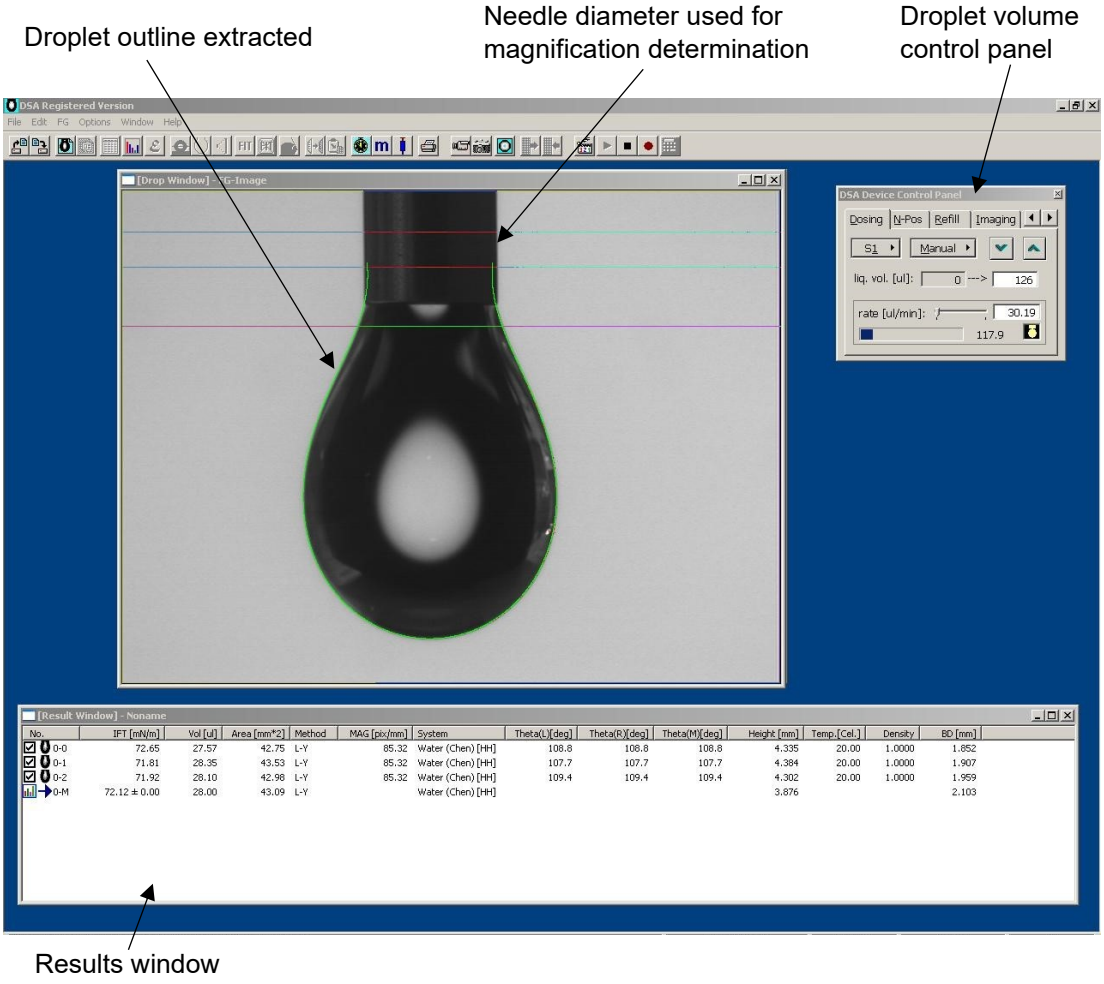


Fig 2.4 – (a) Screenshot of Drop Shape Analyzer (v.192) software, illustrating the droplet dispensing control panel, the results table and a water droplet image with its outline extracted.

$$\Delta P = \gamma \left(\frac{1}{r_1} + \frac{1}{r_2} \right) \quad (1)$$

ΔP = the pressure difference across the interface

r_1 and r_2 = principal radii of curvature (illustrated in Fig 2.5a)

γ = surface tension

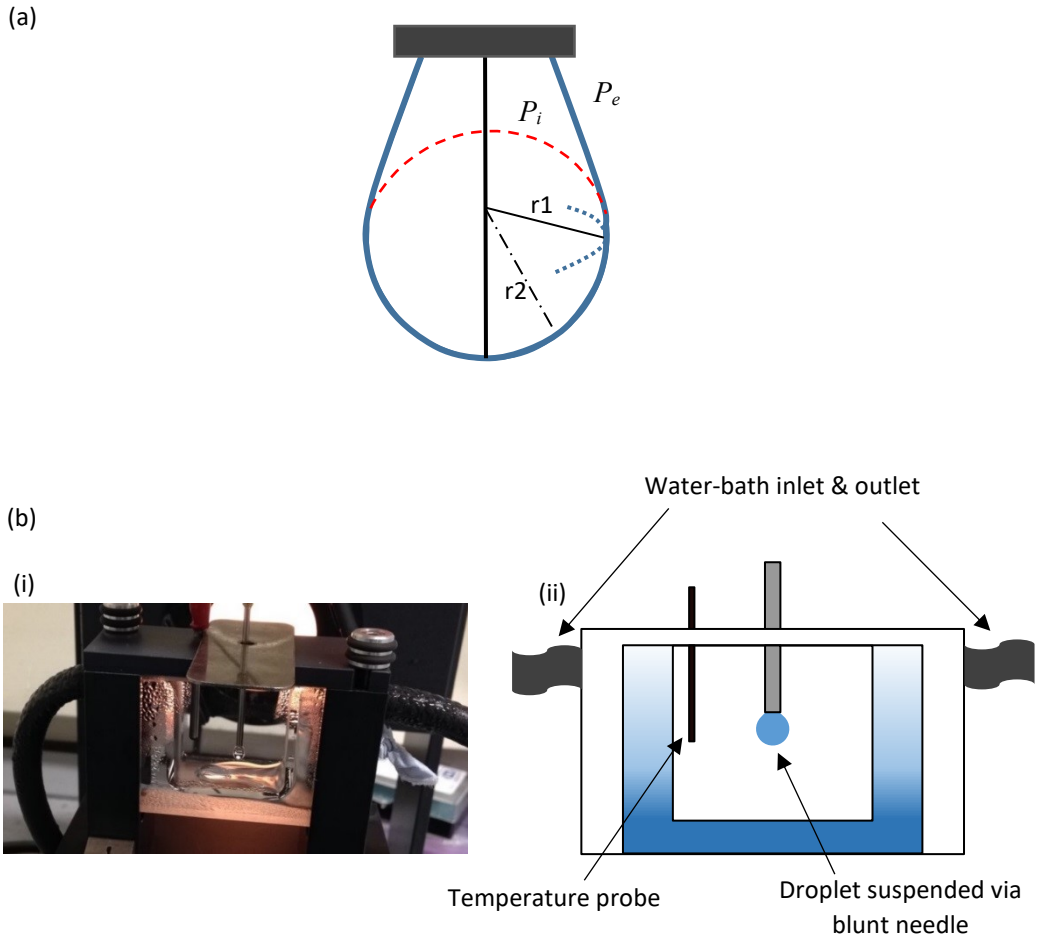


Fig 2.5 – (a) Pendant drop schematic showing $\Delta P = P_i$ (internal pressure) – P_e (external pressure), r1 and r2. (b) (i) Photograph and (ii) schematic of the glass cuvette chamber for temperature control surface tension measurements.

2.6 CONDUCTIVITY EXPERIMENTS

Conductance measurements of SDS surfactant solutions were carried out using the SevenGo Duo Pro Conductivity meter (SG78) (Mettler Toledo), to determine the CMCs for comparison with the surface tension method. The meter was calibrated with potassium chloride solutions of the appropriate concentration range and has a conductivity resolution of 0.01 µS/cm and all measurements were done on fresh samples at 25 °C, with each sample being measured thrice.

2.7 DYNAMIC LIGHT SCATTERING EXPERIMENTS

Particle diameter size and polydispersity measurements were conducted using a Zetasizer Nano S Zen 1600 (Malvern Instrument, UK), dynamic light scattering (DLS) which operates in backscattering mode (theta= 173°) with a 633 nm He-Ne laser and having a particle diameter size range from 0.3 nm to 10 µm. All measurements were done at 25 °C, with the data being processed using Zetasizer software (v7.01) as shown in Fig 2.6, and the mean value ±SD obtained. The data was then imported into OriginLab for analysis and presentation. The parameter for particle size analysis done on all SDS sample were set as: three measurements, with each averaging eleven runs of 30 seconds. Real-time particle size measurements were carried out on liposome-surfactant interaction experiments to track the solubilisation of lipid bilayers, with recordings taken pre and post-addition of surfactants, over a period of time and the parameters were set to: One measurement of the averaging 6 runs of 20 seconds, with measurements taken every 1 minutes.

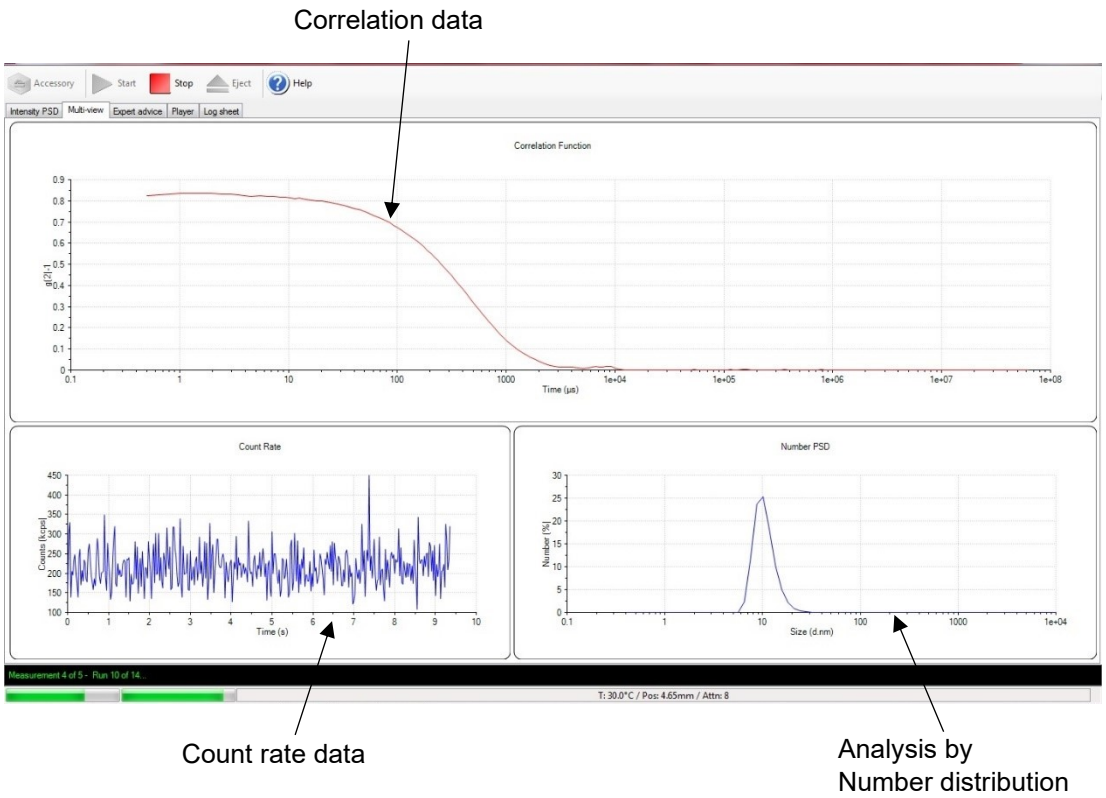


Fig 2.4 – Screenshot of Zetasizer software (v 7.01) showing the real time correlations and measurements.

2.8 DIFFERENTIAL SCANNING CALORIMETRY

PYRIS Diamond Differential Scanning Calorimetry (DSC) (Perkin-Elmer Instruments) was used for thermal analysis to determine solubility temperatures, phase transitions and crystallisation temperatures of various surfactant solutions. The instrument was calibrated with indium, with baseline auto-tuned correction, using the Pyris Thermal Analysis software (v11.1) and has an accuracy of ±0.1 °C. This DSC uses the power-compensation principle, where the reference and the sample materials are in separate calorimeter chambers as shown in Fig. 2.5. As the temperature changes in the sample material, the same energy is compensated for to keep the temperature of the system constant. The power required to maintain this equilibrium is measured as it is proportional to the heat energy changes of the sample, therefore the positions of the thermal transitions can be established.[113]

All samples were freshly prepared and between 8 to 10 mg were weighed in to aluminium pans (Perkin-Elmer 219-0062) and hermetically sealed. A selection of heating/cooling rates were initially tested (1 to 20 °C/min) for SDS-water systems, to determine the optimal rate which produces visually significant peak sizes to identify transformations. The optimal heating/cooling rate was found to be 5 °C/min, which was used for all DSC samples. The lower temperature limit was -10 °C, at which it was held for 10mins before heating the system. The upper temperature limit varied based on the SDS-solvent system. All the data was imported and analysed in OriginLab.

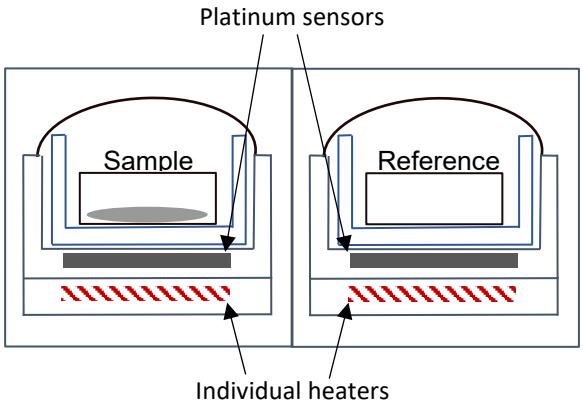


Fig 2.5 – Schematic of the power-compensation DSC.[113]

2.9 X-RAY SCATTERING

Small-angle X-ray scattering (SAXS) and wide-angle X-ray scattering (WAXS) measurements were carried out on the I22 beamline at Diamond Light Source, Oxfordshire, U.K. All SDS solutions in various solvent mixtures analysed were freshly prepared to avoid hydrolysis of SDS and were used within 24 hours. Temperature resolved (isothermal) analysis was carried out using the capillary rack at fixed temperatures with 5 °C increments. Linkam DSC600 capillary stage was used to provide a temperature control from 30 °C to -10 °C with a cooling rate of 5 °C/min. Polycarbonate capillaries with an external diameter of 2.0 mm were used for temperature resolved experiments and Quartz glass capillaries (Capillaries Tube Supplies), 1 mm external diameter, were used for all Linkam experiments. For both the experiment, a 12.398 keV (λ = 0.9998 Å) beam was used.

All x-ray scattering raw data was processed through a set of customised software pipeline developed at the Diamond Light Source, which allowed single image or a series of 2-D data to be converted into suitable data files.[114] These data files were processed using the DAWN Science software, a screenshot of which is shown is Fig 2.6. OriginPro (v.9.0) was used to generate all SAXs and WAXs plots and graphs.

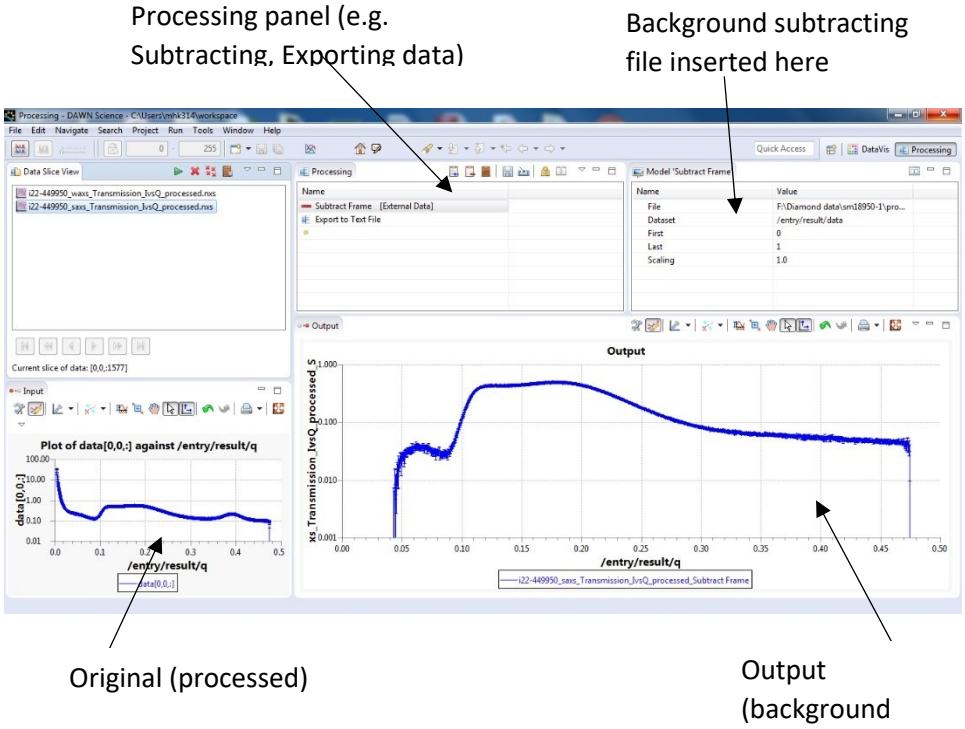


Fig 2.6 – Screenshot of the DAWN Science software used to process X-ray scattering data

2.10 DROPLET INTERFACE BILAYER (DIBS) EXPERIMENTS

PDMS wells were created on a glass slide in which DIBs were formed. This experiment was done to understand the interaction between surfactant systems and lipid bilayers.

2.10.1 DIBs formation

The lipid-in method was used to form DIBs[98], where 20 mg/ml of 100 nm SUVs in an aqueous solution were made through the lipid vesicle method mentioned above. To form the droplets, 1.0 µl of the aqueous SUV solution were pipetted into a well containing 150 µl hexadecane. The droplets were incubated for ten minutes, to allow for monolayer assembly at the interface and for the droplets to stabilise. Then the droplets were brought into contact by pushing them together using a syringe needle. As the bilayer is formed at the interface, there is a deformation of spherical droplet as shown in Fig 2.6.

2.10.2 PDMS well construction.

Firstly PDMS sheets were made using the Sylquard 184 Silicone Elastomer Kit (Dow Corning). The kit contains an elastomer and a curing agent, which were mixed together at a 10:1 mass ratio and then gently stirred together using a glass pipette. The mixture was then poured into a petri dish (10 mm deep) and placed under a vacuum to be degassed and remove any air bubbles. The PDMS mixture was then baked at 70 °C for three hours to cure. 5 mm diameter holes were drilled into the PDMS sheets to create the wells and the sheet was then bonded onto a glass microscope slide (VWR). The seal was created after treating the bonding surfaces to an oxygen plasma for 30 seconds, using a plasma cleaner (Harrick plasma) and pressing the PDMS onto the glass slide. Fig 2.7 illustrates the PDMS well design.

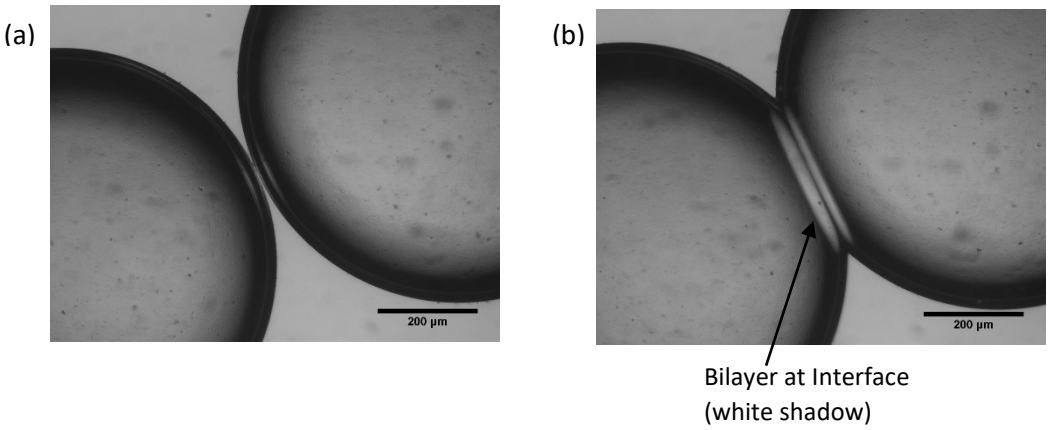


Fig 2.7 –DIBs formation using DPhPC lipid. (a) Lipid droplets incubating in hexadecane before bilayer formation. (b) After contact, illustrating the bilayer formation at the interface.

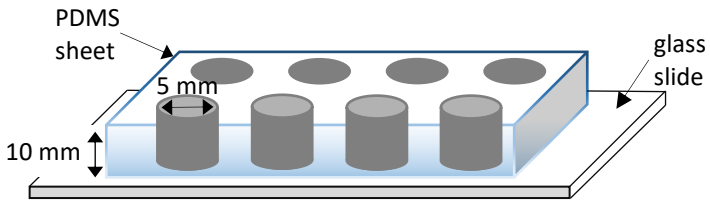


Fig 2.8 – PDMS well design for DIBs formation.

2.11 MICROSCOPY EXPERIMENTS

Optical microscopy experiments were carried out on the Olympus brightfield microscope (1X81F-2) using the Q-Capture (Pro.7) software. With brightfield microscopy, the light source is below the stage and it passes through the condenser lens, focusing the light on the specimen, after which it is refracted as it transmitted through the objective lens. The objective magnifies the light and passes it through the ocular lens. The specimen restricts the light transmission and appears dark and is contrasted against the bright background.[115] Microscopy was used to observe DIBs formation and its interaction with surfactant systems.

2.12 LIPID VESICLE PREPARATION

All lipid vesicles prepared in this thesis were 100 nm small unilamellar vesicles (SUVs). This process of vesicle preparation is illustrated in Fig. 2.9 (a). First a lipid film was prepared by weighing out the required lipid powders in glass vials and then dissolving them in chloroform. After gentle stirring to ensure all the lipids have dissolved and a homogenous mixture is obtained, the chloroform was removed under a light stream of nitrogen. When the glass vial had dried, it was placed in a lyophiliser for a minimum of three hours to remove any trapped chloroform, resulting in a lipid film being formed on the vial walls. The lipid film was then hydrated with the relevant buffer and vortexed to give a homogenous cloudy lipid solution. For lipid vesicles composed of multiple lipids and containing encapsulated calcein, the solution was freeze-thawed five times using liquid nitrogen. This freeze-thawing step is known to increase the encapsulation efficiency of liposomes [104, 107, 116].

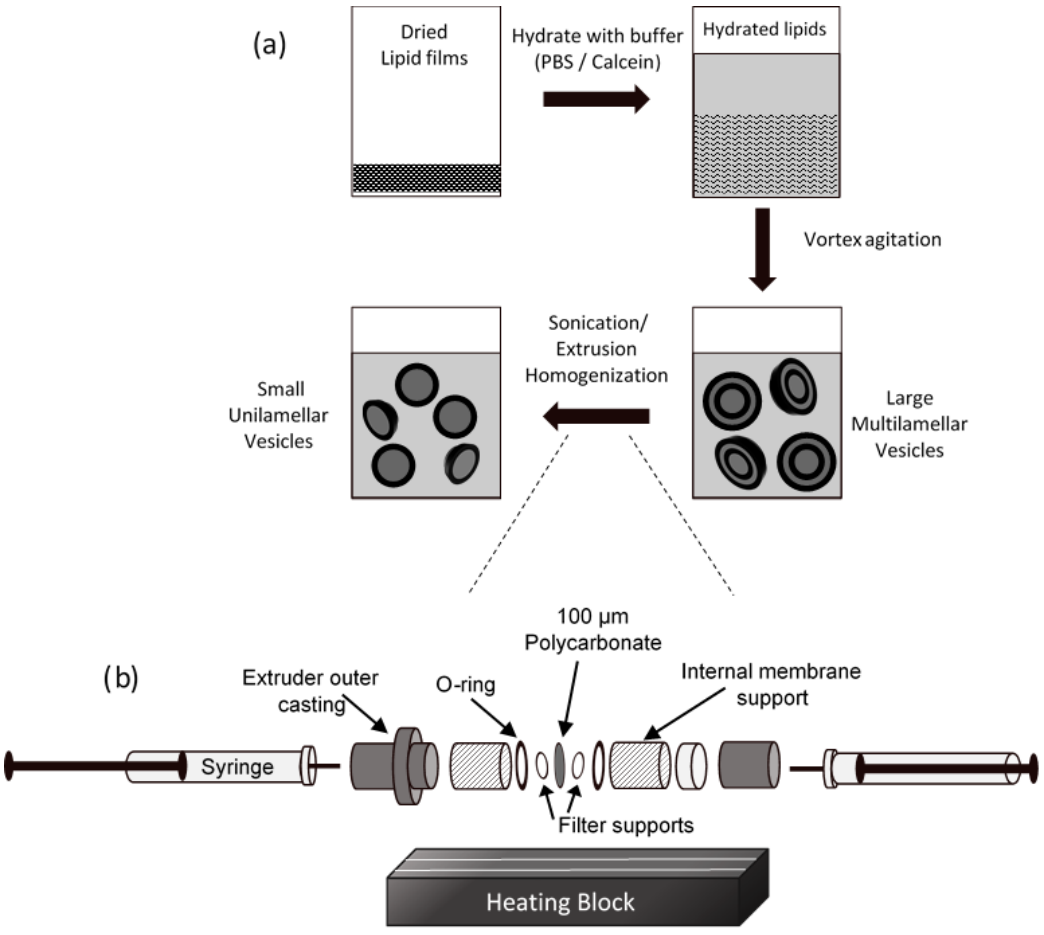


Fig 2.9 – (a) Small Unilamellar Vesicle preparation process with (b) Extrusion kit schematic, redrawn from indicated references[110, 111]

Then the resulting lipid aggregates were passed through an extruder (Avanti Polar Lipid Inc.) 11 times containing 100 nm pore size polycarbonate membrane (Avanti Polar Lipids Inc.) to obtain SUVs, schematic of which is shown in the Fig. 2.9 (b).

2.13 LIPOSOME-CALCEIN RELEASE ASSAY

The Liposome-Calcein Release Assay (LCRA) was performed to determine the permeation of surfactant and detergent solutions through lipid bilayers. Calcein encapsulated 100 nm SUVs were made and used as the liposome throughout this experiment.

2.13.1 Calcein Encapsulated SUV Preparation

SUVs containing encapsulated calcein were prepared through mixing, freeze-thaw, extrusion and gel filtration columns. The lipid film was prepared as described above. The dried lipid film was hydrated with a separately prepared 50 mM calcein dye in Phosphate-buffered saline 1X (PBS, 1.8 mM KH_2PO_4, 10 mM Na_2HPO_4, 137 mM NaCl, and 2.7 mM KCl at pH 7.4, without calcium & magnesium from GE Healthcare). The lipid solution was vortexed and put through 5 freeze-thaw cycles, which produced multi-lamellar vesicles. The lipid solution was then extruded 11 times through a 100 nm pore size polycarbonate membrane to produce 100 nm liposomes containing calcein. The excess calcein was removed by filtering the liposome solution through a Sephadex G-50 column. Sephadex G-50 gel was prepared by mixing Sephadex G-50 fine (GE Healthcare) powder with PBS solution in a ratio of 1:30. The gel solution was vortexed, degassed and then the gel bed was allowed to settle in a column.[107]

To elute the calcein encapsulated SUVs, a 50 mM sucrose dissolved in PBS solution (prepared separately) was run through the column. The PBS solution containing sucrose was used in order to maintain the osmotic pressure balance between the core of the SUVs (containing calcein) and the external bulk phase. As illustrated in Fig. 2.10, the liposome containing encapsulated calcein were first to be eluted and were

collected. This liposome solution was diluted by a factor of 100. The dilution factor was determined through a series of fluorescence measurements done to obtain a total calcein release intensity to be within the instrument's detection limit.

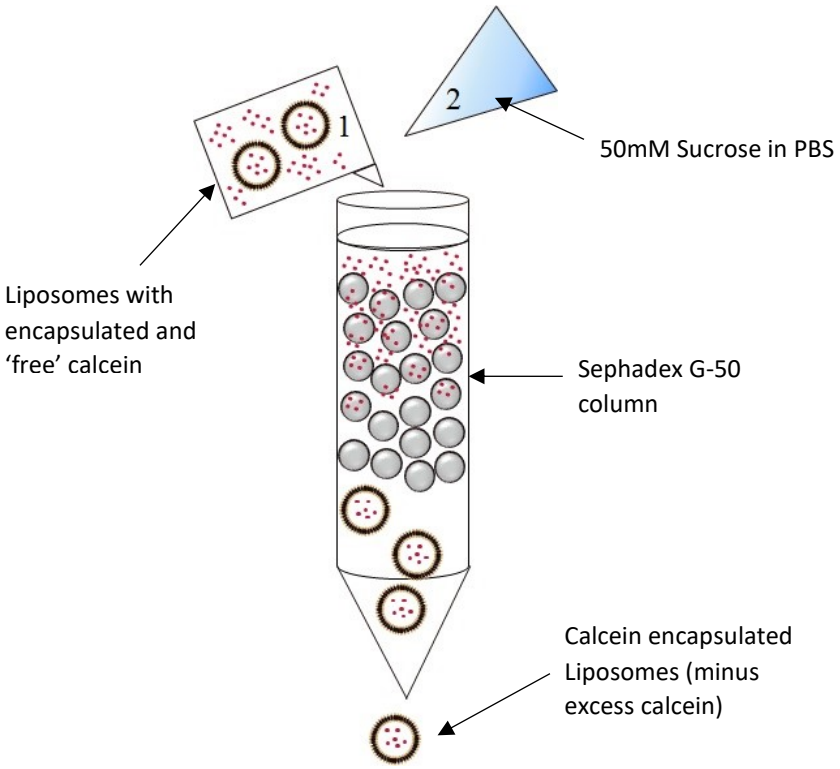


Fig 2.10 – Schematic of calcein encapsulated liposome separation.

2.14 FLUORIMETER EXPERIMENTS

Fluorescence measurements were carried out for the LCRA. These fluorimeter experiments were performed at room temperature using a Varian Cary Eclipse Fluorescence Spectrophotometer (Agilent Technologies, USA) in a 96 well-plates (Thermo Scientific Nunc X50 Microplate Black), with a well volume size of 300 µl. The excitation and emission wavelengths used to measure the release of the entrapped calcein were 494 and 514 nm respectively. To obtain optimal fluorescence intensities and minimal noise levels, fluorimeter parameter settings were tested and set to; Scan collect timings- 1 sec averaging time, 120 nm/min scan rate, 30 sec time interval data collection, 5 nm excitation and emission band slit and 650 V PMT detector voltage.

Chapter 3

Effect of Organic Solvent and Electrolytes on Krafft Point of SDS

The results described in this chapter have been published in the following peer reviewed journal; Haris Khan et al, Effect of glycerol with sodium chloride on the Krafft point of sodium dodecyl sulfate using surface tension, *Journal of Colloid and Interface Science* (2019), **538**, 75-82.[1]

3.1 OVERVIEW

The Krafft point, as explained in chapter 1, is the intercept point between the CMC and the T_K and determining the changes occurring to the Krafft point under various conditions can provide a good understanding of surfactant micellization and changes in the phase behaviour. As polar organic solvents and electrolytes are commonly used in aqueous surfactant based formulations, understanding their individual and combined effect on the surfactant Krafft point has important practical considerations. This chapter details the development of strategies used for exploring and tuning the Krafft point of SDS systems in organic solvents and salt content. The robustness of the pendant drop method and the inefficiency of the conductivity method to determine the CMC in high glycerol content is discussed. Also the effectiveness of the pendant drop method to measure the T_K in high organic solvent is described along with the effect of water-glycerol mixtures with NaCl on the SDS micellization. This knowledge base now provides a platform of understanding for controlling the function and performance of structured, surfactant based product systems for future studies.

3.2 INTRODUCTION

The significance of determining the Krafft point to understand surfactant phase behaviour has been established in the literature.[8, 17, 26, 117] and explained in chapter 1 (section 1.2.4). Also well established in the literature is the phase behaviour of SDS and the effect of various factors previously mentioned [8, 17, 26, 30], but there is limited

insight into the effect of organic solvents on the various phase transitions and particularly the transformations between thermotropic liquid crystalline phases into micelles. The aim of the studies in this chapter is to provide an initial and essential step towards understanding the impact of organic solvent on the micellization of SDS, while developing a high-throughput method allowing us to determine these changes effectively. The micellization of model surfactant SDS, mainly in a full range of water-glycerol mixtures with NaCl, was studied. The efficiency of the surface tension-pendant drop method to measure the CMC was established and compared to that of the conductivity method. Then the pendant drop method was developed to determine the T_K of SDS in organic solvent for the first time, to the best of our knowledge, and its efficiency was compared to published data.

3.2.1 SDS Phase Behaviour

SDS has a fairly high aqueous solubility as it has a high HLB of 40[118], with a T_K of 14-16 °C[9] and a CMC of ~0.23 wt% (8.0 mM) at 20 °C[9, 17, 18]. At low concentration (< 1.0 wt%) and at temperatures below 10 °C, SDS in water is mostly in a hydrated crystalline phase (H_C).[30, 119] As the temperature reaches 14 °C and the surfactant concentration is above its CMC, these H_C start to transition into micelles (L_1), creating a narrow phase where the H_C and L_1 phases co-exist.[8, 30] as shown in Fig. 3.1. Above 16 °C, all the H_C phase are converted into micelles and this complete transition is regarded as the solubility boundary. Therefore the region beyond the Krafft point becomes an important parameter as it determines the essential characteristics required in a surfactant based product, e.g. emulsifying and foaming properties.

The high solubility of this anionic surfactant in water is due to the hydrogen bonding interaction between the water molecule and the negatively charged hydrophilic headgroup (SO_4^-).[8] As other organic solvents and materials are added to the system, the hydrogen bonding interactions are altered, along with the insolubility of the hydrophobic tail, which alters the Krafft point and induces changes to the solubility boundary.[17, 23]

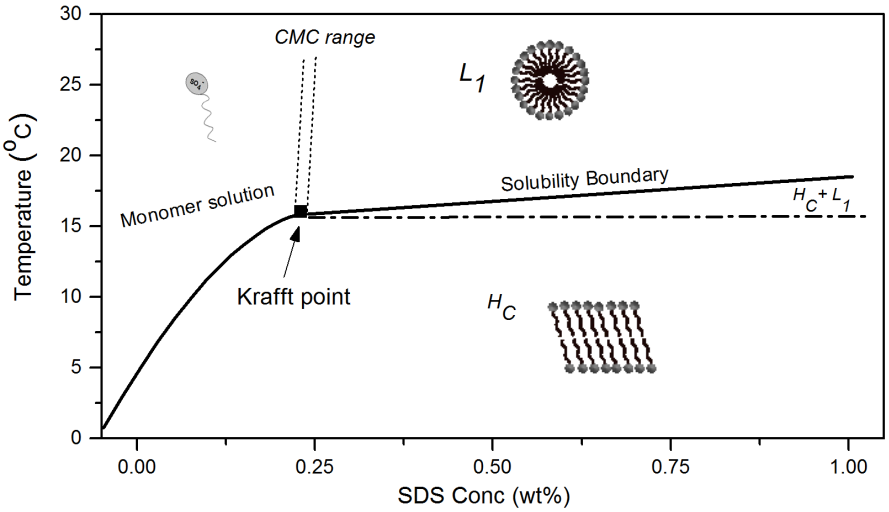


Fig 3.1 – Schematic of SDS phase diagram in water, focusing on the Krafft point region.[1]

3.2.2 Micellization

A detailed characterisation of micelles and an overview of the micellization process has been provided in chapter 1 (section 1.2.2). In this section, the specific properties of the solvent and additives and their impact on the thermodynamics of micellization will be given.

The self-assembly of SDS in water is directed by the combined effect of the hydrophilic tails insolubility and the electrostatic repulsion of the headgroup, causing a negative enthalpy (ΔH^0_{mic}) and a positive entropy (ΔS^0_{mic}) of micelle formation.[37, 120, 121] This leads to a negative change in Gibbs free energy of micellization (ΔG^0_{mic}) enabling the SDS micellization to be favourable at low temperature. ΔG^0_{mic} is temperature (T) dependant as shown in Equation 3.1. As the temperature of the system is increased, the ΔH^0_{mic} become considerably more negative and the ΔS^0_{mic} becomes slightly less positive, therefore the SDS micellization is considered to be an entropy driven process at low temperatures and an enthalpy driven at higher temperatures.[37, 120] The properties of the solvent, which have been found to bring about this spontaneity in surfactant micellization, are: high cohesive energies, high dielectric constant and high hydrogen bonding ability.[21, 121, 122] The replacement of water with other polar solvents and the addition of electrolytes can alter these properties and solvent polarity and hence impact the thermodynamic of micellization.

$$\Delta G^{0}_{\text{mic}} = \Delta H^{0}_{\text{mic}} - T\Delta S^{0}_{\text{mic}} \qquad (3.1)$$

3.2.2.1 Solvophobic Interactions

Solvophobics are defined as species which have low affinity to the solvent that they are present in.[123, 124] The most well know example of the solvophobic effect is the hydrophobic effect of alkanes in water, with the hydrogen bonding network performing a crucial role. Polar protic organic solvents which have more than one labile H^{+}, a lone pair of elections and form spatial H-bonded networks can also ascribe to the solvophobic effect, as it has been reported that the solvophobic interactions are highly dependent on the strength of the H-bond network.[123, 125] These solvophobic interactions are the driving force for the self-assembly of surfactants and influence the thermodynamic behaviour of the solvent and therefore of micellization. Altering the quality of the solvent and adding other self-associated solvents e.g. glycerol or ethylene glycol, the solubility of the hydrophobic tail is increased due to a decrease in the cohesive energy and dielectric constant.[21, 126] This leads to a lower entropies of solvation and high (less negative) values of $\Delta G^{0}_{\text{mic}}$, making the micellization process less favourable.[124, 127] Since these polar solvents form intermolecular hydrogen bonds, micellization does occur but requires higher concentrations of surfactants (higher CMCs).[128]

There have been several studies looking at the micellization behaviour of surfactants in organic solvents such as ethylene glycol, glycerol and formamide, [20, 121, 122, 129-131] giving us an understanding of the solvophobic effect involved and hence the thermodynamic of formation. However, the concentration range of these polar solvents studied and their impact on particularly the T_K has been limited. This is mostly due to the limitations of the traditional techniques involved in determining the CMC and T_K. The most commonly used technique is the conductivity method, as it is an effective tool for less viscous and electrolyte systems, however it has been shown to be inefficient for surfactant systems containing high levels of polar solvents, particular glycerol, due to its poor conductivity and high viscosity.[20, 41, 121] Therefore an initial comparison is carried out between the surface tension and the conductivity methods for SDS in water-glycerol-NaCl systems. For the majority of the studies in this chapter, binary water-glycerol solvent mixtures, with NaCl have been used. Glycerol was

chosen as it is the most widely used polar solvent for a variety of applications such as soaps, detergents, cosmetics, pharmaceuticals and food items.[131] It is a versatile solvent as it is non-toxic, bacteriostatic and completely miscible in water.[132, 133] As mentioned in chapter 1, the surfactant systems we are particularly interested in, with regards to the later part of this thesis, are liquid detergent samples containing solvent mixtures composing of water, glycerol and propylene glycol, therefore the effect of some water-propylene glycol mixtures and a ternary water-glycerol-propylene glycol mixture were also tested on the Krafft point of SDS.

3.2.2.2 Electrolyte Interactions

Electrolytes have the opposite impact on the micellization behaviour of surfactants compared to polar organic solvents. In a control water-surfactant system (with no electrolytes), as the concentration of surfactant is increased above the CMC, the micelles start to elongate into rod-like/worm-like structures.[23, 134] Electrolytes have a synergetic effect on the growth of surfactant micelles, and they induce elongation at lower surfactant concentrations. This effect is known as the salting-out effect.[135-137] For anionic surfactants like SDS, addition of electrolytes e.g. sodium salts reduces the repulsion effect between the SO^{4-} headgroups as the increased concentration of Na^{+} counterions bridge the gap between them, favouring micellization and therefore decreases the CMC.[138-140] Also there are reported to be stronger hydrophobic interactions between the tails due to the hydrated structure round the hydrocarbon tails becoming weaker, caused by the salting-out effect.[137] The effect of increasing salt concentration on surfactant phase behaviour is illustrated in Fig. 3.2. The type of salt used has an impact on the degree of the salting-out effect. Cations which have larger atomic radii and valences have been reported to favour the micellization process more and reduce the CMC further.[137, 139, 140] The electrolytes are effectively changing the packing parameter of surfactants. The packing parameter (PP = v/a_0 x l_c) determines the size and structure of the surfactant aggregates and hence effects the micellization behaviour (explained in section 1.2.2). As electrolyte is added, the effective headgroup area (a0) decreases, whereas the tail volume (v) to hydrocarbon tail length (lc) is unchanged, causing an increase in the packing parameter (PP), increasing the micelle size and altering its overall structure.[23, 139, 141]

The T_K has been reported to either remain fairly constant or slightly increase with the addition of electrolytes depending on the type of cations used.[142-144] This is explained through the changes in the ΔG^0_{mic}, that upon the addition of electrolytes and with increasing counterion concentration, there is enthalpic gain (due to reduced headgroup repulsion) and the entropy is hardly changed, therefore the value of ΔG^0_{mic} becomes more negative, thermodynamically favouring micellization even at lower temperatures. [137, 145, 146]

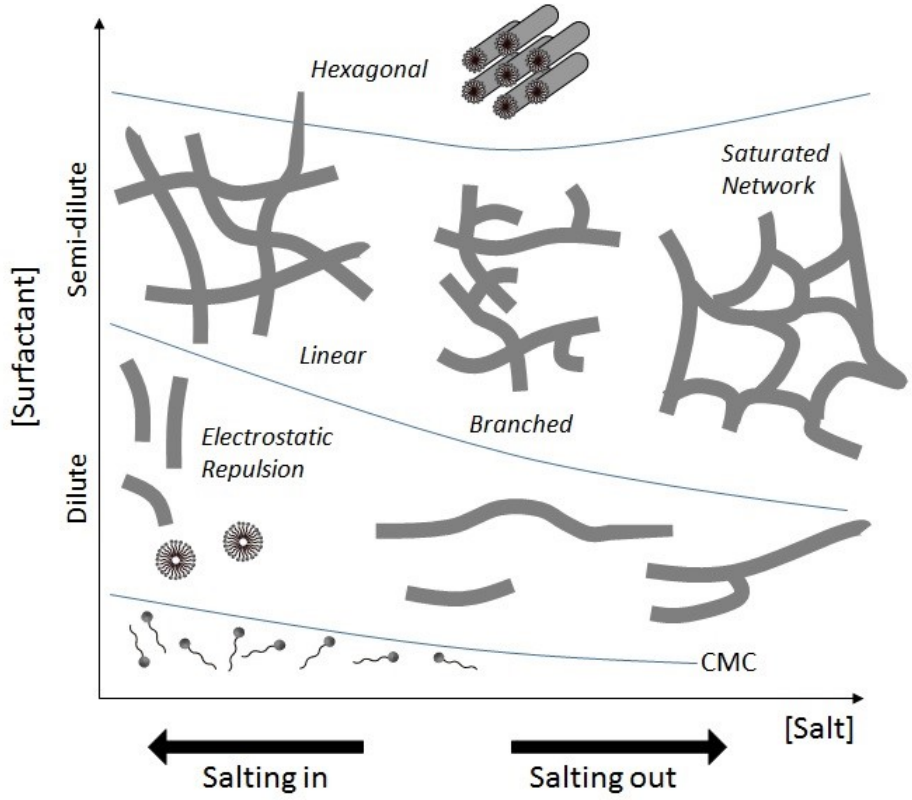


Fig 3.2 – Schematic diagram of salt concentrations over surfactant concentrations, illustrating the salting out effect. Adapted from cited reference[147].

The CMCs of ionic surfactants (in water) are less dependent on temperature and much more on the ionic strength.[148] Salts such as NaCl, KCl and $MgCl_2$ are commonly used to alter the physiochemical properties of anionic surfactant systems to achieve desired characteristics such as viscosity, rheology, surface tension, etc.[138, 149] Most studies looking at the impact of electrolytes on surfactant micellization have carried out on water-surfactant systems and limited work has been done with water-organic solvents

and salt mixtures combined. One of the aims of this chapter is to determine whether NaCl has a similar effect and to what degree, on the SDS micellization process when in water-glycerol solvent mixtures.

3.2.3 Surface Tension

Since surfactants are surface active chemical agents, having the primary function of lowering the surface tension of aqueous systems, efficiently measuring the surface tension of various aqueous-surfactant mixtures becomes extremely important.

In all materials, there is a certain level of intermolecular forces which keep the individual molecules together (e.g. hydrogen bonding in water).[15, 150] At a liquid-air interface, the molecules in the bulk phase are pulled in every direction equally due to cohesive forces, resulting in a zero net force.[15, 112] The molecules at the interface however do not have any neighbouring interactions on top, as shown in Fig. 3.3, and therefore the forces are not balanced. There is greater attraction of liquid molecules to each other than to the molecule on the air, resulting in a net force pointing inwards, creating an internal pressure and a tension (elastic tendency) at the surface.[150, 151] To reduce the unbalanced cohesive forces, a liquid will try to minimize their surface area, i.e. water droplet curving and forming a sphere.[151, 152] A surface tension value is measured as force per unit length (mN/m) and hence it determines the amount of net force exhibited by the intermolecular forces across the length of the contact line at the interface.[153, 154]

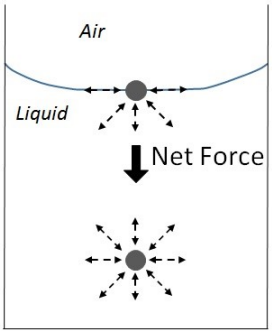


Fig 3.3 – Surface tension- Imbalance of cohesive force creating an inwards net force, resulting in a surface tension at the liquid-air interface. Redrawn from [15].

3.2.3.1 Surface tension methods

There are several established surface tension measuring techniques of a liquid system, each having certain advantages and disadvantages. These methods are generally characterised into two categories; static and dynamic surface tension measurements.[151] Static surface tension measurements are usually carried out on pure or simple liquid-surfactant systems, where the solution is not viscous and the surface tension values are constant over surface age. The common static surface tension measurements techniques are the du Nouy ring[155] and the Wilhelmy plate[156] methods. Both the du Nouy and the Wilhelmy techniques are pull-force methods, where an object of a well-defined geometry (a ring and a plate respectively) is pulled off the surface of a liquid and the pull force measured.[151, 155] These methods require larger volumes of liquid, involve the use of a precision scale and are inefficient for viscous liquids due to the wetting process (of the ring/plate) being affected.[151, 154]

The dynamic surface tension measurements methods are mostly techniques which are modifications of the static models and include techniques such as: the drop method[157], the maximum bubble pressure method (MBPM)[158], which are adapted from the capillary rise technique[159], and the pendant drop method[112]. These techniques have a similar principle where the drop or bubble is formed in the relevant medium (air or liquid) through a capillary or syringe of a known diameter, creating a pressure difference which is taken into account, along with the radius of the sphere/hemisphere, to determine the surface tension.[151, 154, 160] With these methods, the surface tension can vary as a function of time/ surface age and the rate of formation (i.e. the rate at which the bubble or drop is formed).[151, 160] The MBPM, capillary rise and drop weight methods have been found to be the most efficient for time scale/ surface ages of 1-2 seconds and therefore are mostly for studying kinetics of surface adsorption for application such as spray coating, jet printing etc.[159-161] The pendant drop method has been found to be better suited for longer time scales (5-10 seconds), for more viscous liquids and it only required miniscule amounts of liquid as the surface forces cause small volumes to form a spherical shape distorted by the effect of gravity.[112, 160]

3.3 EXPERIMENTAL

An overview of the materials and equipment used was previously described in Chapter 2. Further details on sample preparation, compositions and data analysis carried out to determine the Krafft points are provided in this section.

3.3.1 Materials and Compositions

All the materials in this section were used as received, since they were analytical grades, including sodium chloride (>99%) purchased from Sigma Aldrich. All water-organic solvent mixtures were prepared by mass, with water-glycerol mixture composed from 0 to 100 wt% glycerol, in 10 wt% increments. For water-propylene glycol mixtures, 20, 40 and 60 wt% levels were used. The overall NaCl concentration range covered was from 0.005 to 0.2 M. For the water-glycerol-NaCl systems tested, the compositions were; 0, 20, 40, 60, 80 and 100 wt% glycerol with 0, 0.005, 0.01, 0.025, 0.05M and 0.1M NaCl. A 2 wt% SDS stock solution were prepared for each surfactant mixtures. The stock solution was then diluted down to the required concentration. All samples were tested at least 2 hours after being prepared and used within 48 hours.

3.3.2 Surface Tension

The CMC of SDS was determined for the full range of water-glycerol mixtures at 20 ±1 °C using the pendant drop method as detailed in Chapter 2. Three repeat measurements for each composition were carried out with each composition made in triplicates, for the water-glycerol mixtures and for water-NaCl control solutions. For all other mixtures; water-glycerol-NaCl and water-propylene glycol compositions, an average of three measurements was taken from a single solution.

3.3.2 .1 Pendant drop method validation

The method was validated using a control system; SDS in water, where the accuracy and the reproducibility of the method was determined along with optimising the

experimental parameters. The purity of the SDS solutions was also checked through the CMC determination.

Firstly, the impact of the suspended droplet volume was investigated as the inconsistency in size/volume of the droplet is known to affect the precision of the surface tension averages. [112, 162] It was found that when there was a difference of 2 µl or more in the droplet volume, the difference in the mean surface tension data was significant with the *p*-value less than 0.05, from the two-sample t-test (appendix Table 8.1). Also, that the accuracy of the surface tension values for this method is reported to be improved with larger droplet sizes, where the maximum drop volume (V_{max}) is created, just before the point where the droplet can detach from the needle, as this allows for the maximum deformation of the surface area. [112] Therefore, for all surface tension measurements, the largest possible drop volume was created (that can be sustained) and the drop volumes were kept within 1.0 µl for each set of mixtures during the measurement to reduce the variation. DI water (Milli-Q) was used to calibrate the instrument.

To determine the equilibrium time for the suspended droplet, two factors had to be taken in to account, the dynamic effect[157, 163] and the evaporation effect[112]. The dynamic affect is concerned with the adsorption kinetics of the surfactant solution and is influenced by droplet flow rates. Surface tension of a flowing surfactant fluid is different from an inert solution and therefore an equilibrium time is required after the creation of a droplet for it to become static and reach a consistent value. The pendant drop method is not ideal for fast dynamic surface tension processes of ~1 second time-steps and requires an equilibrium time of at least ~5 seconds or more[112, 157]. For system where liquid-air interfacial tension is being measured, the evaporation of the solvent in air needs to be considered. As the solvent is evaporated, the concentration of the surfactant within the droplet increases, lowering surface tension at the interface.[164] Forming the droplet in a sealed chamber is known to significantly minimise the evaporation effect.[15] This effects was determined by tracking the surface tension of a single droplet over time (60mins) at various temperatures, of different SDS concentrations, using the glass cuvette chamber described in chapter 2. The change in surface tension was negligible, particular at short time frames. At lower temperatures (20 °C), for all SDS concentration tested, the surface tension only decreases by 0.5-0.75% after 5 mins and ~1.5% after 30 mins. For higher temperatures

(40 °C), the decrease was ~1% after 5mins and <3% after 30mins (data shown in appendix Fig. 8.1). Therefore, the equilibrium time of 5 seconds (after the creation of the droplet) was chosen, for all measurements done at 20 °C.

For validation, three separate solutions of SDS in water were prepared and the CMC of all three determined from the pendant drop method, using the parameters mentioned above. The CMC was established through the slope intercept analysis as illustrated in Fig. 3.4 for control sample 1.

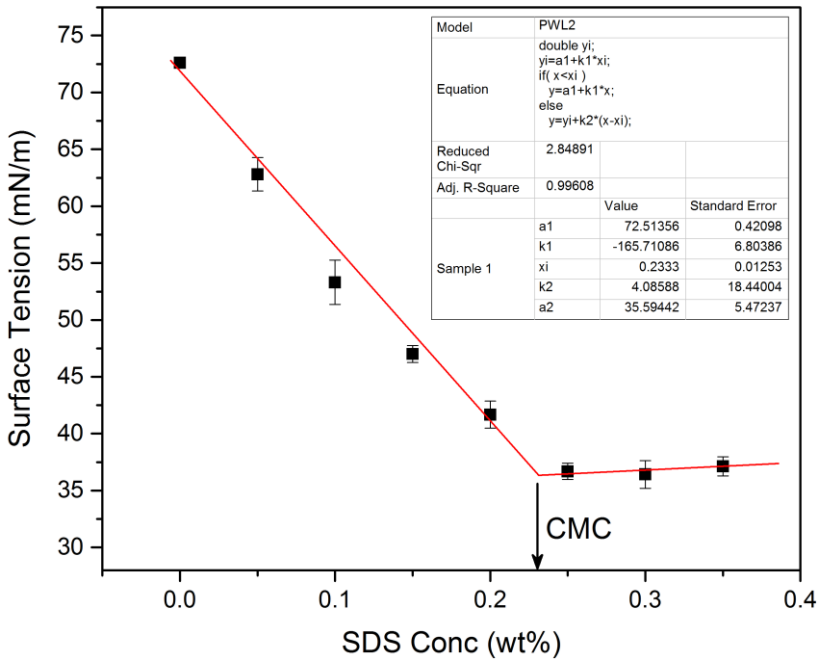


Fig 3.4 – CMC determination of SDS in water (control sample 1), using surface tension-pendant drop method with slope intercept analysis.

3.3.3 Krafft Temperature

The T_K was determined by measuring the surface tension against temperature using the procedure described in chapter 2. For this experiment, the CMCs determined from the previous analysis was used to prepare SDS solutions for each mixture. Three repeat measurements for each composition was carried out including all water-glycerol mixtures and water-glycerol-NaCl solutions. The temperature of the glass cuvette chamber was measured with a precision ±0.1 °C and the measurements were carried out in 1 °C increments. The temperature of the bulk solution was kept at the required

measurement temperature before the surface tension was measured to minimise the temperature gradient. The equilibrium time for the suspended droplet was set to 5 minutes to acclimatise. As previously mentioned, surface tension is known to decrease as temperature is increased, so control experiments were carried on water-glycerol mixtures to determine the degree of change in surface tension over a range of temperatures (data shown in appendix Fig. 8.2). From 10 to 40 °C, there was a 6.2%, 3.8% and 3.5% change in the surface tension for pure water, 50 wt% glycerol and pure glycerol respectively. These percent changes were considered when establishing a significant change (break point) in the surface tension slope to determine the T_K.

3.3.4 Conductivity

Conductivity experiments were carried out as described in chapter 2 for; 0, 20, 40, 60, 80 and 100 wt% glycerol mixtures with 0, 0.005, 0.01, 0.025 and 0.05M NaCl concentrations.

3.3.5 DSC

DSD experiments and analysis were carried out as described in chapter 2 for only SDS-water systems, at varies heating and cooling rates. SDS concentrations tested where 8.0 mM (0.235 %), 34.6 mM (1.0 %), and 69.35 mM (2.0 %), at heating and cooling rates cycles of 1, 5 and 10 degree Celsius per minute.

3.4 RESULTS AND DISCUSSION

The data analysis from the pendant drop method was primarily used to determine the effect of organic solvent with NaCl on the micellization of SDS near the Krafft point and will be discussed in greater details in this section. The efficiency of the pendant drop method along with a comparison with conductivity and DSC measurements is also provided.

3.4.1 CMC Determinations

The CMCs of SDS in water controls, sample 1 (Fig. 3.4), 2, and 3 were; 0.233, 0.235, and 0.225 wt% respectively, given a mean of 0.231 wt%, equivalent to 8.004 ± 0.17 mM. These values were corroborated with published CMC values of SDS in water; 8.00,[18] 8.05,[121] 8.28 [126] and 8.30 mM.[17] The purity of the SDS solution was confirmed from not only the CMCs determined, but also from the surface tension values just above the CMC level, averaging to be ~36.41 ±0.83 mN/m, which are in good agreement with published data.[163, 165, 166] This is shown in Fig. 3.5 along with a comparison of the pendant drop method with other surface tension techniques for SDS in water.

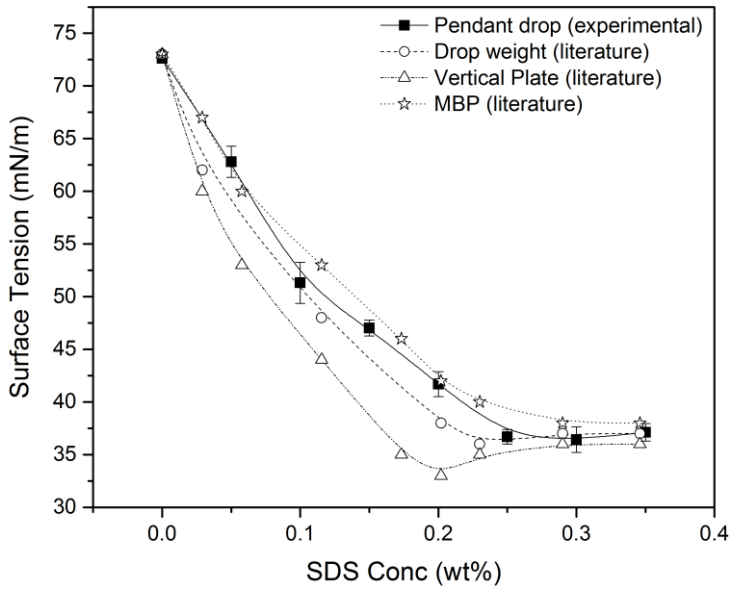


Fig 3.5 – Comparison of the pendant drop method vs other surface tension techniques; Drop weight,[165] Vertical plate,[165] and MBP [166] for SDS in water.

3.4.1.1 Surface tension vs Conductivity

Surface tension and conductivity measurements were carried out for the same set of samples in order to determine and compare the CMCs. Fig. 3.6 shows both the measurements for SDS in 20 wt% glycerol + 0.05M NaCl sample. As SDS levels are increased, the conductivity is also increased due to higher concentration of 'free' anions. As micelles start to form, the increase in conductivity is reduced. The point at which there is a change in the rate of conductivity increase (break point in the curve) against SDS concentration, is taken as the CMC.

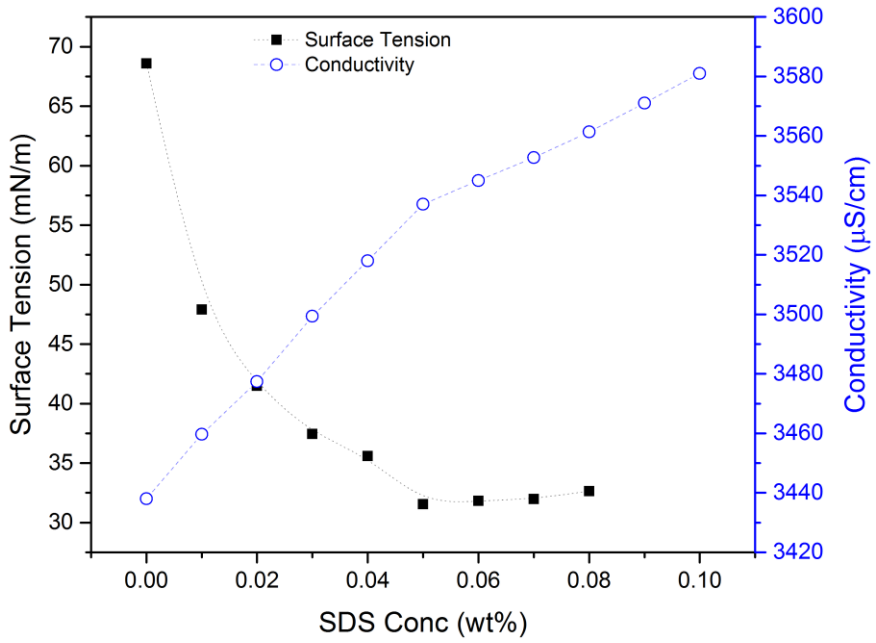


Fig 3.6– Surface tension and conductivity of SDS in 20 wt% glycerol + 0.05 M NaCl solution, as a function of SDS concentration at 20 °C. Mean ± s.d (n=3).

As previously mentioned and shown in appendix Fig. 8.2, surface tension of water-glycerol mixtures decreases as the level of glycerol is increased in the system. This is due to pure glycerol having a lower surface tension value of ~63.4 mN/m at 20 °C compared to DI water (~72 mN/m). Therefore the initial surface tension, in the absence of SDS, decreases with increasing glycerol content shown in Fig. 3.7. From 0 to 40 wt% glycerol systems, there is no significant change in the minimum surface tension values (at the CMC) and are in the range of 36 to 34 mN/m. However, in water-glycerol system above 50 wt%, the minimum surface tension reached increases as glycerol level

increases to 39.4, 39.6 and 41.6 mN/m for 60, 80 and 100 wt% glycerol respectively. Therefore, there is a slight reduction in the ability of SDS to lower the surface tension in higher glycerol mixtures. This suggest that the adsorption of this surfactant at the surface interface is limited, due to the rate of diffusion being kinetically limited. This is also evident by looking at the rate at which the surface tension decreases, against concentration, for higher glycerol systems, showing a much more gradual change.

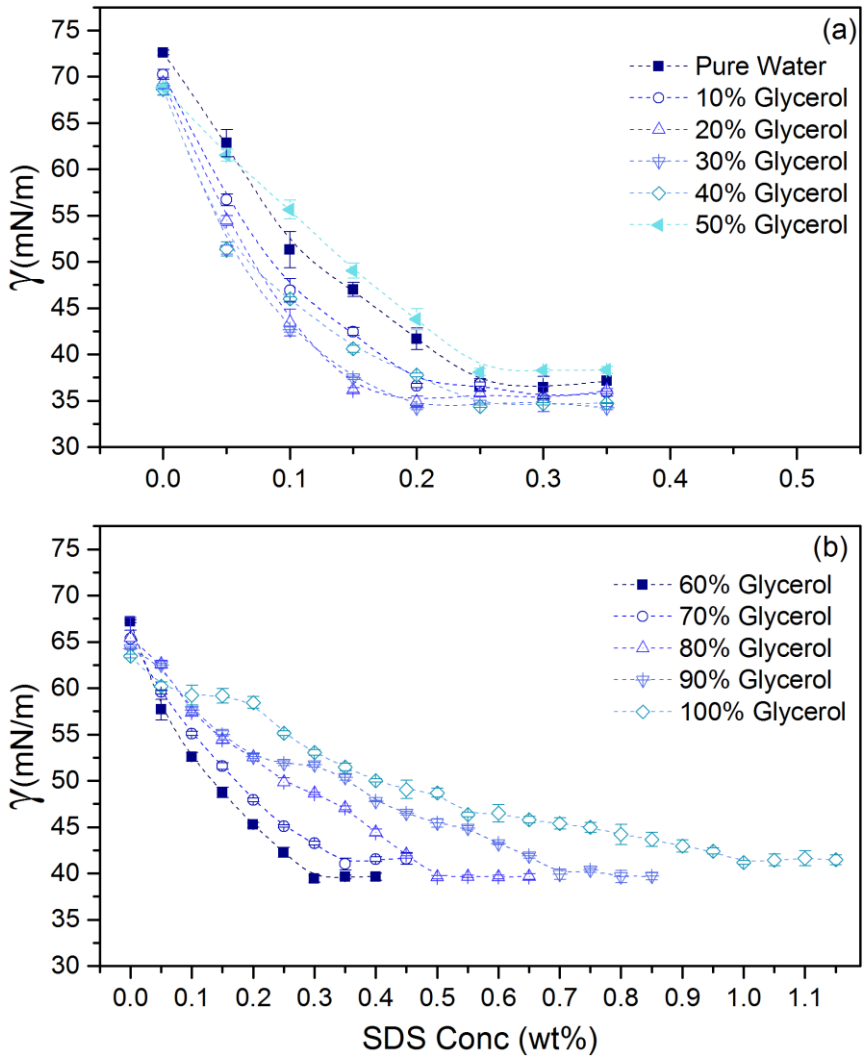


Fig 3.7 – Surface tension of SDS in aqueous solutions as a function of SDS concentration at 20 °C in (a) 0 – 50 wt% glycerol (b) 60 – 100 wt% glycerol. Mean ± s.d (n=3).

The addition of NaCl to the water-glycerol mixture has a reverse effect, where the minimum surface tension is lowered as the concentration of NaCl is increased. This is shown in Fig. 3.8 for a 20 wt% glycerol system with various levels of NaCl added. The surface tension at the CMC, with no NaCl is 36.1 ±0.3 mN/m, whereas with a 0.1 M NaCl addition it is 33.8 ±0.2 mN/m. The lower surface tension observe when NaCl is added, is due to the alteration in the adsorption of the surfactant at the surface layer/ interface. [167] As the concentration of counterions (Na) increases, the packing of the SDS molecules is increased, allowing for a higher concentration of surfactant to be adsorbed at the interface, hence lowers the surface tension further. Since it is highly desirable for surfactant-based formulations such as detergents, disinfectants and cleansers to greatly reduce the surface tension in order for the product to perform effectively, the addition of NaCl to a high glycerol mixture will allow for the surface tension to be lowered and controlled.

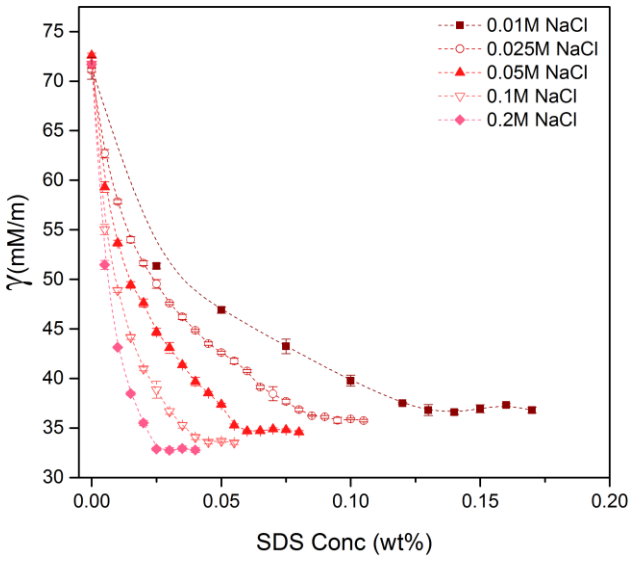


Fig 3.8 – Surface tension of SDS in 20 wt% glycerol + NaCl solutions, as a function of SDS concentration at 20 °C. Mean ± s.d (n=3).

The pendant drop method was effectively carried out on the full range of compositions mentioned the in methods section and the CMCs were successfully determined, which will be discussed later in this chapter. The complete data set and repeats for all the water-glycerol-NaCl systems surface tension measured can be found in the appendix Fig. 8.3.

Also, the full set of conductivity measurements carried out on the same set of samples is shown in appendix Table 8.2 to 8.5. A summary of some conductivity measurements for water-glycerol-NaCl systems is shown in Fig. 3.9. As expected, the conductivity of a SDS and/or an electrolyte only solution increases proportionally with concentration. However, when glycerol was added to the system, the electrical conductivity was compromised. For the system with 0.05 M NaCl and 0.1 wt% SDS concentration, the conductivity was reduced from ~5600 µS/cm in pure water to ~65 µS/cm in pure glycerol.

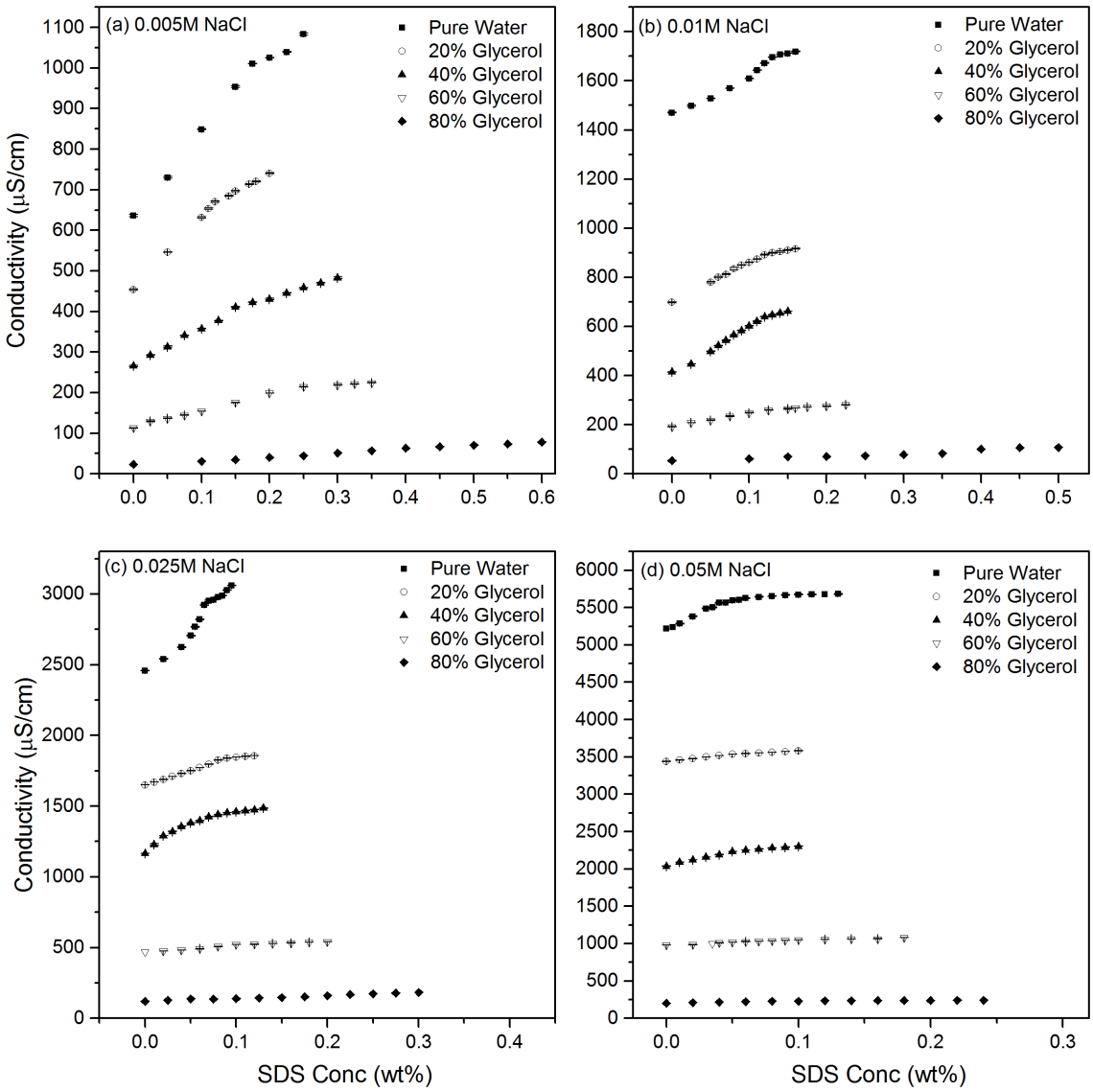


Fig 3.9 – Conductivity of SDS in water-glycerol mixtures as a function of SDS concentration at 20 °C with NaCl concentrations of (a) 0.005 M (b) 0.01 M (c) 0.025 M and (d) 0.05 M. Mean ± s.d (n=3).

The viscosities of water-glycerol mixtures, over the full composition range is well determined in literature and shows an exponential relationship between glycerol concentration and viscosity.[132, 133] (Fig 3.10.). From 0 to 70 wt% glycerol, there is a gradual increase in viscosity from ~1 to ~22 mPa.s respectively. As the glycerol content is increased from 70 to 80 wt%, there is more significant increase in viscosity to ~60 mPa.s. The 'knee' of the exponential curve is in the region between 70-90 wt% glycerol, with pure glycerol being a viscous solvent (~1400 mPa.s).[132]

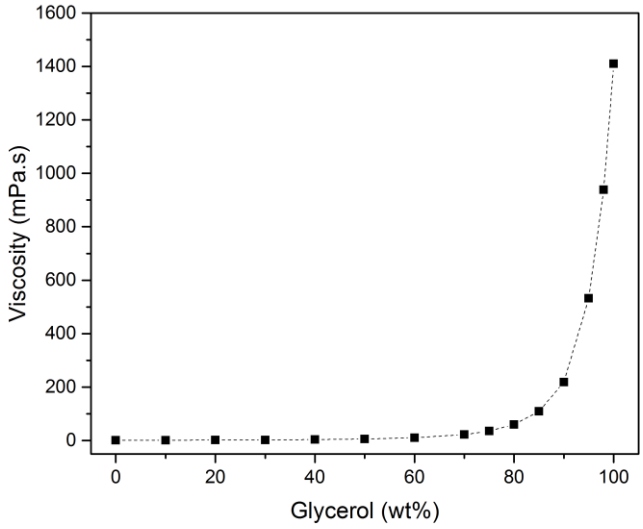


Fig 3.10 – Viscosity of water-glycerol mixtures as a function of glycerol wt% concentration at 20 °C. Viscosity values taken from the provided reference.[132]

The low conductivities shown by the solutions of electrolyte/SDS in high glycerol (>80 wt%), is due to the high viscosity of this organic solvent. The movement of ions in these highly viscous solutions is constrained, leading to poor conductivity measurements.

The typical change in the rate of increasing conductivity (break point), to determine the CMC, was clearly identified for all 0 to 60 wt% glycerol systems. However, for 80 and 100 wt% glycerol samples, the conductivity values were significantly lower due to reduced ion mobility and this change in gradient could not be determined accurately.

Fig. 3.11 shows the conductivity repeat measurements for 80 wt% glycerol systems at four different NaCl concentrations. All those compositions show an overall linear increase in conductivity with increasing SDS concentration. However, the values are

slightly scattered for 0.01 and 0.025 M NaCl systems and therefore the CMC for these samples could not be determined. Only for one of the repeats at 0.005 and 0.05 M NaCl there was a noticeable change in the gradient identified which allowed for the CMC to be deduced.

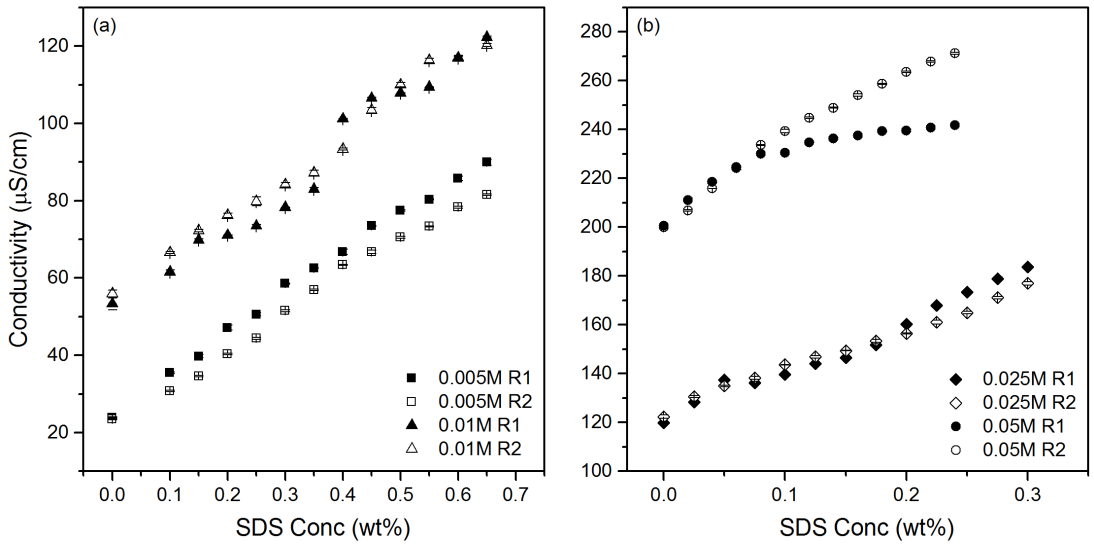


Fig 3.11 – Conductivity of SDS in 80 wt% glycerol at 20 °C as a function of SDS concentration in (a) 0.005 M & 0.01 M NaCl and (b) 0.025 M & 0.05 M NaCl, showing two repeats. Mean ± s.d (n=3).

To get a better understanding of the inefficiency of the conductivity method to establish a CMC at higher glycerol level, the effective degree of micellar dissociation (α) of the counterion (Na^+) as a function of SDS concentration, was determined for 0 to 80 wt% glycerol samples with various NaCl concentrations. The degree of dissociation was derived from the ratio of the slope above and below the CMC in the conductivity vs SDS concentration plots. These ratios are displayed in table 3.1. It is well established that α is dependent on the method used as each method measures a different property to determine the dissociated counterions and therefore there are slight variability in the values of α calculated from different techniques.[20, 33, 168] For the purpose this study, we are only interested in the effect of glycerol on the degree of dissociation. It is clearly seen that as the level of glycerol increases, α also increases, giving a higher counterion dissociation. In pure water systems, as the concentration of NaCl is increased, there is no significant change in α, which is consistence with

previous studies.[33, 169] For some 80 wt% glycerol systems, the ratio is ~1, suggesting that even after micellization has occurred, the dissociation of counterions continues at the same rate (as a function of SDS concentration). Therefore, at higher glycerol levels there are more free Na^+ ions, above the CMC, to carry the current and hence not allowing for the break point in conductivity measurements to be identified accurately.

Table 3.1 – Degree of dissociation for SDS, from CMC conductivity measurements in water-glycerol-NaCl mixtures.

Glycerol wt%	A			
	0.005 M	0.01 M	0.025 M	0.05 M
0	0.27	0.26	0.27	0.21
20	0.49	0.44	0.40	0.44
40	0.52	0.50	0.42	0.50
60	0.53	0.55	0.54	0.52
80	0.73	1.16*	1.03*	0.62

*The break point for these calculations was taken from the CMCs determined from the surface tension method.

For pure glycerol systems, the conductivity measurements (provided in the appendix table 8.6) gave extremely low values from; 9.94 µS/cm, for control (No NaCl) and 65.8 µS/cm, for 0.05 M NaCl solutions. The CMC could not be determined from these measurements for any 100 wt% glycerol samples as there was no significant change in conductivity across increasing SDS levels.

The two CMCs deduced for the 80 wt% glycerol systems at 0.005 and 0.05M NaCl, where found to be significantly lower than the CMCs determined from the pendant drop method, particularly for the 0.05 M NaCl concentration. A comparison of the CMCs determined from the surface tension and the conductivity method is shown in Fig. 3.12. Across all NaCl concentrations, for 0 to 60 wt% glycerol levels, the CMCs from both the methods are in good agreement with each other. For 0.025 and 0.05 M NaCl systems, the CMCs from the conductivity method slightly lower, but still comparable.

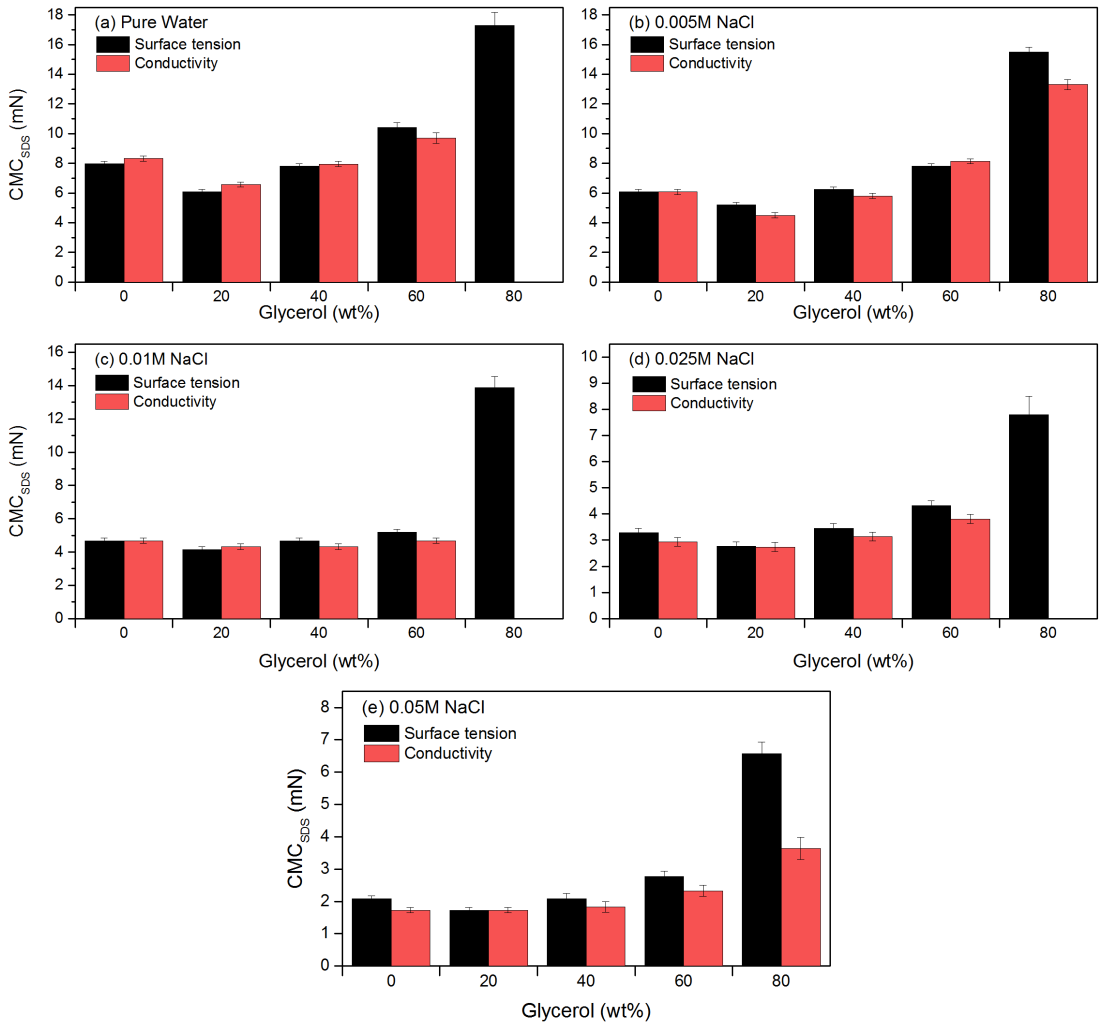


Fig 3.12 – Comparison of the CMCs determined from surface tension and conductivity methods for SDS in water-glycerol mixtures with: (a) 0 M to (e) 0.05 M NaCl concentrations.

At higher glycerol levels, the conductivity measurements have proven to be not as reproducible compared to the pendant drop method and the CMC for some of these compositions could not be extrapolated due to much higher degree of micellar dissociation. Even for the systems where the CMC was established, they are likely to be inaccurate determination. For the remainder of this chapter, the CMCs determined from the surface tension analysis will be used.

3.4.1.2 Solvophobic Effects

From the surface tension analysis, the effect of organic solvent on the CMC of SDS was determined for a full range of water-glycerol mixtures and also for water-propylene glycol mixtures. The CMC of SDS has not been previously determined in more than 60 wt% glycerol and 40 wt% propylene glycol.

The CMCs values obtained for all water-glycerol mixtures is shown in Fig. 3.13, along the literature CMC values using isothermal titration calorimetric (ITC) and conductivity methods. Based on the data from my pendant drop method study, as small levels of glycerol is added, the CMC decreases slightly and reaches a minimum at 20 wt% glycerol. On further increase of glycerol, the CMC starts to increase back to the control CMC value of ~8.0 mM at 40 and 50 wt% glycerol. From 60 wt% glycerol to pure glycerol, there is a dramatic increase in the CMC from 10.4 ±0.17 to 34.7 ±1.73 mM SDS concentration respectively. Dai and Tam observed the same trend for the effect of glycerol on the CMCs, in up to 50 wt% glycerol using the ITC method and also the CMC values are in very good agreement with the pendant drop method.[126] When compared to the literature conductivity data however, the minimum in the CMC at 20 wt% glycerol is not observed and the CMC values are slightly higher, but the overall trend (only determined up to 60 wt% glycerol) is similar.[121]

The slight decrease in the CMC observed upon small addition of glycerol can be explained by the effect of slightly changing hydrogen bonding properties of the solvent mixture. With small levels of glycerol addition to water, 10-30 wt%, the cohesive energy and the dielectric constant remains fairly high,[132] maintaining the high insolubility of the SDS hydrocarbon chain, however the hydrogen bonded network of this system becomes slightly stronger.[170, 171] Hydrogen bonding studies in water-glycerol mixtures have reported that in low glycerol- high water systems, the average H-bond number of water remain fairly constant as there is sufficient amount of bulk water around the glycerol molecules.[170] As glycerol contain three OH groups and the hydrogen bonding ability of hydrogen atoms in glycerol is stronger[171], it forms a slightly stronger hydrogen bonded network with water and particularly the SO_4^- headgroup. This causes the electrostatic repulsion between the headgroups to reduce, favouring micellization and leading to a slight decrease in the CMC.

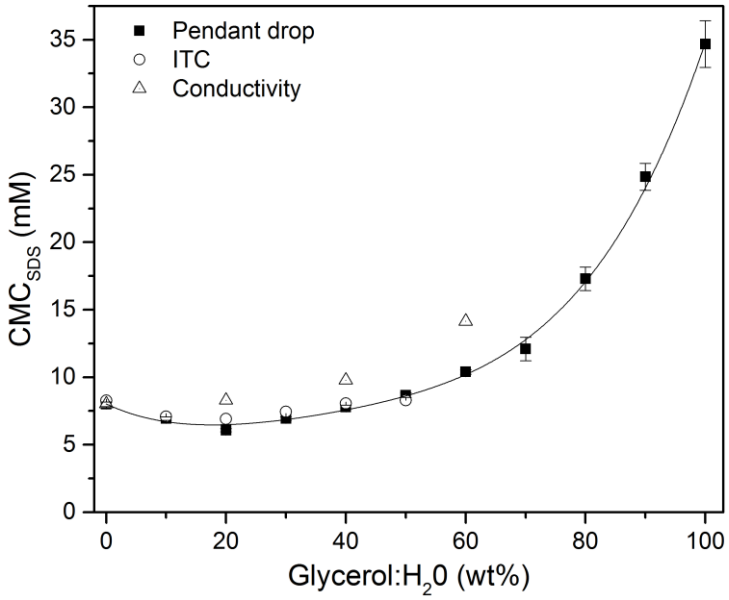


Fig 3.13 – Effect of glycerol on the CMC of SDS in water-glycerol mixtures, comparing (■) experimental data at 20 °C pendant drop method with published values (○) ITC method[126] and (△) conductivity[121] at 25 °C.

When the glycerol content is increased further (40 to 60 wt%), the cohesive energy and dielectric constant begin to reduce with the water structure being disrupted, decreasing solvent polarity.[132] This leads to a decrease in the hydrogen bonding ability of water, as there is a significant decrease in the average number of H-bonds of water with increasing glycerol-glycerol interactions.[170, 171] This causes the solvophobic effect on SDS to reduce slightly as the solubility of the hydrophobic tail is increased, but this also leads to a reduction in the electrostatic repulsion between the headgroup, due to an increase in ionic strength.[21] The effect of increased solubility is more prominent over the reduced electrostatic repulsion[121], causing an overall opposition to SDS micellization and increasing the CMC slightly. At very high levels of glycerol (70-100 wt%), the solvophobic effect is further reduced as the water structure is fully disrupted and the dielectric constant significantly decreases from 64.0 to 40.1 in 50 wt% glycerol to pure glycerol respectively.[132] The hydrogen bonding ability of the oxygen atom in glycerol is weaker than in water[171], so with increasing glycerol-glycerol interaction, the electrostatic repulsion effect is now increasing. Along with the increasing solubility of the hydrophobic tail and due to an increase in

the viscosity of the organic solvent, the SDS micellization is opposed, leading to a significant increase in the CMC.

A similar effect was seen on the micellization of SDS with water-propylene glycol mixtures, however the increase in the CMC values was significantly higher. Fig. 3.14 shows the increasing CMCs of SDS in propylene glycol mixtures and differences with CMCs from water-glycerol mixtures.

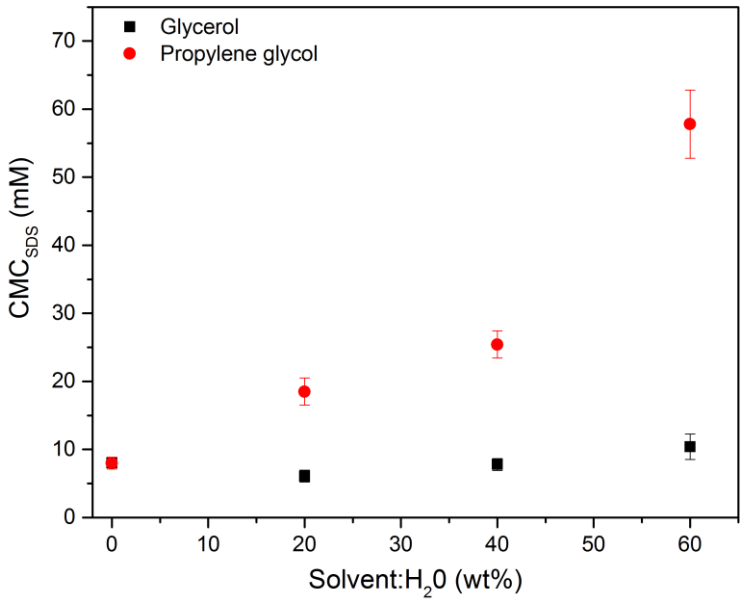


Fig 3.14 – Effect of propylene glycol on the CMC of SDS at 20 °C and a comparison with water-glycerol mixtures. Mean ± s.d (n=3).

The higher CMC values in propylene glycol compared to glycerol is due to the differences in their structural properties with propylene glycol having one less hydroxyl group compared to glycerol, as shown the chemical structure in Fig. 3.15, which leads to a difference in the polarity of the two solvents. Therefore, propylene glycol has a lower dielectric constant, less cohesive energy and weaker hydrogen bonding network compared to water-glycerol mixtures[122, 172], hence opposing micellization more strongly. Similarly, when the ternary water-glycerol propylene glycol mixture (25-15-60 wt% respectively) was tested, the CMC of SDS was determined to be even higher at 92.5 ±5.0 mM, further reinforcing the explanation.

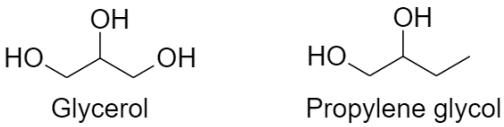


Fig 3.15 – Chemical structure of glycerol and propylene glycol.

3.4.1.3 Effect of Electrolytes

The CMCs determined from the pendant drop method, for the control NaCl-water solutions, were in very good agreement with the published CMC values determined from the conductivity method[139] (shown in Fig.3.16). As expected, the CMC decreases as NaCl concentration is increased due to reduced electrostatic repulsion between the SO_4^- headgroups, favouring micellization.

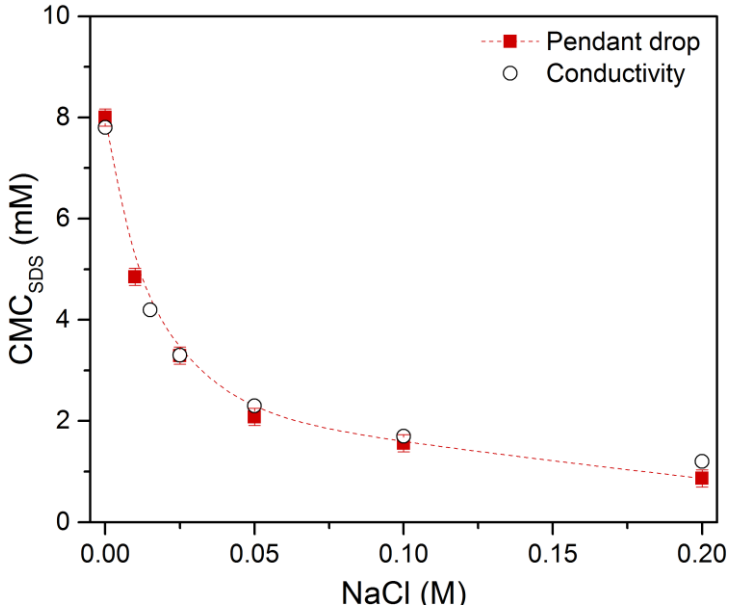


Fig 3.16 – Effect of NaCl on the CMC of SDS, as a function of NaCl concentration, at 20 °C and comparison with published conductivity method[139]. Mean ± s.d (n=3).

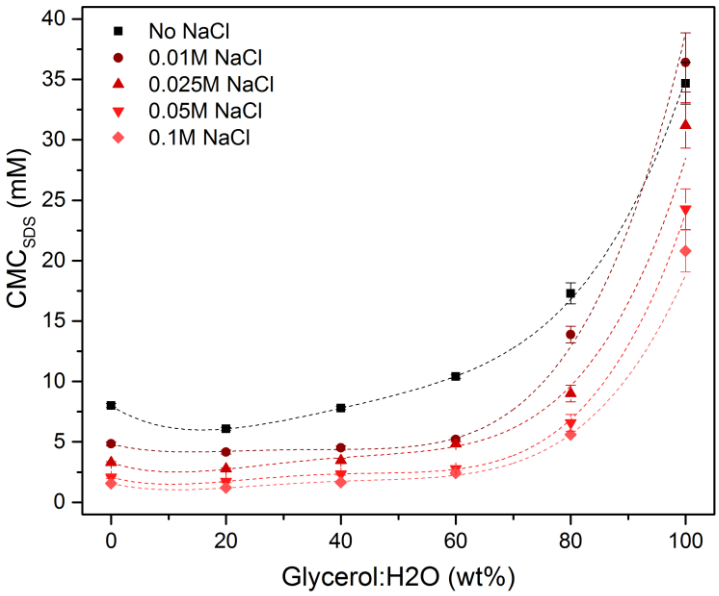


Fig 3.17 – CMC of SDS in water-glycerol + NaCl solutions, as a function of water: glycerol content, at 20 °C. Mean ± s.d (n=3).

The effect of NaCl is very similar across all water-glycerol mixtures as shown in Fig.3.17. Since organic solvent and salt have opposing impacts on the micellization of ionic surfactants, these effects do cancel each other out an extent. However, it can be noted that even with the addition of small levels of NaCl in high glycerol mixtures, the CMC is reduced significantly. For example, in a 80 wt% glycerol mixture, the CMC is reduced from 17.3 ±0.87 mM with no NaCl to 7.8 ±0.69 mM in a 0.025 M NaCl solution, which is similar to the CMC of SDS in pure water (8.0 mM). This suggest that the effect of ionic strength in reducing the headgroup electrostatic repulsion in high glycerol mixtures with salt is slightly more prominent than the effect of increasing solubility of the hydrocarbon tail. It is important to point out that, even though the CMCs in pure water and 80 wt% glycerol + 0.025 M NaCl were similar, their physical properties, i.e. surface tension, viscosity/rheology was different, with the 7.8 mM SDS in 80 wt% glycerol + 0.025 M NaCl solution giving a higher viscosity and surface tension compared to the 8 mM SDS in pure water. Therefore the morphology of the SDS hydrates and micelles and their growth in both these systems are likely to be different as well.

3.4.2 Krafft Temperature Determination

3.4.2.1 DSC experiments

DSC experiments was first carried out on 8.0 mM SDS in water solution (CMC levels) in order to determine the T_K through the heat flow peaks, from a range of heating and cooling rates. From the DSC instrument used (Perkin-Elmer), no peaks were observed at any of the heating/cooling rate used, due to the very low concentration of SDS tested and the low sensitivity of the instrument. Similarly, no peaks could be seen for 16.3 mM (0.5 %) SDS. A significant peak in the heating cycle was eventually seen when at 34.7 mM (1 %) and 69.34 mM (2 %) SDS in water were test. The onset of the endothermic peak was determined to be 14 °C. No peaks in the cooling cycle was observed. Due to no significant peaks seen at the CMC level (8.0 mM SDS), this method was not used any further for T_K determination. All these DSC plots are provided in Fig.3.18.

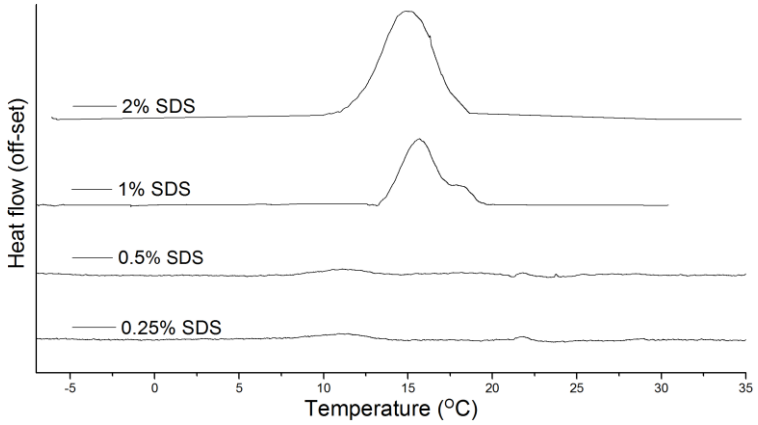


Fig 3.18 – DSC endothermic peaks for heating curves, for low SDS concentrations in water.

3.4.2.2 Surface tension vs Temperature

Since the surface tension of water-glycerol mixtures decreases as the temperature is increased, due to the thermal energy of the cohesive forces being lowered[164], this was taken into account when establishing the break point to determine the T_K.

At the CMC levels, the surface tension of pure water and 20 wt% glycerol mixture, at 8 °C was ~41 mN/m and it decreased to ~35 mN/m at 16 °C (Fig. 3.19). This change in surface tension, over an 8 °C increase in temperature, is significant compared to the

change in surface tension of pure water only. This establishes that the change in surface tension for these SDS-water-glycerol mixtures is due to the changing surfactant aggregation behaviour as a function of temperature and not only due to increasing temperature. As discussed previously, the effect of temperature on the surface tension of water-glycerol mixtures (appendix Fig. 8.2) was determined, showing less than 1 mM/m decrease in surface tension when the temperature is increased from 10 to 20 °C. Also, the 5 minutes equilibrium time set for this T_K analysis, did not allow for the temperature to have any significant effect on the drop to cause a systematic change in the surface tension. In order for the temperature to cause a systematic change in the surface tension, the equilibrium time will need to be more than 10 minutes, as shown in the appendix Fig. 8.1. At lower glycerol levels, a distinct change in the slope of surface tension against temperature can be seen, allowing clear determination of the T_K. The break point was slightly more difficult to determine for higher glycerol level mixture (80-100 wt%), but was still detectable. For pure water, the break point/T_K was determined to be 16 °C which is in good agreement with published values.[8, 9, 17]

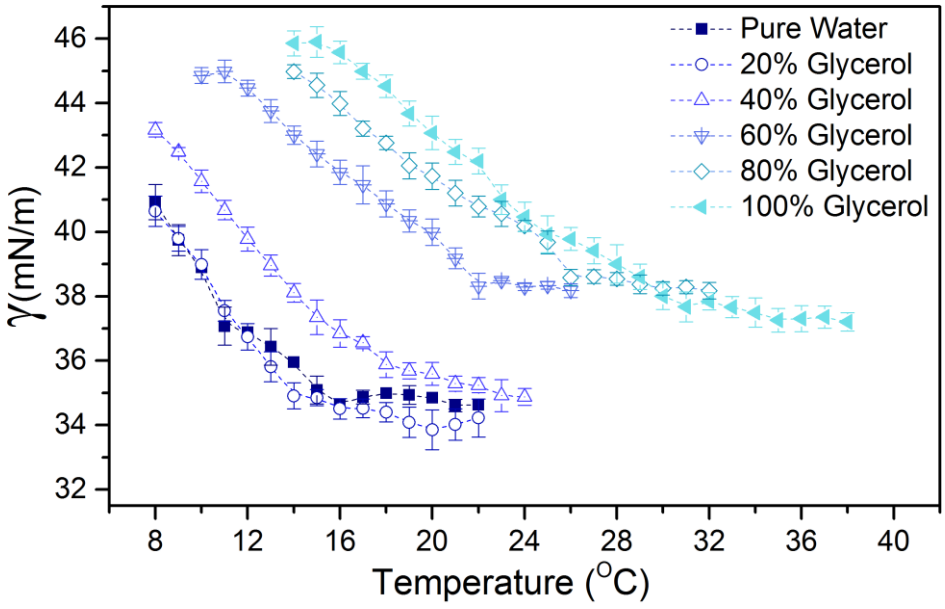


Fig 3.19 – Surface tension of SDS aqueous solutions as a function of temperature at specific CMCs for 0-100 wt% glycerol. Mean ± s.d (n=3).

Fig 3.20. shows the surface tension of SDS aqueous solutions (at their specific CMCs) for various NaCl concentrations, over temperature. Due to SDS-NaCl systems

enabling a higher concentration of surfactant to be adsorbed at the interface, the surface tension values are lower even at lower temperatures. For most of the SDS aqueous solutions with NaCl, the surface tension decreases from 38-39 to ~31 mN/m from 8 to 16 °C respectively, showing a change of ~7 mN/m over an 8 °C increase in temperature similar to the change in water-glycerol mixtures. This suggests that in both, water glycerol and NaCl solutions, the changes in SDS micellization behaviour is equally dependant on temperature.

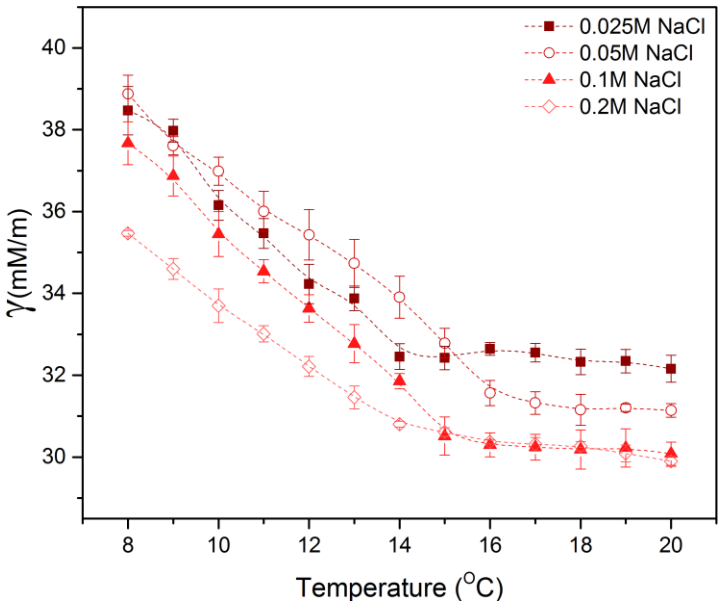


Fig 3.20. – Surface tension of SDS aqueous solutions as a function of temperature at specific CMCs for NaCl solutions. Mean ± s.d (n=3).

3.4.2.3 Effect of Glycerol and NaCl on T_K

The effect of glycerol on the T_K is similar to the effect it has on the CMC of SDS as shown in Fig.3.21. At low glycerol levels, in up to 30 wt% glycerol, there is no significant change in T_K and remains within the 14-16 °C range of the reported T_K of SDS.[9] Although, at 20 wt% glycerol the T_K is at its minimum (14 °C), similarly as was the CMC for the same system, corroboration that there is an increase in enthalpy due to a stronger hydrogen bonded network, leading to more negative ΔG^0_{mic}[121], favouring micellization at lower temperatures.

As the glycerol content is increased further, from 30 to 100 wt% glycerol, there is a linear increase in the T_K from 16 to 31 ±0.5 °C. A linear regression was fitted for this region of the plot and the results are shown in table 3.2.

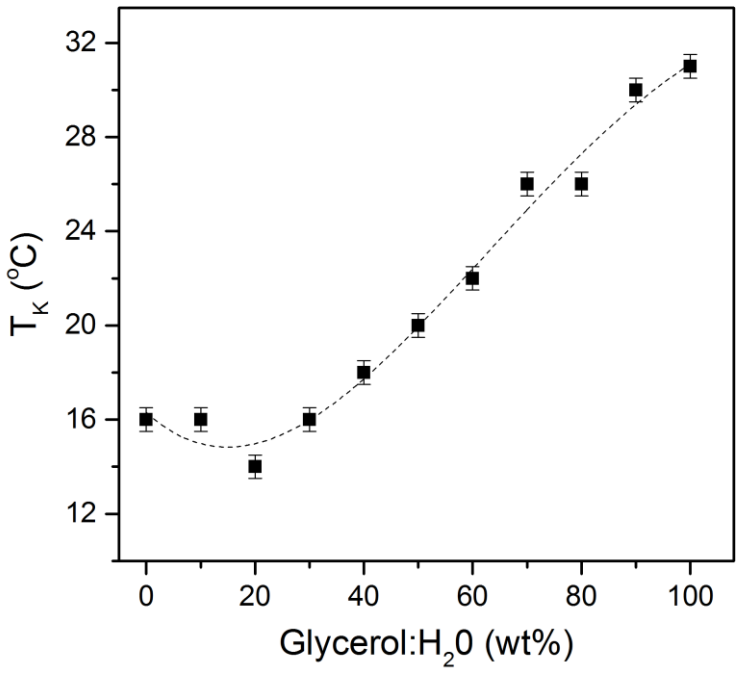


Fig 3.21. – Krafft temperature of SDS aqueous solutions at specific CMCs for 0-100% glycerol. Mean ± s.d (n=3).

The fitted model had a R^2 value of 0.98 and showed that (above 30 wt% glycerol) for every 1 wt% increase in glycerol level, the T_K increases by 0.22 °C. This gradual linear increase in T_K is due to the steady changes in the enthalpy-entropy compensation of micellization.[120] Since the solubility of the hydrophobic tail is now increased, caused by a decrease in the cohesive energy and dielectric constant, leading to a lower entropy and higher ΔG^0_{mic}, hence becoming thermodynamically more favourable for the SDS to not form micelles.[124, 127] Under these conditions, higher temperatures are required for micellization to become thermodynamically favourable. With low entropy, increasing the temperature drives the ΔG^0_{mic} to become more negative. The ionic strength of the SDS system is increased as the temperature increases[129] and therefore decreasing the electrostatic repulsion, allowing micelles to form.

Table 3.2 – Linear regression fit parameters for Glycerol vs T_K (Fig. 3.21), from 30 to 100 wt% glycerol levels.

Equation	$y = a + bx$	
Pearson's r	0.99177	
R^2	0.9798	
	Value	*Standard Error*
Intercept (a)	9.1547	0.83807
Slope (b)	0.22262	0.01216

The addition of NaCl to the water-glycerol mixtures does not have any significant impact on the T_K of SDS, and particular is not similar to the way it impacted the CMCs. The T_K mostly remains within the ±1 °C range for all water-glycerol mixtures with the increasing concentration of NaCl as shown in Fig.3.22. A previous study looking at the effect of NaCl on the T_K of SDS in water (using the conductivity method at a fixed SDS concentration of 0.25 M) found the temperature to slightly increase from 14.4 to 16.3 °C as NaCl was added from 0 to 0.02 M[143]. Although my results did not show this marginal increase in temperature, the overall T_K range for SDS in water was in good agreement, as the T_K was determined to be within 14-16 °C across all the NaCl concentrations tested. This comparison also suggest that the conductivity method provides more sensitive/accurate determinations of T_K, particularly in pure water systems.

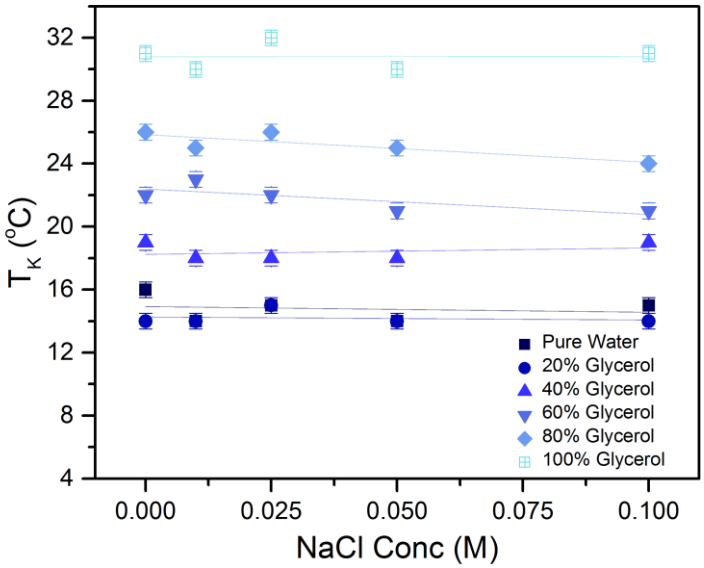


Fig 3.22 – Krafft temperature of SDS aqueous solutions at specific CMCs for water-glycerol + NaCl solutions. Mean ± s.d (n=3).

With the addition of NaCl, the CMC of these SDS systems decreases but the T_K remain fairly consistent due to the counterbalancing thermodynamics of SDS micellization in electrolytes solutions. As the concentration of Na+ counterion increases, there is significant gain in enthalpy (become more negative), due to a reduction in the headgroup repulsion, allowing micellization to become more favourable at lower temperatures.[137, 146] However, the packing parameter of SDS micelles also increases, leading to an increasing SDS aggregation number and larger aggregates, due to which the entropy is slightly reduced.[134, 145]

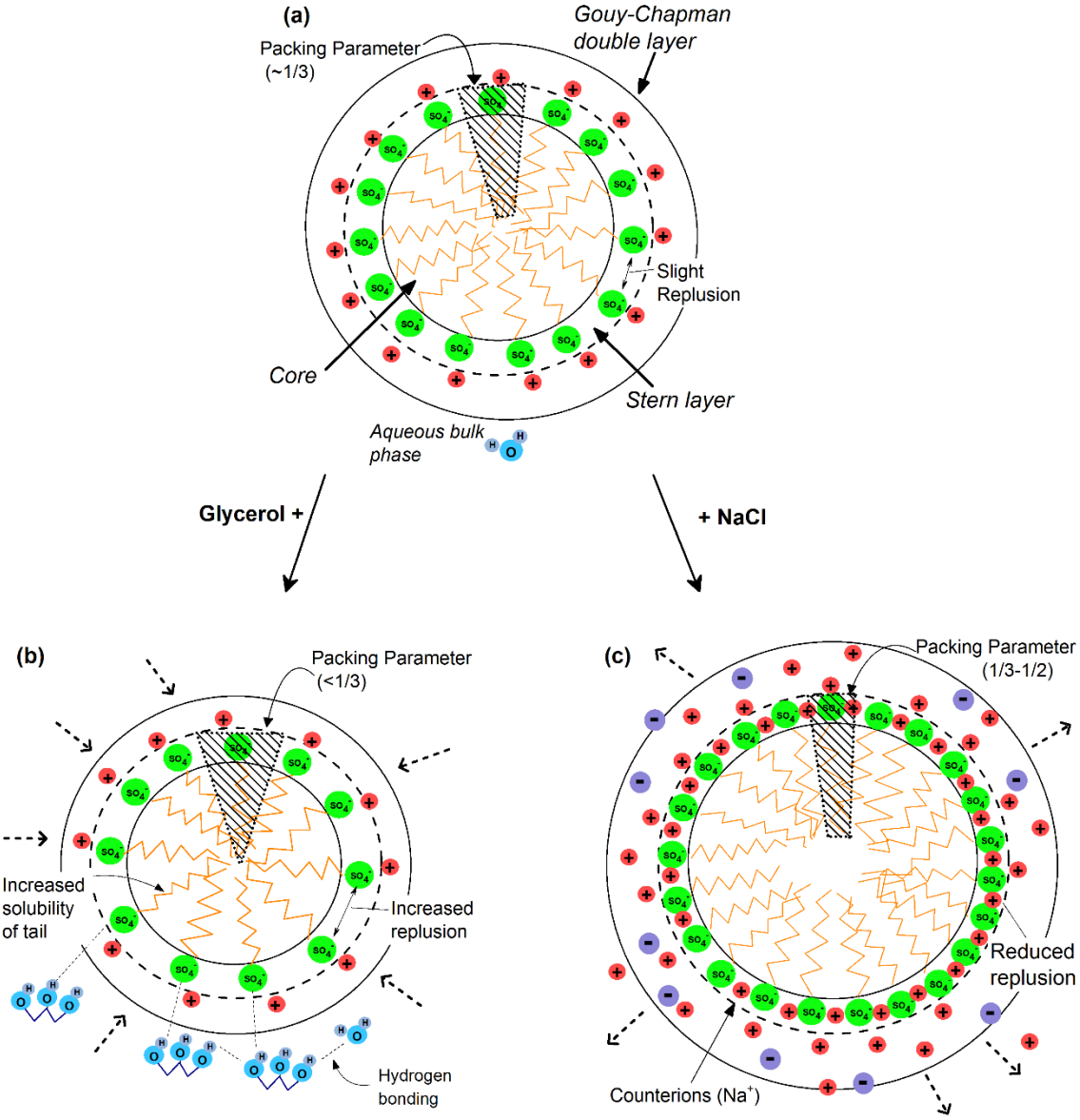


Fig 3.23 – Schematic of SDS micelles showing the changes in the packing parameter in a) high water content, b) higher glycerol content and c) NaCl solution.

Therefore, a maintained temperature is required to counterbalance these changes and hence remain fairly consistent or increases slightly to favour micellization. The changes occurring to the SDS micelles in water-glycerol and NaCl solutions is illustrated in Fig 3.23.

3.4.3 Pendant Drop Method

The pendant drop method, using the EasyDrop tensiometer proved to be an extremely valuable technique in determining the T_K and particular the CMC of SDS in water-glycerol mixtures. Once all the parameters were optimised and the method validated (section 3.3.2.1), all measurements were able to be automated, allowing for a high throughput of surface tension data for CMC determination. For T_K measurements however the process was comparatively less competent as the time-efficiency of the measurements was dependant on the ability of the water-bath to regulate the temperature. Also, the preciseness of the T_K values determined in water only systems was found to be less than the published values, carried out using the conductivity method. This is likely to be due to the conductivity being more responsive to changes in temperature compared to surface tension. However, the pendant drop method was able to, with reasonably good accuracy, determine the T_K of SDS in high glycerol mixtures, where other methods have been inefficient including the DSC. This technique was also very useful for analysing the ternary solvent system used, containing; 15 wt% glycerol, 25 wt% water and 60 wt% propylene glycol, which is more representative of solvent mixtures used in commercial detergents.

3.4.4 Alterations to the Krafft Point of SDS

The CMC and the TK values of SDS determined from all the various mixtures were used together to adequately determine and illustrate the alterations occurring to the Krafft point and its impact on the phase behaviour of SDS. To describe the changes occurring to the Krafft point of SDS, the individual effect of glycerol and NaCl is initially discussed and then their combined effect of explained. Fig 3.24 shows a plot of CMC_{SDS} against T_K, illustrating the shifting Krafft point as glycerol levels are increased. Shift 1 on the plot represents the slight lowering of the CMC and T_K in 20 wt% glycerol, from the original Krafft point. As the glycerol levels is increased to 40 and 60 wt%, the Krafft point changes to higher T_K and back to the original CMC level

(shift 2). On further addition of glycerol, up to 80 wt %, the Krafft point continues to shifts upwards, towards higher T_K and also toward higher SDS concentrations, above the original CMC level represented by shift 3. With the increasing Krafft point in both directions, the solubility boundary will also be shifting towards higher temperatures and the SDS phase transitions shifting towards higher SDS concentrations, as glycerol levels are increased. Shift 4 illustrates the changing Krafft point in pure glycerol, where it shifts to much higher CMC levels, while the raise in TK is not as substantial in comparison.

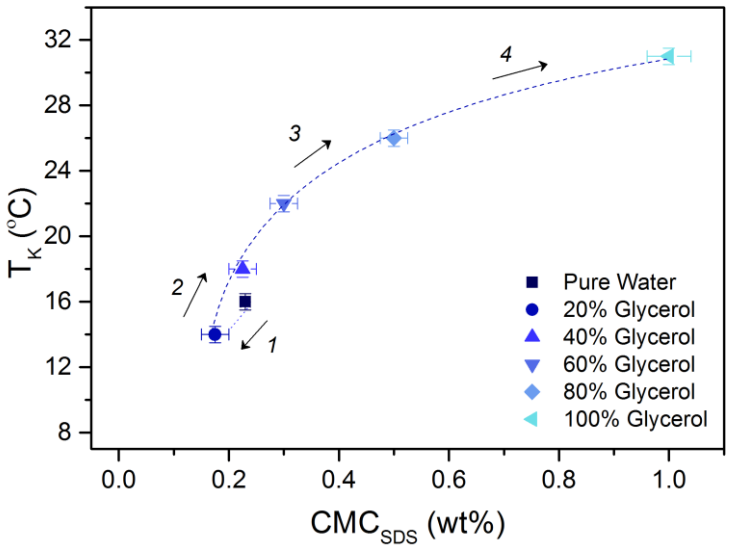


Fig 3.24 – Effect of glycerol on the Krafft point of SDS. The arrows indicate the direction in which the Krafft temp shifts as glycerol level increases. Mean ± s.d (n=3).

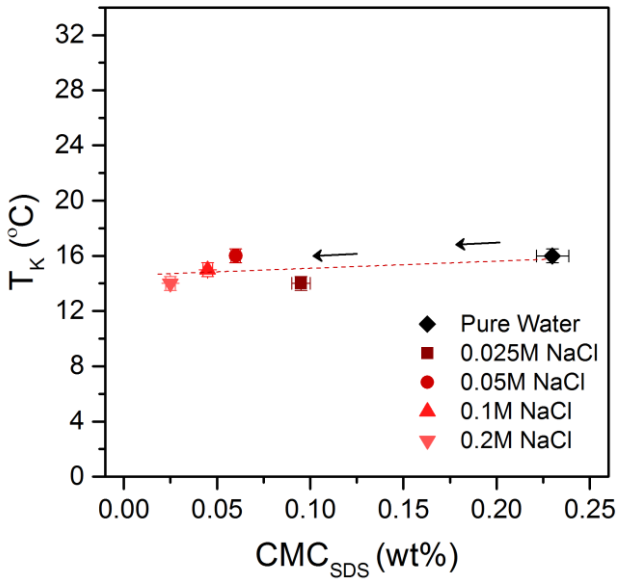


Fig 3.25 – Effect of NaCl on the Krafft point of SDS. The arrows indicate the direction in which the Krafft temp shifts as NaCl concentration increases. Mean ± s.d (n=3).

As mentioned previously, the addition of NaCl does not significantly change the T_K, therefore the alterations to the Krafft point of SDS in the presence of electrolyte mostly occur along the CMC_{SDS} axis as shown in Fig 3.25. The Krafft point shifts towards lower SDS concentrations with increasing NaCl concentration. This suggest that the temperature of the solubility boundary is hardly affected but shifts the SDS monomer-CMC phase transitions towards lower SDS concentration. These findings are also supported by previous studies showing the effect of electrolyte on SDS phase behaviour.[139-141]

These changes occurring to the CMC range and Krafft point with regards to the SDS solubility boundary are mapped out in the schematic phase diagram in Fig.3.26, using 60 wt% glycerol solvent systems as examples. At 60 wt% glycerol mixture, without NaCl, the monomer region becomes broader due to the increasing Krafft point, shifting the lyotropic liquid crystal phase transitions to the right of the phase diagram, towards higher SDS concentration. As the solubility boundary temperature also increases, the thermotropic liquid crystal phase region becomes wider, suggesting that the onset of H_C in to L_1 phase requires higher temperatures in the presence of glycerol. When 0.05M NaCl is added to 60 wt% glycerol system, the Krafft point changes from ~0.3 wt% SDS and 22 °C (in 60 wt% glycerol only) to ~0.08 wt% SDS and 21 °C, causing the onset of the L1 phase transition, from the monomer phase, to much lower SDS concentration.

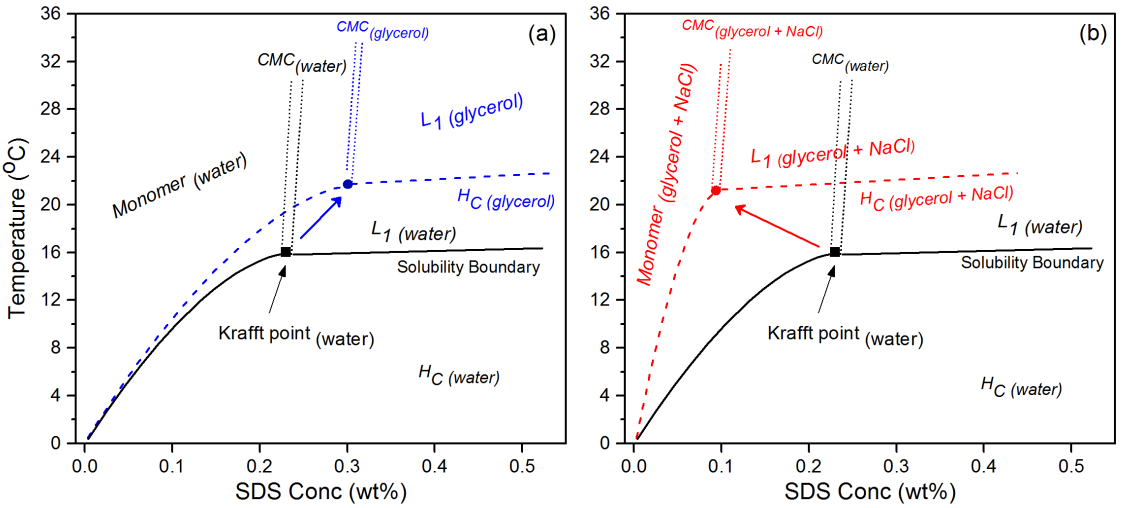


Fig 3.26 – SDS phase diagram showing the changes to the Krafft point and solubility boundary in (a) 60 wt% glycerol content and (b) 60 wt% glycerol + 0.05M NaCl solution. The arrows indicate the direction in which the Krafft temp shifts as NaCl concentration increases.

This addition of electrolyte leads to a narrower monomer region, even less than the monomer region occupied in the SDS-pure water (control) system, however the SDS crystallisation temperature is not affected. Therefore, the addition of salt can induce micellization to occur, in high glycerol content, at lower SDS concentration, but cannot reduce the solubility boundary temperature, hence these high glycerol systems still require higher temperatures for hydrated crystal to transition in to micelles.

The SDS concentration range studied in this chapter is fairly low as it focuses around the CMC- Krafft point region. Surfactant concentrations in commercial formulated products vary and are usually much higher, e.g. 20 to 40 wt% in liquid washes and detergent and therefore the subsequent chapters will build on from this study and investigative the effect of organic solvent on a wider and higher range of SDS concentration.

3.5 CHAPTER CONCLUSIONS

The pendant drop method was developed to provide a robust and a high-throughput tool for efficiently exploring and tuning the Krafft point of SDS in organic solvent and salt content. Using this technique, I have been able to successfully determine the dependency of the Krafft point of SDS in high glycerol content systems where other traditional methods (e.g. conductivity and DSC) have offered limited insight.

We found that with increasing glycerol content, the thermodynamics of micellization changes, due to the change in the solvent polarity and hydrogen bonding ability, which led to the Krafft point of SDS to also increase towards higher CMCs and solubility temperatures. The SDS phase diagram was established, focusing on the monomer/H_C to L_1 transitions and mapping out the alterations occurring to the Krafft point of SDS in water-glycerol-NaCl systems, which can be read off to determine the resulting phase from the changes being made. This study allows for the performance of surfactant based products, such as the final surface tension, Krafft point and hence hydrated crystal/micellar regions to be controlled and directed to a desirable characteristics.

When using the conductivity method for high (80 wt%) glycerol levels, the formation of micelles could not be detected accurately as there is inconsistent and restricted ion motion of the micelles through the glycerol solution and there are more free counterions, shown by the higher degree of dissociation. The DSC instrument used was unsuccessfully at detecting the phase transition temperatures, at the CMC levels, for even the control SDS-water system. Although the T_K was established using the pendant drop method successfully, particularly for high glycerol system, the accuracy of those measurements needs to be investigated and explore tools to further develop this method for more efficient T_K experiments.

The validation and the robustness of the pendant drop method established in this chapter, to determine the CMC of a model anionic surfactant in high organic solvent mixtures with electrolytes, has paved the way to efficiently analyse some commercial detergent formulations, where the solvent system is typically a ternary mixture and has a high organic solvent content with low levels of electrolytes.

Chapter 4
SDS Phase Behaviour in Organic Solvent

4.1 OVERVIEW

This chapter expands on the SDS concentration range/ region examined in the previous chapter for Krafft point investigation. Here, SDS system in the range of 10 to 40 wt% concentration were used to cover surfactant-base formulations of interest, i.e. liquid detergents. The transitions occurring near the SDS precipitation boundary are addressed in further detail, particularly with regards to SDS hydrated crystals. The use of DSC and X-ray scattering analysis in the investigation of surfactant phase behaviour is explained. Through both these techniques, an insight into the effect of altering solvent quality was gained, with DSC providing complimentary transition temperatures to the SAXS data structural analysis, giving confidence in the results obtained. SDS phase diagrams were created from correlating the data and findings in this chapter and chapter 2, allowing for the changes in the various phase transitions, due to changing organic solvent content, to be mapped out and difference tracked.

4.2 INTRODUCTION

The SDS phase diagram in water has been well established in literature as previously discussed in chapter 1 and 2. However, there is still a lack of clear understanding on the surfactant crystallisation occurring at low temperatures, particular for liquid surfactant systems containing organic solvent.[38, 42, 44] The (re)crystallisation at low temperature, can be reversed under most condition, however, they are perceived as unstable/ failed stability system for commercial, consumer products.[5, 42] The SDS precipitates forming at low temperature are hydrated crystals, which can grow with decreasing temperatures or changing compositions.[5, 38, 56] Some understanding of various types of SDS hydrates is required to determine how the negative transformations can be controlled.

4.2.1 SDS Hydrated Crystals

To date, there are four SDS hydrated crystal forms reported in literature.[32, 42, 44] These are: SDS.1/8 hydrate, hemihydrate (SDS.½H_2O), monohydrate (SDS.H_2O) and dihydrate (SDS.2H_2O), and the single crystal structure of only the first three SDS hydrates has been determined and widely reported.[32, 42, 44, 173]. Single crystal X-ray Diffraction (XRD) techniques as well as optical microscopy via differential interference phase contrast and microfluidics methods have been used to determine the structural properties of these hydrates.[32, 173, 174]. As mentioned previously, these hydrates form lamellar structures, consisting of SDS bilayers separated with an inter-planer water layer.[32] The thickness of the bilayer differs for each type of hydrate, due to various degree of tilting of the hydrocarbon chains.[174] Table 4.1 lists the known properties of the three SDS hydrates. It shows that as the hydration level increases, the tilting of the chains also increases, leading to a smaller lamellar thickness.[175] A schematic of the three hydrates with the changing bilayer thickness is shown in Fig 4.1.

Table 4.1 – Dimensions of some known SDS hydrated crystals in water.[32, 175]

SDS Hydrate Structure	Interplanar d-spacing (Å)	Angle between polar plane and chain (°)		Average area per polar headgroup (Å^2)
		ab plane	*ac* plane	
SDS.1/8H_2O	38.8	79	4-7	20.9
SDS.1/2H_2O	30.8	46	40	25.8
SDS.H_2O	28.9	40	15	29.5

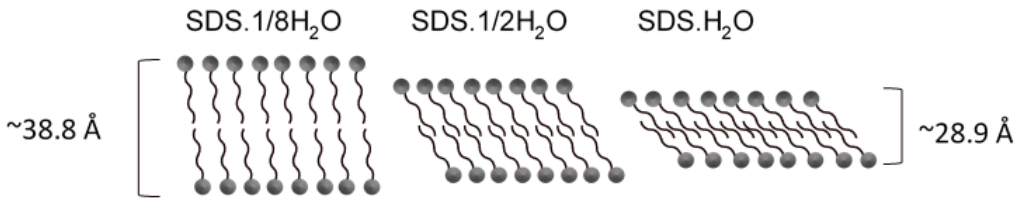


Fig 4.1 – Schematic of SDS hydrated crystals in water.

These hydrates begin to develop as the SDS micelles/hexagonal phases crosses the precipitation boundary, due to lowering of temperature and/or change in system composition.[30] There isn't a clear or single point of complete transformation between the two phases (e.g. micelles and hydrates) and are mostly co-existing together just below the boundary,[29, 30] as illustrated in Fig 4.2. This is the region of interest in the chapter regarding SDS phase behaviour.

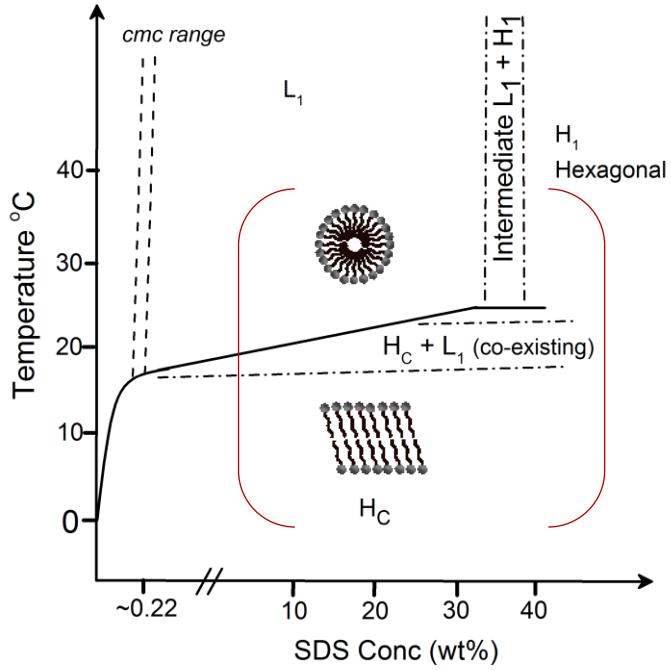


Fig 4.2 – Schematic of SDS phase diagram in water, focusing on the regions near the solubility boundary.

4.2.2 DSC

The DSC technique can measure accurately the changes in the heat capacity of a sample, which is representative of the transitions taking place in a surfactant-solvent system, e.g. phase changes between liquid crystals.[58] Liquid crystals in a surfactant system consist of long-range orientational and translational order with varying degrees, changes in which leads to the transition between the various thermotropic and lyotropic liquid crystalline phases. These transitions are thermodynamically driven. As the temperature of a surfactant system changes, the orientational and translational order of liquid crystals also changes, either requiring or releasing energy as the transition occurs, causing a change in the heat capacity of the sample.[47, 59] Fig 4.3

shows a schematic for typical DSC curve for a simple aqueous surfactant system, where upon heating the system from a low temperature (below the solubility boundary) the hydrated surfactant crystals transforms in to a LLC , e.g. into a L_1 phase as the chains melt causing changes in the orientational and translation order, releasing energy. This phase transition is identified through an endothermic peak (A) on the heating curve and the phase transition temperature is taken as the peak onset point, via the extrapolation method illustrated in Fig 4.3.[176] As the same system is cooled back down to temperatures below the T_K, the nucleation temperature of the hydrates can be detected through the onset of the exothermic peak (B), identifying the recrystallisation process.[30, 42] The onset point and amount of heat exchange can differ depending on the rate of heating and cooling.[30, 42, 177] DSC has been successfully used in determining the thermal behaviour of SDS-water system and mapping out the SDS phase diagram, with the aid of other structural analysis techniques like X-ray scattering.

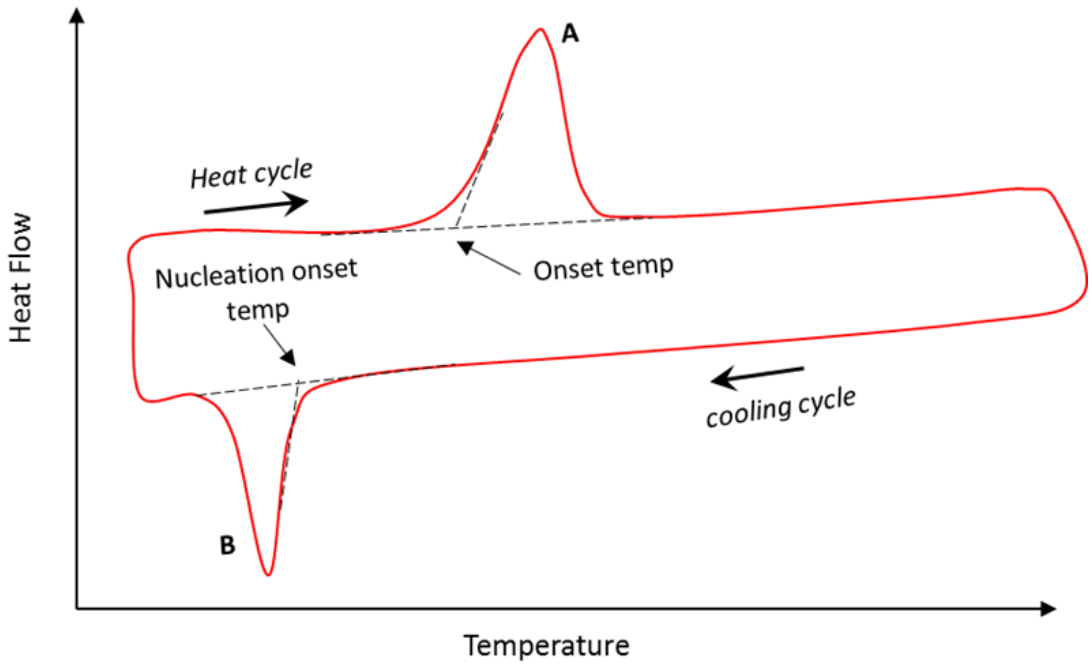


Fig 4.3– Schematic of DSC heat flow curve for a simple surfactant system showing: an endothermic peak on heating (**A**), representing the 'melting' of hydrated crystal and transitioning into a lyotropic liquid crystal. On cooling, an exothermic peak (B) is shown, illustrating the nucleation onset of surfactant hydrated crystal at low temperatures.

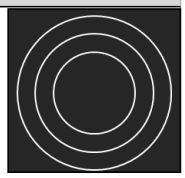
4.2.3 X-ray scattering

X-ray scattering is an extremely useful technique to determine detailed structural properties of liquid crystals as mentioned in chapter 1, along with the principle behind the technique (section 1.2.4.1). In this chapter, the various phase formed across the SDS precipitation boundary will be characterised through X-ray scattering.

4.2.3.1 SAXS

As discussed in chapter 1, LLCs adopts a limited number of specific morphologies, therefore their measured diffraction patterns are not only simplified but can be compared to model diffraction patterns for identification.[178, 179] These patterns are translated into Bragg's diffraction peaks, the positions of which are reciprocal spacing of the lattice planes, characterised by the Miller indices (*h, k and l*).[46, 48] SAXS patterns for the lamellar and hexagonal phases are given in table 4.2, along with the peak positions and indices.

Table 4.2 – Peak position, indices and diffraction patterns for lyotropic liquid crystals.[46, 48]

Lyotropic Phase	Position and Indices					Pattern
Lamellar	1 (100)	2 (200)	3 (300)	4 (400)	5 (500)	
Hexagonal	1 (100)	√3 (110)	2 (200)	√7 (210)	3 (300)	

Analysis of these diffraction pattern provides the repeat spacing within the lattice, i.e. d-spacing.[48, 53] The lamellar phase results in a simple pattern with equally spaced peaks in the ratio of 1, 2, 3, 4..., due to the alternating bilayer structure.[46, 48] After the lattice type is identified from the peak ratios, the spacing within the lattice can be determined. The d-spacing (determined from the repeat distance) is the spacing between the two adjacent bilayer planes, including the hydration layer separating the

two, as shown in Fig 4.4.[52] Therefore d-spacing is a measurement of the bilayer thickness as well as the inter-lamellar water layer.[48] The hexagonal phase is a 2-dimensional lattice of rod-like micelles, giving characteristic diffraction peaks of √1, √3, 2, √7…. [46] For a micellar phase, a characteristic broad peak is observed in the small angle region and does not consist of repeating patterns.[180, 181]

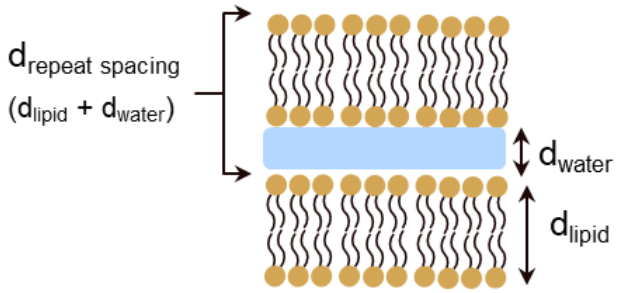


Fig 4.4– Schematic of lipid bilayers, showing the d-spacing determined from SAXS analysis.

4.2.3.2 WAXS

As explained in chapter 1, WAXS analysis is useful for characterising different lamellar phases, as they have differences in their hydrocarbon chain packing.[54] A fluid lamellar phase (L_α) chain are disordered and not fixed in a lattice site, which gives a broad diffraction peak in the wide angle region, centred ~4.6.[48] In the lamellar gel (L_β) phase, the chains are extended and fixed in a hexagonal packing, resulting in symmetrical peaks at about 4.2.[48, 54] In the tilted gel phase (L_β'), relatively sharper peaks are observed and for the lamellar crystalline (L_C) phase also, a series of sharp lines are given due to the hydrocarbon chains being frozen in a fixed lattice.[56]

Therefore WAXS analysis can be used to distinguish between the various lamellar structures observed. For the purpose of this study, SAXS data will be the main focus, in order to identify the lattice types and to determine the d-spacing of the various SDS hydrates being formed.

4.3 EXPERIMENTAL

An overview of the materials and equipment used was previously described in Chapter 2. Specific details on sample preparation, compositions and measurements parameters used for each experiment are provided in this section.

4.3.1 Materials and Compositions

SDS was the only surfactant used in the chapter, along with glycerol as part of the solvent mixture. SDS (>99.5%) and Glycerol (>99.5%) were both purchased from Sigma Aldrich. Full details of the materials used is given in chapter 2 and all the materials in this section were used as received, since they were analytical grades. A range of SDS concentration from 10 to 40 wt% were typically used (unless otherwise stated), in various water-organic solvent mixtures. All water-organic solvent mixtures were prepared by mass, consisting of 20, 40 and 60 wt% glycerol. All samples were tested at least 2 hours after being prepared and used within 48 hours.

4.3.2 DSC analysis

PYRIS Diamond DSC (Perkin-Elmer Instruments) was used for all thermal analysis. Some details of the instrument and the DSC technique is provided in chapter 2 (section 2.8). For all samples, the DSC pans were initially held at -10 °C (unless stated otherwise) for 10 minutes for SDS hydrates to form, after which it was heated and then cooled at 5 °C/min. The upper temperature limit varied based on the SDS-solvent system. Three heating and cooling cycles were applied with the sample being held for 5 minutes at both upper & lower temperature limits. DSC analysis was carried out on a range of SDS concentrations, in various water-organic solvent mixtures as mentioned above.

4.3.3 X-ray scattering

Details of the X-ray scattering experiments, instruments and set-ups is provided in chapter 2 (section 2.9). Since all measurements were carried out at the Diamond Light Source, Oxfordshire, all samples were prepared at least 48 hours prior to testing. For the temperature resolved (isothermal) experiments, four SDS concentrations, 10, 20, 30 and 40 wt%, were used, in a series of water-glycerol mixtures. For the Linkam experiments using the DSC600 capillary stage, only 20 wt% SDS concentration was tested in all water-glycerol compositions.

4.4 RESULTS AND DISCUSSION

The data analysis from the pendant drop method was primarily used to determine the effect of organic solvent with NaCl on the micellization of SDS near the Krafft point and will be discussed in greater details in this section. The efficiency of the pendant drop method along with a comparison with conductivity and DSC measurements is also provided.

4.4.1 DSC analysis

SDS-water system was used as the control system for characterising the various SDS transition phases and validating the DSC analysis. The SDS phase diagram established by Kékicheff, P et al,[30] was used as the reference standard. This validation was then used to analysis SDS in various water-glycerol mixtures.

4.4.1.1 SDS-water control system

An initial isothermal step carried out at -10 °C ensured that SDS hydrates are formed, after which the system was heated and then cooled at 5 °C/min. The highest temperature set for SDS-water systems was 60 °C, which is well within the SDS phase transition temperatures for 10 to 50 wt% concentrations.[30] Three heating and cooling cycles were carried out for all systems to determine the hysteresis effect on the DSC curves. For all DSC measurements carried out on SDS systems, no significant changes were identified in the transition temperatures from the three repeat cycles. Therefore, the transition peaks from the first heating and cooling cycles were analysed for reporting in this chapter.

Upon heating a SDS-solvent system, there are commonly more than one endothermic peak produced, which are merged together (or super imposed), resulting in a large peak consisting of a ‘shoulder’ towards the left, as illustrated in Fig 4.5 showing the phase transitions of 20 wt% SDS in water. These endothermic peaks appear as merged due to the very narrow transition temperature range of SDS hydrate transformations, with each transition requiring a different level of energy intake.[42, 44] The extrapolated onset

temperature (T_O) represents the initiation of H_C melting through the disordering within the H_C alkyl chains. The 'shoulder' in the large peak is indicative of the inter-conversion(s) of the H_C, denoted as T_I and the main highest peak point signifies the phase transition of H_C into L_1 (T_{PT}), with the peak end depicting the completion of the micellization process (T_{PTC}).

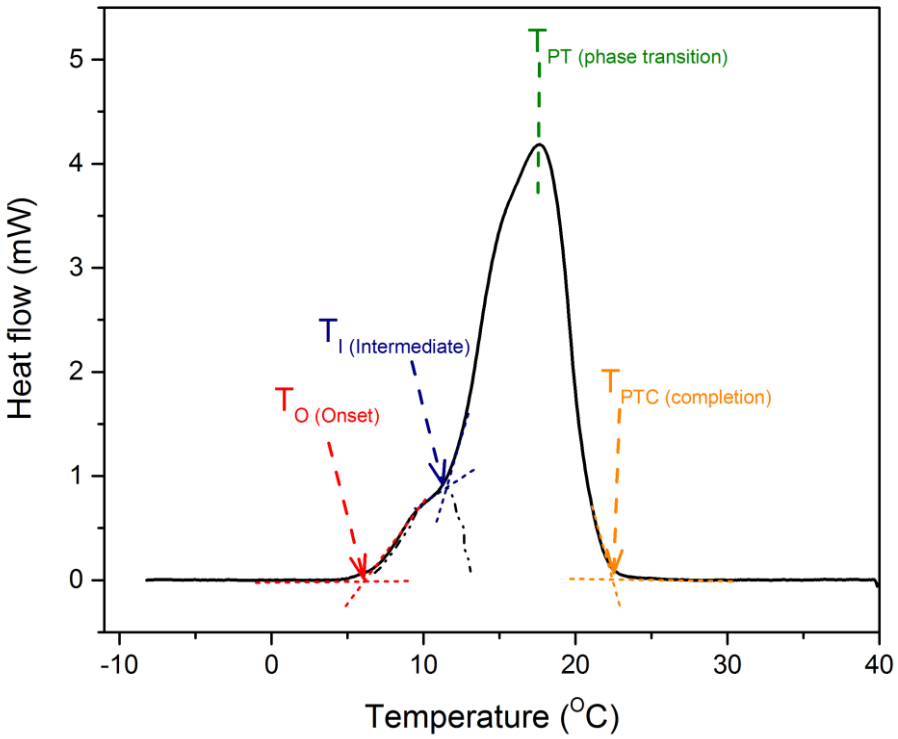


Fig 4.5– DSC endothermic peak for 20 wt% SDS in water, from a heating cycle at 5 °C/min, illustrating: Onset temperature (T_O) of SDS hydrate disordering, Inter-conversion transition temperature (T_I), Phase transition temperature (T_{PT}) and the Phase Transition Completion temperature (T_{PTC}). Determined through extrapolated intercepts (dash lines).

The heating curves for all SDS-water system (10 to 50 wt% concentration) is shown in Fig 4.6 and it can be observed that the endothermic peaks get higher and broader as the SDS concentration increases.

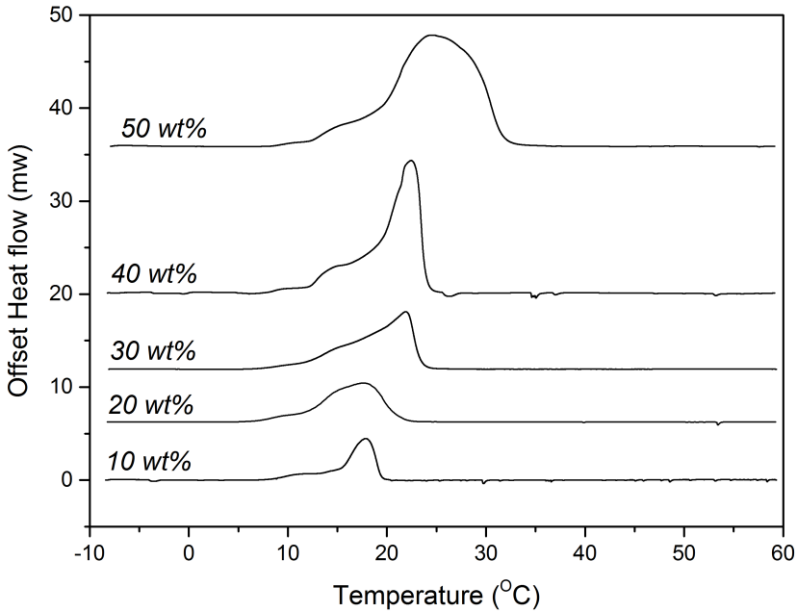


Fig 4.6– DSC endothermic peaks on heating at 5 °C/min, for various SDS levels (wt%) in water.

The various temperatures (i.e. extrapolated onset and peak phase transition etc) were determined for each DSC curve and plotted as a function of SDS concentration in Fig 4.7, representing a partial SDS phase diagram. It can be seen that there is a slight change in the T_O and T_I across surfactant concentrations, with the temperatures increasing from ~8 to 11 °C and ~12-15 °C respectively. However, as evident from the broadening of the peaks shown above in Fig 4.6, there is a more significant increase in the T_{PT} and T_{PTC} across the SDS concentrations. From 10 to 50 wt% SDS, the T_{PT} increases from ~17 to 24 °C and the T_{PTC} increases from ~19 to 32 °C. This broadening of the peak at higher SDS concentrations is due to the multiple morphologies of the liquid crystals being involved and the phase transitions from lamellar H_C interconversions to H_1, requiring higher thermal energy to complete the transformations. The DSC heating curves from 10 to 30 wt% SDS contain at least two endotherm peaks, with the first peak (T_I) in the range of 12-15 °C indicating the melting of the alkyl chains and the inter-conversion between the different H_C forms. The larger second peak (T_{PT}) at ~19 to 21 °C signifies the early stage of H_C to L_1 transformation, where both H_C and L_1 co-exist in a two-phase state, with the peak end (T_{PTC}) between 21-23 °C, showing the completion of the micellization process. This

corresponds to the literature findings, as discussed in section 4.2.1, where in up to ~35 wt% SDS concentration, the surfactant is present in a micellar phase, above the solubility temperature (~23 °C) and the size of the micelles is increasing with increasing SDS concentration. Also mentioned previously that above ~38 wt%, the L_1 phase completely transforms into the H_1 phase, with the solubility boundary increasing to ~27 °C. This explains the broadening of the peaks at higher SDS concentrations. The heating curves for 50 wt% SDS potentially contains at least three endotherm peaks, signifying multiple mesomorphic states, which require higher temperatures to completely transform, causing the broadening of the overall peak. However, due to the superimposing of the peaks, it is difficult to dissect all the endotherm peaks unless a clear 'shoulder/hump is identified.

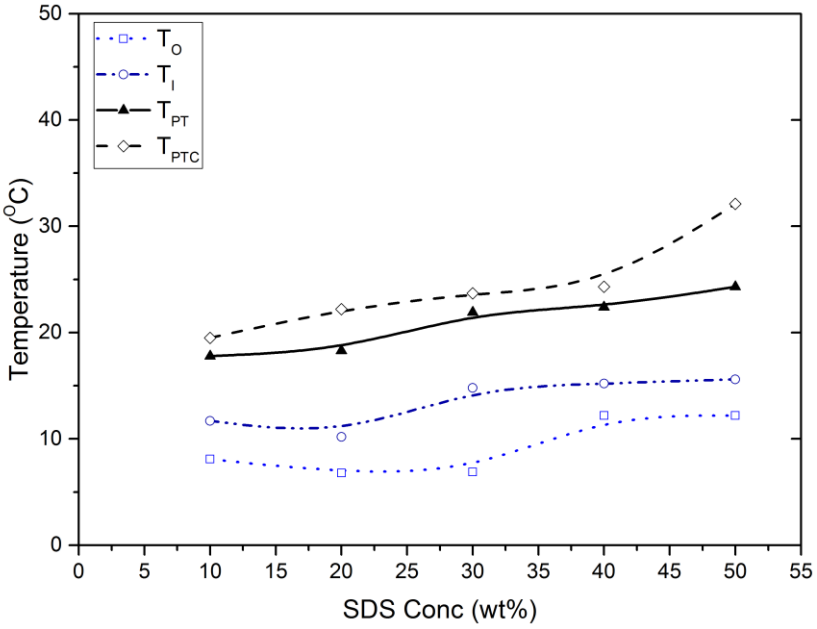


Fig 4.7– Phase transition temperatures as a function of SDS concentration (wt%) determined from DSC endothermic peak analysis, for SDS in water.

At these higher concentrations (40-50 wt%), the H_C intermediates transition temperature (T_I) is similar at ~ 15 °C, whereas the T_{PT} (depicting the H_C+L_1 co-existing state) is increased slightly to ~23 °C. The third endotherm peak is in the range of 25-27 °C, which represents the three-phase state where H_C, L_1 and H_1 co-exist, with the system eventually transforming completely into a single H_1 phase at ~30 °C (T_{PTC}).

These transition temperatures are in good agreement with literature values, with the solubility temperatures reported by Kékicheff, P et al correlating with the T_{PTC} values; The types of SDS H_C formed between T_O and T_I and between T_I and T_{PT} were determined by X-ray scattering analysis (section 4.4.2) and compared with literature findings.

As the SDS-water system is cooled back down, the reverse transition, recrystallization of SDS, takes place and the L_1 / H_1 phase transforms into H_C. The onset of the exothermic peak caused by this transition is characterised as the H_C nucleation temperature (T_N), which is illustrated in Fig 4.8. The peak itself represents the formation and growth of the SDS crystals with increasing order as the temperature is decreased, with the crystallisation temperature denoted as T_{CT} and the end of the exothermic peak as T_{CTC} marking the completion of the H_C formation (i.e. saturation of H_C growth).

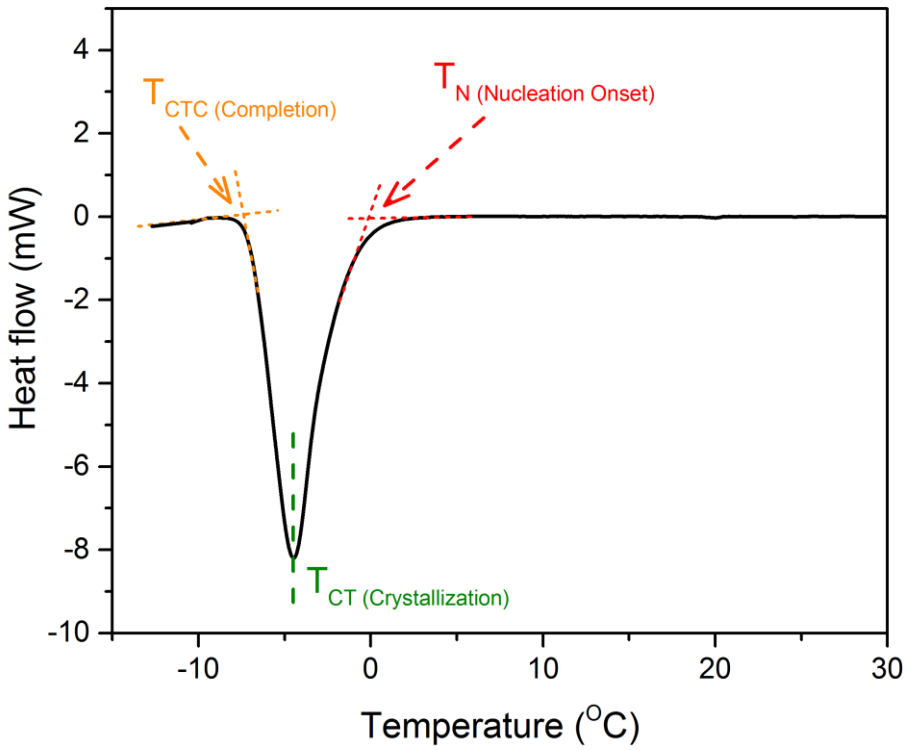


Fig 4.8– DSC exothermic peak for 20 wt% SDS in water, from a cooling cycle at 5 °C/min, illustrating: Nucleation temperature of SDS hydrates (T_N), Crystallization temperature of SDS (T_{CT}) and the Crystallization Completion temperature (T_{CTC}). Determined through extrapolated intercepts (dash lines).

The cooling curves for all SDS-water systems from 10 to 50 wt% concentration is shown in Fig 4.9. It can be seen that as the concentration of SDS increases, not only do the exothermic peaks shift towards higher temperatures, the size of the peak/ peak area also increases, indicating a higher energy release and therefore increased orientational and translational ordering.

For these exothermic peaks also, the nucleation / re-crystallization transition temperatures were extrapolated and plotted as a function of SDS concentration as shown in Fig 4.10. The plot shows that T_N increases from -9 to 1 °C from 10 to 30 wt% SDS, above which, the nucleation temperature plateaus ~ 1 °C at up to 50 wt% SDS. The increase in T_{CTC} however is less, as it increases from -10 to -5 °C from 10 to 50 wt% SDS, suggesting that the temperature at which the growth of SDS hydrates gets saturated is not affected as much as the temperature at which nucleation occurs, with increasing SDS concentration.

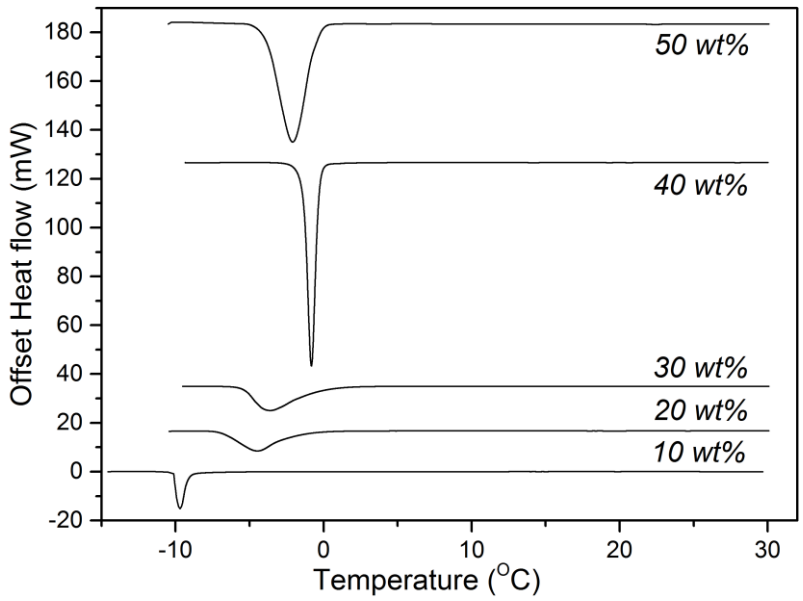


Fig 4.9– DSC exothermic peaks on cooling at 5 °C/min, for various SDS levels (wt%) in water.

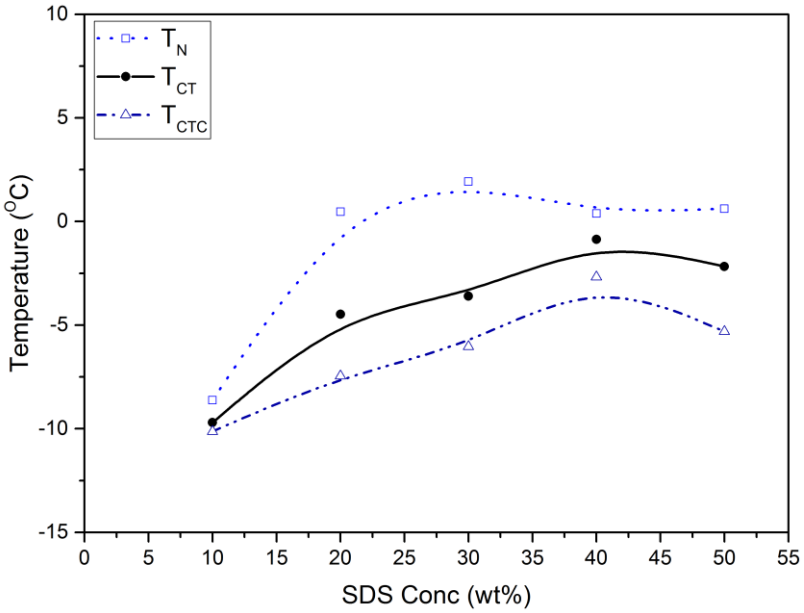


Fig 4.10.– Nucleation / recrystallization temperatures as a function of SDS concentration (wt%) determined from DSC exothermic peak analysis, for SDS in water.

4.4.1.2 Effect of glycerol

The same DSC analysis as the control above, was carried out for SDS in three sets of water-glycerol mixtures of: 20, 40 and 60 wt% glycerol, to determine the effect of increasing organic solvent content.

The endothermic peaks from the heating curve of all the three water-glycerol mixtures is shown in Fig 4.11. For 20 wt% glycerol mixtures, the T_O and T_I are similar to the water only system, especially at lower SDS levels of 10 and 20wt%, where they are at ~ 8 °C. The T_{PT} and T_{PTC} increases slightly, but remain in the range of 18-20 °C and 21-24 °C respectively. At higher SDS concentrations of 30 and 40 wt%, the T_O remains near 10 °C, but the endothermic peaks become broader when compared to water only system, showing more than two endotherms merged together and therefore multiple phase transition occurring. For 40 wt% SDS in 20% glycerol mixture (Fig 4.11 a) it can be seen that one of the endothermic peak starts to separate, with this peak

indicative of the H_C+L_1+H_1 co-existing phase and final transition into the H_1 phase, which occurs at ~33 °C (T_{PTC}).

Upon increasing the glycerol content further, to 40 % glycerol, the endothermic peaks become broader across all SDS concentration, with the number of endotherms increasing, as well as the phase transitions become increasing more visible. The T_O does not increase significantly and remains in the range of 11-12 °C, across all SDS concentration (Fig 4.11 b). Also the transition temperature for the SDS hydrate inter-conversion (T_I) remain ~15-16 °C, similar to the water and 20 % glycerol systems. There seems to be at least three main T_{PT}, which are extracted for phase diagram shown later in this section. The heating curve for 40 wt% SDS level gave a different profile where the first SDS hydrate inter-conversion (sharper) peak is completely separated from the other endotherms with a gap of ~ 26 °C. The broader peak near 50 °C contains two endotherms, which are likely representing the three-phase state and the transformation of H_C into L_1 and then in to H_1 completely at ~ 56 °C.

For 60 % glycerol systems, the SDS concentration range tested was larger, from 5 to 40 wt%. Based on the trends from the previous systems, the range was extended to lower levels of SDS in order to provide a comparison for the phase transition temperatures. At 5 wt% SDS, three separate endothermic peaks can be seen, with the T_O at ~ 12 °C, T_I at ~ 15 °C, T_{PT1} and T_{PT2} at 21 and 30 °C respectively. As the level of SDS increases to 10 wt%, the transition peak at T_{PT1} disappears, resulting in only two endotherms overall, which is similar for 20 and 30 wt% SDS profiles also. At 40 wt% SDS, the much broader second peak contains at least three phase transitions, indicating multiple hydrate inter-conversation. The T_O and T_I remains similar for at ~ 12-13 °C and ~ 15 °C respectively, across all SDS levels. This suggest that the onset of the melting of SDS H_C alkyl chains and the first H_C inter-conversion transformation occurs at similar temperature for 5 to 40 wt% SDS levels.

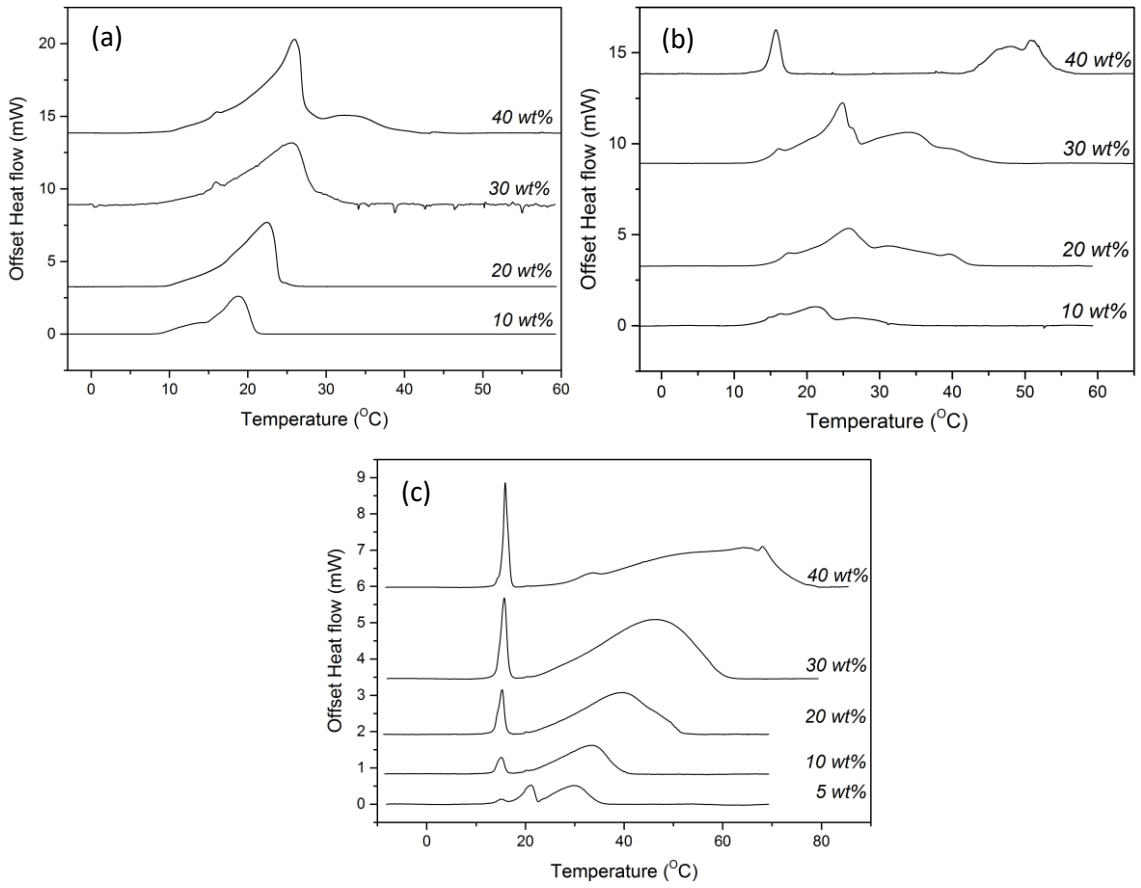


Fig 4.11– DSC endothermic peaks on heating at 5 °C/min, for various SDS levels (wt%) in water-glycerol mixtures, containing: (a) 20 wt% glycerol, (b) 40 wt% glycerol and (c) 60 wt% glycerol.

As with the SDS-water control analysis, the various transition temperature from all the three solvent systems were plotted as a function of SDS concentration (Fig 4.12) to initiate a SDS phase diagram parameter in various water-glycerol content. It can be noticed that T_O and T_I has a near flat curve as the level of SDS increases across all the three glycerol levels, whereas the phase transition temperatures (T_{PT}) and the transition completion temperatures (T_{PTC}) have a linear increase.

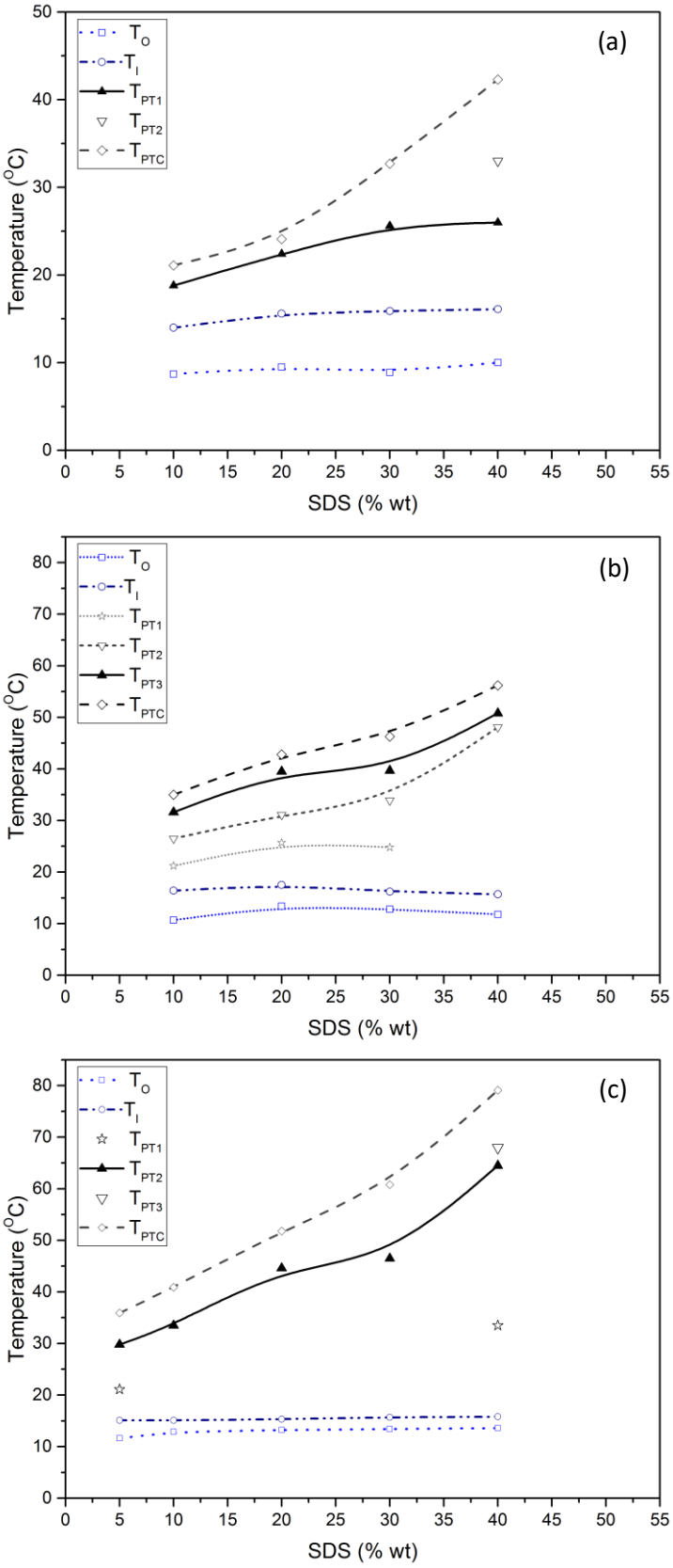


Fig 4.12– Phase transition temperatures as a function of SDS concentration (wt%) determined from DSC endothermic peak analysis, for SDS in: (a) 20 , (b) 40 and (c) 60 wt% glycerol.

The solubility boundary of all the SDS systems, determined from the T_{PTC} values, are plotted in Fig 4.13 to show the changing solubility temperatures as the glycerol content in the solvent system increases. There is no significant change in the SDS solubility boundary between water only and 20 wt% glycerol systems, particularly between 10 to 30 wt% SDS. When the glycerol content increases to 40 wt%, there is a significant increase of around 10 °C in the solubility temperatures overall and a further 5 to 10 °C increase in 60 wt% glycerol system, with precipitation boundary reaching near 70 °C at 40 wt% SDS.

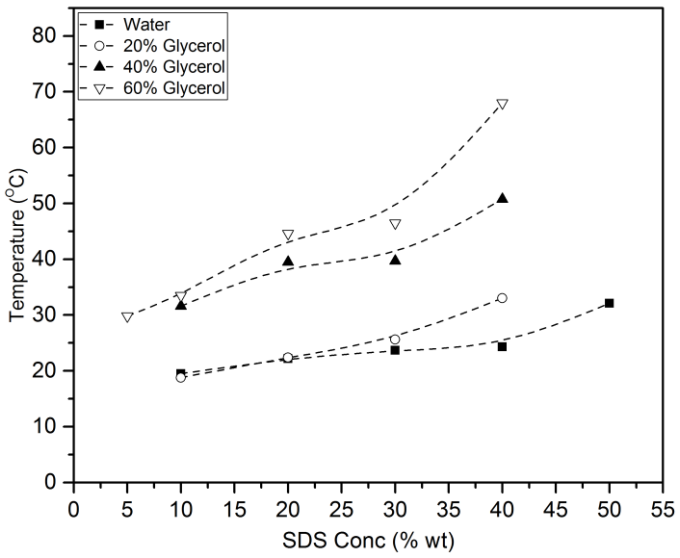


Fig 4.13.– Solubility boundary temperatures (T_{PTC}) as a function of SDS concentration (wt%), for SDS in water and various water-glycerol mixtures.

The DSC cooling curves were also analysed in the same manner as described previously for the SDS-water control system. Fig 4.14 shows the exothermic peaks for all three water-glycerol systems, across the various SDS levels. The 20 wt% glycerol system gave very similar recrystallization curves to the water only system, with both the T_N and T_{CT} increasing as the SDS concentration is increased. For 40 wt% glycerol mixtures, the exothermic peaks were similar for 10 to 30 wt% SDS, showing a single peak with gradual increase in T_N and T_{CT}. However at 40 wt% SDS, two exothermic peaks are produced, with the first peak being much broader, with an onset temperature (T_{N1}) of ~ 36 °C, which is a significant increase of ~ 27°C from the T_N of 30 wt% SDS system. When the glycerol content is increased to 60 wt%, multiple exotherms starts to appear at 20 wt% SDS levels and above.

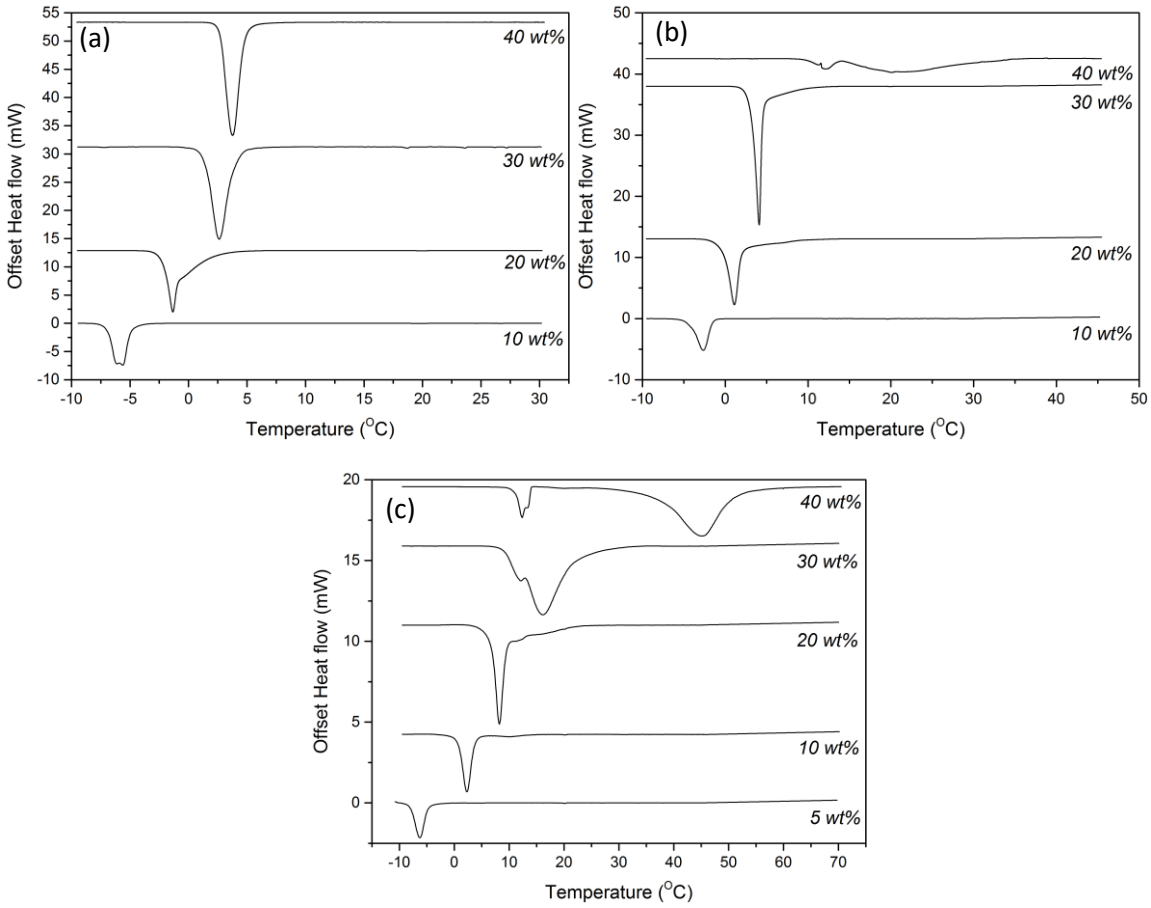


Fig 4.14– DSC exothermic peaks on cooling at 5 °C/min, for various SDS levels (wt%) in water-glycerol mixtures, containing: (a) 20 wt% glycerol, (b) 40 wt% glycerol and (c) 60 wt% glycerol.

These multiple exotherms indicate the numerous inter-conversion of SDS hydrates, therefore suggesting that the number of different hydrates produced increase with increasing glycerol levels. Again, when the SDS level is at 40wt%, the merged exotherms separate producing two distinct exothermic peaks separated by ~14 °C. The nucleation onset temperature of the first peak (T_{N1}) is at 57.2 °C, indicating the start of precipitation at much higher temperatures. The second exothermic peak has an onset temperature (T_{N2}) of 14.3 °C, suggesting that the inter-conversion from the initial set of SDS hydrates nucleated at higher temperature, does not occur until the temperature is reduced to near 14 °C. The nucleation and crystallisation temperatures for all three glycerol mixtures are plotted as a function of SDS concentration in Fig. 4.15, showing that in 20 and 40 wt% glycerol systems, there is a linear increase in T_N and T_{CT}. However, in 60 wt% glycerol, these transition temperatures show an exponential like increase as the SDS concentration is increased.

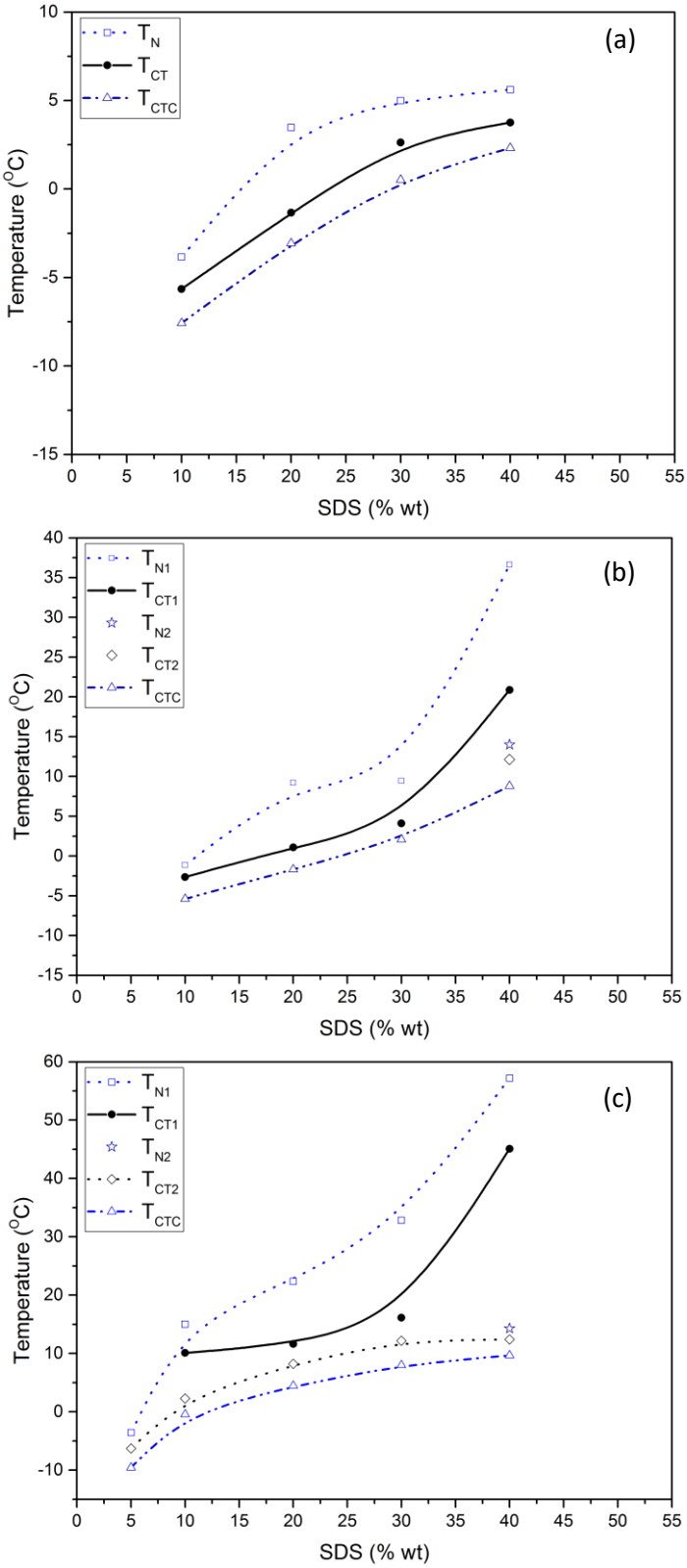


Fig 4.15– Nucleation / recrystallization temperatures as a function of SDS concentration (wt%) determined from DSC endothermic peak analysis, for SDS in: (a) 20 , (b) 40 and (c) 60 wt% glycerol.

Fig 4.16 shows the effect of glycerol on the SDS precipitation temperatures generated from the DSC cooling curves, as a function of SDS concentration. Between the water only and 20 wt% glycerol system, it clearly shows a parallel increase in the precipitation boundary across increasing SDS concentrations. For 40 wt% glycerol system, at SDS levels 10- 30wt%, the recrystallization temperatures are similar to the 20 wt% glycerol, however, at 40 wt% SDS, this transition temperature increases by ~ 16 °C. Similarly between 40 and 60 wt% glycerol systems, there is an increase of ~ 15 °C at 40 wt% SDS, suggesting that impact of increasing glycerol content is more on systems containing higher concentration of surfactants.

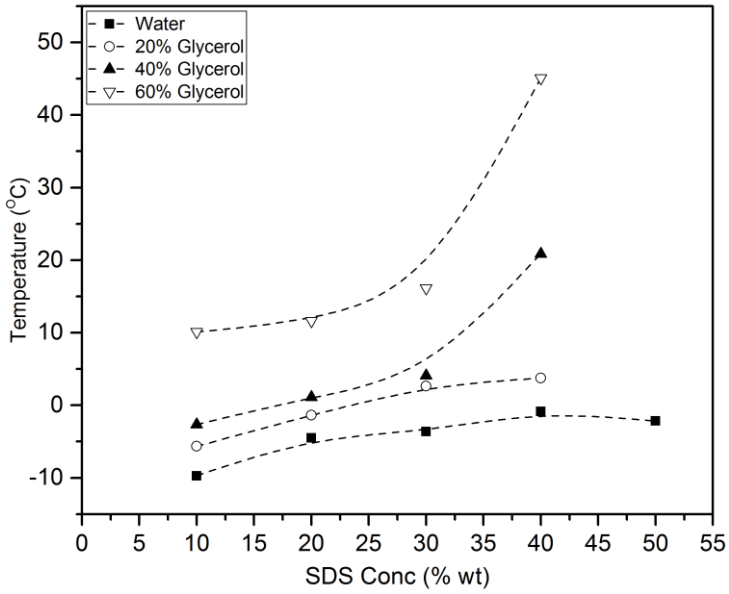


Fig 4.16– Precipitation boundary temperatures (T_{CT}) as a function of SDS concentration (wt%), for SDS in water and various water-glycerol mixtures.

4.4.2 X-ray Scattering Analysis

There were two sets of X-ray scattering analysis carried out, temperature resolved which involved measurements at a range of fixed temperatures and a Linkam analysis, where a continuous cooling scan was applied to determine crystallisation of 20 wt% SDS in various water-glycerol mixtures. For both set of analysis, SAXS data was mainly used for the structural determinations, whereas the WAXS data was used as a confirmatory tool.

4.4.2.1 Temperature Resolved

Fig 4.17 maps out the parameters of the temperature resolved analysis carried out, in relation to the SDS phase diagram. A grid format was used to cover a range of temperatures and concentrations, incorporating the regions of interest on the phase diagram. The measurements using these 'grid parameters' were carried for SDS-water systems as control and then on 20, 40 and 60 wt% glycerol mixtures. For consistency (and due to the instrument set-up), the temperature scan was carried out from low (10 °C) to high temperatures, in 5 °C increments for all systems, with 5 minutes of equilibration time being allowed at each temperature before taking a measurement.

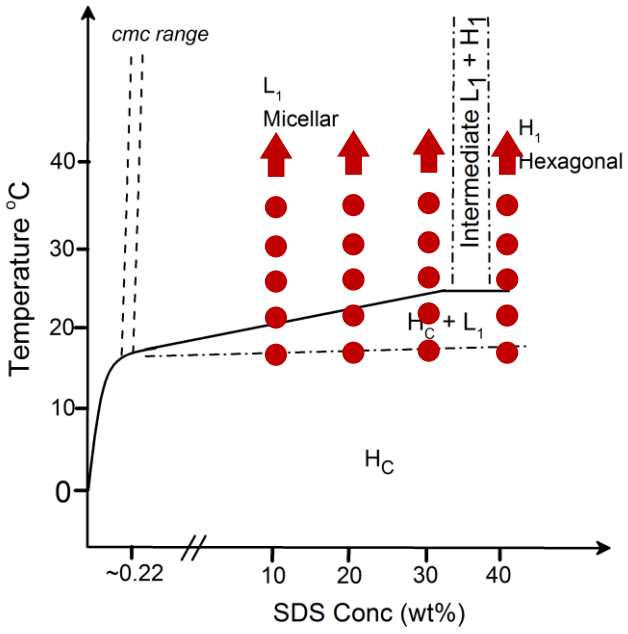


Fig 4.17 – The design of experiment for the temperature resolved X-ray scattering analysis, showing the temperature and concentration grid parameters, in relation to the SDS phase diagram.

4.4.2.1.1 SDS-Water systems

The SDS-water system was used as a control and as a reference since its phases have been established in literature, as detailed in the introduction section. This was particularly useful for identifying the various SDS hydrates in solvent mixtures containing higher levels of glycerol. Fig 4.18 shows the SAXS data for 10 wt% SDS

in water, showing a characteristic broad peak for a micellar phase from 10 to 25 °C. At 10 °C, there are two sets of 'coupled' sharp peaks superimposed on to the broad micellar peak, indicating the presence of a lamellar phase co-existing with a micellar solution. Since it is known that at 10 wt% SDS, below 15 °C, SDS hydrates can co-exist with micelles, these sharp peaks represent that lamellar structure formed by SDS crystals. As the temperature is increased to 15 °C, all the sharp peaks disappear.

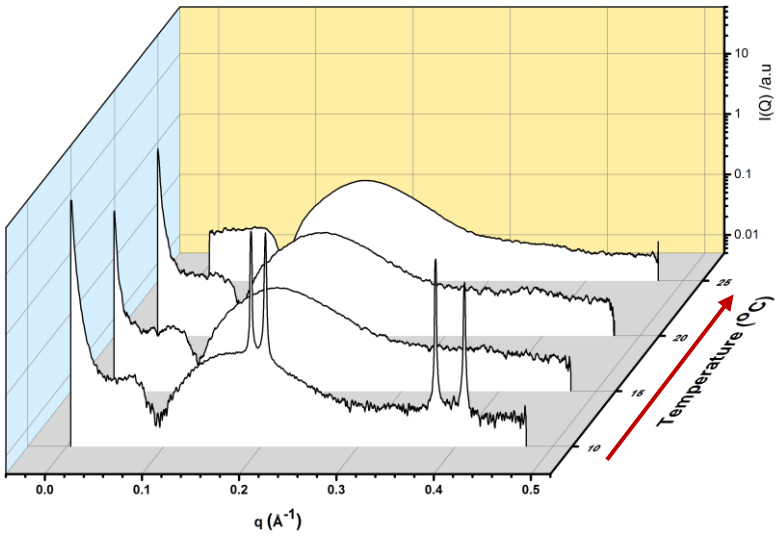


Fig 4.18 – SAXS data for 10 wt% SDS in water at 10, 15, 20 and 25 °C temperatures, obtained in heating direction.

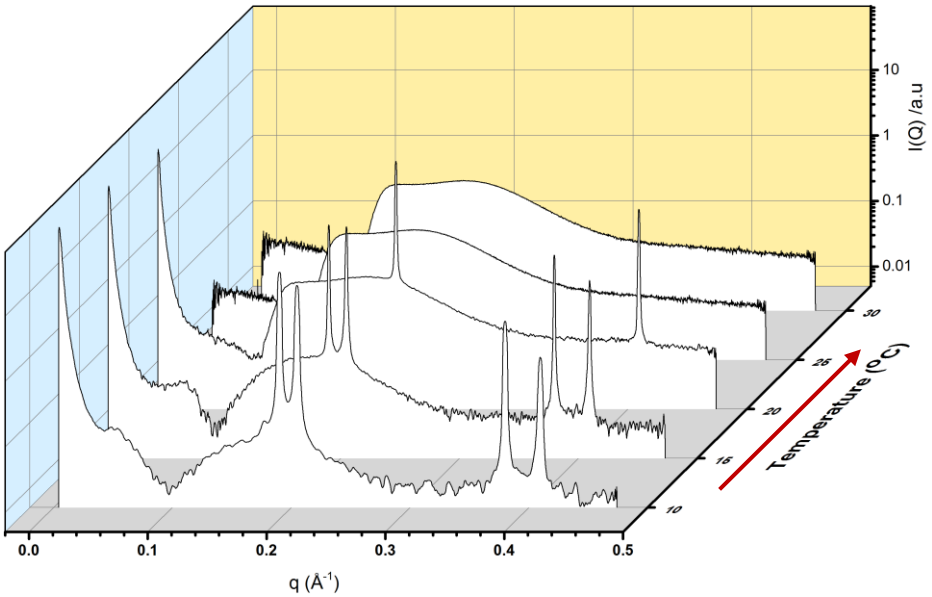


Fig 4.19 – SAXS data for 20 wt% SDS in water at 10, 15, 20, 25 and 30 °C temperatures, obtained in heating direction.

When 20 wt% SDS system was analysed, it showed the similar SAXS profile at low temperatures (Fig 4.19) where both sharp and broad peaks can be observed. The temperatures at which the sharp peaks were seen however were different. At 10 and 15 °C, two set of 'coupled' peaks are produced, with the broad peak being dominant at 15 °C. At 20 °C, one sharp peak from each set disappears, showcasing a broader peak with two separated sharp peaks, which also disappear when the temperature is increased to 25 °C. These SAXS measrements are suggesting that at 10 °C, two different lamellar structures are co-existing and as the temperature is increased to 15 °C, both lamellars remain but a micellar is also formed. At 20 °C, one of the lamellar structure (representing a SDS hydrate) is disassembled and at 25 °C, the other SDS hydrate is also dissolved, with only a micellar phase remaining. These finding correspond to the DSC data shown in the previous section.

To confirm that the sharp peaks observed at lower temperature as representing lamellar structures, and to determine their d-spacing, Braggs diffraction pattern analysis was carried out, as explained in section 4.2.2. Fig 4.20. shows the SAXS data along with the diffraction image for 20 wt% SDS in water at 10 °C, highlighting the two set of 'couple' peaks, a1, b1, and a2, b2.

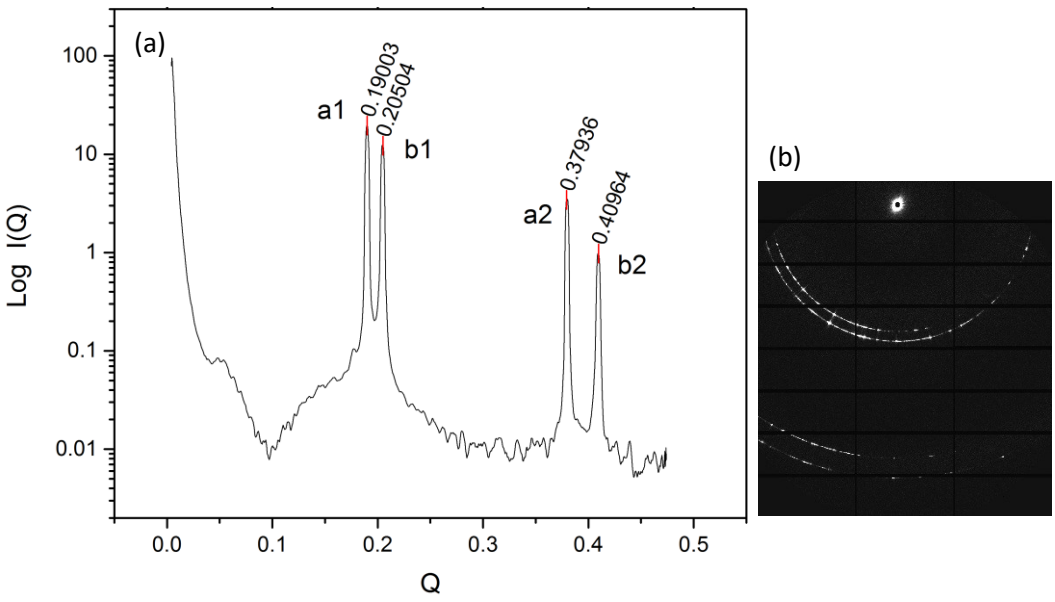


Fig 4.20. – (a) SAXS data and (b) SAXS diffraction image, for 20 wt% SDS in water at 10 °C, showing two lamellar Braggs diffractions, suggesting the presence of two different SDS hydrates.

Peak a1 to a2 and b1 to b2 are both in a ratio of 1 to 2, fitting into the Braggs lamellar diffration patterns (1,2,3,4…). As mentioned in the introduction, these Braggs peak values can be reduced to 1/d throught q/2π. Therefore:

Peak a1 gives; 0.19003 / 2π = 0.030244

Peak a2 give; 0.37936 / 2π = 0.060377

Fig 4.21 gives a graph of these reciprocal d-spacing against the peak ratios, showing the points fitting through a linear plot, which passes through the origin, confirming the indexing as lamellar spacing, with the gradient equal to the reciprocal of d-spacing, hence the d-spacing can be calculated as 1/gradient. For peaks a1-a2 and b1-b2, the d-spacing was determined to be 33.2 and 30.7 Å respectively. Refering to table 4.1 in the introduction, the d-spacing of ~33 corresponds to a SDS.½H_2O and the 30.7 Å d-spacing to SDS.H_2O structure. Therefore, there are two SDS hydrates co-existing for a sampleof 20 wt% SDS equilibrated at 10 °C for 5 minutes.

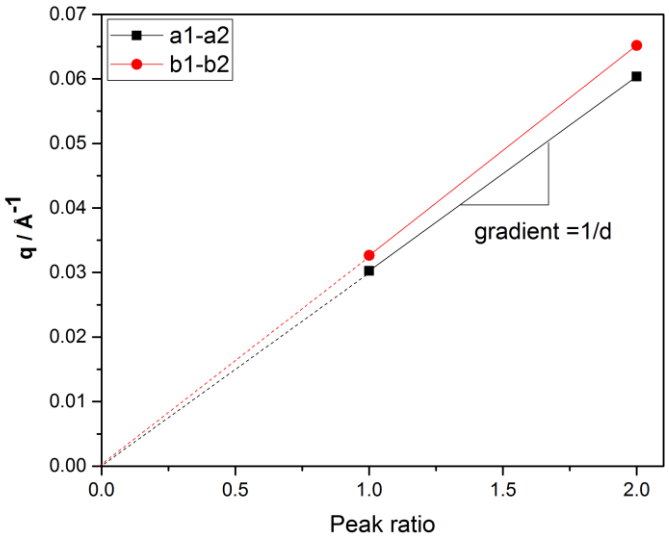


Fig 4.21 – Plot of reciprocal d-spacing against the Bragg's peak ratios.

This analysis was carried out for all SAXS profiles producing sharp Braggs peaks. Fig 4.22 shows the data for 30 wt% SDS in water, giving very similar results to the 20 wt% SDS system analysed above, confirming that at 25 °C, only the micellar phase is present.

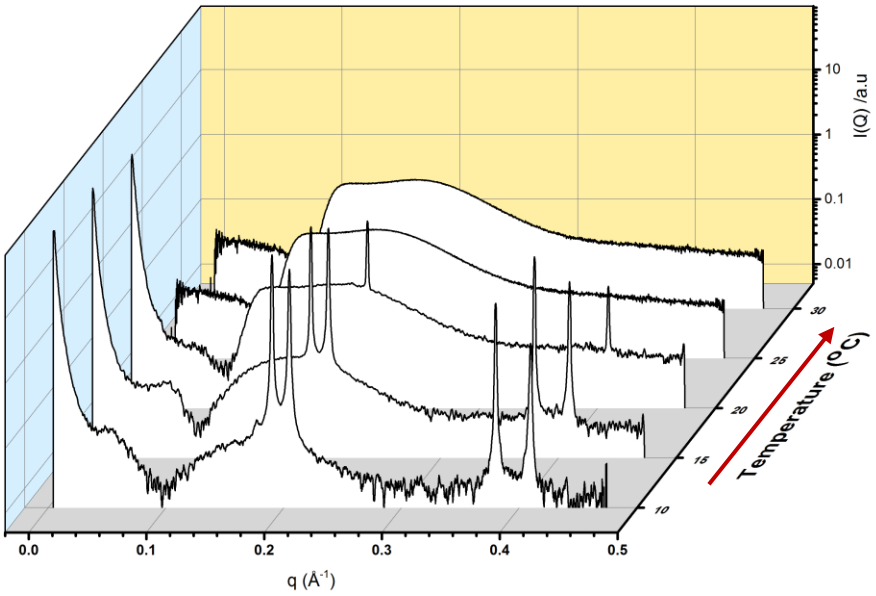


Fig 4.22 – SAXS data for 30 wt% SDS in water at 10, 15, 20, 25 and 30 °C temperatures, obtained in heating direction.

For 40 wt% SDS-water system, a different SAXS profile was observed as expected (Fig 4.23). At 15 and 20 °C, lamellar structures representing SDS.2H_2O and SDS.½H_2O was indicated by the sharp peaks, togther with a possible micellar phase at 20 °C.

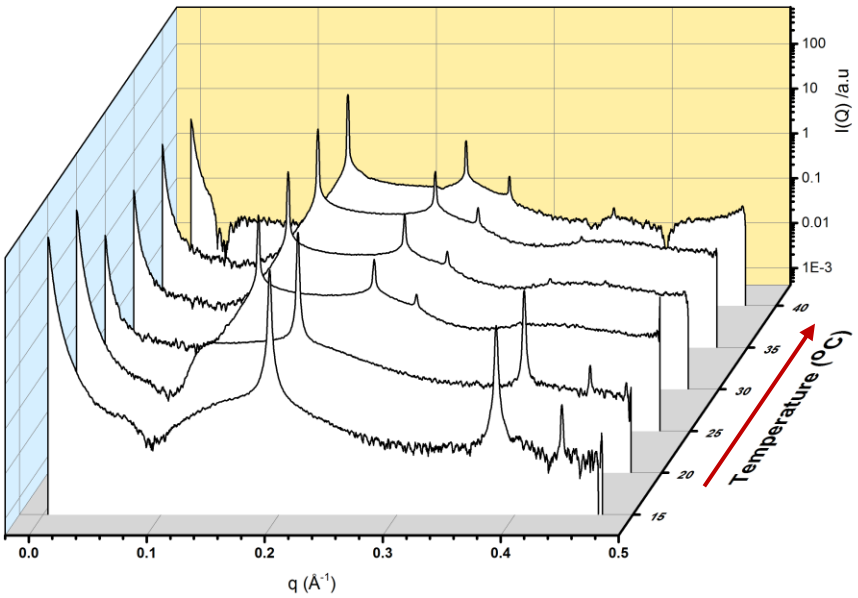


Fig 4.23 – SAXS data for 40 wt% SDS in water from 15 to 40 °C temperatures (with 5 °C increments), obtained in heating direction.

At 25 °C, those sharp peaks disappear and three sharp peaks appear at 0.13395, 0.2324 and 0.2678 positions, which fits into the Braggs hexagonal diffration patterns (1, √3, √4). An image of this SAXS diffraction pattern is shown in Fig.4.24. This conforms to the literature findings, that a hexagonal phase is formed at 40 wt% SDS above 25 °C.

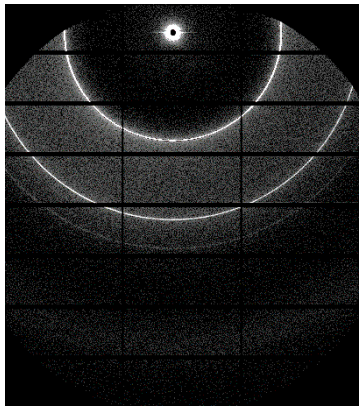


Fig 4.24 – SAXS diffraction image for 40 wt% SDS in water at 25 °C temperatures.

4.4.2.1.2 SDS-Glycerol systems

The same set of analysis was carried out using the three water-glycerol system. Fig 4.25 shows all the SAXS data for 20 wt% glycerol systems, at all four SDS concentrations. These showed similar results to the SDS-water system, where at low temperature, two different SDS hydrates are co-existing, with a micellar phase as the temperature is increased. A similar phase behaviour is seen as the SDS concentration is increased, with a hexagonal phase being formed at 40 wt% SDS.

However, there is a slight difference in the shape of the broad peak representing the micellar phase, suggesting a change in micellar shape and size. Also there is a slight increase in the temperatures at which the lamellar peaks disappear and a single micellar or a hexagonal phase is observed, indicating a small increase in the solubility temperatures, particularly at higher SDS concentrations.

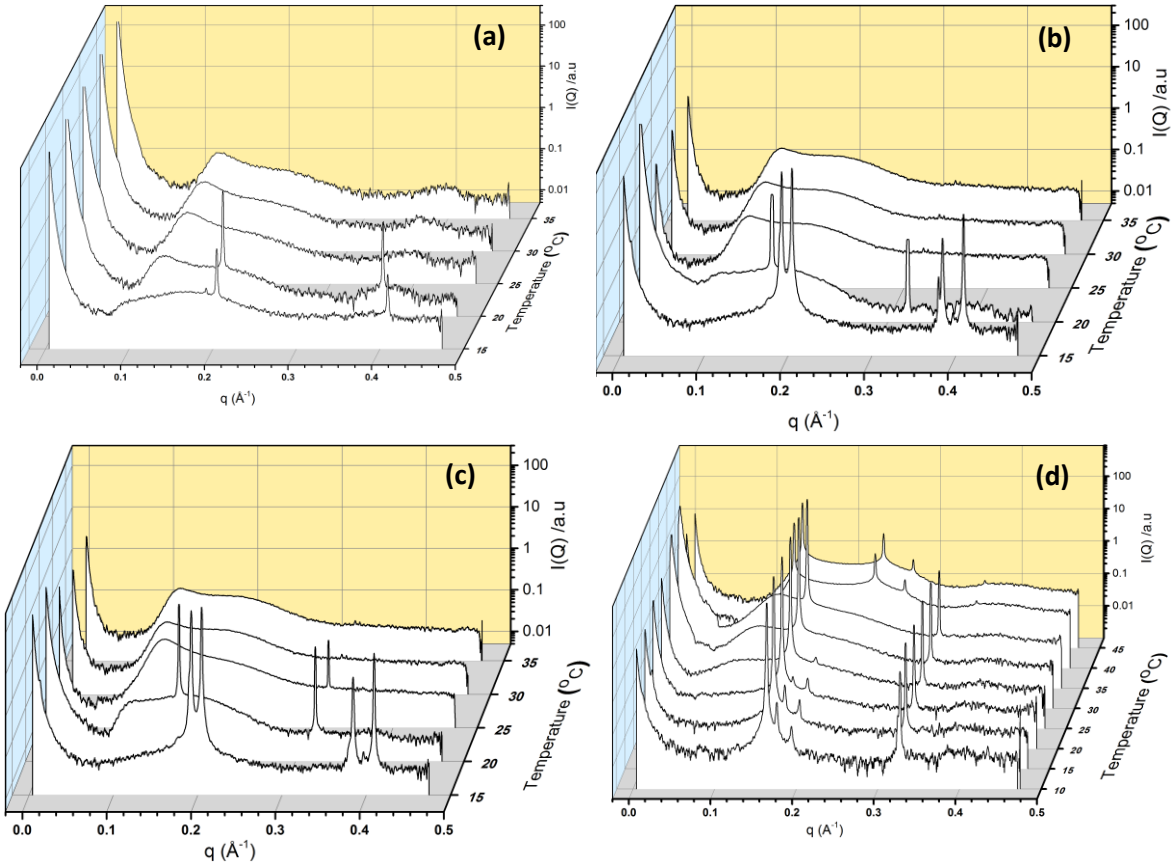


Fig 4.25 – SAXS data for 20 wt% glycerol systems, across increasing temperature (front to back) at: (a) 10, (b) 20, (c) 30 and (d) 40 wt% SDS levels. All data obtained in heating direction.

For 40 wt% glycerol system, a clear change in solubility temperatures can be observed, across all SDS levels, as shown in Fig 4.26. At 10 and 20 wt% SDS levels, Fig 4.26 (a) and (b), only one SDS hydrate (SDS.½H_2O) structure is observed at low temperatures, which completely transforms in to micelles at 25 and 30 °C respectively. At 30 wt% SDS level, the presence of SDS hydrates (SDS.1/8H_2O) can still be seem for up to 45 °C, co-existing with a micellar phase from 25 °C onwards.

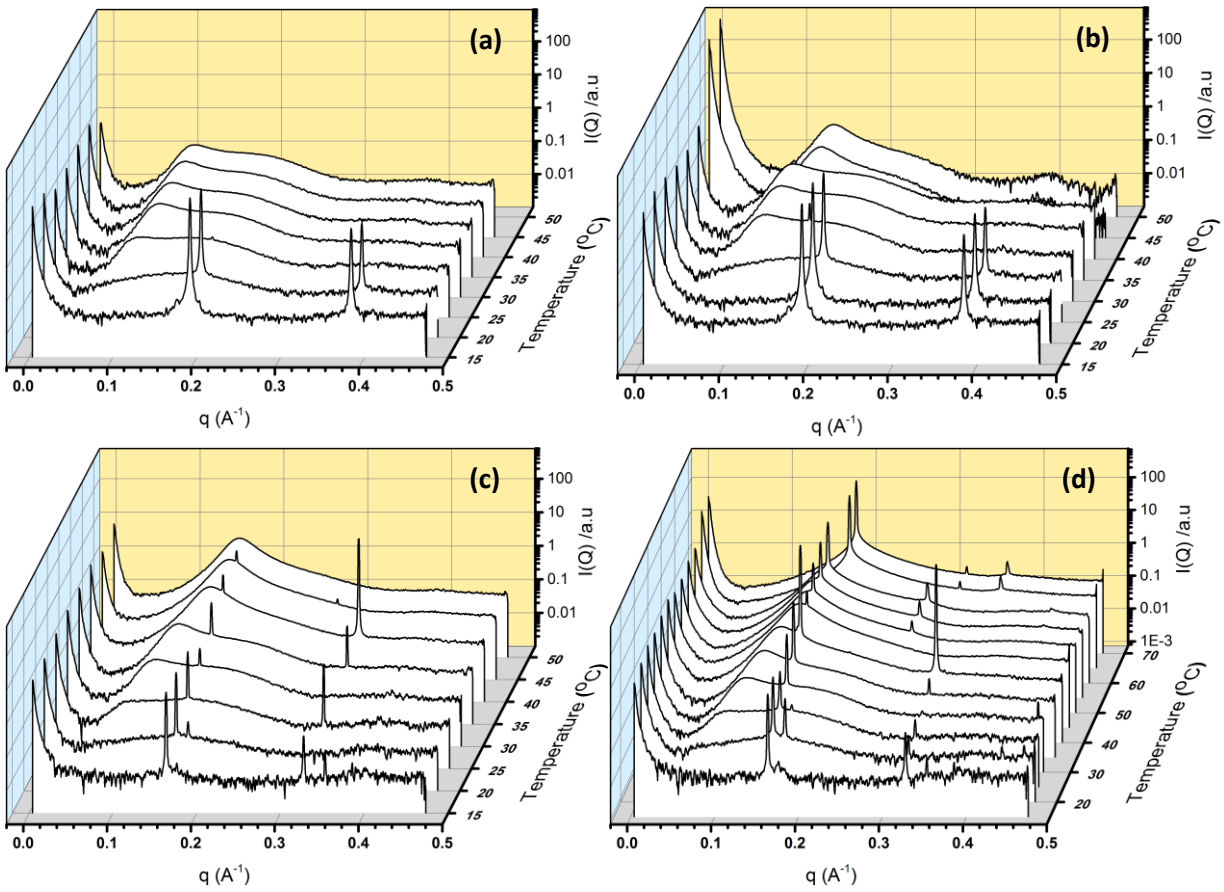


Fig 4.26 – SAXS data for 40 wt% glycerol systems, across increasing temperature (front to back) at: (a) 10, (b) 20, (c) 30 and (d) 40 wt% SDS levels. All data obtained in heating direction.

When SDS concentration is increased to 40 wt%, there are two different SDS hydrates formed, SDS.1/8H_2O and SDS.½H_2O below 25 °C. Between 25 and 30 °C, both these hydrates seem to co-exist with a micellar phase, indicated by the appearance of a broad micelle peak. At 35 and 40 °C, the SDS.½H_2O structure dissolves, with only a two-phase state remaining, consisting of SDS.1/8H_2O and a micellar phase, untill 45 °C, at which the SDS.1/8H_2O structure also starts to transform, and a hexagonal structure begins to form, co-existing with micelles. At high temperatures of 55 °C and above, the system seems to completely transitions into a single hexagonal phase. This correlates to the DSC experiments, where the solubility temperature of 40 wt% SDS in 40 wt% glycerol mixture was determined to be 56.8 °C.

On increasing the glycerol level further to 60 wt%, all transition temperatures seem to increase further, as evident from Fig 4.27.

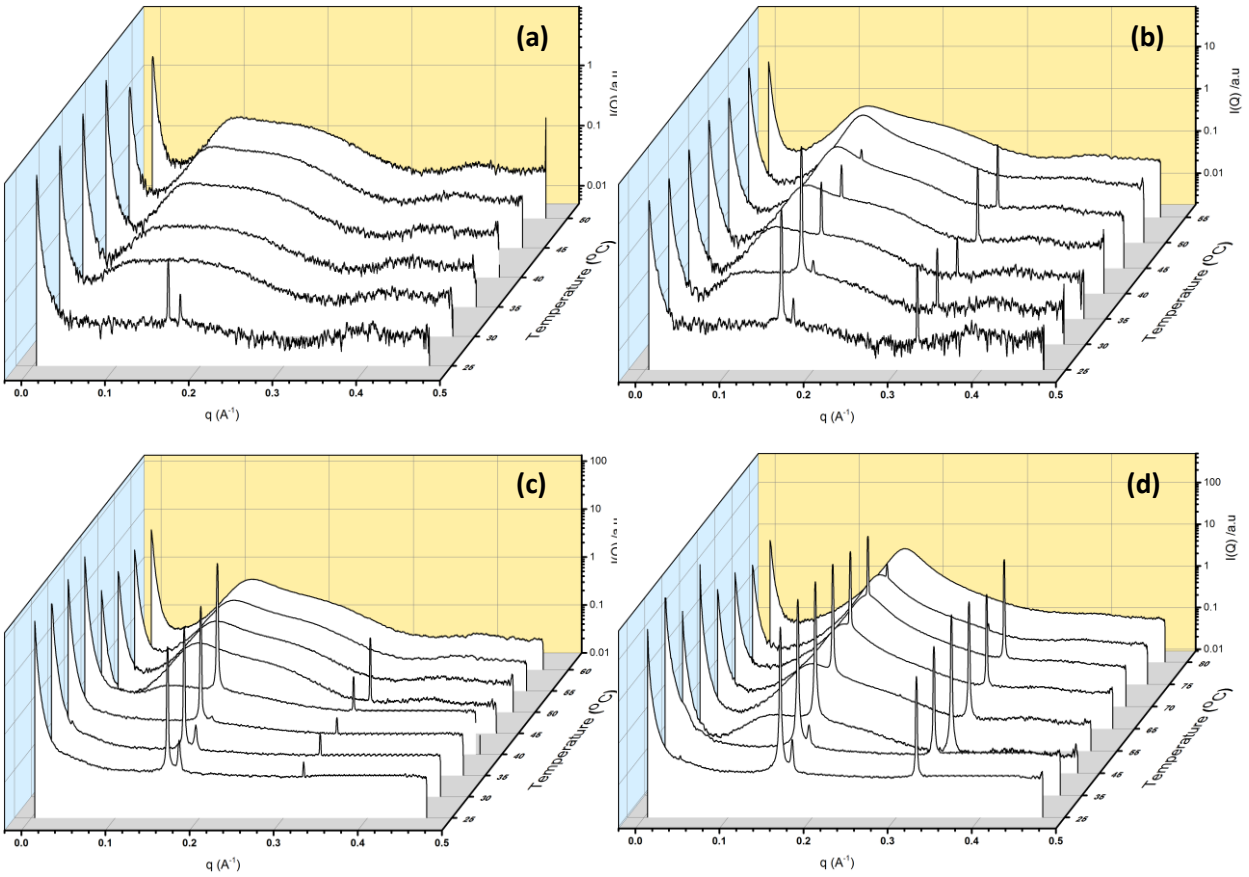


Fig 4.27 – SAXS data for 60 wt% glycerol systems, across increasing temperature (front to back) at: (a) 10, (b) 20, (c) 30 and (d) 40 wt% SDS levels. All data obtained in heating direction.

The types of SDS hydrates formed in this system are similar to the 40 wt% glycerol system, where SDS.1/8H_2O and SDS.½H_2O are identified across all four SDS concentrations, up untill 30 °C. For the 10 wt% SDS system, the solubility temperature is determined to be above 30 °C. At 20 and 30 wt% SDS, both these hydrates (SDS.1/8H_2O and SDS.½H_2O) co-exist with a micellar phase and after 35 °C, only the

SDS.1/8H_2O and a micellar phase remain. The SDS.1/8H_2O then completely transforms in to micelles at 50 °C in a 20 wt% SDS system and at 60 °C for a 30 wt% SDS system. For a 40 wt% SDS system, no hexagonal phase is observed. From 40 to 70 °C, this system also contained the SDS.1/8H_2O co-existing with the micellar phase. Above 70 °C, only large micelles remain as obsevered by the broad peak from the SAXS data. This shows that at high organic solvent content, the phase behaviour of SDS shifts towards higher surfactant concentrations and transition temperatures, allowing for negative transformations to occur at higher temperatures.

Table 4.3 summaries all the SDS states and the phases within them, identified through the SAXS data, for all water-glycerol mixtures and all four SDS concentrations. It includeds the type of SDS hydrate formed at each temperature, for each composition, via the Braggs peak diffraction pattern analysis. This data will be used in the later section to help create SDS phase diagrams in water-glycerol mixtures

Table 4.3 –SDS phases determined from SAXS data analysis, for 10, 20, 30 and 40 wt% SDS concentrations, for different water-glycerol mixtures, across increasing temperatures.

SDS (wt%)	Temp (°C)	Water	20% Glyceorl	40% Glyceorl	60% Glyceorl
10	15	L1	$SDS.H_2O$ + L1	$SDS.1/2H_2O$	$SDS.1/8H_2O$ + $SDS.1/2H_2O$
	20	L1	$SDS.1/2H_2O$ + L1	$SDS.1/2H_2O$	$SDS.1/8H_2O$ + $SDS.1/2H_2O$
	25	L1	L1	$SDS.1/2H_2O$ + L1	$SDS.1/8H_2O$ + $SDS.1/2H_2O$
	30	L1	L1	L1	L1
20	15	$SDS.H_2O$ + $SDS.1/2H_2O$	$SDS.H_2O$ + $SDS.1/2H_2O$	$SDS.1/2H_2O$	$SDS.1/8H_2O$ + $SDS.1/2H_2O$
	20	$SDS.H_2O$ + L1	$SDS.1/8H_2O$ + L1	$SDS.1/2H_2O$	$SDS.1/8H_2O$ + $SDS.1/2H_2O$
	25	L1	L1	$SDS.1/2H_2O$ + L1	$SDS.1/8H_2O$ + $SDS.1/2H_2O$
	30	L1	L1	$SDS.1/8H_2O$ + L1	$SDS.1/8H_2O$ + $SDS.1/2H_2O$ + L1
	35	L1	L1	L1	$SDS.1/8H_2O$ + L1
	40	L1	L1	L1	$SDS.1/8H_2O$ + L1
	45	L1	L1	L1	$SDS.1/8H_2O$ + L1
	50	L1	L1	L1	L1
30	15	$SDS.H_2O$ + $SDS.1/2H_2O$	$SDS.H_2O$ + $SDS.1/2H_2O$	$SDS.1/8H_2O$ + $SDS.1/2H_2O$	$SDS.1/8H_2O$ + $SDS.1/2H_2O$
	20	$SDS.H_2O$ + L1	$SDS.1/8H_2O$ + L1	$SDS.1/8H_2O$ + $SDS.1/2H_2O$	$SDS.1/8H_2O$ + $SDS.1/2H_2O$
	25	L1	$SDS.1/8H_2O$ + L1	$SDS.1/8H_2O$ + L1	$SDS.1/8H_2O$ + $SDS.1/2H_2O$
	30	L1	L1	$SDS.1/8H_2O$ + L1	$SDS.1/8H_2O$ + $SDS.1/2H_2O$
	35	L1	L1	$SDS.1/8H_2O$ + L1	$SDS.1/8H_2O$ + $SDS.1/2H_2O$
	40	L1	L1	$SDS.1/8H_2O$ + L1	$SDS.1/8H_2O$ + L1
	45	L1	L1	L1	$SDS.1/8H_2O$ + L1
	50	L1	L1	L1	L1
40	15	$SDS.H_2O$ + $SDS.2H_2O$	$SDS.1/8H_2O$ + $SDS.1/2H_2O$	$SDS.1/8H_2O$ + $SDS.1/2H_2O$	$SDS.1/8H_2O$ + $SDS.1/2H_2O$
	20	$SDS.H_2O$ + $SDS.2H_2O$	$SDS.1/8H_2O$ + $SDS.1/2H_2O$	$SDS.1/8H_2O$ + $SDS.1/2H_2O$	$SDS.1/8H_2O$ + $SDS.1/2H_2O$
	25	H1	$SDS.1/8H_2O$ + $SDS.1/2H_2O$ +L1	$SDS.1/8H_2O$ + $SDS.1/2H_2O$ + L1	$SDS.1/8H_2O$ + $SDS.1/2H_2O$
	30	H1	$SDS.1/8H_2O$ +L1	$SDS.1/8H_2O$ + $SDS.1/2H_2O$ + L1	$SDS.1/8H_2O$ + $SDS.1/2H_2O$
	35	H1	$SDS.1/8H_2O$ +L1	$SDS.1/8H_2O$ +L1	$SDS.1/8H_2O$ + $SDS.1/2H_2O$
	40	H1	H1	$SDS.1/8H_2O$ +L1	$SDS.1/8H_2O$ +L1
	45	H1	H1	H1 + L1	$SDS.1/8H_2O$ +L1
	50	H1	H1	H1 + L1	$SDS.1/8H_2O$ +L1
	55	H1	H1	H1 + L1	$SDS.1/8H_2O$ +L1
	60	H1	H1	H1 + L1	$SDS.1/8H_2O$ +L1
	65	H1	H1	H1	$SDS.1/8H_2O$ +L1
	70	H1	H1	H1	$SDS.1/8H_2O$ +L1
	75	H1	H1	H1	L1
	80	H1	H1	H1	L1

4.4.2.2 Linkam Analysis

The Linkam stage was found to be a useful tool for determining the structural changes of the SDS system over a consistent rate of temperature decrease, down to very low temperatures (minus 10 °C). However, a limitation with using the Linkam set up was that only one sample at a time can be measured as only one capillary is designed to fit on to the stage.

A concentration of 20 wt% SDS was used for all Linkam based measurements as it falls in the middle of the concentration range tested in previous analysis. Fig 4.28 shows the SAX data for 20 wt% SDS in water. It confirms that at 30 °C the system is in the micellar phase. On cooling this system at 5 °C/min, minor sharp peaks are observed as the temperature reaches 0 °C. As the system continues to cool, the number and intensity of the sharp peaks increases, suggesting an increase in the types of SDS hydrates formed along with their sizes.

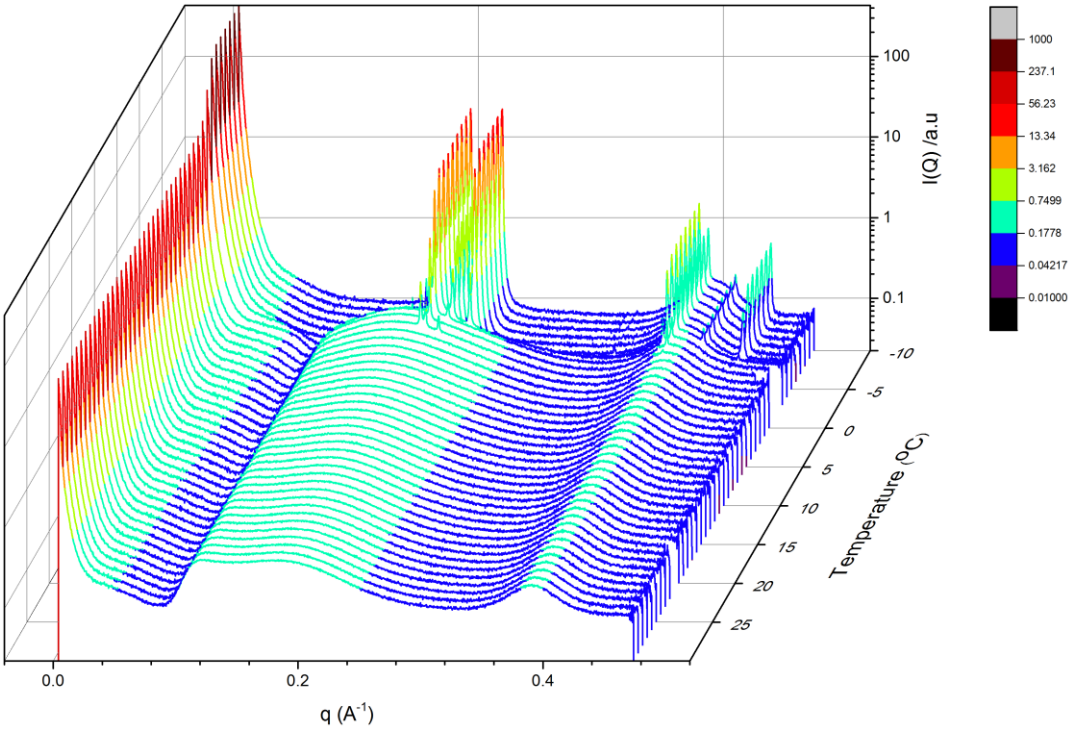


Fig 4.28 – SAXS data for 20 wt% SDS in water, using the Linkam stage to cool the system from 30 to -10°C, at a rate of 5 °C/min.

The temperatures at which the sharp peaks appear, i.e. nucleation of hydrates occurs, were looked at closely for both SAXS and WAXS data and is shown in Fig 4.29. For the WAXS data, the sharp peaks do not appear untill the system reached -2 °C, becoming more intense at -3 °C, which is lower than the SAXS data nucleation temperature (0 °C). This suggest that the long-range orientational order within the system starts changing by 0 °C, initiating the forming of lamellar structures, whereas the alkyl chain required slightly lower tempertures to transition from a more fluid/ untilted gel phase (L_α / L_β) to a tilted gel (L_β'), with eventually forming lamellar crystalline (L_C) at -3 °C, where the hydrocarbon chains are frozen in an all trans configuration.

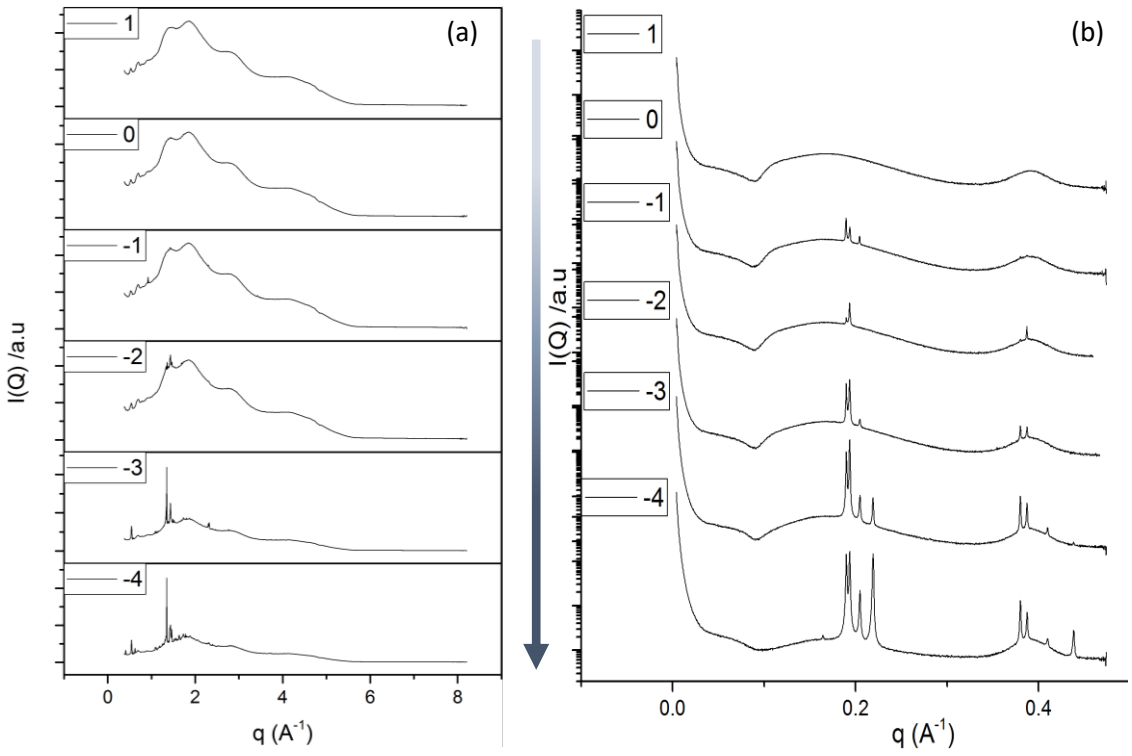


Fig 4.29 – (a) WAXS and (b) SAXS data for 20 wt% SDS in water, using the Linkam stage for cooling at a rate of 5 °C/min., focusing on nucleation onset of SDS hydrate from 1 to -4°C.

The Braggs diffraction peaks from the SAXS data were used to determine the d-spacings and identifying the SDS hyrates. It was found that at 0 to -2 °C, the

SDS.½H_2O and SDS.H_2O are co-existing with a micellar phase and as the temperature lowers further to -3 °C, a SDS.2H_2O (dihydrate) is also formed, producing a four-state phase containng three different hydrates and a micellar phase. By -4 °C, the micellar phase is no longer observed, as shown in Fig 4.28b. Interestingly, on cooling the sytem further, a SDS.1/8H_2O is also identified (with d-spacing of ~38.8 Å). The intensity of the peak representing the SDS.2H_2O (0.219 and 0.438) was relatively lower compared to other hydrate peaks. Therefore at temperatuer from -4 to -10 °C, all four SDS hydrates were observed, under these particular conditions, in different ratios.

This same analysis was carrid out on all other water-glycerol solvent mixtures, for the Linkam experiments.using the same 20 wt% SDS concentration, as shown in Fig 4.30., 4.31 and 4.32.

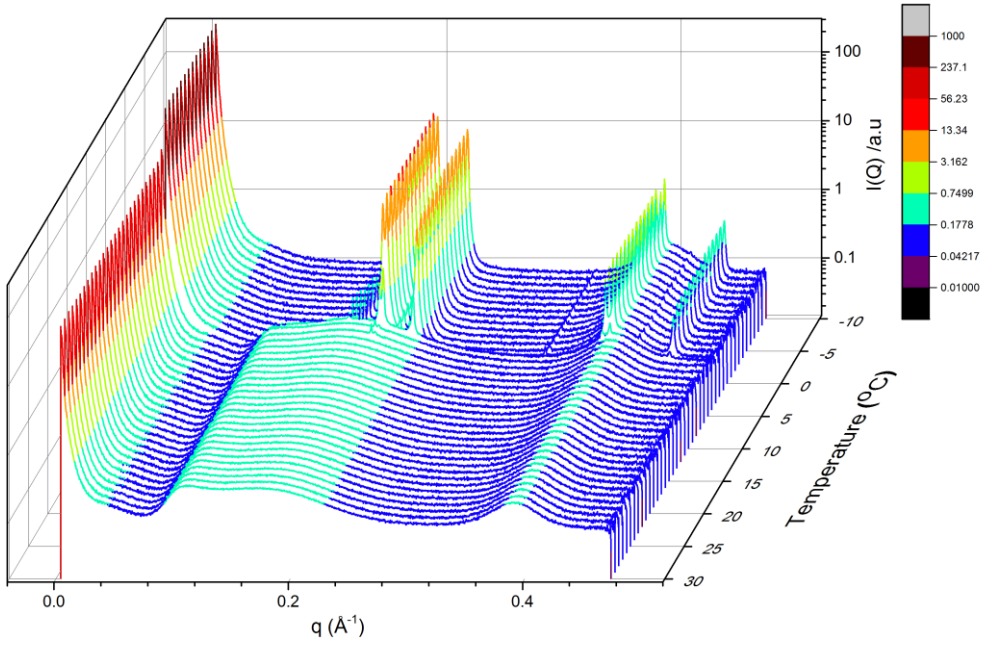


Fig 4.30. – SAXS data for 20 wt% SDS in 20 wt% glycerol, using the Linkam stage to cool the system from 30 to -10°C, at a rate of 5 °C/min.

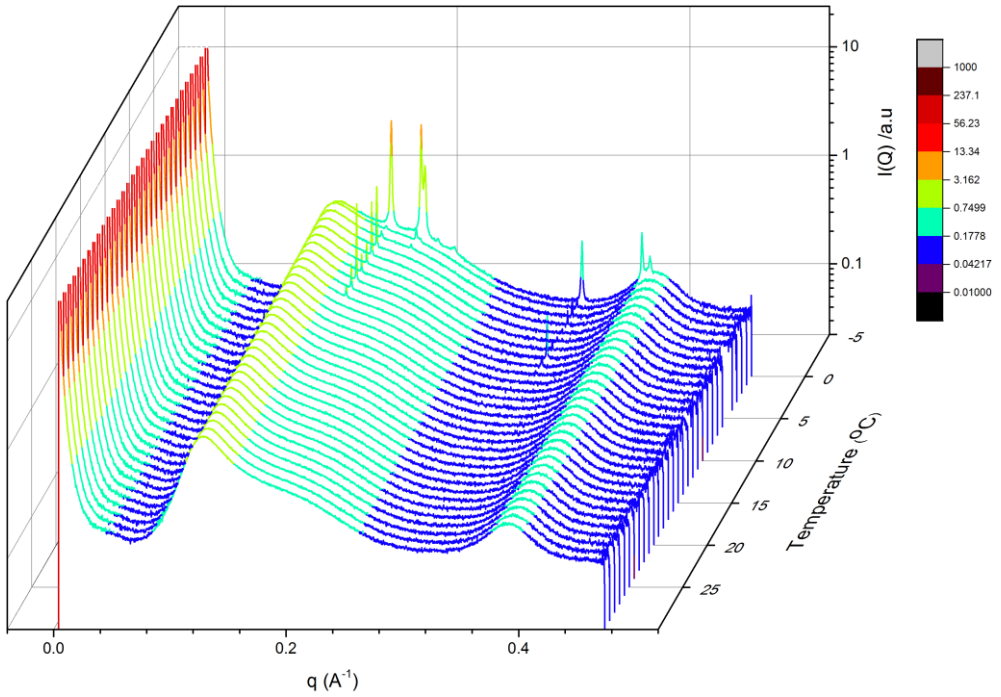


Fig 4.31 – SAXS data for 20 wt% SDS in 40 wt% glycerol, using the Linkam stage to cool the system from 30 to -5°C, at a rate of 5 °C/min.

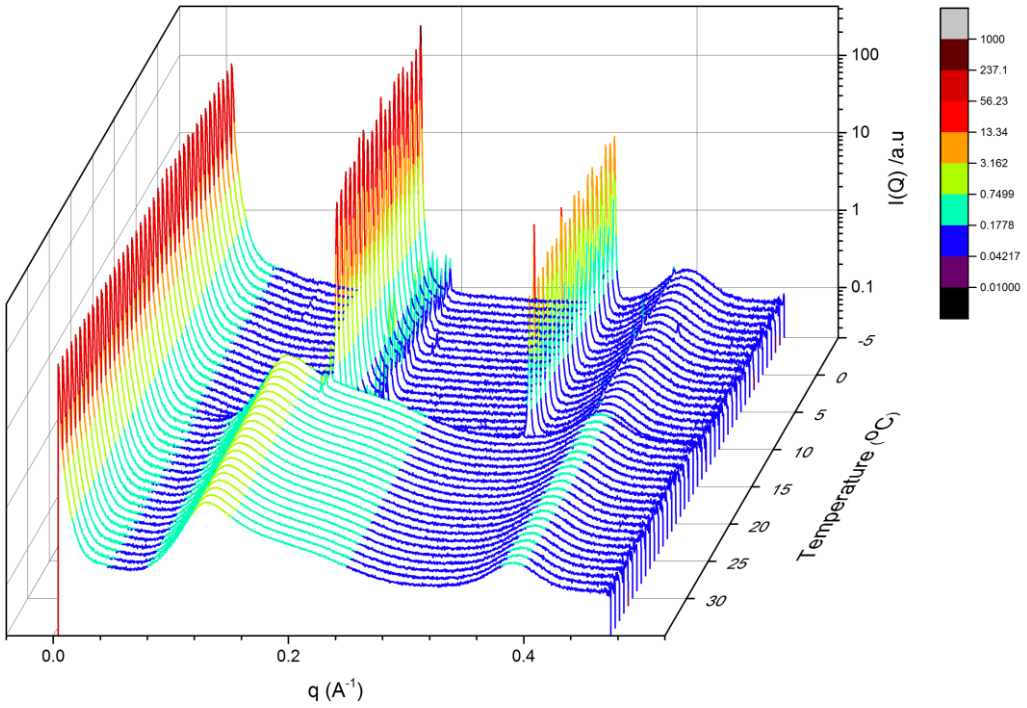


Fig 4.32 – SAXS data for 20 wt% SDS in 60 wt% glycerol, using the Linkam stage to cool the system from 30 to -5°C, at a rate of 5 °C/min.

These measurments again confirmed that as the level of glyerol is increased, the precipitation temperature of SDS hydrates also increases, with an nucleation onset temperatures of 4, 9 and 17 °C for 20, 40 and 60 wt% glycerol levels respectively.

For the 20 wt% glycerol system, unlike the pure water system, there was no SDS.H_2O observed below the solubility temperatures, with only SDS.1/8H_2O, SDS.½H_2O and SDS.2H_2O detected at 3 C and below. For the 40 wt% system, the first hydrate to form and co-exsit with the micellar phase is the SDS.1/8H_2O and then later SDS.½H_2O and SDS.H_2O at 2 and 0 °C respectively. Similarly with 60 wt% glycerol system, the SDS.1/8H_2O is the first to form, followed by SDS.½H_2O at 14 °C. These two hydrates, SDS.1/8H_2O and SDS.½H_2O, remain over a range of temperatures, with the peaks representing the SDS.1/8H_2O being more intense. Only when the temperature reaches -9 °C, a SDS.H_2O is also formed.

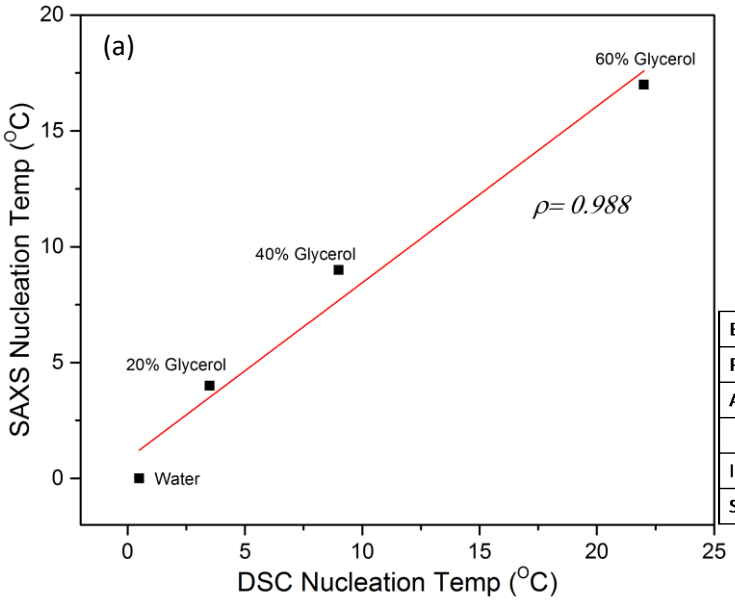
Overall it was also observed that as the glycerol level increases, the number of different SDS hydrates co-existing decreases. SDS-water system produced all four hydrates, whereas in 60 wt% glycerol systems only two were formed for the bulk of the range.

All SDS phases identified, across all the temperatures, with the each type of SDS hydrates determined are collected in Table 4.4, showing the trends as the level of glycerol content in the solvent mixture is changed.

Table 4.4 – 20 wt% SDS phases determined from Linkam cooling SAXS data analysis, displaying data from 20 to -10 °C, in different water-glycerol mixtures.

Temp (°C)	Water	20% Glycerol	40% Glycerol	60% Glycerol
20	L1	L1	L1	L1
19	L1	L1	L1	L1
18	L1	L1	L1	L1
17	L1	L1	L1	SDS.1/8H_2O + L1
16	L1	L1	L1	SDS.1/8H_2O + L1
15	L1	L1	L1	SDS.1/8H_2O + L1
14	L1	L1	L1	SDS.1/8H_2O + SDS.1/2H_2O
13	L1	L1	L1	SDS.1/8H_2O + SDS.1/2H_2O
12	L1	L1	L1	SDS.1/8H_2O + SDS.1/2H_2O
11	L1	L1	L1	SDS.1/8H_2O + SDS.1/2H_2O
10	L1	L1	L1	SDS.1/8H_2O + SDS.1/2H_2O
9	L1	L1	SDS.1/8H_2O + L1	SDS.1/8H_2O + SDS.1/2H_2O
8	L1	L1	SDS.1/8H_2O + L1	SDS.1/8H_2O + SDS.1/2H_2O
7	L1	L1	SDS.1/8H_2O + L1	SDS.1/8H_2O + SDS.1/2H_2O
6	L1	L1	SDS.1/8H_2O + L1	SDS.1/8H_2O + SDS.1/2H_2O
5	L1	L1	SDS.1/8H_2O + L1	SDS.1/8H_2O + SDS.1/2H_2O
4	L1	SDS.1/2H_2O + SDS.2H_2O + L1	SDS.1/8H_2O + L1	SDS.1/8H_2O + SDS.1/2H_2O
3	L1	SDS.1/8H_2O + SDS.1/2H_2O + SDS.2H_2O + L1	SDS.1/8H_2O + L1	SDS.1/8H_2O + SDS.1/2H_2O
2	L1	SDS.1/8H_2O + SDS.1/2H_2O + SDS.2H_2O	SDS.1/8H_2O + SDS.1.2H_2O + L1	SDS.1/8H_2O + SDS.1/2H_2O
1	L1	SDS.1/8H_2O + SDS.1/2H_2O + SDS.2H_2O	SDS.1/8H_2O + SDS.1.2H_2O + L1	SDS.1/8H_2O + SDS.1/2H_2O
0	SDS.1/2H_2O + SDS.H_2O + L1	SDS.1/8H_2O + SDS.1/2H_2O + SDS.2H_2O	SDS.1/8H_2O + SDS.1/2H_2O + SDS.H_2O	SDS.1/8H_2O + SDS.1/2H_2O
-1	SDS.1/2H_2O + SDS.H_2O + L1	SDS.1/8H_2O + SDS.1/2H_2O + SDS.2H_2O	SDS.1/8H_2O + SDS.1/2H_2O + SDS.H_2O	SDS.1/8H_2O + SDS.1/2H_2O
-2	SDS.1/2H_2O + SDS.H_2O + L1	SDS.1/8H_2O + SDS.1/2H_2O + SDS.2H_2O	SDS.1/8H_2O + SDS.1/2H_2O + SDS.H_2O	SDS.1/8H_2O + SDS.1/2H_2O
-3	SDS.1/2H_2O + SDS.H_2O + SDS.2H_2O + L1	SDS.1/8H_2O + SDS.1/2H_2O + SDS.2H_2O	SDS.1/8H_2O + SDS.1/2H_2O + SDS.H_2O	SDS.1/8H_2O + SDS.1/2H_2O
-4	SDS.1/2H_2O + SDS.H_2O + SDS.2H_2O + L1	SDS.1/8H_2O + SDS.1/2H_2O + SDS.2H_2O	SDS.1/8H_2O + SDS.1/2H_2O + SDS.H_2O	SDS.1/8H_2O + SDS.1/2H_2O
-5	SDS.1/8H_2O + SDS.1/2H_2O + SDS.H_2O + SDS.2H_2O	SDS.1/8H_2O + SDS.1/2H_2O + SDS.2H_2O	SDS.1/8H_2O + SDS.1/2H_2O + SDS.H_2O	SDS.1/8H_2O + SDS.1/2H_2O
-6	SDS.1/8H_2O + SDS.1/2H_2O + SDS.H_2O + SDS.2H_2O	SDS.1/8H_2O + SDS.1/2H_2O + SDS.2H_2O	SDS.1/8H_2O + SDS.1/2H_2O + SDS.H_2O	SDS.1/8H_2O + SDS.1/2H_2O
-7	SDS.1/8H_2O + SDS.1/2H_2O + SDS.H_2O + SDS.2H_2O	SDS.1/8H_2O + SDS.1/2H_2O + SDS.2H_2O	SDS.1/8H_2O + SDS.1/2H_2O + SDS.H_2O	SDS.1/8H_2O + SDS.1/2H_2O
-8	SDS.1/8H_2O + SDS.1/2H_2O + SDS.H_2O + SDS.2H_2O	SDS.1/8H_2O + SDS.1/2H_2O + SDS.2H_2O	SDS.1/8H_2O + SDS.1/2H_2O + SDS.H_2O	SDS.1/8H_2O + SDS.1/2H_2O
-9	SDS.1/8H_2O + SDS.1/2H_2O + SDS.H_2O + SDS.2H_2O	SDS.1/8H_2O + SDS.1/2H_2O + SDS.2H_2O	SDS.1/8H_2O + SDS.1/2H_2O + SDS.H_2O	SDS.1/8H_2O + SDS.1/2H_2O + SDS.H_2O
-10	SDS.1/8H_2O + SDS.1/2H_2O + SDS.H_2O + SDS.2H_2O	SDS.1/8H_2O + SDS.1/2H_2O + SDS.2H_2O	SDS.1/8H_2O + SDS.1/2H_2O + SDS.H_2O	SDS.1/8H_2O + SDS.1/2H_2O + SDS.H_2O

Since the DSC experiments were also conducted using a cooling rate of 5 °C/min, the nucleation onset from both DSC and SAXS analysis were compared, for all 4 water-glycerol -20 wt% SDS systems, as shown in Fig 4.33. The T_N from both the techniquies were in good agreement with each other, producing a linear fit with a correlation coeffiecnt (Pearons' r) of 0.988.



(b)

Equation	y = a + b*x	
Pearson's r	0.98815	
Adj. R-Square	0.96466	
	Value	Standard Error
Intercept	0.8371	1.004
Slope	0.7612	0.083

Fig 4.33 – (a) Correlation between nucleation temperatures determined from DSC and SAXS analysis and (b) the parameters of the correlation linear fit.

4.4.3 SDS Phase Diagrams

From the DSC analysis carried out in section 4.4.1 and the temperature-resolved SAXS analysis in section 4.4.2, an insight in to the precipitation boundaries, types of hydrates forming and the temperature at which these transitions occur has been gained. All these findings were collected to established SDS phase diagram. The SDS-water phase diagram in Fig 4.34 is created base on the data from the control experience carried out in this chapter, with the outcome corroborated with literature findings as previous discussed. The Krafft point determinations in the previous chapter (3), were also referred to when mapping of the solubility boundaries for the water-glycerol system. Fig 4.35, 4.3 and 4.37 displayed the SDS phase diagrams created for 20, 40 and 60 wt% glycerol systems respectively.

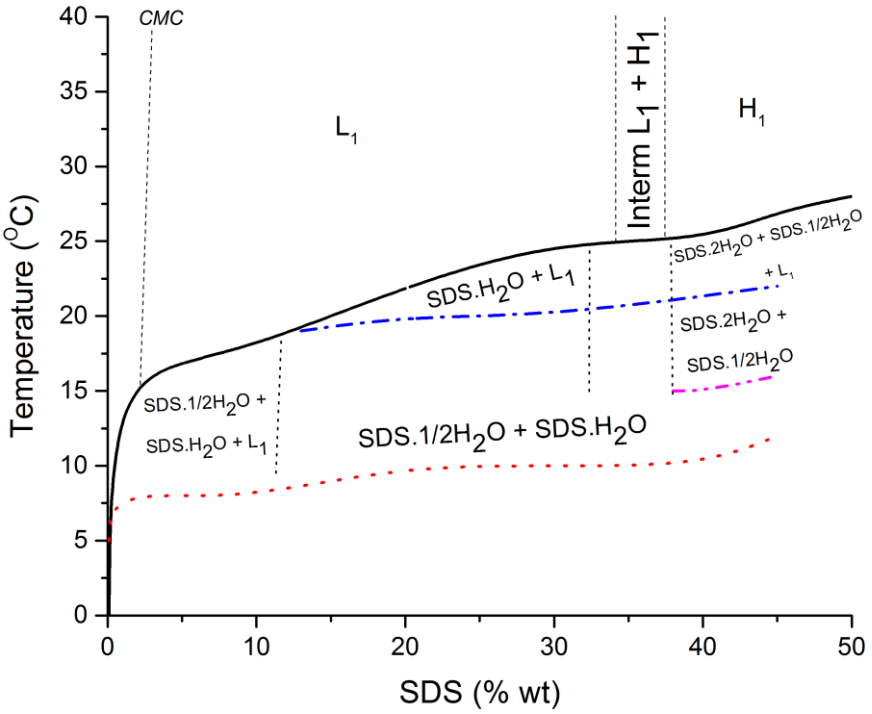


Fig 4.34 – SDS phase diagram in water.

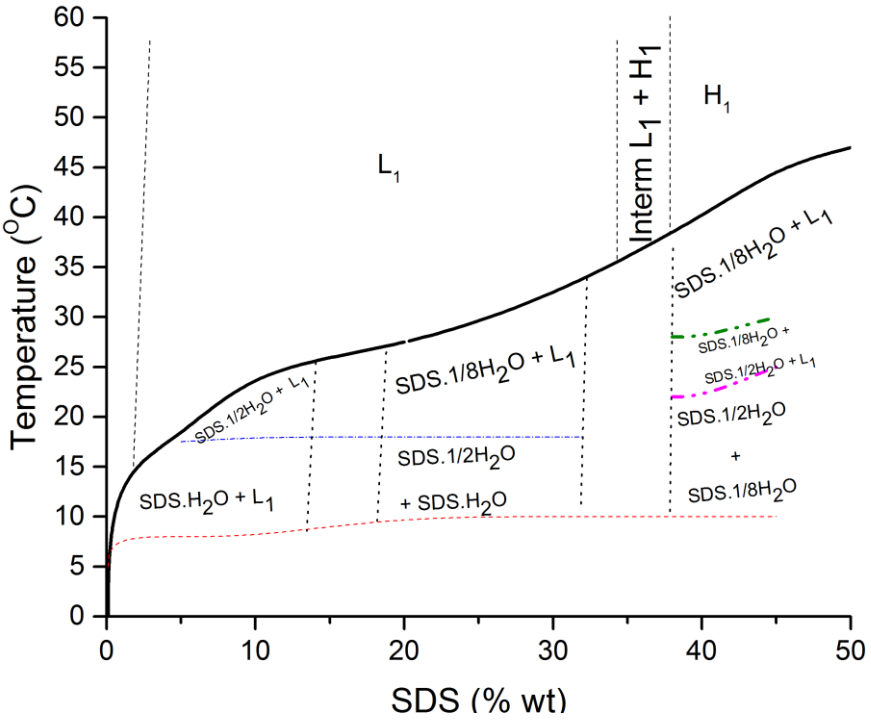


Fig 4.35 – SDS phase diagram in 20 wt% glycerol.

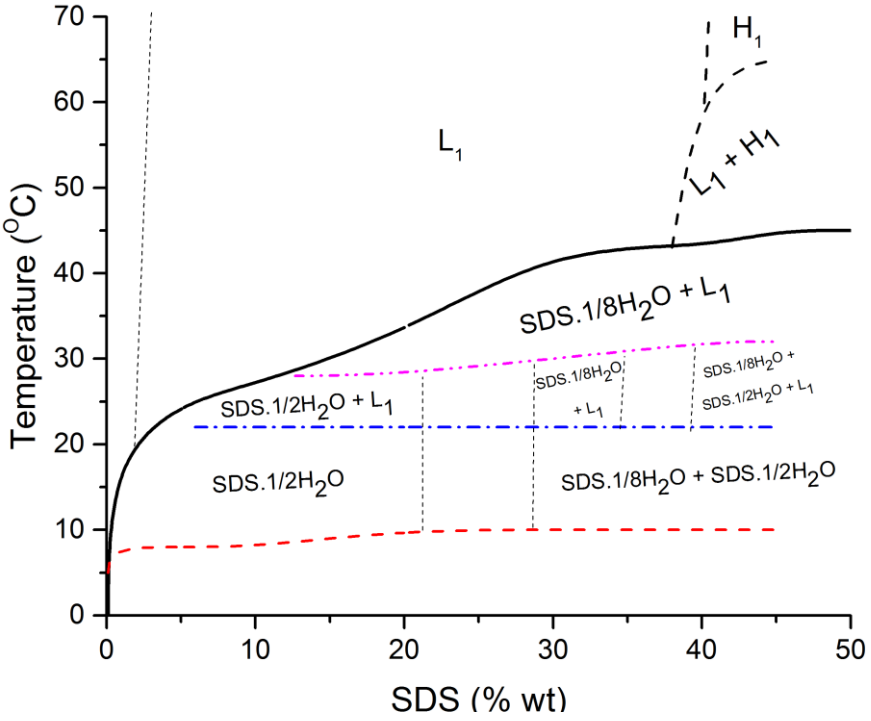


Fig 4.36 – SDS phase diagram in 40 wt% glycerol.

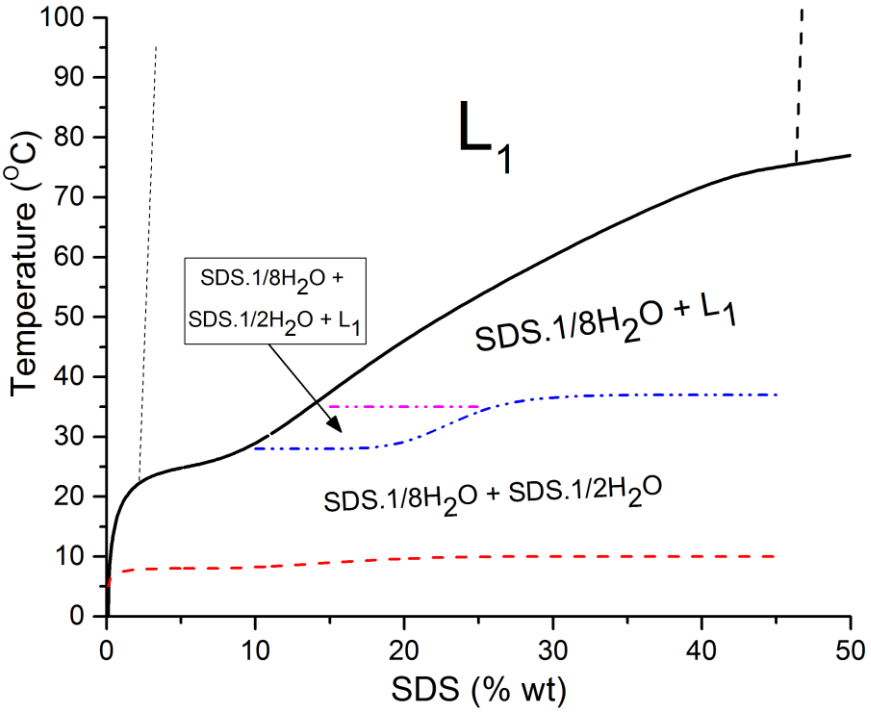


Fig 4.37 – SDS phase diagram in 60 wt% glycerol.

From these phase diagrams, the shifting precipitation boundary, to higher tempertures with increase glycerol content can be clearly observed. Also the shift in the lyotropic phase transitions can also be notice as glycerol levels are increased, with the H_1 phase formed at 40 wt% SDS above 35 °C in a 20 wt% glycerol system, but a SDS.1/8H_2O co-existing with a L_1 phase and a SDS.1/8H_2O + SDS.½H_2O phase is formed at the same conditions for a 40 and 60 wt% glycerol sytems respectively. The transition between the L_1 and H_1 does not occur until the SDS concentration is ~40 wt% and temperature is above 65 °C, in a 40 wt% glycerol sytem.

The identity of the various SDS hydrates formed below the precipitation boundary and the transition temperatures of the inter-conversions between these hydrates are also determined and mapped out on the phase diagrams, showing more regions with multiple hydrates co-existing with the L_1 phase. For 20 and 40 wt% glycerol systems, it can be noticed that near the precipitation boundaries (between 20 to 30 °C), across a range of SDS concentration, there are various hydrates inter-converting, while c-existing with the L_1 phase. Since these DSC and X-ray scattering experiments parameters were designed in a grid format, there are regions in the phase diagrams which have been left blank (vertical dotted line), as there is no experimental or literature data to determine that exact state. However, in cases where the same phases have been identified for two consecutive SDS concentrations, it is assumed that the phases in between these concentrations are also the same.

4.5 CHAPTER CONCLUSIONS

The DSC and SAXS analysis of SDS in various water-glycerol systems provided complimentary insight in to the surfactant's phase behaviour. A detailed analysis of the DSC endothermic peaks enabled multiple transition temperatures to be determined, which later allowed for the various SDS hydrates inter-conversion boundaries and transformation across the solubility boundary to be established in corroboration with X-ray scattering measurements. The examination of the exothermic peaks provided an

insight into the changing nucleation temperatures of the hydrated crystals. The optimised heating and cooling rate used, (5 °C/min) was able to produce peaks with detectable phase transitions, however there were some merged peaks which can be separated, for which a more sensitive DSC instrument is required.

One of the interesting learning from the DSC analysis was that, although increasing the level of glycerol content in the solvent mixture increased the solubility boundary, across all SDS levels, there was an endothermic peak consistently produced ~10 °C, for all water-glycerol compositions and all four SDS concentrations, representing the melting of the hydrocarbon chain within the SDS hydrate and its inter-conversion. This suggest that there is always a transformation occurring within the ordering of the SDS hydrocarbon chains at 10 °C leading to an inter-conversion of the hydrated crystal.

The two different SAXS experiments, temperature-resolved and Linkam based measurements, were successfully employed for providing detailed structural information on the numerous phases present and distinguishing between the multiple SDS hydrates formed. In SDS-water systems, all four SDS hydrates types were identified below -4 °C in the Linkam analysis. Near the precipitation boundary for the same system, the SDS.H_2O and SDS.½H_2O are the two dominant crystals formed, whereas in the glyceorl systems, particularly for 40 and 60 wt% glycerols, the SDS.1/8H_2O followed by the SDS.½H_2O are always identified. This suggest that inceasing glycerol levels is dehydrating the crystals, favouring the formation of SDS.1/8H_2O.

Bridging the learnings and outcomes from both the techniques used in this chapter and also from Krafft point investigation in chapter 3, enabled SDS phase diagrams to be mapped out, allowing for the effect of organic solvent on phase behaviour to be tracked and understood more efficiently. Although the phase diagrams focuses on a particular range of SDS concentrations, this range covers the surfactant systems of interest, e.g. detergents. This study establishes a platform for understanding and controlling the negative transformations, leading to improved stability and hence shelf-life of surfactant-based products.

Chapter 5

Eye irritation determination for complex surfactant formulations.

5.1 OVERVIEW

The ocular irritancy, particularly of domestic products (e.g. detergents) is of a great interest especially for FMCG companies as they have to ensure objective safety of their products to the consumers. To data, there is no single *in-vitro* eye irritation test method that can fully replace the historic animal test (OECD TG405). Also, the existing *in-vitro* methods are time consuming and expensive and therefore not suitable for high-throughput mechanistic studies. Liquid detergent formulations contain complex concentrated surfactant systems and hence it has been challenging to test and predict their ocular irritancy. In this chapter, the complexities of liquid detergent formulations are discussed, along with current ICE test method used to measure and predict eye irritancy. Also, some lipid membrane models/methods were developed and their efficiency determined. The results from this chapter encouraged me to further extend the application (chapter 6) of one of the assays to gather a better understanding of the mode of action of surfactants in lipid membrane permeation with regards to eye irritation.

5.2 INTRODUCTION

The significance of accurately and efficiently determining ocular irritancy is due to the physiological importance, the structure and sensitivity of the eye. As mentioned in chapter 1 (section 1.3), the chemicals and ingredients used in household products are of a hazardous nature and therefore government agencies across the globe (e.g. FDA, ECHA) have made it a legislative requirement (i.e. REACH regulations) to evaluate the risk associated with these products and communicate them down to the end user under the CLP regulation.[182, 183] This includes the *'serious eye damage/eye irritation'* health hazard group, where the potential damage the substance can cause to the eye is

classified as set out by the Globally Harmonised System of Classification and Labelling of Chemicals (GHS rev.7).[62, 184] These classification categories have been given and explained in chapter 1 (table 1.3). The responsibility of identifying and classifying these hazards are on the research & development and manufacturing companies.[5] Accurately determining these hazards has been challenging due to the increasing restrictions/limitations of the traditional in-vivo methods used and the complexity of the human eye.[67, 70] Development and validation of methods to identify such sensitive hazards is extensive and time-consuming.[66, 185, 186] When determining the eye irritation hazard of liquid detergent samples, the added challenge is the complexity of the detergent formulation as it contains a combination of different types of surfactants, polymers and solvents. In order to develop an efficient method for testing eye irritancy, a good understanding of the formulation chemistry, along with the eye structure and its lipid membrane composition is required.

5.2.1 Liquid Detergent Formulations

Household cleaning product such as detergents are considered concentrated surfactant formulations as they contain 30-40 wt% surfactants.[13, 28] Commercial liquid detergent formulations, which were developed by P&G for eye irritation examination were used in this research project. Development of these liquid detergent samples is considered successful overall when they attain the desirable detergency performance (efficacy), stability (shelf-life) and safety (health/ environment hazards).[5, 187] To achieve acceptable efficacy and stability attributes, liquid detergent formulation are typically composed of: Surfactants, builders, enzymes, polymers, rheology/viscosity modifier, optical brighteners, dye-transfer inhibitors, pH controllers/neutralisers, preservatives, perfumes and solvents/dispersing agents.[5, 13, 188] The function of each of these ingredients is summarised in chapter 1, table 1.1.

Since surfactants are a major component in liquid detergents and due to their physiological effect, they are the most significant contributor towards eye irritation.[189] Typically a mixture of 3 to 4 different surfactants are used in liquid laundry detergents as each surfactant is more effective against a particular type of stain/dirt. Also the different surfactant mixtures help stabilize the formulation.[5] The

details of the type of surfactants used and their role in liquid laundry detergents is discussed in the next chapter (chapter 6), where the main focus with regards to eye irritation is the effect of surfactant only systems.

The series of commercial liquid detergent formulations tested in this chapter contained the same list of ingredients/chemicals, mainly consisting of; surfactants LAS, AES and AE with a total combined level of 38-41 wt%, fatty acids, polymers, monoethanolamine (MEA) and propylene glycol-water-glycerol solvent mixture. The main difference between the various formulations were the levels/ ratio of the three surfactants. Details of these formulation series is given in the next section (5.3 Experimental).

5.2.2 Ocular Irritancy

Following an accidental or deliberate submission of a substance to the anterior of the eye, changes occur in the corneal cells causing irritancy, which leads to a response from the eye to protect and/or prevent further damage.[70] The severity of the irritancy and hence the kind response depends on the extent of the penetration caused by the substance.[66] An understanding of the eye structure and particularly the cornea is needed to help recognise the different levels of irritancy categories/classification involved.

5.2.2.1 Eye Structure

The cornea is the outer most part of the open eye and hence the first point of contact of any foreign substance.[190] The human cornea thickness at the centre is ~0.52 mm, less than one-hundredth of the thickness of the entire eyeball (Fig. 5.1).[191] Besides forming a barrier to protect the lens, the cornea also refracts the incoming light on to the lens[192]. The outer part of the cornea is protected by a layer of tear film which is secreted from multiple tear ducts contained within the conjunctiva (inner linings of the eyelids[191, 193]. The tear film maintains the optical property of the cornea and it's fluid composed of layers of lipids and aqueous phases. The fluid is replaced after every blink and this acts as a first defensive response to excrete any unwanted substances.[193]

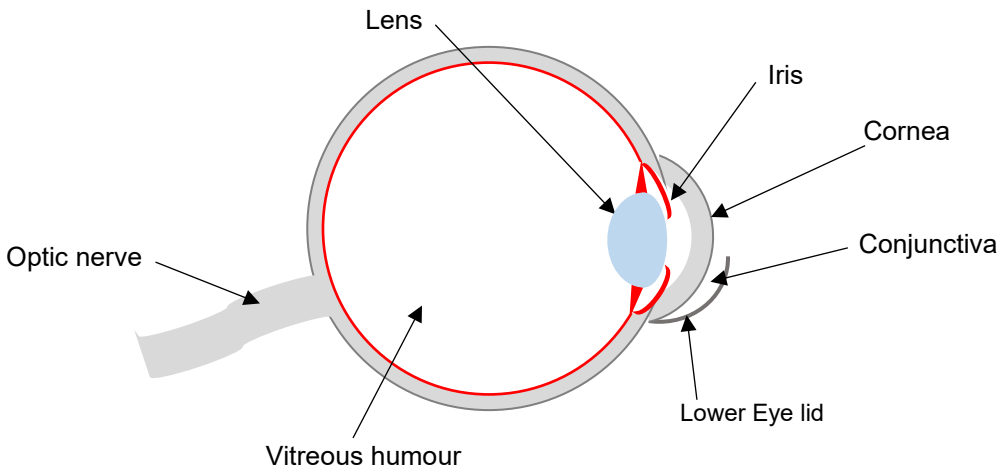


Fig 5.1 – Diagram of the eyeball, illustrating the main parts including the cornea. Redrawn from given references.[190, 191]

The cornea itself is a multi-layered structure consisting of (from outside in); epithelium, Bowman's membrane, stroma, Descement's membrane and endothelium.[191] The corneal epithelium, the first part which is exposed to external substance, has a stratified, squamous structure ~ 50 µm thick, consisting of three distinct parts. The outermost part contains 2-3 layers of flattened cells, followed by 2-3 layers of goblet cells and the inner part consisting of columnar basal cells. The squamous epithelial cells are sequentially shredded off into tear films and replaced by the migrating goblet and basal cells[191, 194]. Basal cells are involved in the modulation and maintenance of the corneal epithelial by controlling cell adhesion and migration amongst other cellular functions.[195] An illustration of the corneal epithelium structure, showing the various layers, is given in Fig. 5.2.

Below the basal cells is the Bowman's membrane followed by the stroma. If a foreign substance has penetrated through to the bowman' membrane and the stroma, it can use serious damage and potentially permanent damage to the eye. With regards to this thesis, I am only interested in the penetration of concentrated surfactant system through the corneal epithelium and not beyond the basal cell (for reasons explained later on in this chapter).

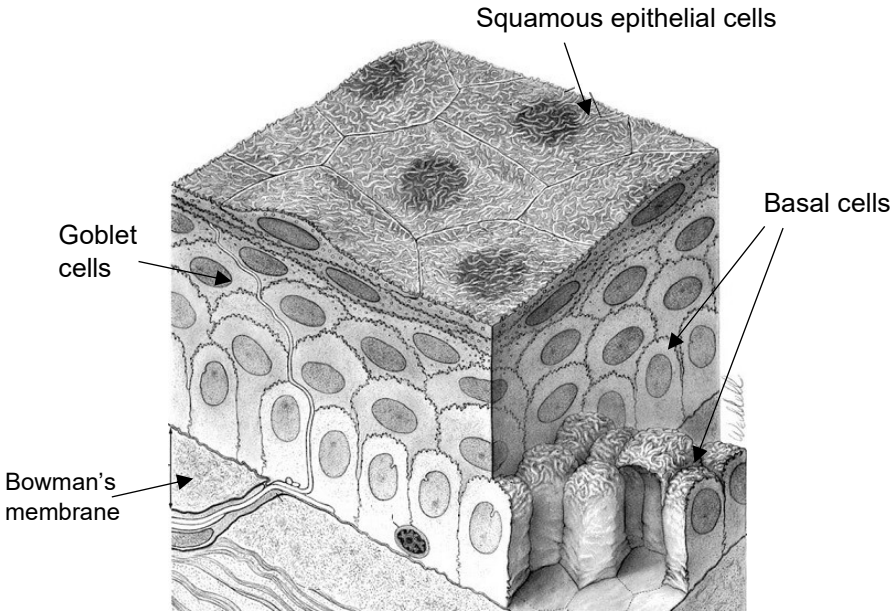


Fig 5.2 – Illustration of the corneal epithelium structure, adapted from given reference.[191]

5.2.3 Current methods

The purpose of an eye irritation test is to effectively and accurately classify the hazard posed from a substance to the eye. With the new global standard, UN GHS rev.7 (2017) in place, eye irritation classifications have become particular distinctive and therefore their test methods have to be discriminative as well as being representative of the human eye. As explained in the introduction chapter (section 1.3.2), over the last few decades there has been major efforts to validate alternative *ex-vivo*/ *in-vitro* methods to replace the traditional and controversial Draize eye irritant test. However, to date, there has been no single method found which is capable of replacing the *in-vivo* Draize eye test.[63] This is due to a few reasons, including; difficulty in comparison between the *in-vivo* and *in-vitro* tests (due to the responsive nature of *in-vivo* testing), the interaction/reaction of certain substances can be different from *in-vivo* to *in-vitro* and the subjective scoring evaluation.[67, 70, 185] One of the alternative methods, the ICE test, which is accepted for category 1 and no category classifications of the eye irritancy, is explained below as the results from an ICE test was used in this project.

5.2.3.1 *Ex-vivo* – Isolated Chicken Eye test

As per the OECD guidelines for testing chemicals (an intergovernmental organisation), the Isolated Chicken Eye (ICE) test method (Test No.438) is currently one of the two adopted alternative tests for '*identifying i) chemicals inducing serious eye damage and ii) chemicals not requiring classification for eye irritation or serious eye damage'*, and hence can be used to classify substances under UN GHS Category 1 or No Category.[74] (For details regarding these UN GHS eye irritation categories please refer to table 1.2). The ICE method stems from Burton 1981,[196] when he used isolated rabbit eyes and then later developed by Koëter & Prinsen in 1985 [197] amongst others, eventually becoming what is now an approved *in-vitro* method using enucleated chicken eyes. The ICE test uses eyes donated from slaughterhouses, from chicken solely used for human consumption. Therefore, there is always a large quantity for chicken eyes available for experimental purposes.

In brief, the test involves; the enucleated eye to be mounted on to a clamp and examined to check whether it is fit/suitable for testing. If approved, the test sample (0.03 mL of liquid) is applied to the entire surface of the cornea. The cornea is evaluated before and at 30, 75, 120, 180 and 240 minutes after treatment. The evaluation includes the examination of three parameters, which are: Corneal Swelling (CS), Corneal Opacity (CO) and Fluorescein Retention (FR).[198]

Corneal swelling is measured using an optical pachymeter slit-lamp microscope and expressed as a percentage using the Equation 5.1 given below and hence is an objective evaluation.[74]

Equation 5.1:

$$\%\ Corneal\ swelling = 100 \times \left(\frac{\text{corneal thickness at time t} - \text{corneal thickness at time} = 0}{corneal\ thickness\ at\ time\ = 0}\right)$$

The resulting percent corneal swelling values are classified into ICE categories from I to IV. Corneal opacity and fluorescein retention are evaluated using an observational scoring system (based on standardised guidelines) similar to the Draize test as shown in Table 5.1, and assigned to ICE categories.

Table 5.1 – Scoring system and corresponding ICE categories for (a) Corneal Opacity and (b) Fluorescein Retention.

(a) Corneal Opacity Observation	**Score**	**ICE Categories***
No opacity	0	I (0-0.5)
Very faint opacity	0.5	
Scattered or diffuse areas; details of the iris are clearly visible	1	II (0.6-1.5)
Easily discernible translucent area; details of the iris are slightly obscured	2	III (1.6-2.5)
Severe corneal opacity; no specific details of the iris are visible; size of the pupil is barely discernible	3	IV (2.6-4.0)
Complete corneal opacity; iris invisible	4	

* based on maximum mean score observed at any time point

(b) Fluorescein Retention Observation	**Score**	**ICE Categories***
No fluorescein retention	0	I (0-0.5)
Very minor single cell staining	0.5	
Single cell staining scattered throughout the treated area of the cornea	1	II (0.6-1.5)
Focal or confluent dense single cell staining	2	III (1.6-2.5)
Confluent large areas of the cornea retaining fluorescein	3	IV (2.6-3.0)

* based on maximum mean score observed at 30 minutes post-treatment

The corneal swelling mean percentages and mean scores from opacity and fluorescein retention are assigned to particular ICE classes ranked from I to IV. The resulting ICE classes for these three parameters are formed into various combinations of categories to obtain a UN GHS Classification. These ICE classes for all the 3 parameters and the various combinations assigned to GHS classifications are shown in Table 5.2.

Table 5.2 – Overall ICE test categorisation.[74, 198]

UN GHS Classification	General Classification	Combination of ICE categories
No Category	No Category Non-irritant	3 × I 2 × I, 1 × II
Not classified- No Predictions can be made	Category 2B Slightly Irritating / Mild Irritant	2 × II, 1 × I 3 × II 2 × II, 1 × III 1 × I, 1 × II, 1 × III
	Category 2A Moderately Irritating / Irritant	2 × III, 1 × I 2 × III, 1 × II 3 × III 1 × IV, 2 × I 1 × IV, 2 × II 1 x IV, 2 × III 1 × IV, 1 × III, 1 × II
Category 1 Serious eye damage	Category 1 Severely Irritating	2 × IV, 1 × I 2 × IV, 1 × II 3 × IV

The ICE test achieved approval status after extensive validation studies against the Draize test data and over-coming some of issues previously mentioned, i.e. not using live animals, objective scoring with corneal swelling, eyes easily attainable etc. Enucleated eye test methods has also been applied to rabbit,[196] porcine[199] and bovine eyes[200], but none of as these were found to be a significantly better representation of the human eye (compared to the chicken eye). There is an approved *in-vitro* method using isolated bovine eyes, the Bovine Corneal Opacity and Permeability (BCOP) assay, which operates on a similar principle.[75] However, the corneal proportion, structure and thickness of the chicken and human eye are found to be quite similar and hence deemed the best available and most cost-effective representation.[189] Still the ICE test (or any other method) is not approved by itself to classify UN GHS Category 2A/2B irritants as represented in Table 5.2. Much like the Draize test, this method also presents certain drawback. The ICE test data also contains a consistently high variability across all three parameters, particularly for corneal opacity and fluorescein retention due to eye to eye variability and subjective scoring of the latter two

parameters.[198] There is no conjunctival damage/interaction and no reversibility/ recovering assessment in the ICE test, like there is for the Draize test.[68] However it is well understood that the recovery response assessment is extremely unlikely to be achievable for any *ex-vivo* testing.[201]

In this chapter, the main focus is the ICE test method as one of the accepted and partial replacements of the Draize eye test, due to sufficient ICE test data for a series of detergent sample being available and was obtained externally through P&G, to use for comparison and correlation analysis with the methods I developed. The method developmental work carried out in this chapter is to determine the potential of lipid membrane models as eye irritation test for high surfactant systems, and whether they can become a complimentary method to the ICE test to provide classification of UN GHS category 2.

5.2.4 Lipid membrane models

The concept behind the two model membrane techniques trialled in this chapter is discussed in a bit more detail here.

5.2.4.1 Droplets Interface Bilayers (DIBs)

DIB formation involves two or more aqueous droplets coated with lipid monolayers, submerged in an oil reservoir, brought into contact with each other forming an interfacial lipid bilayer membrane[94, 98, 202] (previously explained and illustrated in chapter 1, section 1.4.3.1). There are two approaches which can be used in forming DIBs, known as the 'Lipid-out' and 'Lipid-in' methods.[94] In the lipid-out method, the lipids are added to the oil reservoir creating an oil-lipid solution, into which an aqueous droplet is added. After an incubation period, the droplet becomes laden with lipids, forming a monolayer.[94, 100] The lipid-in approach, shown in Fig 5.3, involved aqueous droplets of liposomes to be injected into the oil well, allowing the vesicles to fuse and lipids migrate to the oil-water interface.[94, 98]

Over the years, DIBs have been successfully engineered for studying membrane permeability involving ion channels and tailored networks to mimic cell tissues.[98-100, 203, 204] However, to the best of my knowledge, they have not been used to investigate the interaction between detergents and lipid membranes. In this chapter, DIBs were one of the bilayer model membrane explored for studying the detergent-lipid membrane interactions.

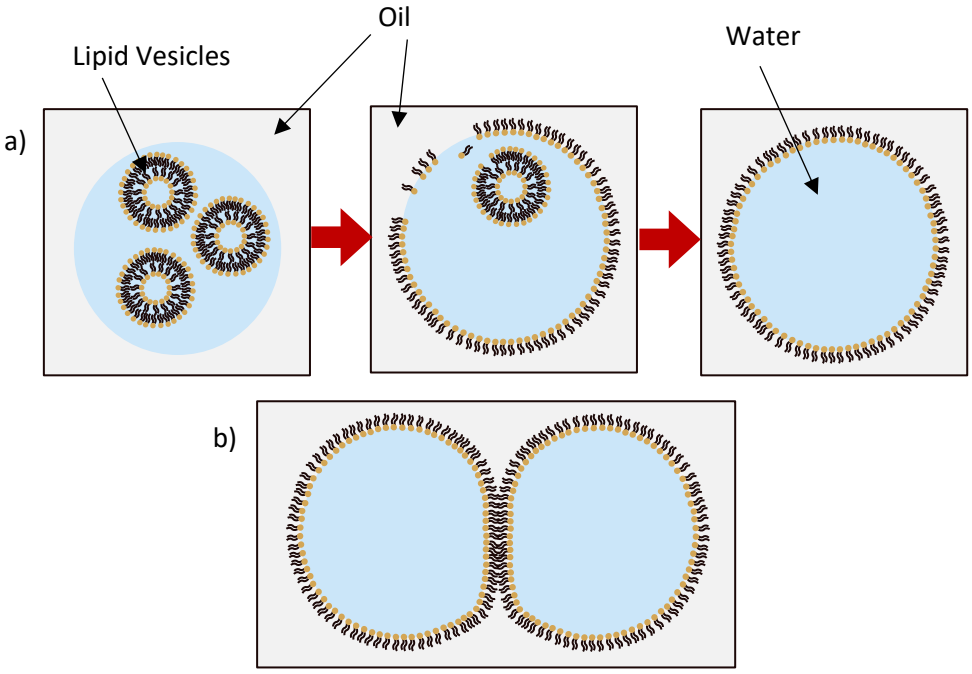


Fig 5.3 – DIBs schematics (a) Showing lipid-in method as liposomes form a lipid monolayer at the water-oil interface and (b) Formation of DIBs.

5.2.4.2 Liposomes Leakage Assay

Liposomes have been used for decades as pharmaceutical drug carriers and as models for cell membrane to investigate chemical mechanisms.[95, 103, 105] Details of liposome characterisation and application has been discussed previously in chapter 1, section 1.4.3.2). A well-known liposome application is the liposome-leakage assay which involves a dye being encapsulated within a lipid vesicle, usually a SUV, and the permeation of the lipid bilayer induced by a substance is determined as the dye is leaked.[205, 206] The amount of dye being released can be measured and tracked over time, providing an insight in to the mechanisms of bilayer action or the degree of

bilayer solubility. The principle behind this assay is illustrated in Fig. 5.4 using calcein as an example.

Calcein is a membrane impermeable, self-quenching fluorescent dye commonly used as a probe.[205, 207, 208] Calcein is estimated to have a molecular radius of 13 Å [109, 209] and is de-quenched at low concentrations.[208] As the concentration of calcein increases, its fluorescence also increases until a threshold level (typically ~50 mM) is reached.[208, 210] Beyond this threshold concentration, calcein self-quenches and the fluorescence signal diminishes. This concentration quenching property of calcein, together with its lipid bilayer impermeability, allows membrane permeability experiments to be fluorescently quantified.

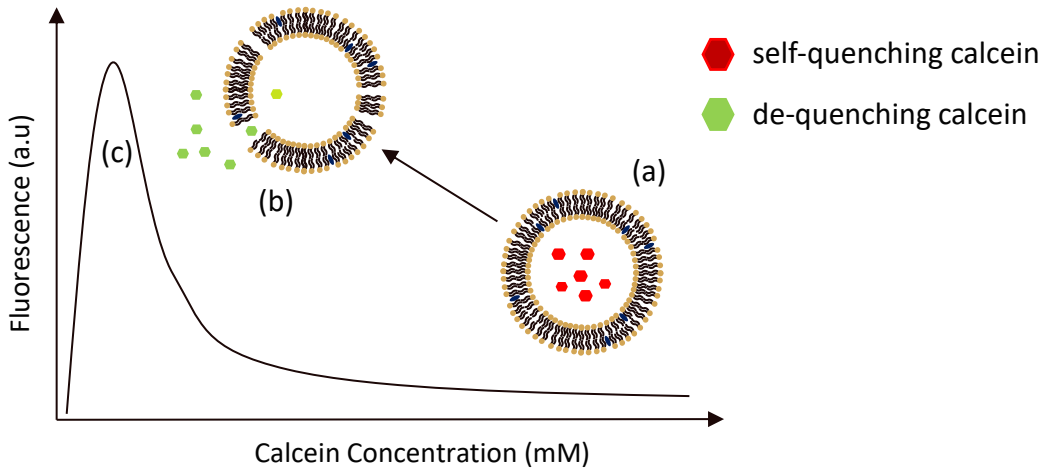


Fig 5.4 – Liposome-Calcein Release Assay – (a) Encapsulated calcein at self-quenching concentrations shows little fluorescence. (b) When the lipid bilayer disrupts, calcein leaks into the external medium, de-quenching as it becomes significantly diluted, (c) leading to an increased fluorescence.[106, 210]

Liposome based assays have also been used for the evaluation of ocular irritancy. Some studies have been carried out to develop an in-vitro alternative to the Draize test, by using liposomes as mimics of corneal epithelium membrane and determining its permeability caused by individual surfactants.[108, 206, 211] However, only a few have found a good correlation between the in-vivo Draize test scores and the in-vitro liposome leakage measurements, due to the subjective evaluation and multi-

component scoring system of the Draize score compared to a straightforward quantitative spectroscopy measurement of the liposome assay.[206] Therefore insufficient success and progress has been made using liposome leakage assay as an alternative and hence its use has not been as widespread as other in-vitro alternatives.

In all the previous studies, the liposome-leakage assay was carried out on individual surfactants and only correlated with Draize test scores. For this project, a liposome-calcein release assay was developed to determine the lipid bilayer permeability upon the exposure to liquid detergents and its measurements correlated with the ICE test scores obtained from P&G. Since the ICE test scores contain an evaluation of objective corneal swelling measurement, it may provide a better correlation. As the main endeavour is for these lipid bilayer models to provide a complimentary method to the ICE test for identifying mild to moderate irritants, the composition of the liposome needs to be representative of the chicken corneal epithelium.

5.3 EXPERIMENTAL

An overview of the materials and equipment used has been previously described in Chapter 2. Further details on sample preparation, compositions and data analysis carried out for testing lipid membrane models against detergent samples are provided in this section.

5.3.1 Detergent formulations

A series of 23 complete liquid detergent formulations were used in this chapter, all received from P&G. All the detergent samples contained the same set ingredients/ raw materials. The main difference between these 23 samples were the ratio of the three surfactants present, the concentration of fatty acid and polymer used. Each sample was coded as 1a, 1b, 1c, 2a, 2b and so on.

In all the formulations, the total level of surfactants altogether was 38-40 wt%. The variation in these formulations was mainly created by changing the ratios of the three surfactants, LAS, AES and NI to make up the 38-40 wt%. Also the level of fatty acid (Topped Palm Kernel Acid) and Polymer (PEG-400) was altered between samples denoted ‘a’, ‘b’ and ‘c’. The solvent mixture used in all these detergent samples was a

ternary system containing on average; 15 wt% Glycerol: 25 wt% Water: 60 wt% Propylene glycol. A stock solution of this mixture was made and each formulation was diluted, using the solvent mixture of the detergent, to the required levels before testing.

5.3.2 Surface tension

The CMC of each detergent samples was determined at 20 ±1 °C using the pendant drop method as detailed in Chapter 2. The detergents were diluted using the solvent mixture as described above. Three repeat measurements for each formulation were carried out.

5.3.3 DIBs

Full details for the Droplet Interface Bilayer (DIBs) preparation and formation procedure and the creation of the PDMS wells, in which the DIBs were formed, is given in chapter 2 (section 2.10). 10 mg/ml DPhPC lipids in DI water were used to form the 100 nm SUVs and later transformed into DIBs using the lipid-in approach. (Lipids details provided in section 2.3). After the formation of the DIB, optimisation experiments were carried out trialling various volumes and concentration of the detergent samples to be used against the bilayer interface. The visualization of the DIBs and its interaction with diluted detergent samples was carried out using the Olympus brightfield optical microscope (1X81F-2) and recorded through videos and images.

5.3.4 Liposome-Calcein Release Assay

100 nm SUVs were prepared in PBS 1X solution with encapsulated calcein (50 mM) for the liposome-calcein release assay (LCRA) to be performed, in order to determine the permeation of detergent samples on the lipid bilayer. Full details of the lipid vesicles preparation and the LCRA, including calcein encapsulation procedure, are all explained in chapter 2 (section 2.12 – 2.13). All detergent samples were tested at a range of concentrations.

5.3.4.1 Liposome composition

As the SUV lipid profile was required to be representative of the chicken corneal epithelium, the liposome composition was based on corneal epithelium lipid profile gathered from given references as shown in Table 5.3.

Table 5.3 – Lipid profile of the chicken corneal epithelium from different studies.

Phospholipids	Lipid concentration (Mol %)		
	My study	Zelenka, P[212]	Rintoul et at[213]
Phosphocholine (PC)	50	50	48
Phosphoethanolamin(PE)	20	25	18
Phospho-L-serine (PS)	15	12	16
Sphingomyelin (SM)	10	8	8
Others (CH, PI)*	5 (CH)	5	10

*Other; CH = Cholesterol, PI = Phospho-myo-inoaitol.

The detailed composition of SUVs used in this study was: 50 % DMPC, 20 % DOPE, 15 % DOPS, 10 % SM and 5 % CHOL (expressed as mol%). For full lipid names and structure details, refer to chapter 2, section 2.3.

5.3.4.2 Fluorimeter experiments

The measurements for the LCRA was carried out using fluorimetry, on the Varian Cary Eclipse Fluorescence Spectrophotometer (Agilent Technologies, USA). Details of this experiment set up is provided in chapter 2, section 2.14. Optimisation experiments were initially carried out to determine certain parameter such as the dilution factor for the calcein encapsulated liposomes and the liposome-detergent ratio. Triton X-100 was used as the negative control to completely solubilise the liposomes and give the total calcein release fluorescence measurements, while ternary solvent mixture was used as the positive control. The calcein encapsulated liposomes solution were diluted by 100 folds, in order for the total calcein release intensity to be within

the instrument's detection limit. The ideal liposome-detergent ratio was determined to be 4:1 respectively, with 50 µl of the dilute detergent solutions being added to 200 µl of the liposome solution pre-loaded in the well plates. All 23 detergents were tested using the same range of concentrations, which included, 0.005, 0.01, 0.015, 0.02, 0.05 and 0.1 %.

5.4 RESULTS AND DISCUSSION

All the surface tension and fluorescence data in this chapter was analysed using OriginPro (v.9.0). All the DIB experiment images were processed using ImageJ (1.151K).

5.4.1 Detergent samples CMC and ICE irritation correlation

Some studies have suggested that there could be a potential relationship between the CMC of a surfactant system and the eye irritancy.[214-216] This idea is based on the theory that surfactants monomers are more likely to penetrate the epithelium membrane compares to micelles and hence cause more irritation.[214, 215] Therefore it has been proposed that surfactant systems with higher CMCs will contribute to higher eye irritation.[216] Therefore the CMC of all the detergent samples were determined with the main purpose of establishing whether there is any correlation with the ICE test data.

5.4.1.1 Surface tension and CMC of detergents

The work carried out in chapter 3, with determining the CMC of SDS in high glycerol content, allowed for the CMCs of detergent samples to measured using surface tension pendant drop method. The optimization and automation of the pendant drop method enabled a high-throughput CMC analysis of these 23 detergent samples.

A series of dilutions were carried out for each detergent samples and the surface tension measured over a range of concentrations. Fig.5.5 shows the surface tension over detergent concentration expressed as dilution percentages (%) for all the detergents. The solvent mixture was used as the dilution liquid and as the control,

giving a surface tension of ~45 mN/m. The lowest surface tension, above the CMC, across all detergent samples was between 28 to 31 mN/m. This is consistent with typical surface tension values of ~30 mM/m commonly reported for ternary surfactant systems.[217]

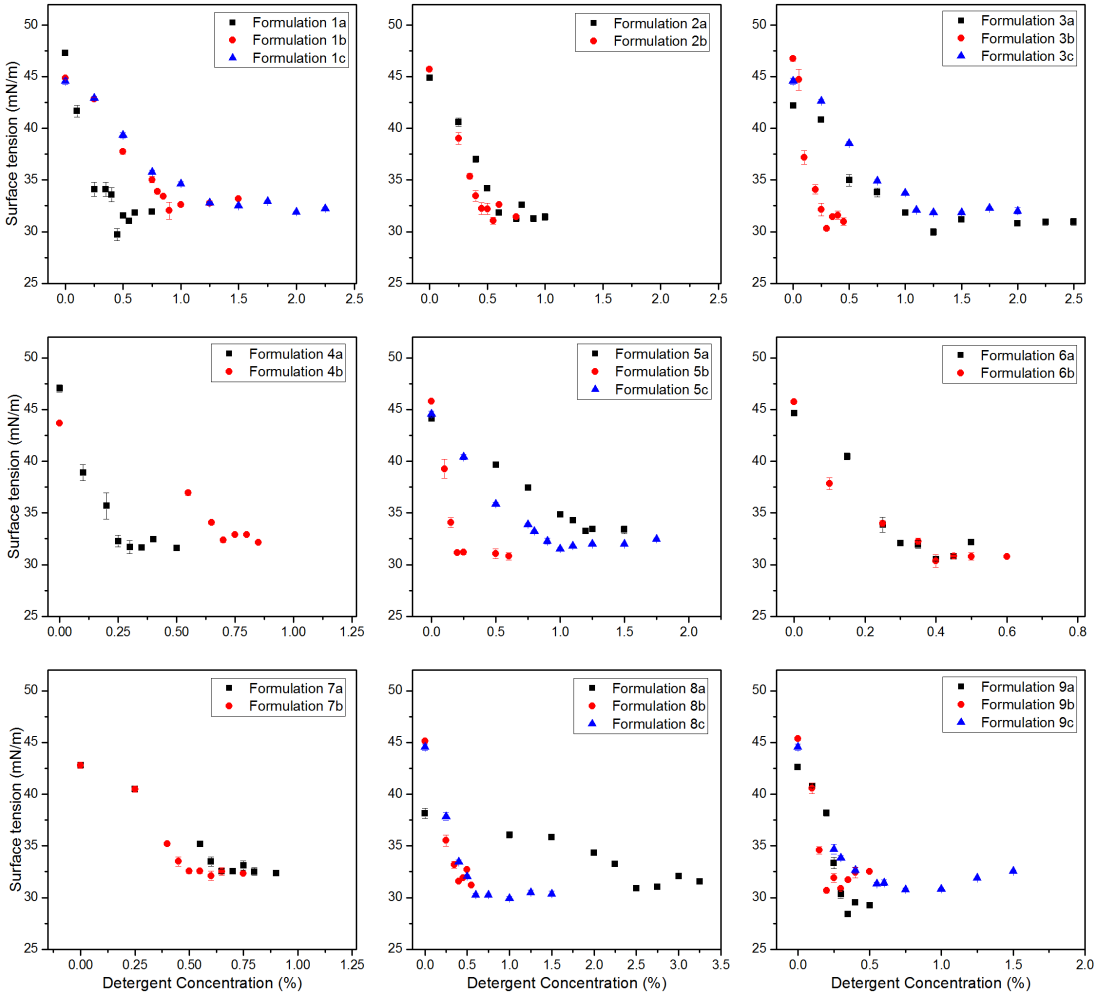


Fig 5.5 – Surface tension measurements of liquid detergent samples for CMC determination

The CMCs derived from these surfactant tension measurements are listed in Table 5.4. A range of CMCs from 2.5% to 0.2% were determined for these series of detergent, showing that changing the surfactant ratios has an impact on the CMC. An initial assessment was done to determine how the changes in the individual surfactant levels impact the CMC. Since these samples contained 3 different surfactants in various combinations along with varying levels of fatty acid and polymer, no meaning trend or correlation could be established between composition and the CMC of the detergent

sample. A correlation study was also carried out to establish any links between the composition and the ICE test data by P&G. Due to the high number of variables within these detergent samples and the ICE test, this study was challenging and no clear conclusions could be drawn.

Table 5.4 – CMCs of each detergent composition.

Detergent formulation	**CMC**				
	Repeat 1	Repeat 2	Repeat 3	Average	St.dev
1a	0.45	0.55	0.4	0.47	0.076
1b	0.9	1.0	0.9	0.93	0.058
1c	1.25	1.2	1.3	1.25	0.050
2a	0.6	0.55	0.65	0.60	0.050
2b	0.45	0.45	0.5	0.47	0.029
3a	1.25	1.25	1.2	1.23	0.029
3b	0.3	0.25	0.35	0.30	0.050
3c	1.2	1.25	1.2	1.22	0.029
4a	0.25	0.25	0.3	0.27	0.029
4b	0.7	0.75	0.65	0.70	0.050
5a	0.2	0.2	0.3	0.23	0.058
5b	1.25	1.1	1.3	1.22	0.104
5c	1.0	0.9	1.1	1.00	0.100
6a	0.4	0.35	0.45	0.40	0.050
6b	0.4	0.4	0.45	0.42	0.029
7a	0.7	0.7	0.65	0.68	0.029
7b	0.5	0.55	0.5	0.52	0.029
8a	2.25	2.15	2.2	2.20	0.050
8b	0.4	0.5	0.4	0.43	0.058
8c	0.6	0.55	0.65	0.60	0.050
9a	0.5	0.5	0.55	0.52	0.029
9b	0.2	0.25	0.2	0.22	0.029
9c	0.6	0.55	0.6	0.58	0.029

5.4.1.2 CMC vs ICE irritation

The CMC values calculated were correlated with the corresponding ICE test data as per the main aim of determining whether surfactant systems with higher CMCs leads to higher irritancy. As the ICE test data contains scores from three different parameters, an overall 'irritation index' was generated by P&G in-house to obtain a single value to represent the *ex-vivo* irritancy level. This irritation index gave equal weight to the corneal swelling and corneal opacity scores and less weight to the fluorescein retention score. The calculated irritation index was first correlated with the CMC results as shown in Fig.5.6. No clear trend can be established from this plot. Two samples which gave the lowest irritation index, 5a and 8a, have significantly different CMC of 0.23 and 2.20 % respectively. If sample 8a ICE test data is assumed to be an abnormality, it could be argued that there is a slight positive correlation between the irritation index and the CMC.

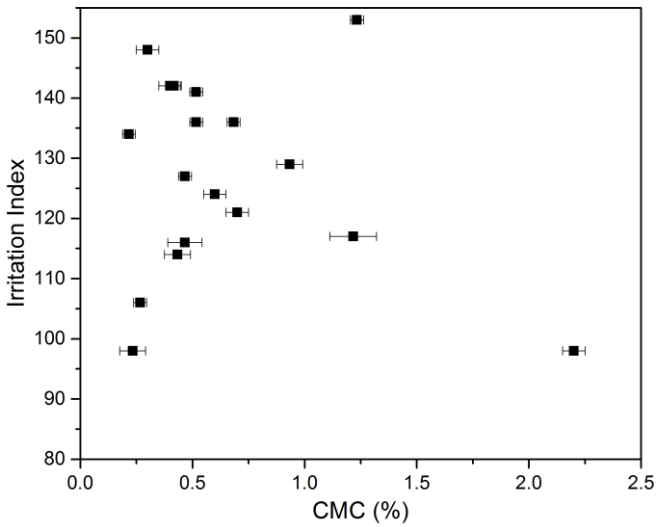


Fig 5.6 – CMC vs ICE Irritation Index correlation graph.

The lack of a clear correlation between the irritation index and the CMC could be due the three different parameters having an opposing relationship to the CMC and/or to each other. Therefore, the CMC was also correlated with the individual scores of the three parameters. Fig 5.7 (a) shows a similar plot for the corneal swelling against the CMC as seen previously in Fig 5.6 and no clear trend can be concluded. It can be seen in the plot that there is large standard deviation in the corneal swelling measurements

which makes any likely relationship unreliable. Also there is no relationship between the CMC and the other two parameters, corneal opacity and fluorescein retention as shown in Fig.5.7 (b) and (c) respectively. This is not unexpected as these two parameters are based on subjective observations with a much smaller scoring scale, which gives rise to high standard deviation.

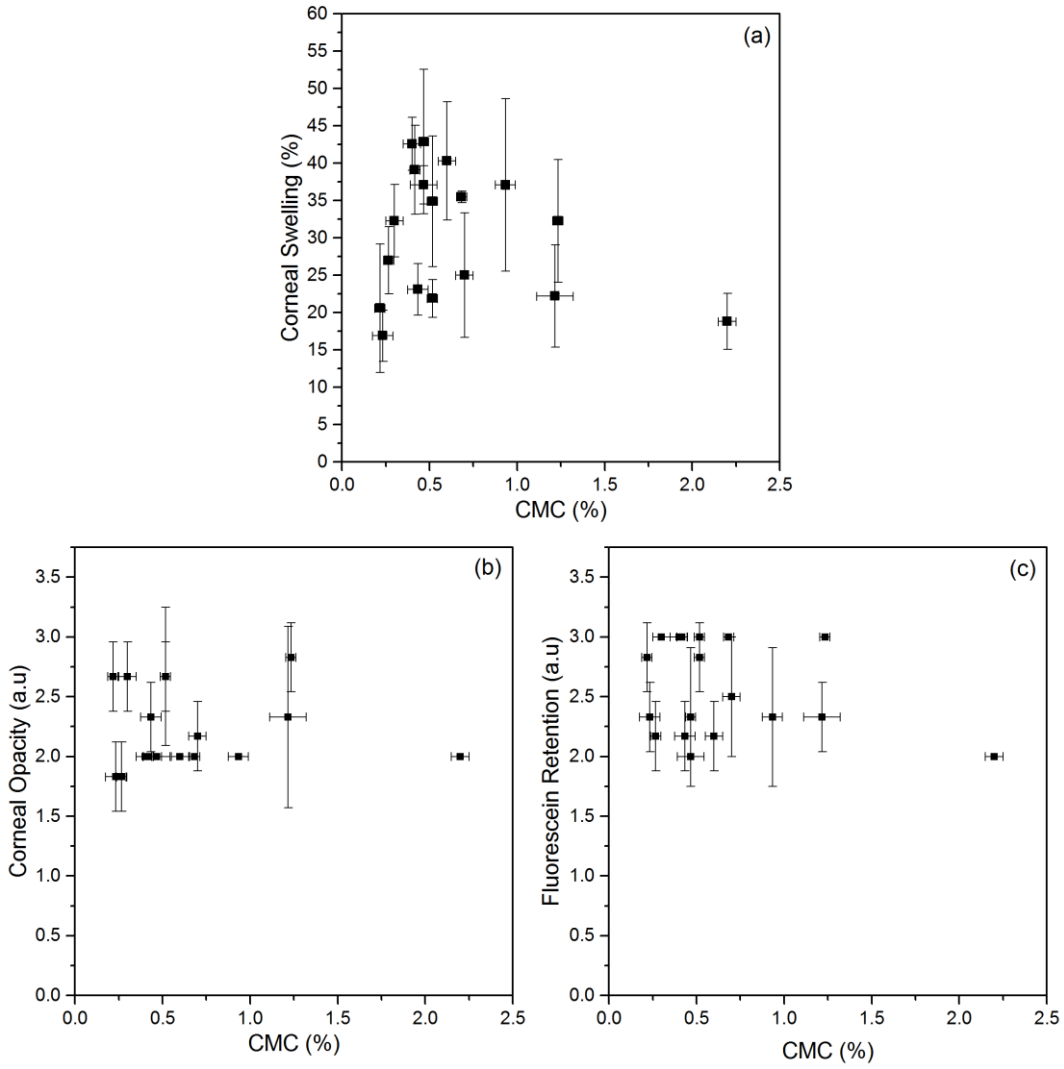


Fig 5.7 – CMC vs (a) corneal swelling, (b) corneal opacity and (c) fluorescein retention.

5.4.1.3 ICE test data review

The correlation of the ICE test data with any other measurement will be partially dependant on the precision of the ICE test scores as observed in the analysis above. The standard deviations for all the scores are based on three repeats for each sample and the actual score value is the mean average of those repeats. The corneal swelling

measurements for these detergent samples showed a reasonable amount of variation considering they are objective analysis. A larger number of repeats would give better confidence on the true spread of the data, however due to the high cost of carrying out the ICE test, more repeats are not desirable. For the corneal opacity and fluorescein retention scores from the ICE test, large variation is expected, similar to the variations observed in the Draize test scores. As one of the main criticisms of the Draize test has been the low precision of its subjective scores, therefore having a larger number of repeats is unlikely to significantly improve the standard deviation of those two parameters in the ICE test.

To get a better understanding of the overall ICE test data, the relationships between its three parameters needs to be identified. All the three parameter scores where plotted against each other to determine whether one irritancy characteristic is associated to another. The corneal swelling measurements and corneal opacity scores correlation plot, Fig. 5.8 (a), shows a slight positive relationship, but a clear association cannot be concluded due to the large error bars. When comparing corneal swelling with fluorescein retention, it can be evidently seen in Fig.5.8 (b) that there is no relationship between these two characteristics for the liquid detergent samples tested, regardless of the large variations in the scores. There was however a positive correlation found between the two subjective parameters, the corneal opacity and fluorescein retention, with a Pearson's correlation coefficient of 0.84 (Fig. 5.9b). Still, the linear relationship between the two does not give a very strong correlation coefficient due to the large standard deviation in their scoring.

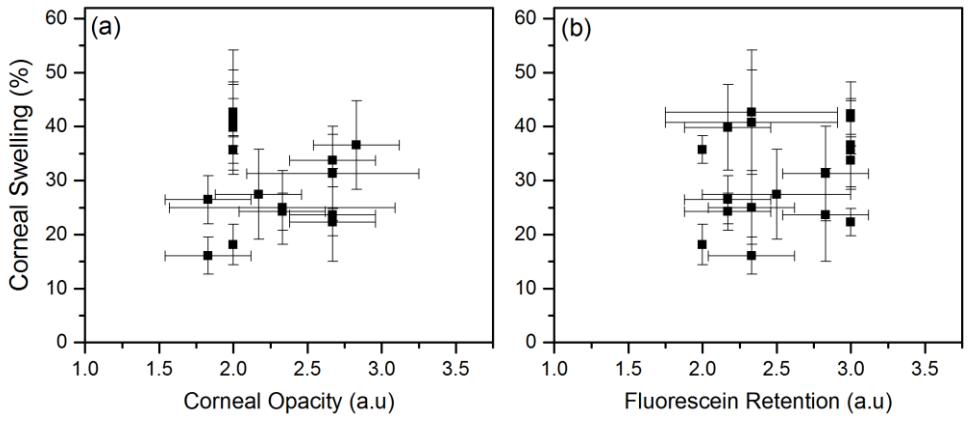
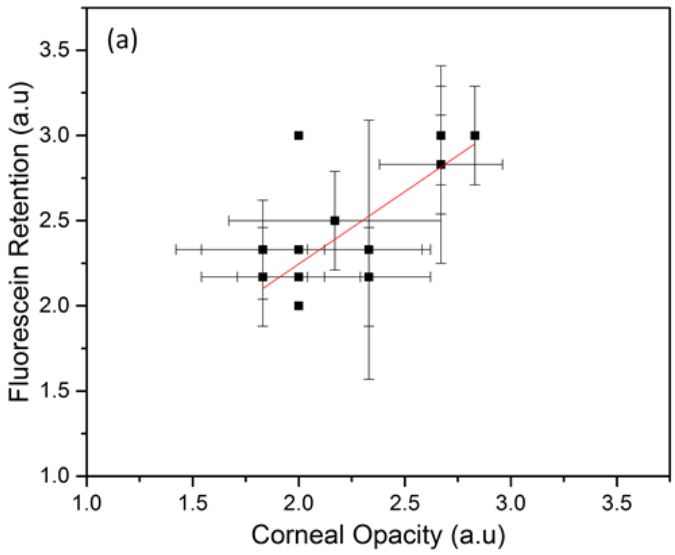


Fig 5.8 – Correlation between ICE test parameter corneal swelling vs (a) corneal opacity and (b) fluorescein retention.



(b)

Equation	y = a + b*x	
Pearson' r	0.84429	
Adj. R-Square	0.69487	
	Value	Standard Error
Intercept	0.54796	0.32782
Slope	0.84906	0.13473

Fig 5.9 – (a) Correlation between ICE test scores of corneal opacity and fluorescein retention, with the red line representing the linear fit (b) Correlation linear fit parameters.

The suggestive positive correlations of the corneal opacity scores with corneal swelling and fluorescein retention is likely arising from the irritancy characteristic that the corneal opacity evaluation observes. Opacity can be caused by: cuts to the cornea, tearing of the membrane chemically or physically, swelling of the membrane and internal infection.[70] Depending on the cause of damage, corneal opacity can be associated with one of the other parameters or both, i.e. if the damage is due to chemical tearing of the membrane, this is likely to lead to high opacity score from corneal surface damage and high fluorescein retention score due to increased permeability. This understanding was used when developing lipid membrane models and carrying out further correlation studies.

5.4.2 DIBs as corneal epithelium membrane model

The primary objective of using the DIBs approach in this study was to determine its suitability for studying the interactions between complex surfactant systems and lipid bilayer and its potential as a corneal membrane model for ICE test data correlations. Initial experiments were carried out to ensure stable DIBs can be formed and optimise

the various parameters involved, such as volume of liposome solution and concentration of the detergent samples.

5.4.2.1 DIBs formation and stability

1, 1.5 and 2 µl volumes of liposome drops were tested for stable DIBs formation. 2 µl drop volumes gave unstable DIBs, as the two droplets would merge into one after a few seconds of contact. 1 and 1.5 µl droplets formed stable DIBs over whole duration of the experiment of three hours. The formation of DIB using 1 µl droplet volume size is shown in Fig.5.10. and this volume was chosen for all further experiments.

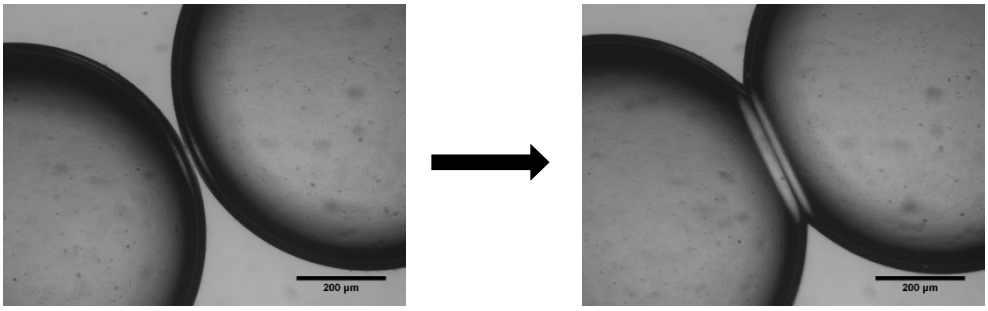


Fig 5.10. – DIBs formation by the lipid-in approach, using 1 µl of 10 mg/ml DPhPC SUVs. Lipid droplets incubating in hexadecane (left) and then after contact, the bilayer formed at the droplets interface (right). Scale bar = 200 µm.

Control experiments were carried out using the detergent solvent mixture (15 wt% Glycerol: 25 wt% Water: 60 wt% Propylene glycol) to test the stability of the DIBs upon the addition of external solvent (without the presence of surfactants). 1 µl volume of the solvent mixture was added to the DPhPC DIB formed in the hexadecane filled well as shown in Fig. 5.11. The lipid bilayer remained intact and the solvent formed its own droplet in hexadecane next to the DIB. This demonstrates the ability of the lipid droplet monolayers to keep the externally added polar solvent mixture out, while maintaining the bilayer at the droplet interface.

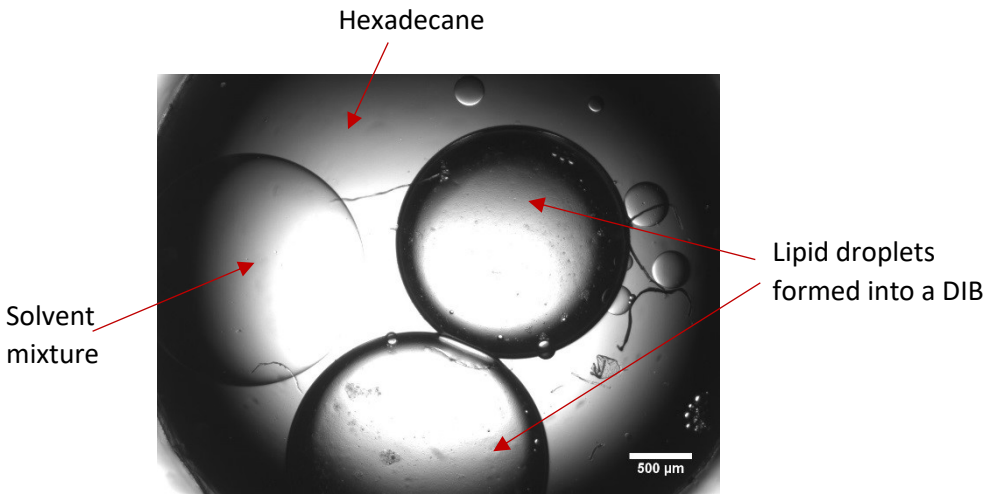


Fig 5.11 – Control experiment- DPhPC DIB shown to remain intake after the addition of the polar solvent mixture.

5.4.2.2 Detergent interactions with DIBs

Sample 3a was used as the main detergent standard for all DIBs experimental work, as this sample gave the highest overall irritancy score from the ICE test. Initially the detergent concentration tested was at the CMC level of 3a, which was 1.23 %. 0.5 µl volume of the 3a detergent sample was added to the pre-formed DIB. Upon addition, the DIB instantly merged into one droplet. Therefore, proceeding with this experimental work, a series of detergent concentrations below the CMC were tested against the DIBs to slow down the interactions enough to visualise them.

Fig 5.12 shows the experiment with sample 3a added at 0.1 % concentration. After the formation of a stable DIB for several minutes, 0.5 µl of the diluted detergent was added to one of the lipid droplet (top droplet as seen in image a). Again, within seconds after addition, the bilayer was disrupted and the droplets merged. The size of the merged droplet seems to decrease in diameter from its formation (image b) to when it has been reformed and stabilised after one minute of adding the detergent (image c). During this step, the merged lipid droplet seems to be adjusting itself to incorporate the additional surfactants and the extra polar solvent while minimising its surface area to form a stable lipid-surfactant monolayer droplet.

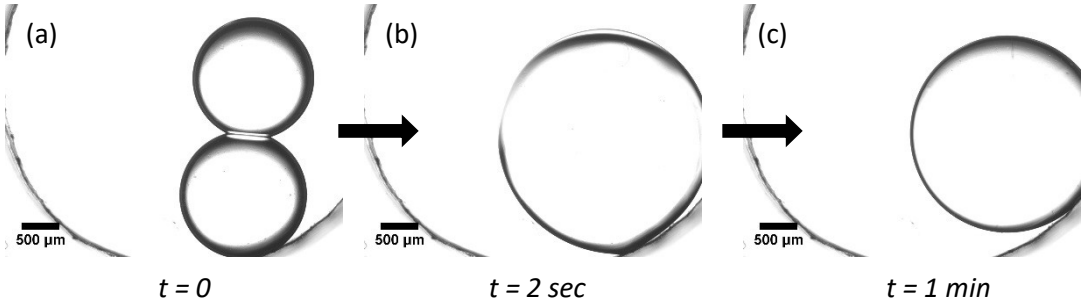


Fig 5.12 – DIB interaction with 0.1 % 3a detergent sample. (a) DPhPC DIB formed for over 5 minutes. As 0.1% of detergent is added (b) the bilayer disrupts, merging the droplets within seconds. (c) The merged droplet reforms and adjust itself to the additional surfactant and solvent present. Scale bar = 500 µm, t = time after detergent addition.

The detergent was further diluted to 0.01 % and test with DPhPC DIB. The results were similar, with the bilayer interface being disrupted and droplets merging into one as shown in Fig 5.13.

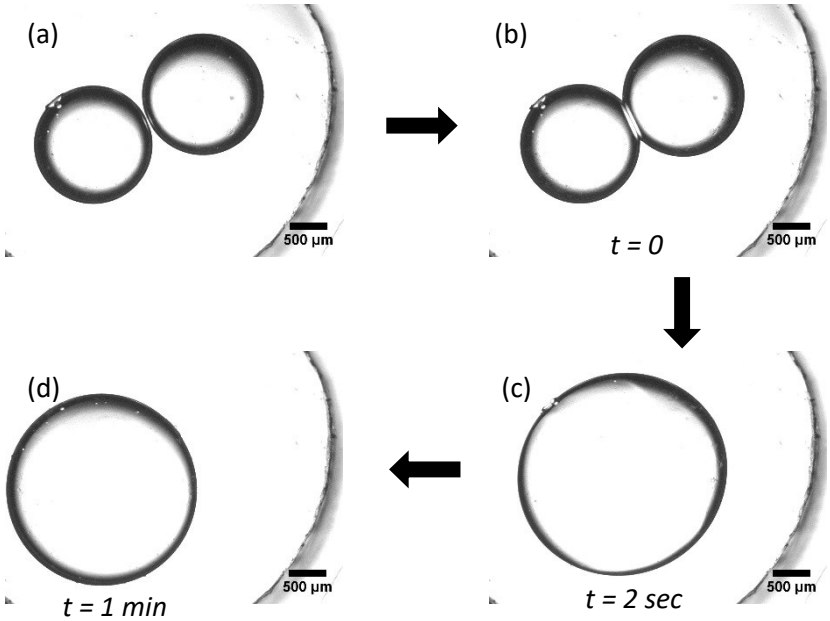


Fig 5.13 – DIB interaction with 0.01% 3a detergent sample. (a) DPhPC liposome droplets incubated in hexadecane (b) Stable DIB formed over several minutes. 0.01 % detergent added at t = 0 (c) the droplets merge after bilayer interface disrupts within seconds. (d) The merged lipid-surfactant droplet reforms and stabilises. Scale bar = 500 µm, t = time after detergent addition.

When adding detergent at 0.1 and 0.01 % dilutions, the rate at which the interaction takes place is extremely quick and the bilayer is disrupts within seconds. The surfactant monomers seem to get incorporated within the lipid monolayer instantly and causing a rippling effect leading to the disassembly of the bilayer. The rippling effect is likely to occur due to changes in the lipid monolayer curvature at the aqueous solvent-hexadecane interface. In an attempt to slow down the merger of the droplets, the detergent sample 3a was diluted to 0.001 %. This dilution attempt did manage to reduce the rate at which the droplets merged and gave an insight into the interactions taken place (Fig 5.14). As the diluted detergent is added to the droplet on the right (as seen in image a), the droplet begins to expand in size, incorporating the surfactant monomers and the solvent mixture, while maintaining the bilayer at the droplet interface (image b). The surfactant monomers seem to assimilate themselves into the lipid monolayer as the extra solvent enlarges the droplet. This time the bilayer is not disrupted at the interface immediately and continues to hold together for over 1 minute.

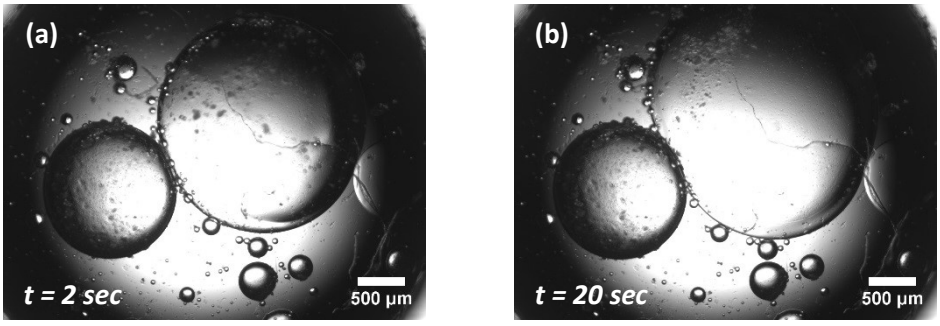


Fig 5.14 – DIB interaction with 0.001% 3a detergent sample. (a) Diluted detergent added to DPhPC droplets on the right, which leads to the droplet enlarging. (b) Droplet continues to enlarge while retaining the bilayer at the droplet interface. Scale bar = 500 µm, t = time after detergent addition.

This dilution concentration of detergent sample 3a was repeated two more times to determine the reproducibility of the experiment and whether the rate of the interactions (enlarging and then merging of droplets) can be measured. Both the repeat experiments gave inconsistent results as in one of the repeats, the bilayer disrupted immediately and droplets merged whereas in the other repeat, the droplet enlarges first similar to

that shown in figure 5.14, but merged with the adjacent droplet shortly after (within 5 seconds).

To explore the interactions taking place upon the addition of diluted detergent and the disruption of the interfacial bilayer, DPhPC liposomes loaded with 50 µm calcein were made and used as one of the droplets for the lipid-in DIBs approach. This created a DIB system with one droplet containing the calcein encapsulated within its lipid monolayer, while the droplet on the other side of the bilayer interface contained DI water, as illustrated in Fig 5.15 (a). The idea behind this setup was to determine the point and speed at which the bilayer starts to disrupt, which can be visually tracked by the diffusion of calcein across the droplet interface. When 0.001 % diluted 3a detergent sample was added to the 'standard' droplet, the droplet swelled up and immediately disrupted the bilayer, merging the two droplets together. As the merger occurs, the internal solvent content within the lipid monolayers get exchanged. However, as seen in Fig.5.15 (b), calcein does not completely diffuse across the internal area of the droplet. This could be due to that area of the droplet containing a higher concentration of the detergent solvent mixture (glycerol: water: propylene glycol), preventing calcein from spreading across the entire droplet.

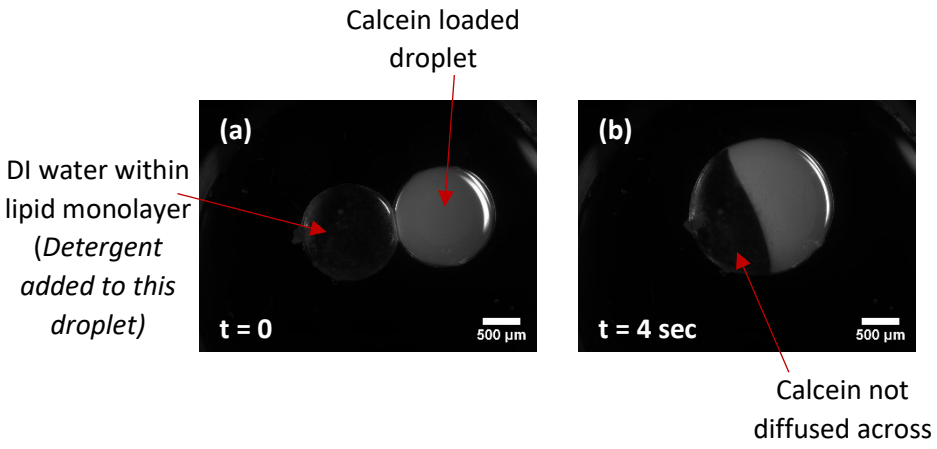


Fig 5.15 – (a) Formation of a DPhPC DIB with one droplet containing calcein (b) Post-merging of the droplets after bilayer is disrupted upon addition of 0.001% 3a detergent. Calcein does not diffuse completely across the merged droplet. Scale bar = 500 µm, t = time after detergent addition.

Repeat experiments for this same setup using calcein was carried out, giving a similar result but with a slight time delay. As shown in Fig 5.16, after the addition of 0.001 %

3a detergent to the left droplet (as seen in image a), it begins to enlarge first over a few seconds while keeping the DIB intact, before disrupting the bilayer and merging the two droplets together, causing the calcein to diffuse across. Similarly to the previous repeat, a smaller area remains within the lipid-surfactant monolayer where the calcein is not fully incorporated.

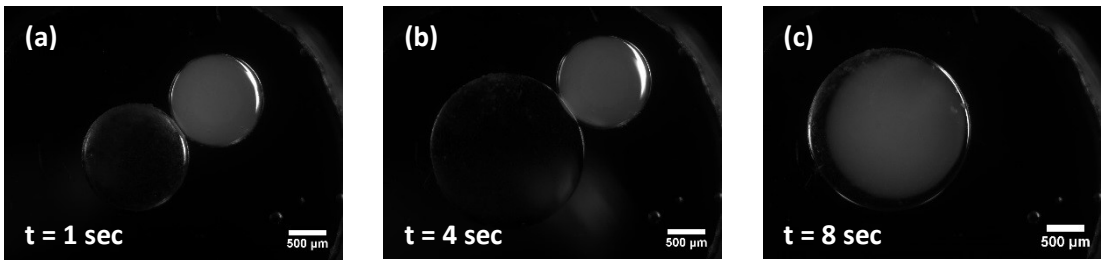


Fig 5.16 – (a) DPhPC DIB with one droplet containing calcein, as 0.001% 3a detergent is added (b) Enlarging of the droplet, while maintaining the DIB (c) Post-merger of the droplets and calcein diffusing across. Scale bar = 500 µm, t = time after detergent addition.

A schematic of the interactions taking place in this experiment is shown in Fig. 5.17 and the likely mechanism suggested. The inclusion of surfactant monomers in the initial lipid droplet monolayer seems to be altering the droplet's curvature as it enlarges. The interactions at the interface is stable enough to keep the bilayer intact as long as possible. The continuing enlargement and changing curvature are likely causes for the weakening of the bilayer, leading to the droplets merger.

Although the experiments were slowed down enough to visualise the interactions with using a very diluted level of 0.001 % detergents, there are still reasonable inconsistencies when using this DIBs model. These inconsistencies makes it difficult to quantify the interactions occurring, i.e. rate of droplet enlargement and disruption of bilayer- merging of droplets. Due to the lack of reproducibility, this approach is inefficient for differentiating between various detergent concentrations and formulations. Therefore, exploring DIBs as a tool for investigating detergent interactions with lipid bilayer proved ineffective in the context of membrane permeability and wasn't developed further.

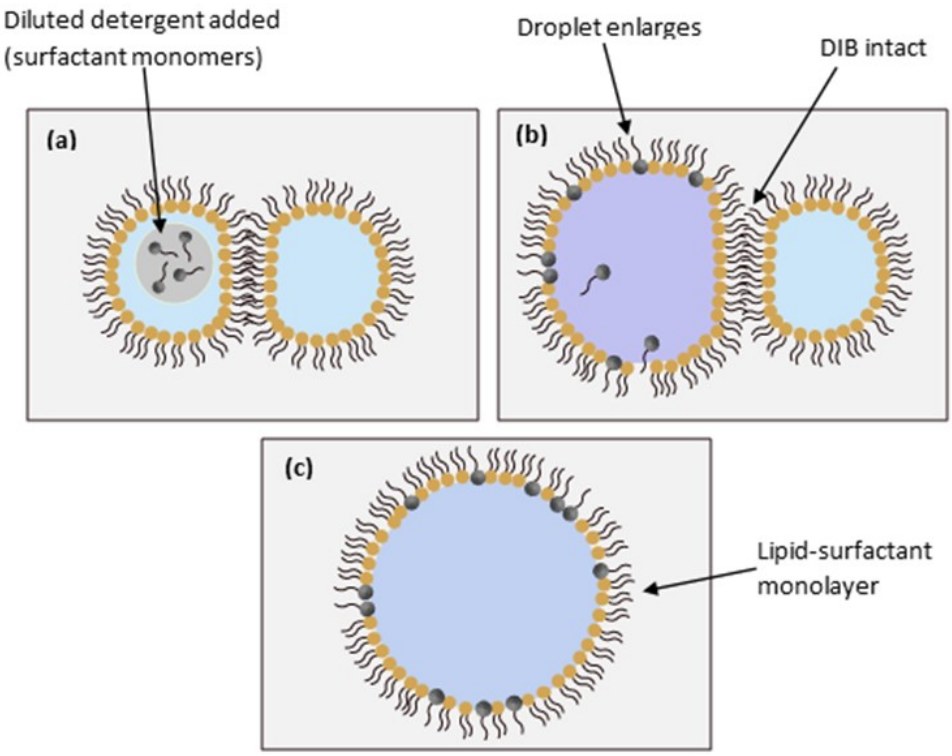


Fig 5.17 – DIB experiment schematic. (a) DIB formed and diluted detergent added to one of the droplets (b) Droplets incorporates the surfactant monomers and solvent mixture, while the DIB remains intact. The bilayer at the interface disrupts shortly after, (c) merging the droplets together, forming a lipid-surfactant monolayer.

5.4.3 Liposomes as corneal epithelium membrane models

In this section, the potential of liposomes as a model for corneal epithelium membrane and the calcein release assay as a tool for determining irritancy is discussed. Liposomes were created to be representative of the corneal epithelium membrane, details of which are provided in section 5.3.3 and the aim here was to determine whether any correlation can be established between LCRA and the ICE test data.

5.4.3.1 SUVs Characterisation

Once the 100 nm SUVs were created using the extrusion technique mentioned in chapter 2 (section 2.12), they were characterised using DLS. The particle size distribution by volume of these SUVs is shown in Fig. 5.18. The distribution was

consistence across all the repeats and the mean particle size was measured to be 98.96 ± 2.46 nm.

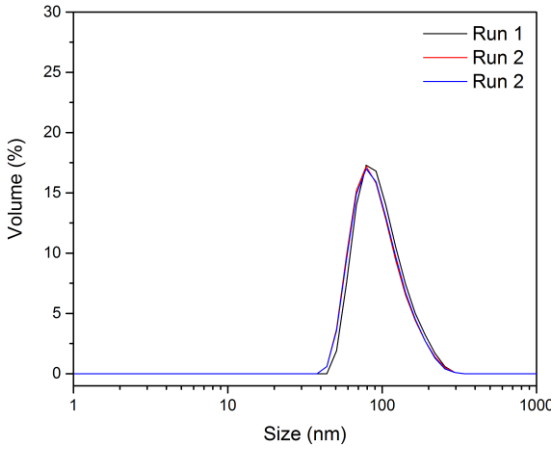


Fig 5.18 – Particle size distribution by volume of 100 nm SUVs produced for the LCRA.

Alongside the size analysis, the characterisation of the encapsulated calcein in the SUV was carried out and the dilution factor determine to ensure that the total fluorescence intensity of the released calcein is within the detection limit. A series of dilutions were carried out starting with a dilution factor of 30 and then reaching 100 fold, which gave consistently high total intensity within the detection limit.

5.4.3.2 LCRA controls

For this assay, the two sets of controls, the ternary solvent mixture as the 'positive' control and 5 mM triton X-100 as the negative control were used for each batch of calcein encapsulated liposomes made. The purpose of the 'positive' control was to determine whether the addition of the solvent mixture alone contributed to the release of the calcein from the liposome and also to determine the change in intensity as the liposomes becomes slightly diluted. Across all the experiments, the addition of the solvent mixture to the SUV solution did not give any significant changes to the fluorescence intensity readings as shown in Fig. 5.19 a. This figure also shows the intensity reading for the negative control experiments. Upon addition of 5 mM triton X-100, the fluorescence intensity increases instantly (within 30 seconds of addition) from 120 to 940. This negative control experiment showed that this concentration of

triton X-100 is sufficient to completely solubilise my composition of SUVs and give the total release of calcein.

The fluorescence intensity readings for each 30 seconds time intervals were converted to % calcein release using equation 5.2, to standardise the results for comparison. These results are shown in Fig. 5.19 b.

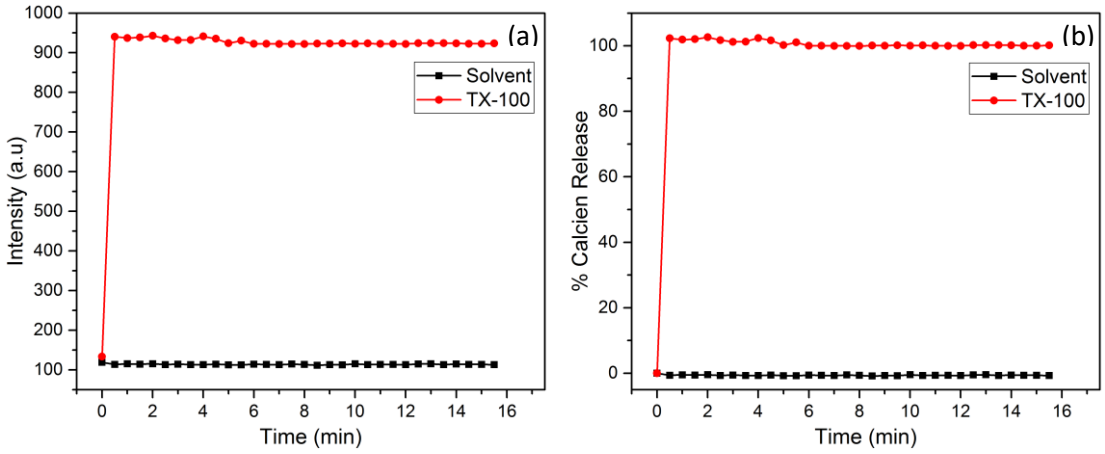


Fig 5.19 – (a) Calcein fluorescence intensity over time after the addition of 5 mM triton x-100 and solvent mixture control (b) % calcein release over time for 5 mM triton x-100 and solvent mixture control.

Equation 5.2:

$$\%\ Calcein\ Release = 100 \times \left(\frac{F_x - F_0}{F_{total} - F_0}\right)$$

F_0 = Fluorescence at time 0

F_x = Fluorescence at time x

F_{total} = Fluorescence at total calcein release

5.4.3.3 Calcein release data analysis

All 18 detergent samples were tested using the same experiment parameters and the same concentration range. An example of the raw fluorescence intensity data measured over 15 minutes, for detergent sample 1a at 0.02 % is shown in Fig. 5.20. At this concentration, the calcein intensity response over time in a typical 'positive concave downwards' curve, showing a rapid increase in fluorescence intensity initial as the detergent is solubilising the liposome, after which the increase in fluorescence slows down, eventually levelling off when all the detergent has been used up and a few calcein encapsulated liposomes remain intact. To confirm whether some liposomes remain un-solubilised and to get a total calcein release, the negative control triton X-100 was used, the fluorescence intensity of which is illustrated in Fig. 5.20. The initial fluorescence intensity (F_0) and the total fluorescence intensity (F_{total}) values obtained from these experiments are used in equation 5.2, for each time interval point, to calculate the % calcein release values. This data was then plotted against time to create a curve for % calcein release over time for each sample, at various concentrations, with 3 repeats per each concentration. An example of the % calcein release –time response for sample 1a at three different concentrations is shown in Fig 5.21.

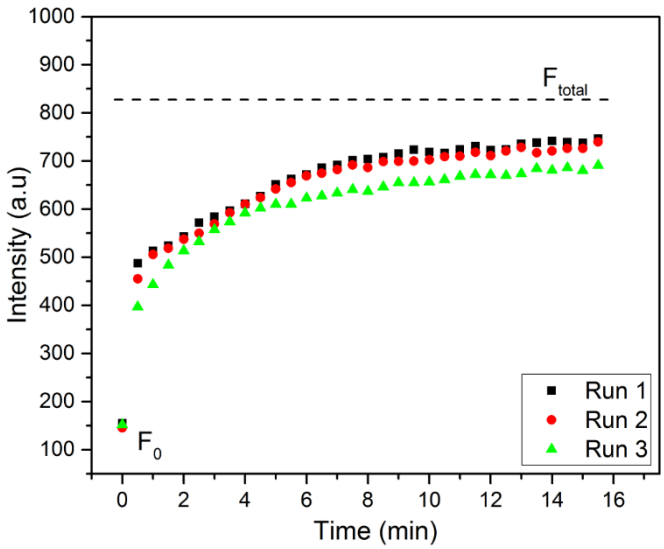


Fig 5.20. – Time response- Calcein fluorescence intensity for detergent sample 1a at 0.02 % concentration, three repeats (F_0 – Initial fluorescence, F_{total} – Total fluorescence).

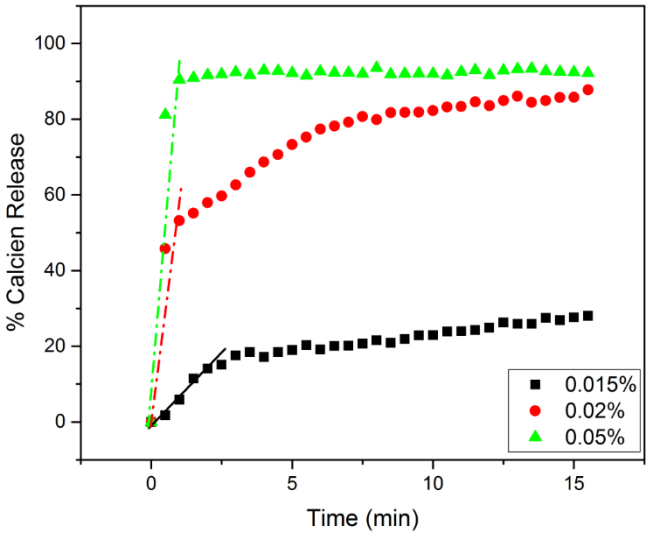


Fig 5.21 – % calcein release over time for detergent sample 1a, at three different concentrations. Dotted lines show initial gradient used to determine the initial rate of release.

Time response

Across all detergent samples and all concentrations, the time response to the addition of detergent was similar. As the detergent was added at low concentrations (~0.01 %), the calcein fluorescence intensity increases gradually over time and starts to reach a plateau (i.e. maximum % calcein release) after 10 minutes. This plateau at low concentrations is typical around 30- 40% calcein release and never reaches higher than 50 %. This suggest that under half of the liposomes are solubilised. At higher concentrations (e.g. from 0.05 to 0.1 %), the rate of fluorescence increase over time and the maximum fluorescence intensity are both higher, as expected, with a plateau being reached close to 100 % within 5 minutes. A schematic of this time response at low and high detergent concentrations and the interactions occurring is illustrated in Fig.5.22.

Concentration response

From the time response curves, the maximum % calcein release values at 15 minutes established reasonable differentiations across the range of concentrations tested. These differentiations can be used to determine the difference in the ICE test irritancy data.

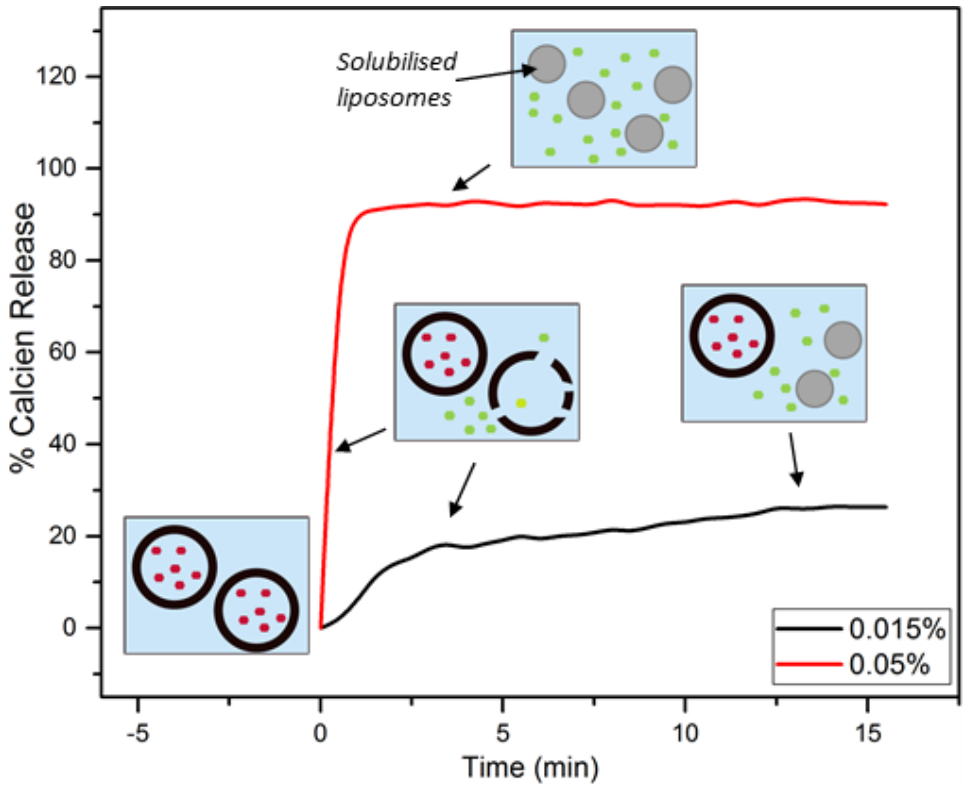


Fig 5.22 –Schematic of calcein release over time as the detergent is added to liposomes, at low (0.015 %) and high (0.05 %) detergent concentrations. At low concentrations, not all the liposomes are solubilised, hence some calcein remains encapsulated. At higher concentrations, all the available calcein is released in less time, as the lipid bilayer is solubilised.

Therefore, the results at 15 minutes were used to generate a 'max % release - concentration response curve' for each detergent sample, as shown in Fig 5.23. A mean average of the max % calcein release from the 3 repeats was taken. This allows for the concentration response of each detergent to be compared directly. There were also significant differences in the rates at which calcein was released from the SUVs, for the various concentrations across all the detergent samples. To take into account the effect of detergent concentration on the rate of calcein release, an initial rate of release (% /min) was calculated from the % calcein release – time response curves, as illustrated in Fig 5.21. This initial rate of calcein release data was plotted against detergent concentration, provided in Fig 5.24, to allow for a comparison between the rates of permeation for each detergent sample.

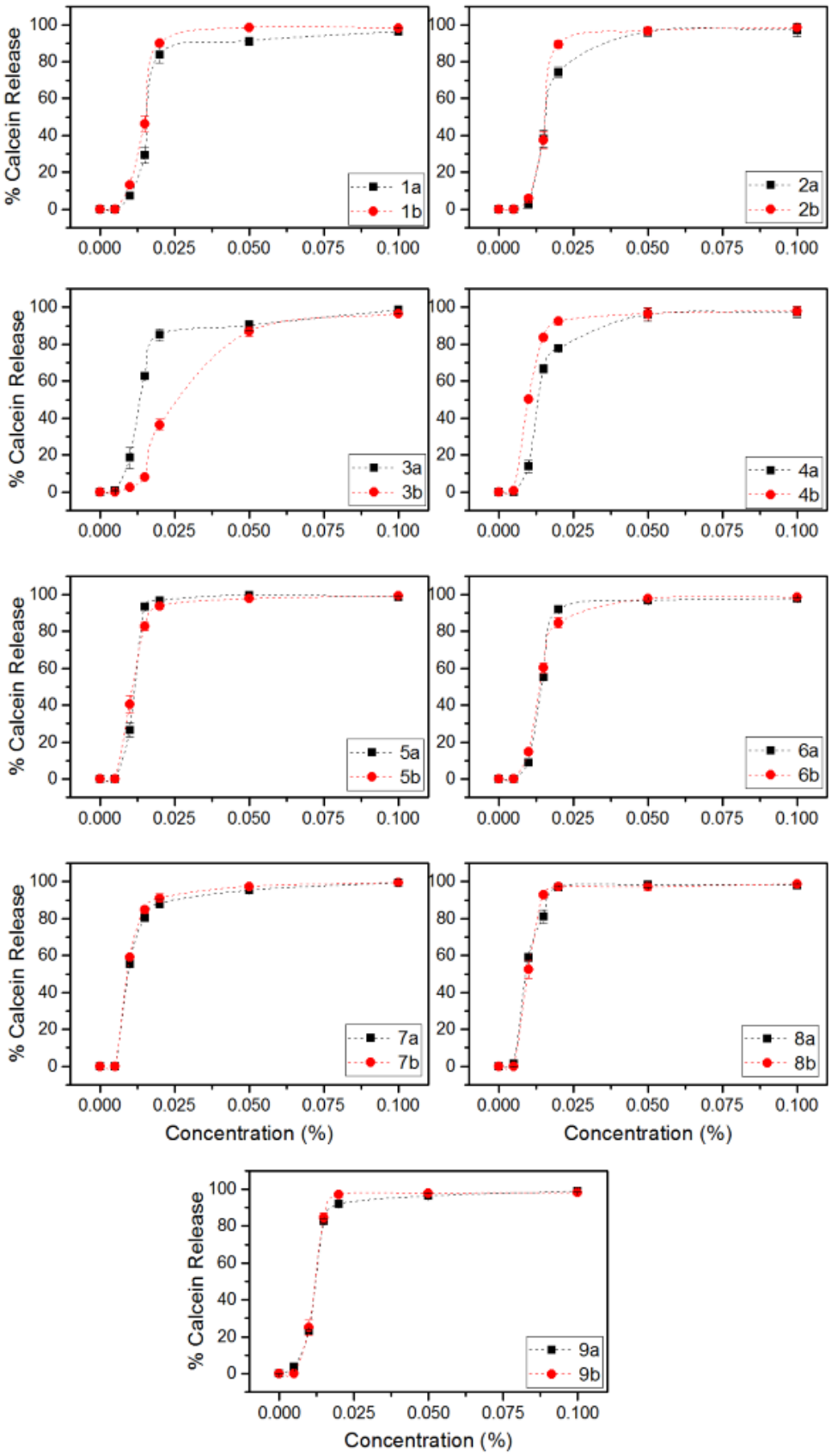


Fig 5.23 – Max % calcein release – concentration response for 18 detergent samples: 1a to 9b. (squares- sample a, circles- sample b)

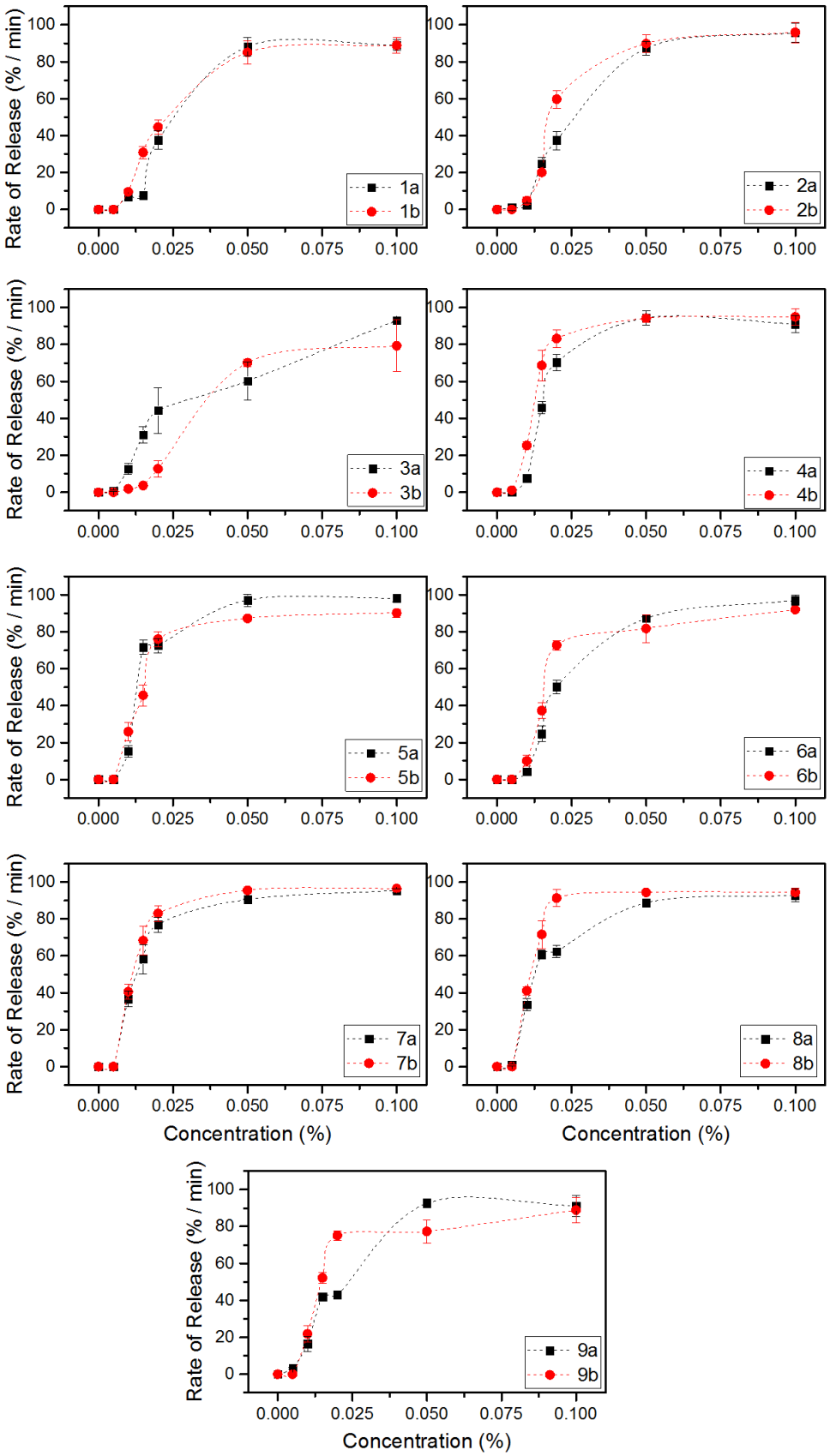


Fig 5.24 – Rate of calcein release – concentration response for 18 detergent samples: 1a to 9b. (squares- sample a, circles- sample b)

All the18 detergent samples gave a similar 'Sigmodal growth' shaped concentration response profile as shown in Fig. 5.23. This reiterates the process explained before that, at very low concentrations, the increase in calcein release is very gradual, with further increase in concentration causing a rapid increase in % release and then eventually plateauing out near 100 % as all the calcein has been released.

This 'S' shaped concentration response provides an insight into the process which with the detergent interacts with the lipid bilayer of the vesicles. The small release of calcein at low detergent concentrations suggest that there aren't sufficient surfactant monomers to significantly permeate the bilayer. As the detergent concentration increases, the ratio of surfactant monomers also increases, increasing the amount, as well as the rate at which the lipid bilayer is permeated, causing the rapid increase in calcein release over a narrow range of detergent concentration. Above a certain detergent concentration 'threshold', the ratio of surfactant monomers to lipids is significantly higher, causing the liposomes to be completely solubilised, releasing all the encapsulated calcein. This 'threshold' concentration is slightly different across all the detergents. This 'S' shaped response to concentration has been reported in literature for studies involving individual surfactants.

When comparing these concentration response curves between each sample, the region of rapid increase showed the most differentiation as highlighted in Fig. 5.25. Therefore, a concentration of 0.015 % was chosen in this region as a single point of comparison, for both % calcein release and rate of release data.

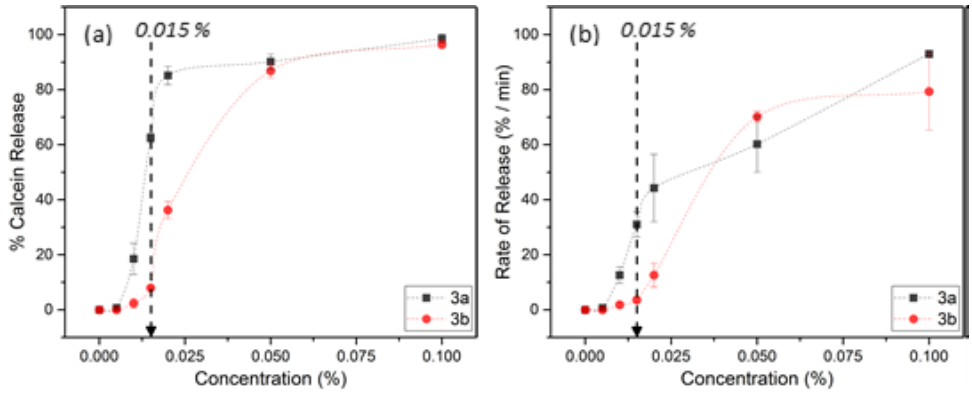


Fig 5.25 – (a) % Calcein Release and (b) Rate of Release for detergent sample 3a and 3b, showing differentiation at 0.015% concentration.

5.4.3.4 Calcein release vs ICE test data

The values gathered from the concentration response curves at 0.015 % detergent, from both, max % calcein release and the rate of release analysis, were plotted against the ICE test data to determine any potential correlation. First, the calcein release values were plotted against the ICE test irritation index as shown in Fig.5.26. In both the % calcein release and rate of release plots (a and b respectively), shows a fairly scattered relationship with the irritation index, therefore no meaningful correlation can be established between these data sets. This is likely due to the irritation index being an 'overall' index score for all the three parameters combined in the ICE test, with different weighing given to each parameter as explained previously. As I showed in section 5.4.1.2, that even the three ICE test parameters did not have a clear strong relationship with each other, particular the corneal swelling test verses the corneal opacity and fluorescein retention.

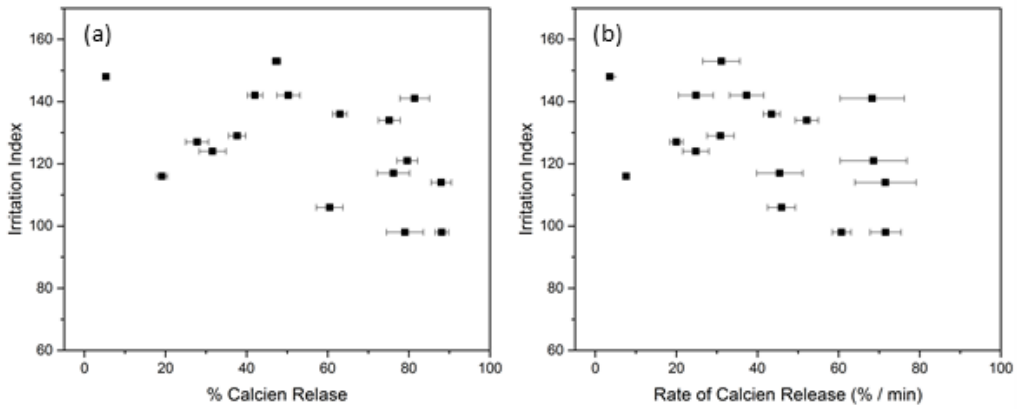
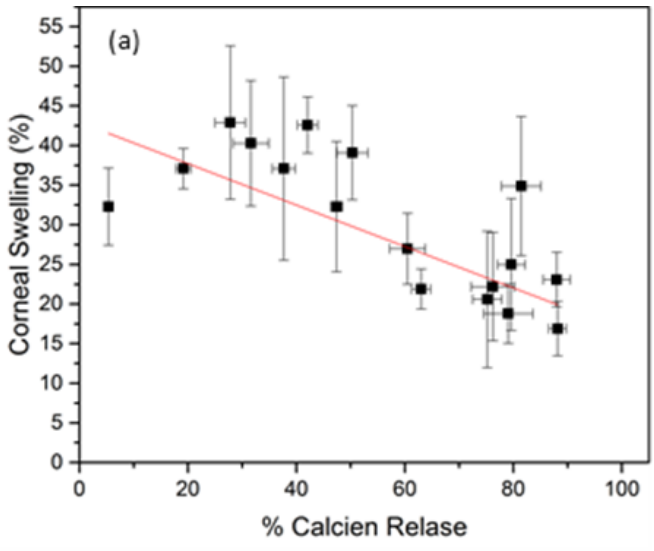


Fig 5.26 – The ICE irritation index against (a) % Calcein release and (b) Rate of Calcein Release for all 18 detergent samples.

Therefore, I decided to plot the both the calcein release data set with each of the three ICE test parameters individually, to determine any potential relationship with the specific characteristic irritation response. Fig 5.27 (a) shows the plot for max % calcein release against the objective % corneal swelling measurements. This showed a decent negative linear correlation between the two, with the Pearson's r value of –0.80 and an adjected R-sqaure of 0.60. The low R-square value can be explained by the large standard deviation in the corneal swelling measurements.



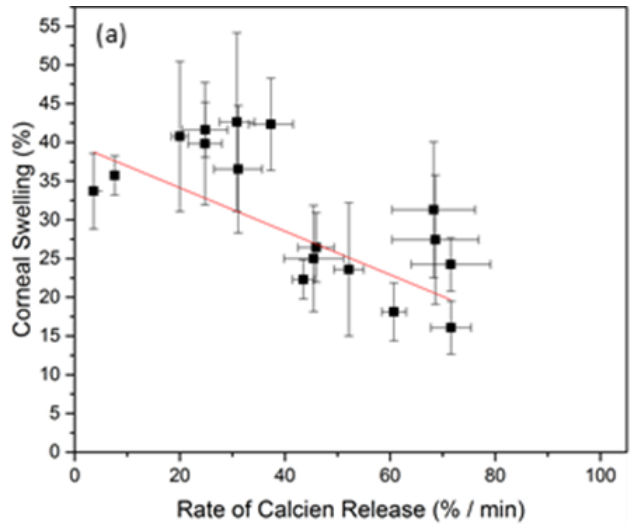
(b)

Equation	y = a + b*x	
Pearson's r	- 0.7919	
Adj. R-Square	0.60224	
	Value	Standard Error
Intercept	42.9402	3.20617
Slope	-0.26129	0.05202

Fig 5.27 – (a) Correlation between ICE test score of corneal swelling and % calcein release with the red line representing the linear fit. (b) Correlation linear fit parameters.

The plot for rate of release against corneal swelling also shows an inverse relationship between the two, with a slightly lower Pearson's r and R-square values of –0.77 and 0.56 respectively (Fig. 5.28). This small difference is likely due to the slightly larger variation in the rate of release data from the LCRA. These correlation analysis between the calcein release experiments and corneal swelling measurements suggest that the permeation and solubility of the lipid bilayer is inversely linked to the swelling of the corneal epithelium membrane, with higher rate of permeation and level of liposome solubility, the amount the corneal swelling decreases.

The potential theory for this inverse relationship can be explained through the physiological changes occurring in the corneal epithelium membrane as it swells due to irritation. An inflammation in the outer layers of the cornea is commonly caused by a build of fluid and substances (edema),[191, 218] which can occur due to irregular cellular function for fluid control.[198, 218] Increasing permeation of the lipid membranes caused by a mixed surfactant system could be damaging the cornea in such a way which does not allow a build-up of fluid, hence causing less corneal swelling.



(b)

Equation	y = a + b*x	
Pearson's r	- 0.76609	
Adj. R-Square	0.55935	
	Value	Standard Error
Intercept	39.75	2.83317
Slope	-0.28066	0.608

Fig 5.28 – (a) Correlation between ICE test score of corneal swelling and rate of calcein release with the red line representing the linear fit. (b) Correlation linear fit parameters.

When the calcein release data is compared against the corneal opacity and fluorescein retention scores, no relationship can be observed as shown in Fig 5.29. In theory, calcein release data and fluorescein retention scores should suggest a potential positive correlation as both these analyses indicate the level of lipid bilayer permeation being caused by the detergent. However, since both the corneal opacity and fluorescein retention scores are subjective and contain large variations, obtaining any meaningful correlation with these two parameters has been challenging.

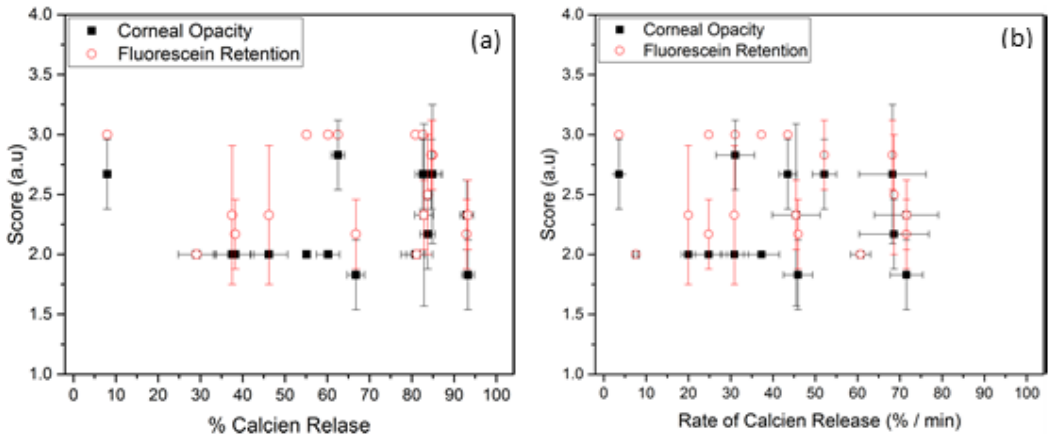


Fig 5.29 – Correlation between ICE test scores of corneal opacity and fluorescein retention against (a) % calcein release and (b) rate of calcein release.

Another factor which should be considered when determining any relationship between the ICE test data and an alternative in-vitro method for liquid detergent samples, is the complexity of the formulation. Since these detergent formulations contain a mixture of different surfactants, polymers and fatty acid, each chemical can be contributing to a particular irritancy characteristic and may not cause an effect on all three parameters. Therefore, it is important to investigate the interactions between the individual surfactants used in these detergents and the lipid bilayer to gather a better understanding on how these particular compositions are contributing to ocular irritancy.

5.5 CHAPTER CONCLUSIONS

Analysing the data from the ICE test has shown the challenges involved in correlating this data with an alternative in-vitro method and also explains why the ICE test, as its stands currently, is not accepted to classify UN GHS category 2 (mild to moderate irritation) substances. An attempt to develop a complimentary tool to the ICE test for ocular irritancy categorisation, led to three sets of investigations, CMC analysis, DIBs approach and the LCRA.

The theory that CMC of a complex surfactant system could be linked to eye irritancy could not be proven based on the ICE test. The DIBs approach required the detergent samples to be tested at extremely diluted levels and did not show a good potential for studying the permeation of the lipid bilayers caused by surfactant mixtures. Hence developing DIBs as model for corneal epithelial membrane is likely to be ineffective and non-discriminatory.

The liposomes developed as a model for chicken corneal epithelial membrane, together with the LCRA established, provided a decent premise for comparison with the ICE test data as it managed to differentiate between the potential irritancy of the various complex surfactant formulations. These differentiation lead to establishing a meaningful negative correlation between the calcein release data and the corneal swelling measurements from the ICE test. Once the procedures and the method parameters were optimised, this assay also proved to give a high throughput, reproducibility, and is less expensive compared to other in-vitro alternatives as it

involves the standard vesicle producing equipment and a straightforward fluorescence spectrometer step-up.

All the learnings from the LCRA in this chapter had encouraged me to further extend this application in the next chapter to study the impact of individual surfactants used in these detergent formulations and get a better understanding of their mode of action in lipid membrane permeation with regards to eye irritation.

Chapter 6

Interactions between Surfactants and Lipid Membrane.

6.1 OVERVIEW

The success of the LCRA in the previous chapter using detergent sample was carried forward to determine the effect of the three surfactants present in the liquid surfactant formulation. Each of the three surfactants were tested individually as well as in various binary and ternary surfactant systems to get a better understanding of how each surfactant and their mixtures permeates the lipid bilayer. The robustness and the high-throughput ability of the LCRA for this application was further reinforced by this study, which provides confidence to further develop this technique as a complimentary *in-vitro* eye irritation test method. Real-time DLS-particle size analysis was also carried out alongside the LCRA to track the solubilisation of the liposomes by the surfactant systems. The learnings from both these techniques in this chapter allowed for a better understanding of the mode of action of these surfactants in lipid membrane permeation and also provides a potential theory into the relationship between calcein release data and ICE test corneal swelling measurements established in the previous chapter.

6.2 INTRODUCTION

The LCRA developed in chapter 5 showed its capability of screening to help identify a range of potential eye irritants quickly and economically, which has been a significant drawback of other *in-vitro* methods.[66, 185, 186] The LCRA study was able to differentiate between the different detergent samples and establish a correlation with the corneal swelling measurements on the ICE test data. In this chapter, that study was extended to understand this inverse relationship, which would help in further developing this assay for a better representative *in-vitro* method for eye irritancy. Given the complexity of the detergent formulation, containing a combination of three

different surfactants in various ratios, these surfactants needed to be isolated and their individual, binary and ternary effect studied to understand how they accomplish the permeation and solubilisation of the lipid bilayer.

6.2.1 Surfactant systems

Complex concentrated surfactant systems such as cleaning and washing products, typically contain more than two different surfactants at levels of 35 wt% or above.[13, 28] As previously mentioned in the introduction chapter (section 1.3.1), actual commercial liquid detergent samples, provided by P&G, were used in this research project. Multiple surfactants are used in such formulations as they help reduce the surface tension of water even further compared to when using a single surfactant system.[5, 13, 188] Also, a multiple surfactant system is more efficacious in combatting a range of different stains and dirt, alongside assisting to stabilize the formulation.[5] The properties of the three surfactants used in this study is discussed below.

6.2.1.1 Anionic Surfactants

Anionic surfactants are the most commonly and abundantly used surfactant type in laundry detergents, due to their economical cost of manufacture and detergency abilities.[13, 28] Within anionic surfactants, synthetic linear alkyl benzene sulfonate (LAS) is the most widely used,[13, 187, 188] containing a linear alkyl chain (typically 12 – 14 carbon units) attached to a sulphated aromatic ring at the para position as shown in Fig 6.1a. The ring can be attached to the linear alkyl chain at any position, except the terminal carbons (typically attached at C_2 to C_4 position). The alkly chain lengths and aromatic positions along the chains varies depending on the manufacturing process and therefore, commercial LAS used in detergents consists of a mixture of different homologues and isomers.[5, 187] A molecular mass distribution of the surfactant 'mixture' is used to determine the average molecular mass. LAS is typically present at 20-25 wt%, which can be more than half the total surfactant concentration present in a detergent.

One of the drawbacks of LAS is that it precipitates in hard water due to the divalent cations and is secluded from the solution, causing its detergency to be less effective.[13, 219] This shortcoming is very commonly solved by adding a co-surfactant. Alkyl ethoxy ether sulfate (AES), shown in Fig. 6.1b, is a commonly used co-anionic surfactant in liquid detergents with LAS.[5, 13, 219] AES reduces the surface tension and CMC of LAS only systems and their mixed micelles have a higher hard water tolerance, leading to less precipitation and better detergency.[13, 188, 219] Anionic surfactants are generally effective for the removal of grease and soil, with LAS being very efficient at the removal of greasy food stains, whereas AES is more effective against hydrophilic stains such as grass and body soil.[5, 188, 220]

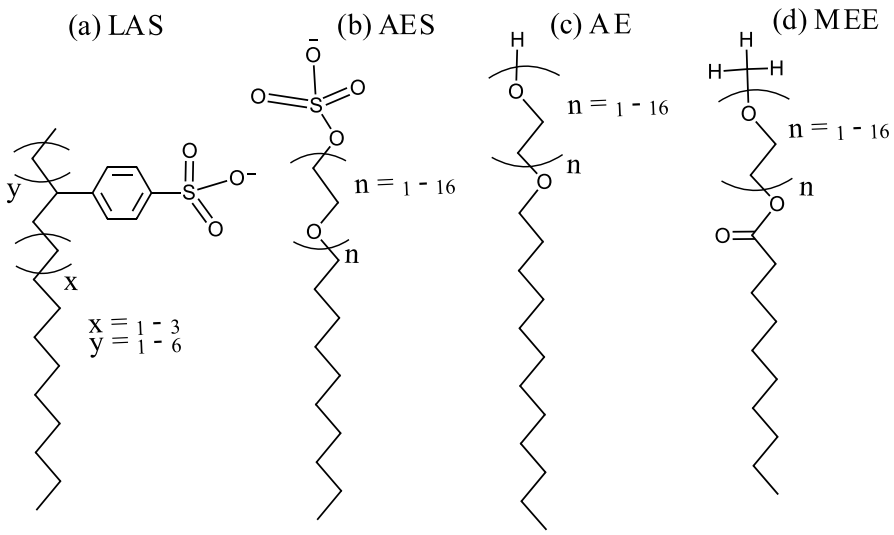


Fig 6.1 – Chemical structure of some common surfactants used in liquid laundry detergents (a) Linear alkylbenzene sulfonate- LAS (b) Alkyl ethoxy ether sulfate- AES (c) Alcohol ethoxylate- AE and (d) Methyl ester ethoxylate- MEE.

6.2.1.2 Non-ionic Surfactants

Non-ionic (NI) surfactants are also used in detergents in combination with anionic surfactants to provide better efficacy and stability.[5, 13] Compared to anionic surfactants, the detergency property of non-ionic surfactants is not affected in hard water, as there is no precipitation caused by the divalent ions.[13, 188] However, NI surfactants generally have higher aquatic toxicity and biodegradability verses anionic

surfactants[221, 222] and therefore are used in much lower concentrations. Alcohol ethoxylate (AE) and Methyl ester ethoxylate (MEE) are two of the most widely used NI surfactant in liquid detergents [13, 188, 221]. AE consist of generally a C10-16 hydrocarbon chain linked to the ethylene oxide unit(s) via ether linkage, whereas MEE contains a methyl terminal and an ester bond linking the ethylene oxide and hydrocarbon chains, as shown in Fig. 6.1c and 6.1d respectively. NI surfactants are only very effective against paraffinic oils, such as waxes in make-ups[5]. It is in the formulation mostly because it improves the physical stability of the formulation and that to at much lower concentrations, as compared to the other surfactants.

As explained in chapter 5, the series of commercial liquid detergent formulations tested previously mainly consist of three surfactants: LAS, AES and AE with a total combined level of 38-41 wt%. Since the main difference between the various formulations were the levels/ ratio of the three surfactants, I created a design of experiments (DOX) system with various combinations of these three surfactants, which will be explained later in this chapter.

6.2.2 Lipid bilayer- surfactant interaction

The interactions between lipid bilayers and surfactants have been studied over a few decades with great interest as both have the ability to form various morphologies due to their amphiphilic properties and as they play a key role in the diversity of the biological membrane. Solubilisation of membranes is commonly carried out to separate and extract its components, e.g. lipids, integral proteins etc, to learn more about the complexities of the biological membrane. The solubilisation mechanisms determined from these studies can be used to develop an understanding of how these surfactants are interacting with corneal epithelial membranes.

6.2.2.1 Triton X-100 mode of solubilisation

Triton X-100 (TX-100) is a widely used non-ionic surfactant for completely solubilising lipids and lipid vesicles, in a range of applications including the

encapsulated fluorescence dye based studies. TX-100 is a very effective surfactant for such applications due to its chemical structure. It contains an aromatic, branched hydrocarbon chain of 1,1,3,3-tetramethylbuyl with a polyethylene oxide chain (average EO units ~9.5) as the polar headgroup as shown in Fig 6.2, which gives TX-100 a large headgroup to tail ratio and a relatively low CMC of 0.2 – 0.4 mM in water.[223-225]. Therefore as TX-100 self assembles, just above its CMC, the micelles are of a relatively small size[226]. This makes TX-100 efficient at permeating and solubilising the lipid membrane.

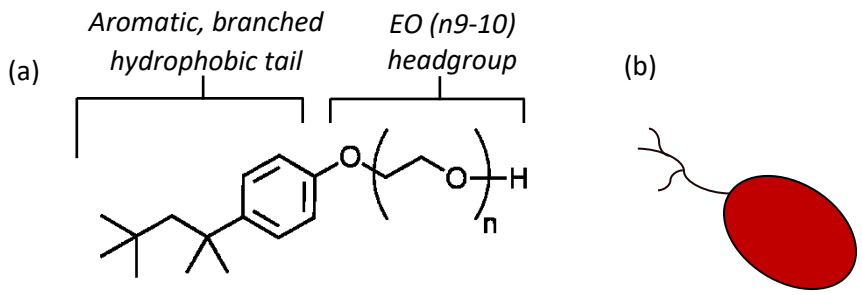


Fig 6.2 – (a) Chemical structure of Triton X-100 illustrating the headgroup and the hydrophobic tail with (b) a schematic of the surfactant monomer.

A widely accepted mechanism of solubilisation has been the three-stage model originally conceptualised in 1975 by Helenius and Simons.[227] The model is illustrated in Fig 6.3, which involves: stage 1- the surfactants are incorporated into the lipid bilayer.[227, 228] As the concentration of surfactant increases, the bilayer becomes saturated with surfactants, which induces curvature in the bilayer (stage 2).[90, 227-229] This is regarded as the onset of solubilisation, where the lipids with the aid of the surfactants are transformed into mixed micelles. Stage 3 is the complete disruption of the lamellar structure and the lipids are dispersed in the solvent as solubilised mixed lipid-surfactant micelles.[90, 227, 229] Within the last decade however, it has been suggested that the solubilisation mechanism is a more intricate, multi-steps process.[90, 228-230] Although the basic three-stage model still applies overall, there are complex sub-stages involved which are highly dependent on the lipid membrane composition as well as on the detergent type and concentration.[228, 231]

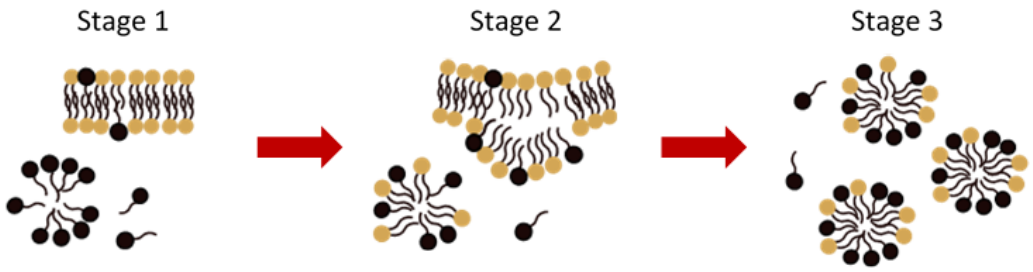


Fig 6.3 – Schematic of the three stage model for lipid membrane solubilisation (Black monomer = surfactant, yellow monomers = lipids). Stage 1- Partitioning of surfactant between lipid bilayers, Stage 2- Dissociation of the lipid bilayer and formation of mixed micelles and Stage 3- Complete solubilisation of lipid membrane. Redrawn from given references.[228, 229]

The intricate multi-step mechanisms occurs during stages 1 and 2, where the mechanism through which the onset of solubilisation transpires can differ.[228] As the surfactant initially gets incorporated in the lipid bilayer, it partitions into the outer monolayer first. Depending on the surfactant type, it can either remain in the bilayer for some time or start to induce curvature within the outer phospholipid monolayer.[228, 229] The curvature in the outer monolayer is suggested to be stimulated by surfactants which have moderate hydrophobicity and/or contain a large head-group to hydrocarbon tail ratio.[230] This leads to shedding of the lipids from the outer monolayer and formation of mixed lipid-surfactant micelles, which causes a mass imbalance between the lipid monolayers. Subsequently, the surfactant equilibrates across to the inner monolayer, to complete the solubilisation process.[229, 230]

For surfactants that have considerable hydrophobicity, dissipative particle dynamic (DPD) simulation techniques have found that they prefer to remain in the lipid bilayer and cause the vesicle / bilayer size to grow initially and then eventually, through altering the curvature of the bilayer, form vesicular intermediate followed by large mixed micelles, completing solubilisation.[230] The efficiency of this solubilisation mechanism has been equated to the ability of the surfactant monomers to flip-flop within the bilayer.[228-230] A rapid trans-bilayer movement of the surfactant from the outer monolayer to the inner monolayer leads to rapid saturation of the whole bilayer, allowing quick solubilisation. If the surfactant cannot effectively flip across to the inner monolayer, the solubilisation process will be delayed.[90, 229] Some studies have

found his flip-flop mechanism to be dependent on the composition of the bilayer and in particular, if it is in a gel or fluid phase. However, there have been conflicting findings on whether the ability of the surfactant to fully saturate the lipid bilayer is phase-dependant, with some studies stating the different solubilisation mechanisms cannot be attributed to the changes in the lipid phases,[232, 233] while some show that lipids in the gel state require less surfactants to fully saturate the bilayer and have a quicker of onset solubilisation[90, 231, 234]. A practical conclusion at this time is that intricate, sub-stages of bilayer solubilisation mechanisms (curvature, flip-flop, micellization) are unique to the type of detergent and lipids bilayer models being used.

6.3 EXPERIMENTAL

An overview of the materials and equipment used was previously described in Chapter 2 and 5. Specific details on the systems used and data analysis carried out to study the interactions between surfactants and lipid bilayers are provided in this section.

6.3.1 Materials and Compositions

The three main surfactants, LAS, AES and NI were industrial grade materials provided by P&G. AES and NI were used as received whereas the LAS was neutralised to pH 7 with monoethanolamine (MEA) before use. Neutralisation was carried out by using 2.45 g of MEA for every 10 g of LAS. The details of all the materials used in preparing the calcein encapsulated liposomes are the same as in chapter 5. All other materials in this section were used as received, since they were analytical grades, including the Triton X-100 purchased from Sigma Aldrich and PBS solution (1X 1.8 mM KH_2PO_4, 10 mM Na_2HPO_4, 137 mM NaCl, and 2.7 mM KCl at pH 7.4,) purchased from GE Healthcare. The solvent mixture used was the same ternary water-glycerol-propylene glycol system described in earlier chapters.

6.3.2 Surface tension

CMC of each surfactant was determined at 20 ±1 °C using the pendant drop method as detailed in chapter 2. The CMCs of the surfactants were determined in two different

solvent mixture, the PBS 1X solution and water-glycerol-propylene glycol standard mixture used throughout the project. Three repeat measurements for each surfactant system was carried out. A 10 mM stock solution of each surfactant system was made and diluted down to the required levels. All solutions were tested at least 2 hours after being prepared and used within 48 hours.

6.3.3 LCRA

The same method was used to prepare the SUVs for the LCRA in this chapter as was in chapter 5, containing the same lipid composition with 50 mM encapsulated calcein within 100 nm SUVs, prepared in PBS 1X solution. Full details of the lipid vesicles preparation, including the calcein encapsulation procedure, are all explained in chapter 2 (section 2.12 – 2.13). The fluorimeter experiments set-up and parameters optimised in the previous chapter were used for this investigation also, using the same Varian Cary Eclipse Fluorescence Spectrophotometer. Details of this experiment set up is provided in chapter 2, section 2.14, and the optimisation of parameters explained in chapter 5, section 5.3.3.2. This was done to keep the LCRA- fluorimeter experiments consistent and comparable. The temperature dependant experiments were carried out using Peltier multicell holder (Varian 100755). The three surfactants were tested individually using a range of concentrations, along with binary and ternary surfactant systems with PBS 1X solution and 5 mM TX-100 being used at the positive and negative controls respectively.

6.3.4 DLS- Particle size analysis

DLS (Zetasizer Nano S Zen 1600 Malvern Instrument, UK) was used to measure the particle size and polydispersity of liposomes-surfactant interaction experiments as detailed in chapter 2 (section 2.7). Real-time measurements were carried out at 25 ±1 °C, with recordings taken before and after the addition of surfactants, over a period of time, until consistent readings were observed. The ratio of liposome mixture to surfactant system was kept the same as the LCRA experiments at 4:1 ratio respectively for all DLS experiments. This was done to track the solubilisation of the SUVs by the surfactants through the changes in particle size distribution and correlate the date with

the LCRA results. Each of the three surfactants were tested individually at different concentrations, along with binary and ternary surfactant systems and TX-100 was used as the negative control. The 100 nm liposomes used for these DLS experiments did not contain calcein and were prepared as per the procedure outlined in chapter 2 (section 2.12). Encapsulated calcein was not required for these experiments as the solubilisation of the lipid bilayer was being assessed through the changes in the SUV diameter.

6.4 RESULTS AND DISCUSSION

All the surface tension and fluorescence data in this chapter was analysed using OriginPro (v.9.0). All the DLS-particle size data was processed through the Zetasizer software (v 7.01) and analysed/plotted using OriginPro (v.9.0).

6.4.1 CMC of various surfactant systems.

The CMCs of the three surfactants were measured to determine whether there is any relationship between the CMC and the level of lipid bilayer permeation caused by the surfactant. As mentioned in the previous chapter, there is a notion that surfactants monomers are more likely to penetrate the lipid membrane compares to micelles and therefore surfactant systems with higher CMCs will contribute to higher eye irritation.[214-216] Although, no clear relationship between the CMCs of detergent samples and the calcein release data or between the CMC and ICE test data could be established, individual surfactants experiments could provide a better clarity on this theory.

The CMC of the each of the three individual surfactants and co-surfactant systems were determined in PBS solution and in the water-glycerol-propylene glycol solvent mixture, using the surface tension pendant drop method. The proven efficiency of the pendant drop method from the earlier chapters to determine the CMC in high organic solvent content and electrolyte solution allowed me to use this technique with confidence for two different solution/solvent mixtures to give reliable and reproducible results.

6.4.1.1 Single surfactant systems

Surface tension measurements were initially carried out on a series of single surfactant systems of LAS, AES and NI, over a range of concentration. The extrapolation method was used to determine the CMC from these measurements, as previously established in earlier chapters.

A vast range of CMC for LAS in deionised and hard water have been reported.[235-237] This is due to the varied distribution of the number of carbon atoms in the alkyl chain of commercial LAS and therefore directly comparing the CMC of LAS of different LAS samples is not possible. Overall, a linear relationship has been established in literature between CMC and the number of carbon atoms.[237] As the number of carbon atoms in alkyl chain increases, the CMC is decreased, therefore LAS with higher average number of carbon atoms in the alkyl chain and higher molecular weight have a lower CMC[235, 237]. The reported range of CMC for various LAS in DI water are: C_{10}LAS - 6.9 mM; C_{11}LAS - 4.0 mM; C_{12}LAS - 1.2 mM; C_{13}LAS - 0.44 mM.[237]

Similarly with AES and the NI surfactants used in this project, increasing the linearity of the alkyl chain decreases the CMC.[238] Since the distribution of the number of carbon atoms in the alkyl chain of these surfactants varies from other commercial samples, their CMCs are not comparable. The average molecular weight of these surfactants are: LAS- 326 g/mol, AES- 405 g/mol and NI- 475 g/mol.

The surface tension measurements for LAS in PBS 1X solution and the ternary solvent mix is shown in Fig. 6.4. The minimum surface tension of LAS in PBS, after the CMC point, was measured to be 30.17 ±0.19 mN/m which is lower compared to 36.15 ±0.16 mN/m obtained in the solvent mix. This is consistent with my previous findings where the minimum surface tension of anionic surfactants in electrolyte solution is lower than in polar organic solvents. AES had a similar minimum surface tension value reached in PBS of ~30 mN/m and was lower than the one measured in the solvent mixture (~33.42 mN/m) as shown Fig.6.5. Also, as expected the point of minimum surface tension extrapolated for both these surfactants in PBS is at lower concentration compared to the concentration in the ternary solvent mixture.

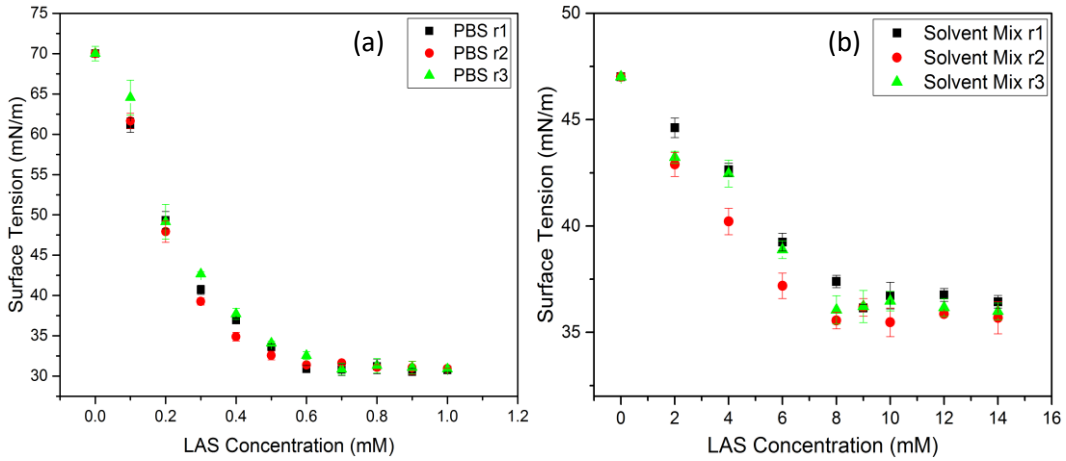


Fig 6.4 – Surface tension measurements of LAS in (a) PBS 1X solution and (b) ternary organic solvent mixture, for CMC determinations.

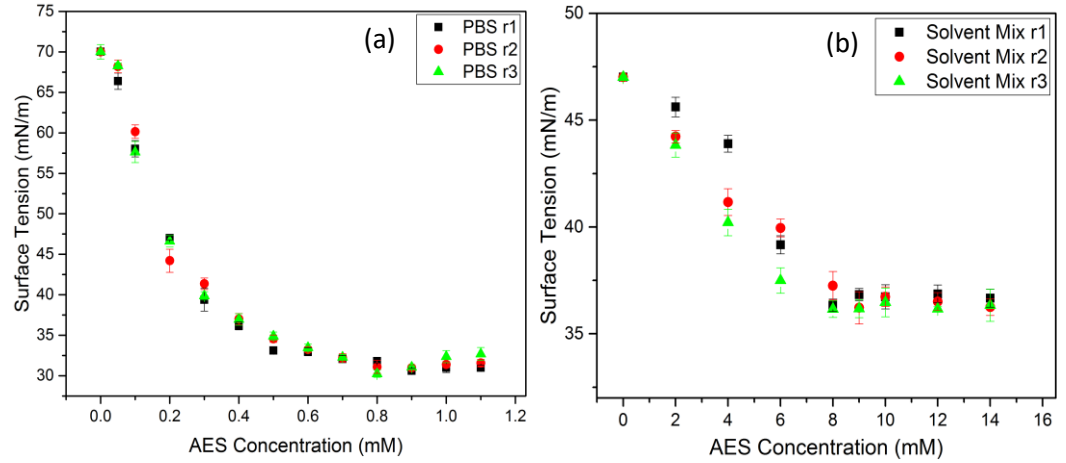


Fig 6.5 – Surface tension measurements of AES in (a) PBS 1X solution and (b) ternary organic solvent mixture, for CMC determinations.

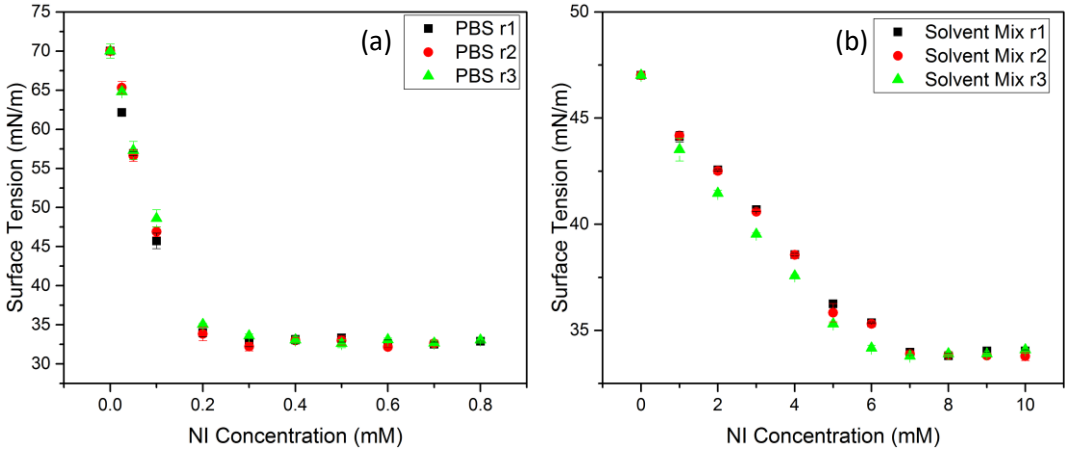


Fig 6.6 – Surface tension measurements of NI in (a) PBS 1X solution and (b) ternary organic solvent mixture, for CMC determinations.

The minimum surface tension for NI in PBS was slightly higher (~32.2 mN/m) in comparison with the two anionic surfactants as shown in Fig. 6.6. For NI, the surface tension value after the micellization concentration in the solvent mix is slightly higher also. The CMCs determined for NI show a significant difference between the PBS and solvent mix mediums. The CMC of a NI, containing C12/EO7, in DI water is reported to be between 0.17-0.19 mM.[239] As shown in Fig.6.7, the average CMC of the commercial NI used by me, was 0.26 mM in PBS, similar to the CMC range reported above. This reconfirms that the presence of electrolytes in water does not affect the CMC of non-ionic surfactants as it does with anionic surfactants. The CMC of NI in the ternary solvent mix was measured to be much higher at 7.17 ±0.28 mM, showing that the polar organic solvent also have a significant impact on the micellization of non-ionic surfactants. Fig 6.7 also presents the CMCs of the two anionic surfactants in both PBS and the solvent mix for comparison. Both LAS and AES have a similar CMC in both PBS and solvent mix at 0.7-0.8 mM and 8.0-8.2 mM respectively, whereas NI has a lower CMC in comparison as expected.

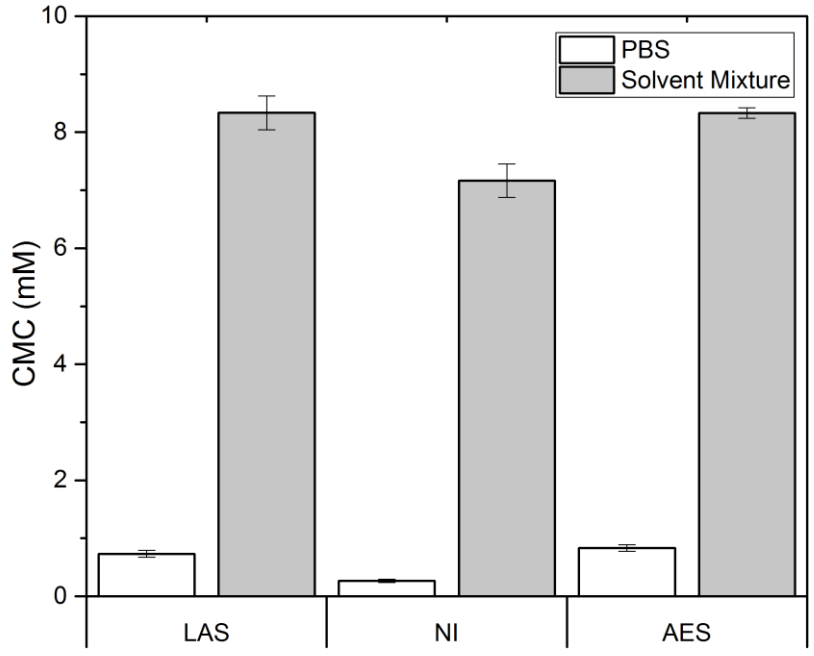


Fig 6.7 – Comparison of the CMCs determined from surface tension for LAS, AES and NI in PBS 1X solution (white) and ternary organic solvent mixture (grey).

6.4.1.2 Co-surfactants systems

Co-surfactants systems of LAS with both AES and NI were tested as in a 1:1 ratio as binary mixtures and also all three together in a ternary surfactant system in 1:1:1 ratio, both in PBS 1X solution only. Fig 6.8 shows the CMC data for the two binary systems and the ternary system. As expected, adding a co-surfactant to the system decreases the surface tension at the CMC, due to the attractive interaction and synergetic effect between the surfactants. The bulkier hydrophobic regions of the co-surfactants allow adsorption of at the surface more spontaneously, driving the Gibbs free energy of absorption (ΔG^{0}_{abs}), of the surfactants at the air-aqueous interface, to become more negative and hence becoming more surface active.[240, 241] Binary mixture of LAS and AES lowered the minimum surface tension from 30.17 ±0.19 mN/m (LAS only) to 29.88 mN/m and to 29.4 mN/m for the LAS-NI system. Adding co-surfactants also leads to an increase in the packing parameter for the micelles which changes the curvature and hence the phase behaviour of the surfactant system.[240] These changes also reduce the Kraft point of the system, increasing the efficiency of the mixed surfactant to form micro-emulsions and remove dirt/oil at lower temperatures.[241, 242]

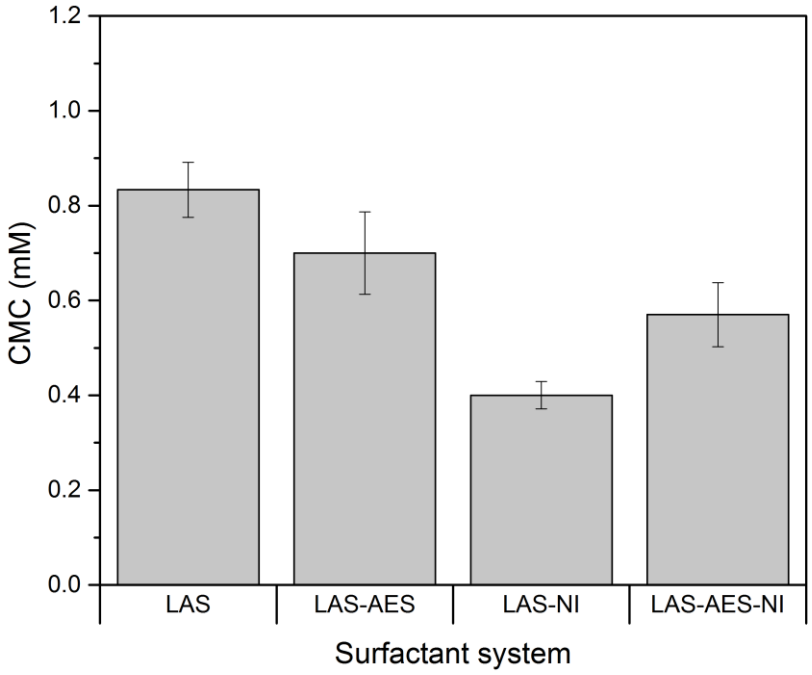


Fig 6.8 – Comparison of CMCs determined from surface tension measurements for LAS co-surfactant systems; LAS-AES, LAS-NI and LAS-AES-NI, in PBS 1X solution.

However, there was no significant change seen in the actual CMC with the co-surfactants, for my surfactant system. The CMC of LAS, AES and NI only in PBS is considerably low to begin with (0.83, 0.73 and 0.27 mM respectively) and is changed to 0.70 mM for LAS-AES system and 0.40 mM for LAS-NI system. The ternary mixture of all three surfactants at equal ratios gave a minimum surface tension of 31.2 mN/m and a CMC of 0.57 ± 0.07 mM. The minimum surface tension of the ternary surfactant mix is comparable to the minimum surface tension for the individual systems.

6.4.2 LCRA

The LCRA analysis was carried out using the instrument and parameters optimised previously for the detergent experiments. One of the differences for these set of experiments was the 'positive' control solution used, which was PBS 1X instead of the ternary organic solvent mixture. The negative control, 5 mM triton X-100 in DI water remained the same. The same % calcein release equation (5.2) described earlier in this thesis was used to compare the amount of calcein released and determine the level of lipid bilayer permeation. The initial fluorescence intensity (F_0) and the total fluorescence intensity (F_{total}) values obtained from these experiments are used in equation 5.2, for each time interval point. Similar to the previous analysis, a time-response curve at each concentration was plotted, from which a concentration-response curve at a specific time was derived for % calceion release values as well as for the rate of release data, with 3 repeats per each concentration.

A Design of Experiment (DOX) was carried out to cover a range of surfactant compositions to allow a methodical analysis of the single, binary and ternary surfactant systems and their impact on liposome solubilisation. The DOX, shown in Fig.6.9 was particularly useful for systemically analysing the ternary surfactant mix at various ratios. This allows to track the impact of each surfactant on the lipid bilayer permeation.

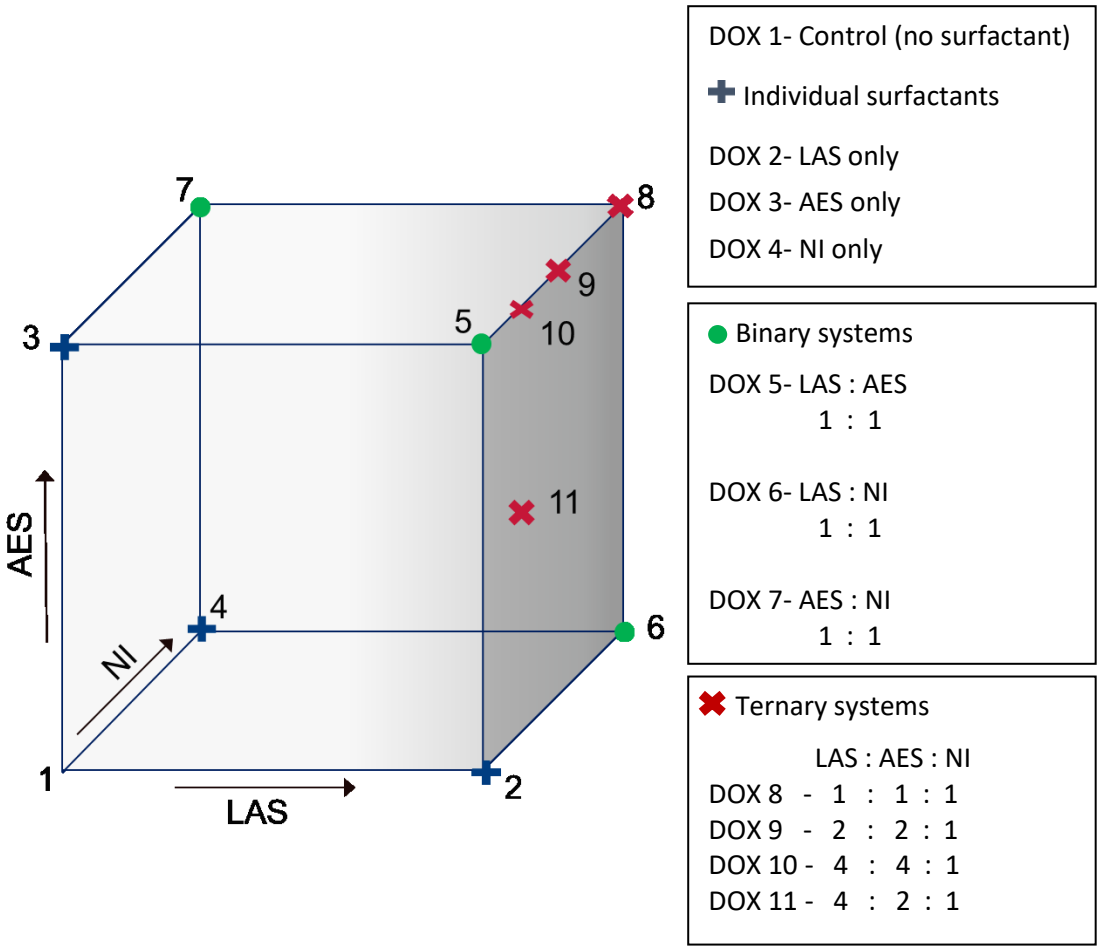


Fig 6.9 – Design of Experiment (DOX) used for methodical analysis of various surfactant mixtures, annotated with corresponding surfactant ratios.

6.4.2.1 Individual surfactant systems

A series of initial trial runs were carried out for the LCRA, for each surfactant individually to determine the overall time it takes to reach maximum fluorescence intensity. Fig 6.10 provides the trials carried out at one of the concentrations (6.4 mM) for all the three surfactants including the controls. It can be clearly seen that the NI surfactant reacts every similarly to the negative control TX-100 and give a complete release of calcein at 6.4 mM within 30 seconds. The LAS on the other end requires much longer, ~55 minutes to plateau out and reach a maximum calcein release of 53%. At this concentration, LAS does not completely release all the calcein, hence not solubilising all the SUVs. The other anionic surfactant, AES has a higher rate of

reaction compared to LAS and takes ~25 minutes to reach a maximum calcein release of 83.4% at 6.4 mM concentration. The addition of positive control, PBS 1X to the liposome-encapsulated calcein system did not give significant changes to the fluorescence intensity readings when monitored over 15 minutes. Based on these initial trials, a separate time range was set for each surfactant. For all LAS only systems, across all concentrations, the time range was up to 60 minutes, whereas for AES and NI only systems the range was 30 and 15 minutes respectively.

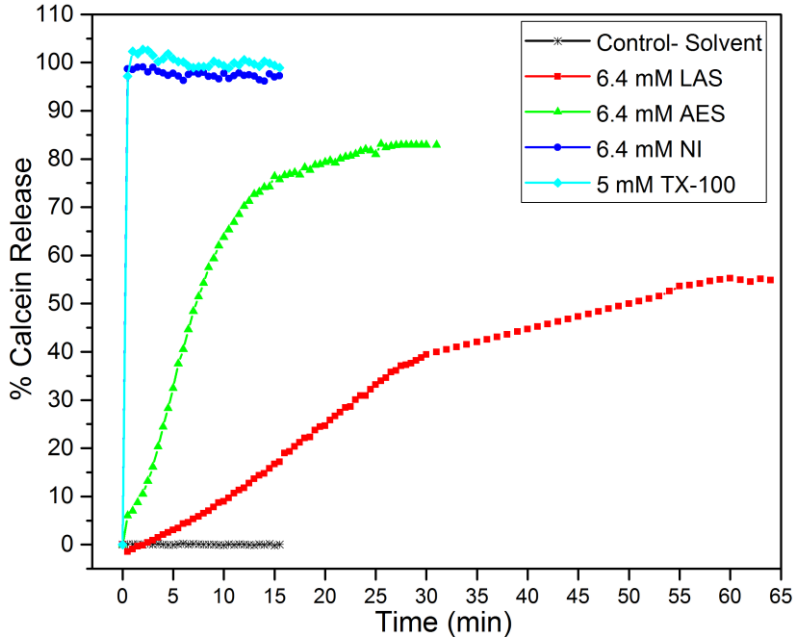


Fig 6.10 – Time-response of % calcein release for LAS, AES and NI at 6.4 mM, with controls 5 mM TX-100 and PBS 1X.

For the LAS concentration-response curve, the maximum % release at 60 minutes was used and initial rate of reaction was determined from the first 15-20 minutes of the experiment, an example of which is illustrated in Fig.6.11. The time response curves for LAS across all the concentration, including the three repeats is provided in appendix Fig 8.4. The time response was quicker for AES in comparison, across all concentration and the max % release was also higher. Therefore the max % release was taken at 30 minutes and the initial rate of reaction over the first 5 minutes. For NI, even at very low concentration (0.5 mM), the time-response was swift and a maximum was reached within 3-5 minutes across all concentration, so the max % release was

taken at 15 minutes and initial rate of reaction over 0.5-1 minutes. The complete set of results for AES and NI time-response is given the appendix, Fig 8.5 and Fig 8.6 respectively. The max % release and the initial rate of release was extracted from those time-response curves, using a linear fit for each concentration. All that data was then used for the concentration response plots.

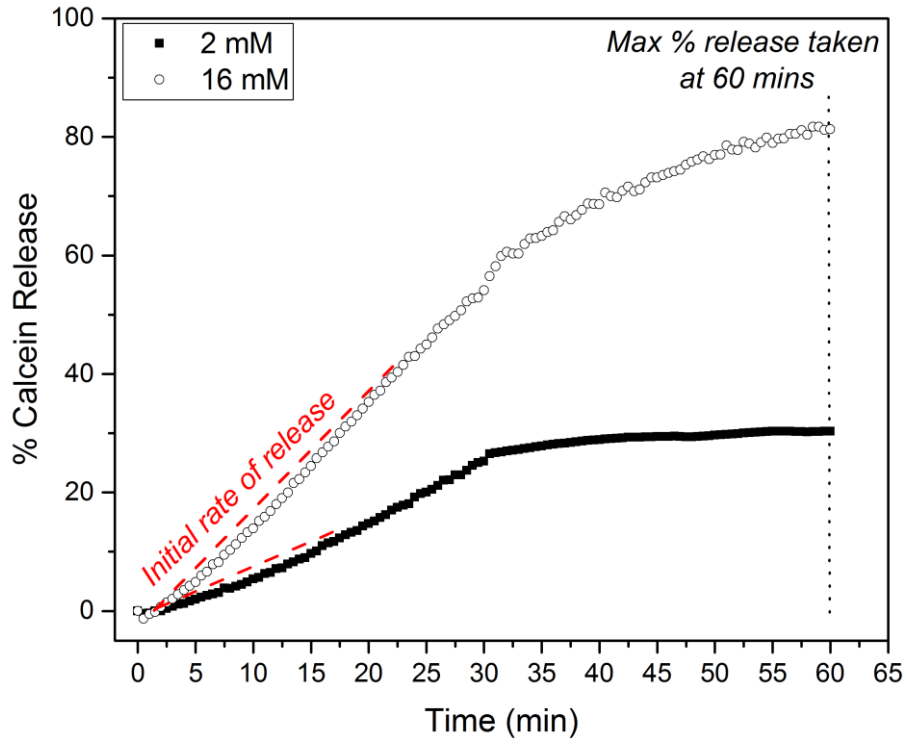


Fig 6.11 – Time-response of % calcein release for LAS at two different concentrations, illustrating the max calcein release and initial rate of reaction derived.

Fig 6.12 shows the max % release - concentration response for all three surfactants. LAS gave a consistently lower max % calcein release in comparison to the other two surfactants and reached a plateau after 8 mM. Even at high LAS concentration (above 16 mM), the max % calcein release only reached ~83 % and therefore LAS by itself does not completely solubilise all the SUVs. AES gave a similar concentration response but reached a plateau at a lower concentration of 4 – 5 mM and reached a slightly higher max % release levels (~90%), suggesting it is more efficient than LAS at permeating the lipid bilayer. The NI, as expected was very effective at solubilising these liposomes and achieved near 100 % calcein release at very low concentrations

(below 0.5 mM), as shown in Fig 6.12. The rate of release – concentration response further confirms this trend as shown in Fig 6.13. Both the anionic surfactants gave a very low rate of release across the whole concentration range. LAS and AES gave their highest rate of release, of 2.1 and 6.9 % /min respectively. Fig 6.13 b shows that the rate of release plateaued after 10 mM for both surfactants, showing that increasing the concentration further does not increase the rate or the level of liposome solubilisation. In contrast, the rate of release for NI was extremely fast, ~190 %/min, at very low concentrations of 1.0 mM, as most of the SUVs are solubilised by NI within 30 seconds of addition.

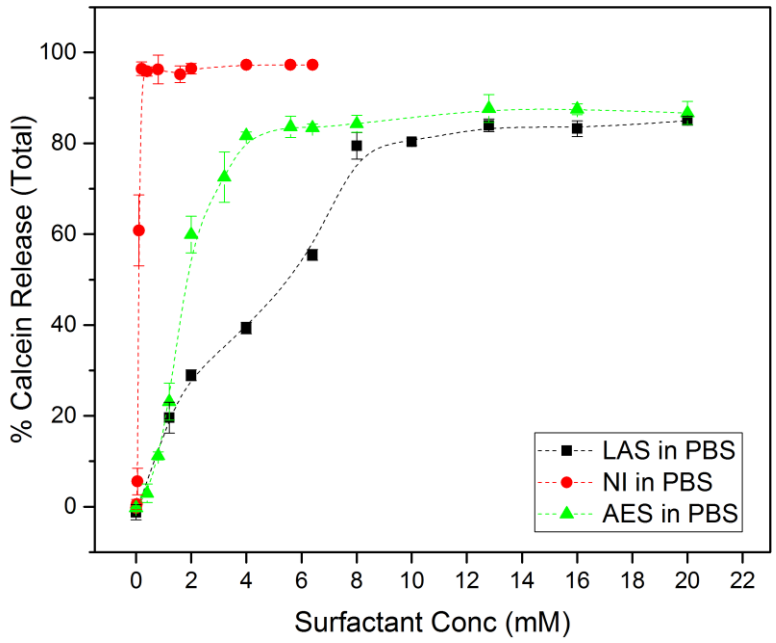


Fig 6.12 – Concentration-response for max % calcein release for LAS, AES and NI individual surfactant systems in PBS 1X.

It can be established from these experiments that non-ionic surfactant is the most potent at permeating through the lipid bilayer and solubilising the liposome completely, compared to the two anionic surfactants. Further experiments in the DOX, with binary surfactant systems were carried out next to determine how the efficiency of the surfactant system to solubilise the liposomes is altered when present as co-surfactants.

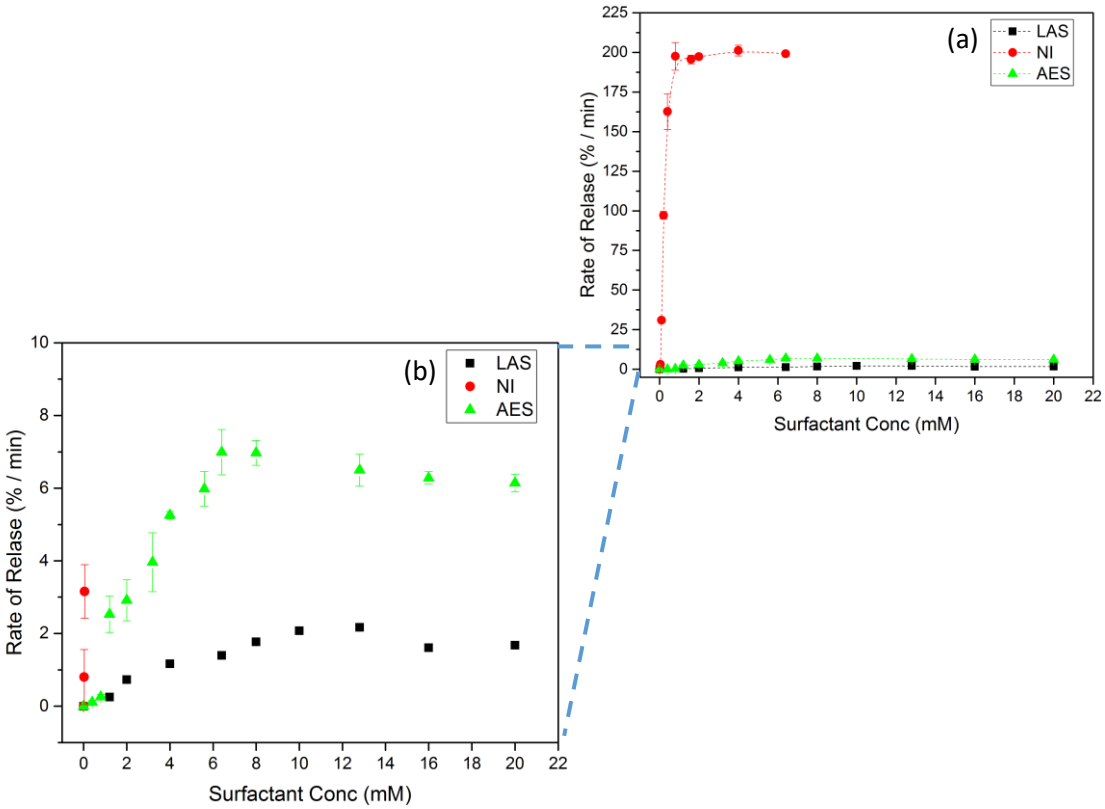


Fig 6.13 – Concentration-response for rate of calcein release for (a) LAS, AES and NI individual surfactant systems in PBS 1X. (b) Zoomed in axis scale, showing the rate of release curve for LAS and AES.

6.4.2.1.1 Temperature effect on liposome permeation

To determine the effect of temperature on liposome solubilisation, LCRA was carried out over a range of temperatures using the three surfactants. The purpose of this temperature response experiment was to confirm whether the state of the lipids in these liposomes is not altered significantly to substantially affect the interactions between the surfactant and the lipid bilayer. Control experiments were carried out to check the permeability of these liposomes at various temperatures, by adding PBS 1X solutions to the SUV mixture. The experiments were ran for 15 minutes for temperatures ranging from 15 to 40 °C. There was no significant change in the fluorescence intensity as the temperature was increased and the % calcein release remained ~0 %.

LAS and AES were both tested at10 mM concentrations and NI at 2 mM. For LAS and AES experiments, the maximum % calcein release increased overall as the temperature was increased, as shown in Fig 6.14 (a), however it can be argued if this change is significant. The % release for 10 mM LAS increases from ~79 % at 15 °C to 84 % at 40 °C, showing a different of 5 % over 20 °C. These results show that even at higher temperatures, LAS does not fully solubilise all the liposomes. Similar for AES, the different in % release from 15 °C to 40 °C was 4 %. For NI, there was no change over temperature and its % release was near 100% even at low temperatures of 15 °C. The effect of temperature on the rate of release is given in Fig 6.14 (b) showing minor increases from 1.3 to 2.2 % / min and from 5.1 to 6.7 % / min for both LAS and AES respectively. Again, these increases in the rate of release seems limited to be attributed to the potential changes in the lipid bilayer phases, particularly at these temperature ranges. These slight changes in the rate of solubilisation over temperature can be associated with the weakening of the hydrogen-bonded network and an increase in the Brownian motion.[243]

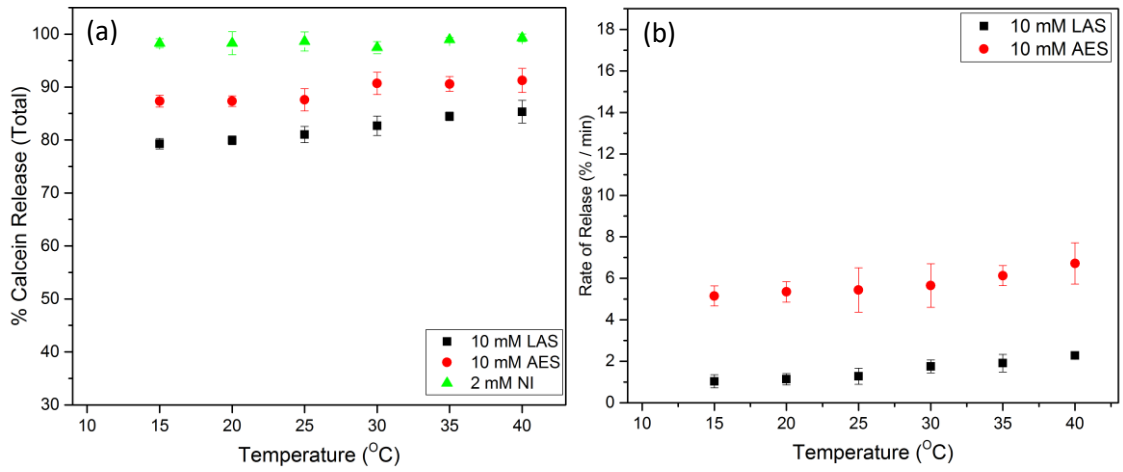


Fig 6.14 – Temperature-response of all three individual surfactants for (a) % calcein release and (b) rate of release.

SAXs and WAXs analysis were carried out by Liu, J (2018), a colleague within the Chemical Biology research group at Imperial College London, using the same liposomes composition, to determine the state of the lipid bilayer over a range of temperatures. The 30 to 40 °C temperature range were of particular interest as

temperature of central cornea is reported to be between 32-35 °C.[244] She found that between 20 to 35 °C the lamellar phase is in the gel state. Increasing the temperature further, between 35 to 40 °C, the gel and fluid states seems to co-exist, with the lipids becoming increasingly fluid beyond 40 °C. For a similar lipid bilayer composition, it has also been reported that below 45 °C, the lipid bilayers are in the gel or crystalline states [231] Therefore, the LCRA results gathered from room temperature experiment are comparable to interactions at 30-35 °C.

6.4.2.2 Binary systems

Binary systems with 1:1 ratio of LAS-AES (DOX-5) and LAS-NI (DOX-6) were tested to determine whether AES and NI help the LAS solubilise the liposomes completely and at a higher rate or the permeation of LAS is still limited. Again, a range of concentrations were tested for both these binary systems. At a total surfactant concentration of 1.6 mM, the time taken for the LAS-AES system to reach a consistent maximum fluorescence intensity and hence % calcein release was 15 minutes as shown in Fig. 6.15, whereas the LAS-NI systems was extremely quick to reach maximum intensity, within 1 minute at the same total concentration. Therefore, these experiments were ran for a duration of 20 minutes.

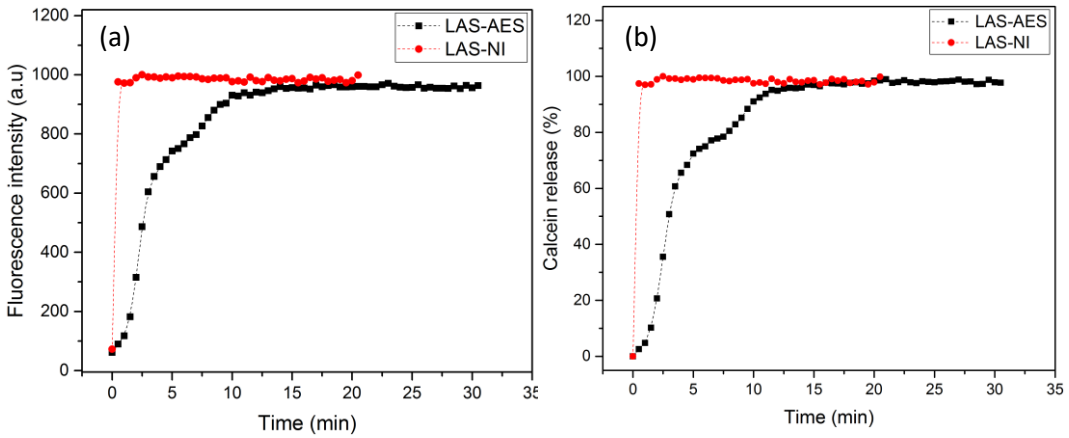


Fig 6.15 – Time-response for binary system LAS-AES and LAS-NI at 1.6 mM total surfactant concentration against (a) fluorescence intensity and (b) % calcein release.

Concentration response of both the binary systems, for max % calcein release and rate of release are provided in Fig 6.16 (a) and (b) respectively. Included also is the LAS only data for direct comparison. The surfactant concentration across the x-axis is the total (combined) surfactant concentration.

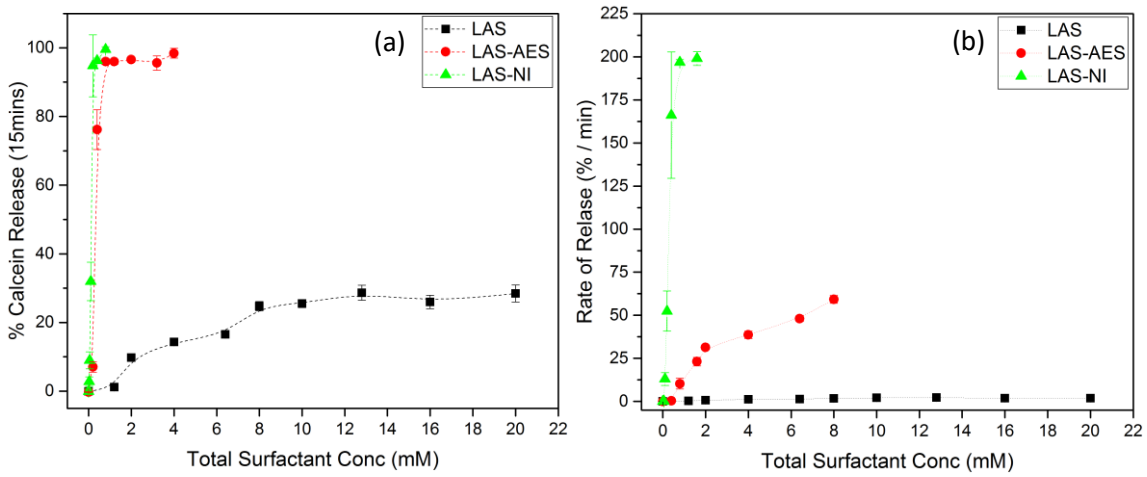


Fig 6.16 –LAS binary systems concentration-response for (a) % calcein release and (b) rate of release, with AES and NI in PBS 1X.

The system with two different anionic surfactants, the max % calcein release is reached at 1.0 mM, which is lower than the LAS only system. The rate of reaction for this co-surfactant system is slighter higher compared to both LAS and AES only systems. For the LAS-AES co-surfactant system, the rate of release is increased to 31.29 % / min from 2.07 % / min from a LAS only system, at 2 mM total surfactant concentration.

The other binary system with an anionic and a non-ionic surfactant, showed a very similar response as the NI only, showing complete solubilisation of liposomes at very low concentrations of 0.2 mM, with a rate of calcein release at ~ 180 % / min. These results clearly show that adding a co-surfactant does increase the solubilisation of the liposomes. As co-surfactants lower the interfacial tension of the system, the fluidity of the interface and the mobility of the hydrocarbon tails is increased,[245] which allows for better permeation of the lipid bilayer.

6.4.2.3 Ternary systems

Four sets of ternary systems were tested with various ratios of the three surfactants as illustrated in the DOX design (Fig. 6.9). The first ternary mixture is the 1:1:1 ratio of all the three surfactants (DOX-8), with subsequent mixtures containing a reduced ratio of NI (DOX 9 & 10) and AES (DOX-11). Since NI is the most potent at solubilising the liposomes, these experiments were carried out to determine the impact of reducing the ratio of NI in the ternary surfactant systems. A range of total surfactant concentrations were tested for these systems. As expected, these ternary systems were quicker at solubilising the SUVs and releasing the calcein compared to the binary systems. The maximum % release was determined from the fluorescence intensity data at 15 minutes for all mixtures and the initial rate of release calculated from the first 5 minutes. The concentration response-max % release for all the ternary systems is shown in Fig 6.17.

The DOX-8 mixture with equal levels of all three surfactants gave a similar response to the LAS-NI binary system, with rapid and complete release of calcein at low surfactant concentrations. At the total surfactant concentration of 0.60 mM (0.20 mM concentration of each), a near 100% calcein was release, hence all the SUVs were completely solubilised. Reducing the ratio of NI to LAS and AES by half (DOX-9), the maximum % release reached is ~97 % at a higher total concentration of 2.0 mM. At this point the NI concentration in this mixture is 0.40 mM, whereas LAS and AES are at 0.80 mM each. Upon further reduction of the NI ratio in the system (DOX-10), the maximum % release is not significantly affected and is similar at ~95 %. Also similar is the total surfactant concentration (~2.0 mM) at which a plateau is reached. At this point the concentration of NI is ~0.22 mM and the two anionic surfactants are at 0.89 mM. Even when the ratio of AES is reduced in these ternary systems (DOX-11), the maximum % release stays at a similar level of ~ 95%, however the total concentration at which it reached a plateau is lower, at ~1.75 mM. Here the ternary system consists of ~0.25 mM NI, ~0.50 mM AES and ~1.0 mM LAS. Therefore, from the concentration-response curves, no significant difference can be seen in the total solubilisation levels of the SUVs from lowering the NI ratio, however, some noticeable differences can be observed in the total surfactant levels at which the maximum

solubilisation is achieved. It is apparent from this set of data that for complete solubilisation of these liposomes using any ternary system, NI concentration as low as 0.20 mM is only required.

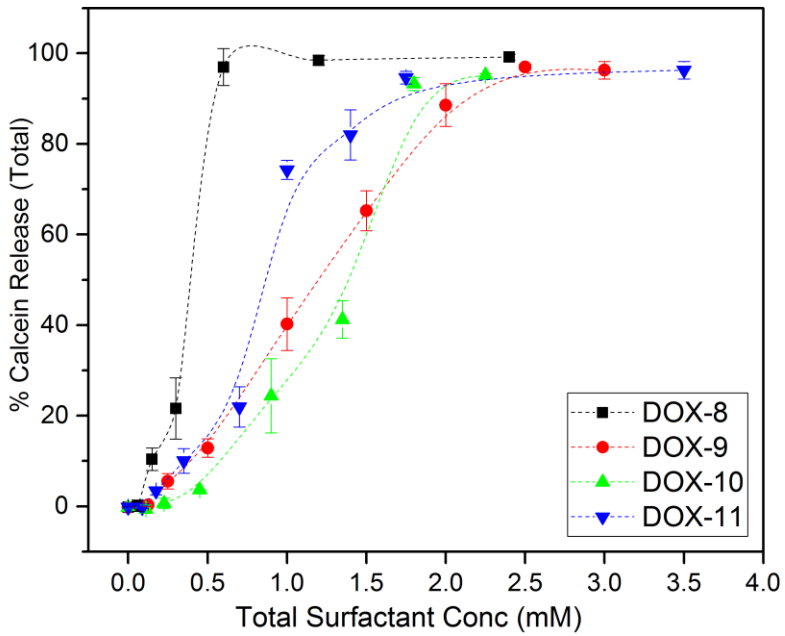


Fig 6.17 – Concentration-response for max % calcein release for all four ternary surfactant systems in PBS 1X.

More significant differences for these ternary systems were noticed from the rate of release analysis provided in Fig 6.18 for all ternary systems, derived from the time-responses. It can be clearly observed that the DOX-8 system gives a very high rate of release, ~136 % /min at low total surfactant concentration of 0.60 mM and then reaching a maximum rate of 188 % /min at 2.0 mM surfactant concentration. As the ratio of NI is reduced, the rate of release also decreases. At 2.0 mM total surfactant concentration, the maximum rates of release were reduced to ~88 % /min for DOX-9 and to ~68 %/mins for DOX-10. The ternary system where the ratio of AES is reduced (DOX-11), the rate of release is increased back to ~88 %/min.

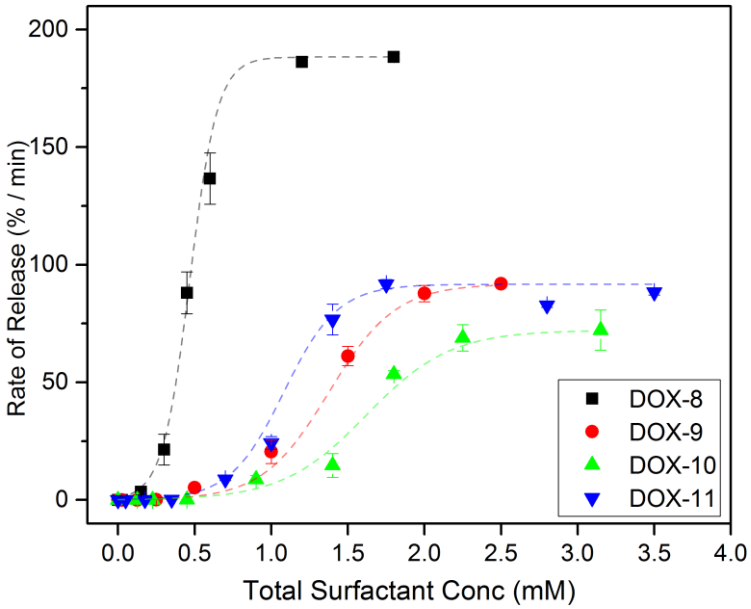


Fig 6.18 – Concentration-response for rate of release for all four ternary surfactant systems in PBS 1X.

These analyses provide two key learnings, 1) the NI surfactant is driving the rapid solubilisation of these SUVs, as the rate of release/ solubilisation is proportional to the ratio of NI surfactant present in the ternary system and 2) the AES surfactant, present at a higher ratio, is 'hindering' the rate of solubilisation in the ternary mixtures. This is further supported when comparing these results with those of the binary and individual surfactant systems, as it can be observed that increasing the concentration of the two anionic surfactants in a system does not increase the rate of release. Fig 6.19 shows a comparison between the maximum % calcein release between the LAS only, LAS binary and ternary (DOX-8) systems, at a total surfactant concentration of 0.4 mM. These comparison summaries the learnings mentioned above and show that LAS and AES are affecting the ability of the NI to rapidly and completely solubilise all the liposomes.

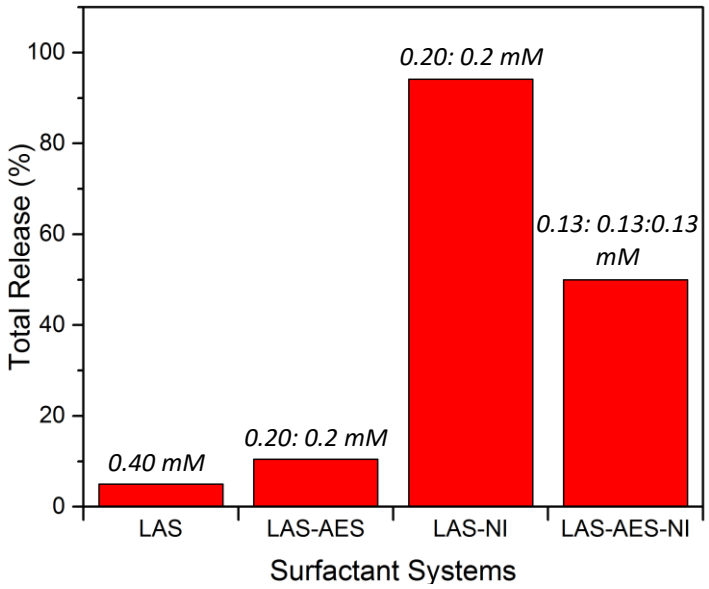


Fig 6.19 – Total % calcein release comparison between LAS only, LAS binary and ternary surfactant systems at 0.40 mM total surfactant concentration. Annotated with the individual concentrations of each surfactant.

6.4.3 DLS-particle size analysis

Optimization and control experiments were carried out to determine the measuring parameters for this real time particle size tracking. The main parameters which required optimising were; duration of a scan and number of scans for averaging. It had to be ensured that the duration and number of scans are sufficient to allow for a reliable average particle size measurement, but also shortest as possible to capture the changing particle size at the intended time. Since each surfactant has a different rate of reaction/solubilisation, the duration and number of scans were optimised for each surfactant system as detailed in the methods section 6.3.4. The control experiments were carried out using 100 nm liposomes (made in PBS 1X) and 5 mM TX-100 as the surfactant. The results from the control experiments are provide in Fig 6.20.

For the initial measurement / baseline, the 100 nm SUVs were measured first, before the addition of TX-100, giving an average particle size distribution of 102.2 ± 23.3 nm (1 S.D). After the addition of TX-100, the measurements were carried out at every 1 minute interval, over 10 minutes. As shown in Fig. 6.18, after 1 min of addition, the

average particle size of the SUVs is reduced from 102.2 to 9.7 nm and after 4 minutes increases slightly to 10.8 ±4.9 nm where it stabilises for full duration of the measurement. Also shown on the graph is the average particle size distribution of 5 mM TX-100 in PBS 1X, measured separately, give a micelles diameter of 5.8 ±2.3 nm. This set of control experiment proves that 5 mM TX-100 solubilises these 100 nm liposomes instantly, forming mixed surfactant-lipid micelles with an averaging size of 10-11 nm. This experiment also shows that there are no significant number of TX-100 only micelles present after being added to the SUVs, suggesting the all the surfactant is mixed with the lipids.

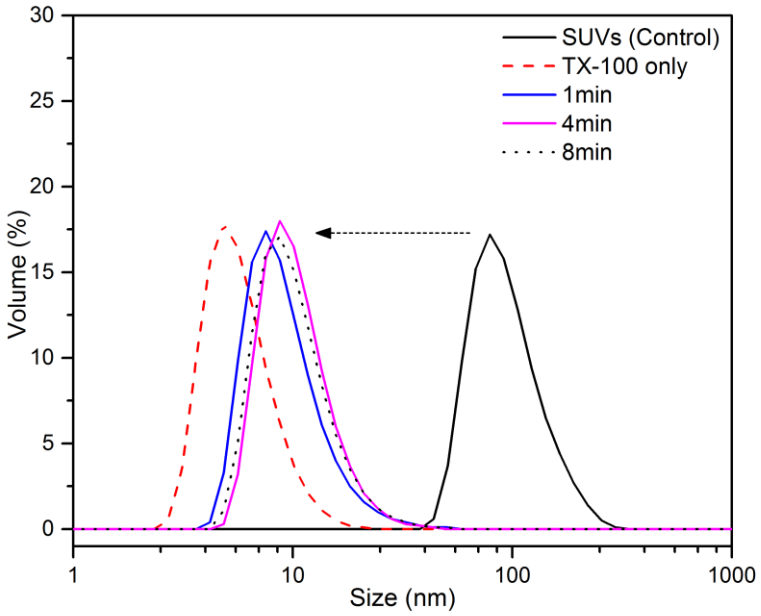


Fig 6.20 – Particle size distribution by volume for 100 nm SUVs, before and after the addition of TX-100 (negative control) at 1, 4 and 8 minutes. Also showing the particle (micelle) size distribution of 5 mM TX-100 solution in PBS 1X (red dash line).

6.4.3.1 Individual surfactants

A series of measurements was first carried out for each individual surfactants at concentrations above their CMC levels, to determine their micellar sizes. Fig 6.21

shows the average particle of the three surfactants, from three repeats, at 5 mM concentration in PBS 1X. The micellar size of LAS was slightly larger at 12.8 ±2.9 nm, compared to the AES and NI micellar size of 8.8 ±2.4 nm and 9.98 ±1.6 nm respectively. Since the molecular mass distribution of these surfactants is unique, as they are industrial surfactants, no direct comparison of the micelle size comparison can be made. For the LAS measurements, the large variations in size distribution from the repeats can be seen, which is reflective of the large variations in the chain lengths and hence variations in the molecular mass distribution of the industrial LAS sample being used. The variation in the particle size distribution of AES and NI is much less in comparison, as their molecular mass distribution is much narrower.

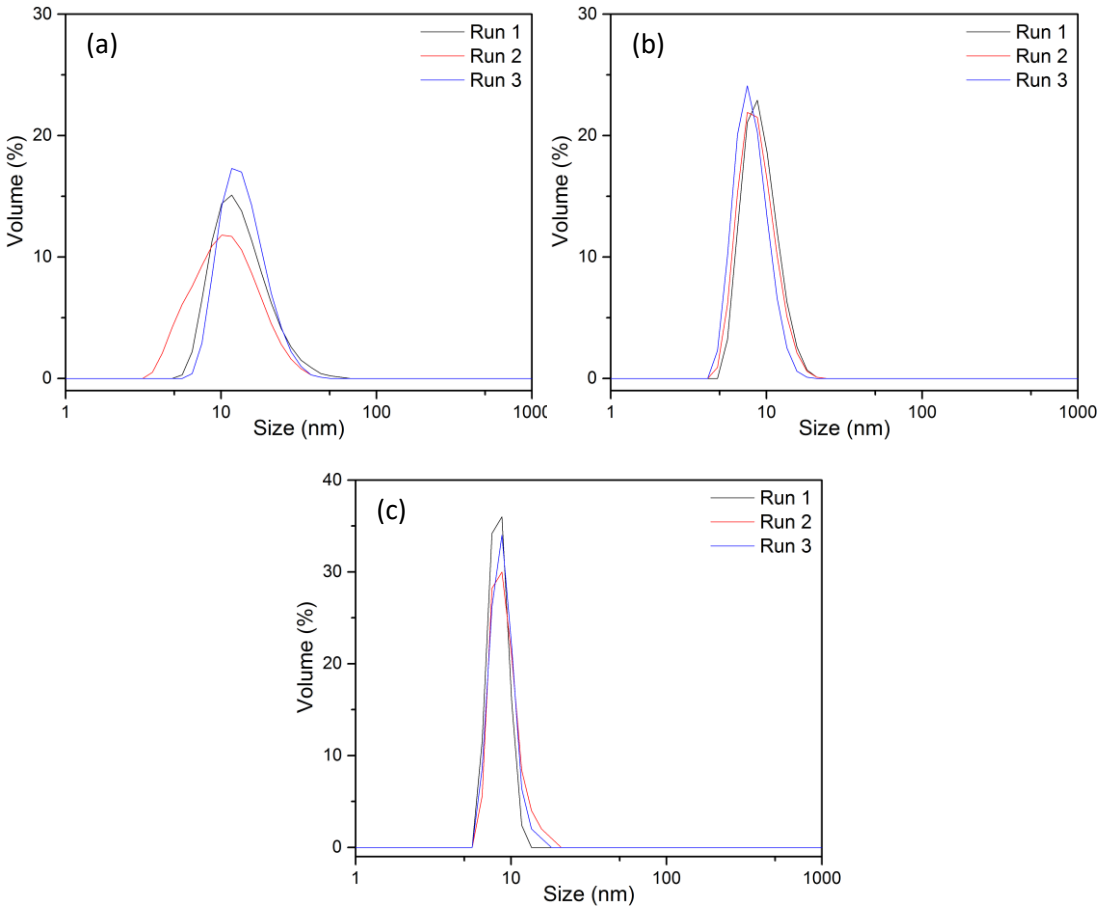


Fig 6.21 – Particle size distribution by volume for (a) LAS (b) AES and (c) NI, at 5 mM concentration in PBS 1X, showing three repeats.

The NI surfactant was first tested with the liposomes at 5 mM concentration and then at 2 mM, and as expected, both gave a very similar result to the 5mM TX-100 control. At both concentrations, the particles size distribution of the SUVs was reduced within 1 minute of addition, re-confirming the potency of the NI at permeating the lipid bilayer and completely solubilising the liposomes. Even at low levels of 2 mM, the NI surfactant very efficiently solubilised the SUVs to produce mixed NI-lipid micelles with averaging particle size of 16.8 ±5.7 nm at 1 minute as shown in Fig 6.22. Also illustrated in Fig.6.21 are the schematics of the SUVs and the mixed surfactant-lipid micelles above their corresponding distribution curves. The average micellar size of 2 mM NI in PBS 1X solution, measured separately, was 8.3 ±1.2 nm. This indicates that NI micelles quickly dismantle themselves after being added to the liposomes to permeate the bilayer and then all the NI monomers are involved in forming mixed micelles with the lipids to completely reduce the surface area as much as possible, resulting in an average particle size of ~17 nm.

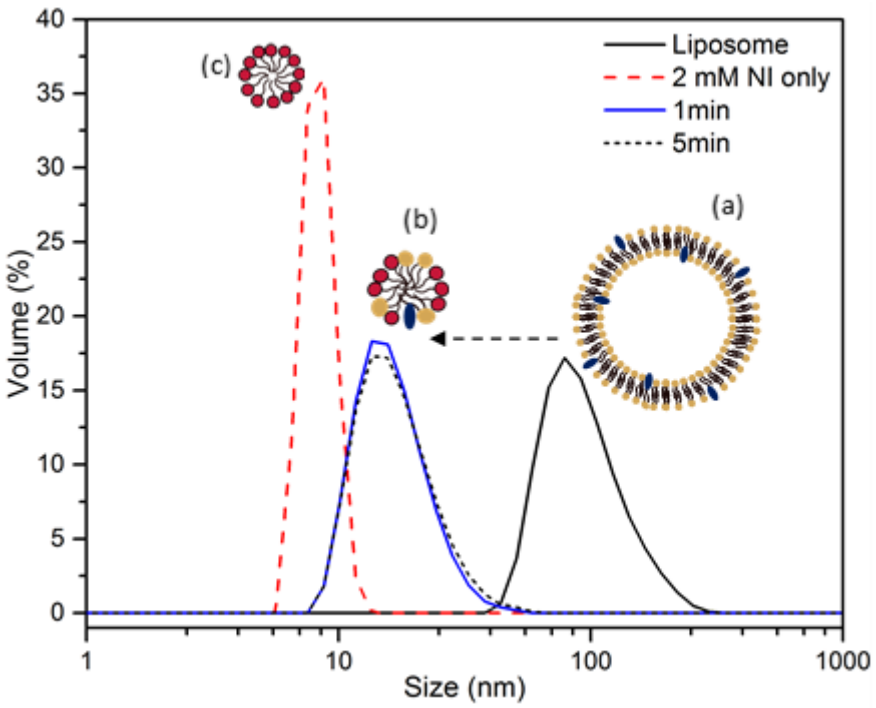


Fig 6.22 – Particle size distribution by volume for 100 nm SUVs, before and after the addition of 2 mM NI at 1 and 5 minutes. The particle (micelle) size distribution of 2 mM NI solution in PBS 1X (red dash line) is also shown. Illustrated with schematics of (a) un-solubilised liposomes, (b) solubilised liposomes / mixed NI-lipids micelles and (c) NI only micelles.

As established from the LCRA, the AES reacts much slowly with the SUVS compared to the NI, therefore the DLS experiments with AES were carried out for longer durations of over 35 minutes. Fig 6.23 shows the real-time particle size distributions of the lipid vesicles over time, after the addition of 5 mM AES. It can be seen that not only the rate of reaction/solubilisation is slower, but the shape and size of the distribution curves are also different compared to the NI experiments.

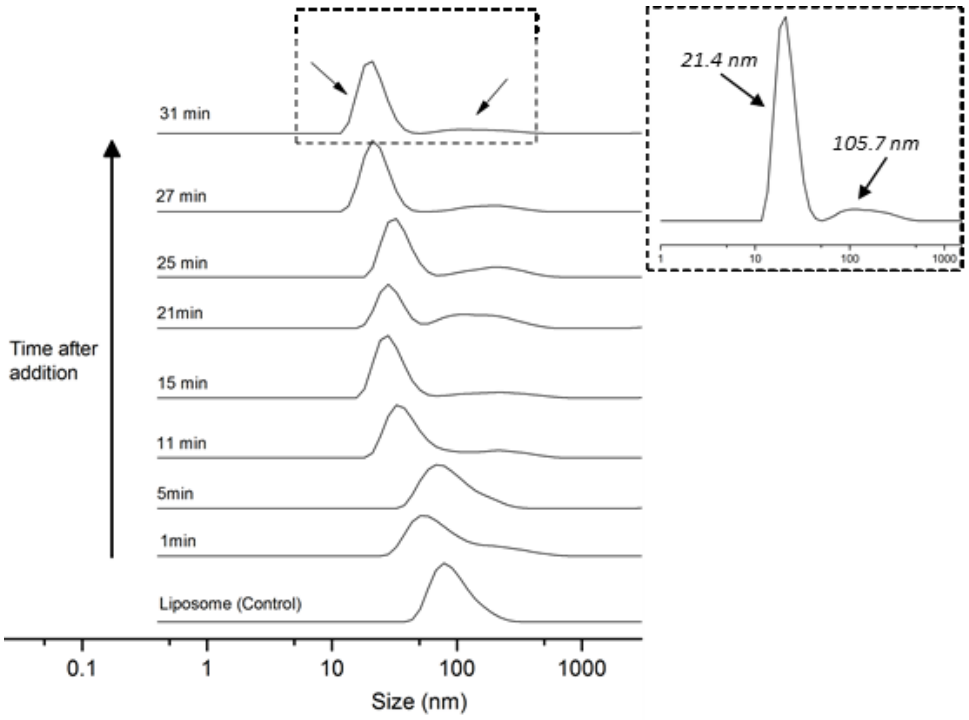


Fig 6.23 – Particle size distribution by volume for SUVs before and after the addition of 5 mM AES over time. The arrows indicates the separate particle size populations. Inset plot provides a closer look at the two separate particle size distributions.

As the AES surfactant is added, a large particle size distribution range with two peaks is observed (at 1 min), with a larger peak at 50.75 nm and a much smaller peak at 164 nm. This seems to suggest that while there is a slow permeation of the liposomes by the AES, the AES is assembling into mixed surfactant-lipid (elongated) micelles simultaneously, as soon as the lipid bilayer is being penetrated. The smaller distribution peak around 164 nm is likely representing the un-solubilised and the 'in-process' of being solubilised liposomes. Since these are real-time measurements, the

averaging of the particle size is occurring as the solubilisation is taking place, explaining the large particle size distribution range observed. As the reaction progresses over the next 10-15 minutes, the mixed AES-lipid micelles seem to be adjusting themselves and slowly settling with two distinct particle size distributions after 20-25 minutes, with an averaging size of 32.7 nm (97.6%) and 122.4 nm (2.4%), representing the mixed micelles and the un-solubilised SUVs respectively. Eventually at 27-30 minutes, the averaging mixed micelles size settles at 21.4 ±7.8 nm (97.9%), while some SUVs (2.1%) remained intake with an average size of 105.7 ±26.3 nm.

The same experiment was carried out with 10 mM AES, which gave very similar distribution curves over time, but having a slightly higher rate of reaction as expected. The two separate particle size populations settled after ~25 minutes and were measured to have an average particle size of 24.4 ±7.17 nm (98.2%) and 122.4 ±30.6 nm (1.8%). This confirms that even at higher AES concentrations, the liposomes are not completely solubilised. These results correlated with the data from the LCRA, where the maximum % calcein release was determined to be ~85 % and ~90% at 5 mM and 10 mM AES respectively, validating my findings.

Based on LCRA findings, LAS has an even slower rate of solubilisation compared to the AES and therefore the DLS experiments for LAS only systems were ran for over 45-50 minutes with a measurement reading taken after every two minutes intervals. Experiment with LAS were also carried at 5 and 10 mM concentrations in PBS 1X solution, results for which are shown in Fig 6.24 (a) and (b) respectively. As was the case with AES, 5 mM LAS reaction took longer ~45 minutes to settle and reach a consistent particle size distribution curve compared to the experiment at 10 mM LAS, which settled after ~35 minutes. The other significant differences between the two concentrations were the variation in the particle size distribution during the interactions and the number of separate particle size distributions observed during and after the experiment.

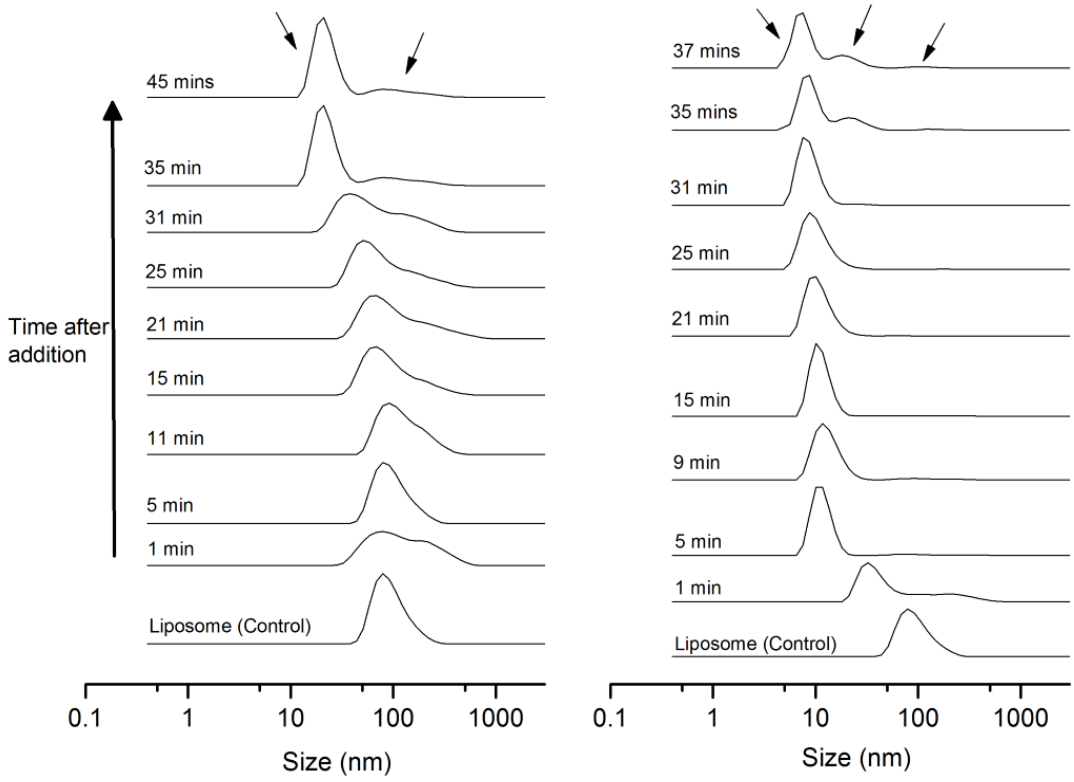


Fig 6.24 – Particle size distribution by volume for SUVs before and after the addition of (a) 5 mM and (b) 10 mM LAS over time. The arrows indicate the separate particle size populations.

For the real-time analysis at 5 mM LAS, large variations in the size distributions are seen over the first 25 minutes, with particle size peaks at 46.98 and 125.80 nm but large distributions from 18.70 nm to 295 nm. After 35 minutes the reaction starts to settle and two distinct particle size distributions are produced. The average particle sizes at 45 minutes are 24.96 ±2.8 nm (81.8%) and 124.50 ±37.5 nm (18.2%), representing the mixed LAS-lipid micelles and un-solubilised liposomes respectively. The 10 mM reactions gave less variations in the distributions overall and produced two distinct particle size populations in the initial 5 minutes of addition, averaging at 13.67 ±2.3 nm (96.2%) and 98.01 ±22.8 nm (3.8%). As the reaction progresses, the smaller particle size distribution keeps shifting whereas the larger size distribution remains between 90-120 nm range. Eventually after 35 minutes the reaction settles and three separate particle size populations are obtained. A separately plot of the particle size distribution at 37 minutes is provided in Fig 6.25, where the three distinct particle size

populations can be clearly seen with average particle sizes of 8.7 nm (75%), 30.7 nm (23%) and 94 nm (2%).

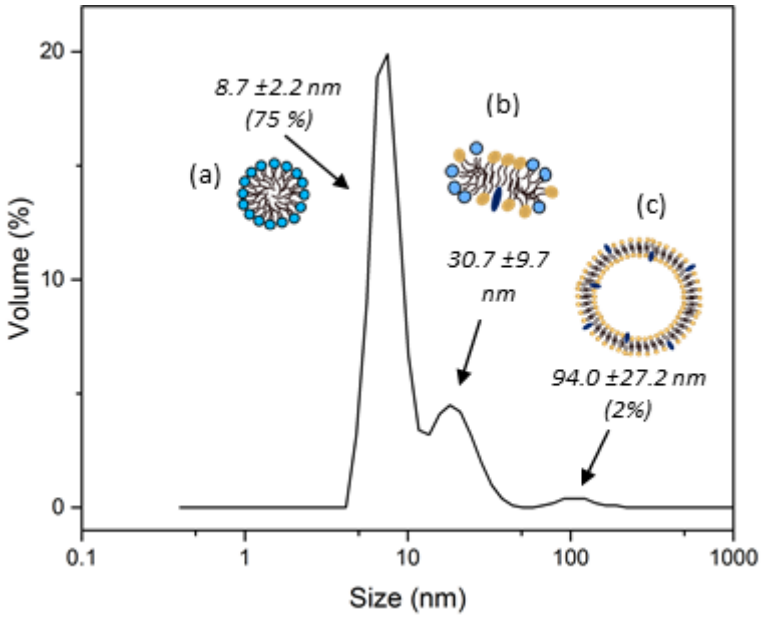


Fig 6.25 – Particle size distribution by volume for SUVs with 10 mM LAS added, at 37 minutes showing three distinct particle size populations, annotated with the average particle size values and distribution percentages. Each peak illustrated with a corresponding schematic; (a) LAS only micelles, (b) mixed LAS-lipid micelles and (c) un-solubilised SUVs.

As shown in Fig 6.24, soon after 10 mM LAS is added to the liposomes, a large volume of the particles have an average size of ~13.7 nm, which is very similar to the control LAS only micelles measurements (Fig 6.20 a) with an average size of ~12.8 nm. When 5 mM LAS was added, the initial particle distribution is much more varied with a higher average particle size (~30-50 nm). This suggest that as LAS is added, only a small portion of the monomers interact with the liposomes initially and try to permeated the lipid bilayer. At higher LAS concentrations (10 mM), since there is a higher concentration of surfactant monomer and limited interaction with lipid bilayer, LAS initially forms surfactant only micelles in large quantities (~96 % by volume). From the plots in Fig 6.24 it can also be noticed that over time, the quantity and the average particle size of the LAS only micelles decreases. Another plot was created to

track the changes in the average LAS only micelles size and quantity over time, which is shown in Fig 6.26.

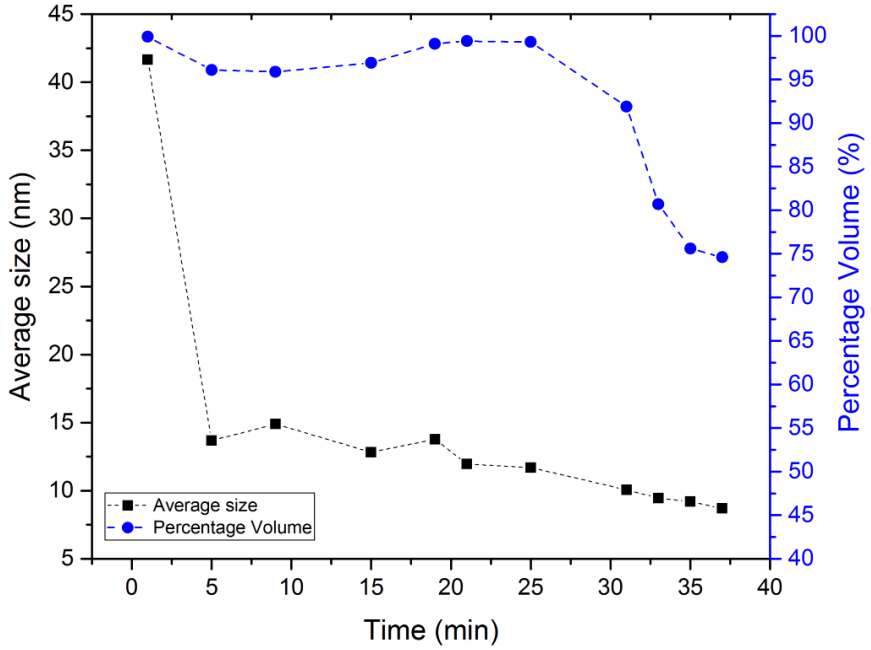


Fig 6.26 – Tracking of the average particle size and the percent level (volume) of LAS only micelles over time, for the reaction between 10 mM LAS and SUVs.

From these analyses, it can be deduced that, when LAS is added to the SUVs, above a certain concentration (i.e. 10 mM), due to the slow interaction between the LAS and the lipid bilayer, LAS monomers prefer to self-assemble and form surfactant only micelles (at 5 minutes). As some of the surfactant monomers permeate the lipid bilayer and start the solubilisation process, the LAS only micelles begins to disassemble as the reaction progress, slowly producing more mixed LAS-lipid micelles, as shown by the reduction in the particle distribution ~ 100 nm and an increase in average particle size around 30-50 nm. There is a significant decrease in the percentage volume of the LAS only micelles after 25 minutes of addition, where the average micelle size is also decreasing. Ultimately, this creates a mixture/system with the three different particle size populations (for 10 mM at 37 minutes, Fig 6.25), where it seems to be thermodynamically more favourable for the rest of the LAS monomers to keep their micellar formation. Therefore, there are no 'free' LAS monomers available to solubilise the remaining liposomes. This explanation is also complimented by the

LCRA results, where the maximum % calcein release at high LAS concentrations was 82-84 %, proving that small levels of un-solubilised SUVs remain in the system despite the increasing surfactant concentration.

6.4.3.2 Binary system

The same two binary systems were tested as the ones for the LCRA (DOX-5 and 6). As it was expected for the LAS-NI system to behave similarly to NI only system, based on the LCRA results, therefore the same testing parameters were used as the ones used for the NI only reactions, measuring the average particle size every minute for 10 minutes. Since the rate of reaction was also expected to be high, the LAS-NI experiment were carried out at 2.0 mM total surfactant concentration (1.0 mM each) and the results for which are provided in Fig 6.27 (a). The control for this experiment was the 2 mM LAS-NI in PBS IX solution (distribution for which is shown as the dash line), giving an average particle size of 13.85 ±3.05 nm, for the LAS-NI mixed micelles. Upon addition of this co-surfactant mixture, the solubilisation of SUVs seems to take place within a minute, producing a wide particle size distribution with an averaging size of 11.62 nm. At 2 minutes, the wide distribution turns into two particle size populations at 6.82 ±1.85 nm (68.3%) and 19.95 ±3.7 nm (31.7%). A minute later, the two particle size populations transform into one, narrower distribution, averaging at 16.89 ±3.5 nm. These distributions from the first few minutes suggest that as the liposomes are being solubilised rapidly, producing mixed surfactant-lipid micelles, the LAS and NI are also forming surfactant only micelles, possibly because there is an excess of surfactant monomers (more than what's required for complete SUVs solubilisation). The surfactant only micelles are also likely to be produced in the first place due to the limited/slow interaction between the LAS and the lipid bilayer as established in previous experiments. As the reaction proceeds, the surfactant only micelles seem to disassemble again and the mixed surfactant-lipids micelles adjust themselves to incorporate all the surfactants, producing an average mixed micelle size of ~16 nm. This particle size distribution remains fairly consistent beyond this point as shown in Fig 6.27 (a).

Fig 6.27 (b) shows the results for the other binary system, LAS-AES, which was tested at 5.0 mM total surfactant concentration (2.5 mM each) for over 30 minutes. The control experiment with 5 mM LAS-NI in PBS 1X solution (dash line) gave an average

particle of 13.76 ±2.2 nm, representing the mixed LAS-AES micelles. As this binary surfactant mixture is added to the liposome solution, there is an initial increase in the average particle size and the distribution range, from ~100 nm to 140 ±24.5 nm at 1 minute and to 142.8 ±30.2 nm at 4 minutes.

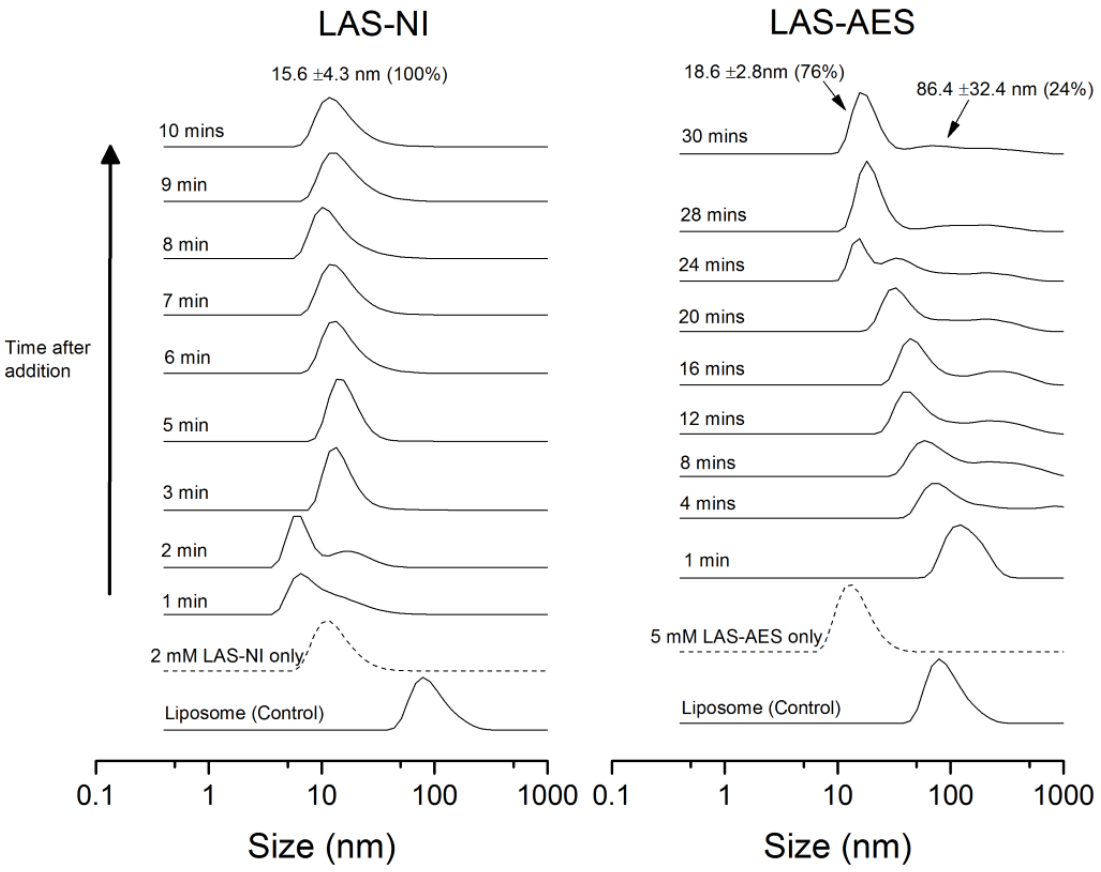


Fig 6.27 – Particle size distribution by volume for SUVs before and after the addition of (a) 2 mM LAS-NI and (b) 5 mM LAS-AES over time. The arrows indicate the separate particle size populations. Also shown are the LAS-NI and LAS-AES only micelles size distribution (dash lines).

As the reaction progresses, the LAS and AES seem to begin solubilising the liposomes, as after 8 minutes, two separate particle size distribution appear to form with averages of 18.6 ±2.8 nm and 86.44 ±15.6 nm.

As both LAS and AES have shown to have a low rate of reaction from previous experiments, the initial increase in the particles size to ~140 nm is likely to be due to the LAS and AES monomers incorporating themselves in to the lipid bilayer without causing solubilisation and increase the diameter of the SUVs. Gradually these anionic surfactants start to solubilise the lipid bilayer, producing some mixed surfactant-lipid micelles and some SUVs (with slightly smaller diameter). The slow interaction between the surfactants and liposomes continues, with the mixed surfactant-lipid micelles adjusting itself to accommodate the lipids being solubilised, which can be observed from the distribution curves from 12 to 24 minutes. After this time, the reaction seems to settle, ultimately producing the two distinct particle size populations with average size of 18.6 ±2.8 nm (76 %) and 86.4 ±32.4 nm (24 %). The distribution at ~18 nm is representing the mixed LAS-AES-lipid micelles, whereas the other wider particle size distribution near 90 nm is likely to be the un-solubilised SUVs. This outcome is supported by the LCRA carried out for the LAS-AES binary system, as the rate of release was shown to be low (~40 % /min) at 5 mM surfactant concentration. However, the LCRA results showed this binary system to completely solubilise all the SUVs at 5 mM total surfactant concentration, after 15 minutes whereas the DLS experiments show some SUVs remain un-solubilised. This could be due to the differences in the sheer volume of the reaction mixtures between these sets of experiments. The LCRA was carried out in a 300 µl well with 200 µl of liposome solution and 50 µl of the surfactant mixture, while for the DLS experiments, the ratio was kept the same, but a 3 ml cuvette was used with 800 µl and 200 µl of liposome and surfactant respectively. The scaling up of the reaction volume for the DLS was required in order to have sufficient solution volume for an adequate signal intensity.

6.4.3.3 Ternary system

The DOX-8 ternary system (containing equal ratio of all three surfactants) was tested at 2 and 5 mM total surfactant concentrations, results from which are provide in Fig.6.28. The response of the reaction with 2 mM total surfactant concentration (0.67 mM each) is similar to the LAS-AES binary system explained in the previous section, where there is a wide spread particle size distribution initially after addition which

gradually transforms into two particle size pollutions over time. There does seem to be some immediate solubilisation of the SUVs, shown by the distribution peak at ~35 nm after 1 minute, representing the mixed surfactant-lipid micelles, with another wider peak around 115 mM representing the remaining SUVs interacting with the surfactants. As the reaction progresses, the average particle size keeps changing but has the similar overall distribution curve, suggesting that SUVs are in the process of solubilisation. The reaction settled after 15 minutes and eventually produces two particle size populations, with averages of 26.9 ±6.7 nm (65 %) and 96.3 ±26.9 nm (35 %) at 19 minutes, signifying the mixed surfactant-lipid micelles and the un-solubilized liposome respectively.

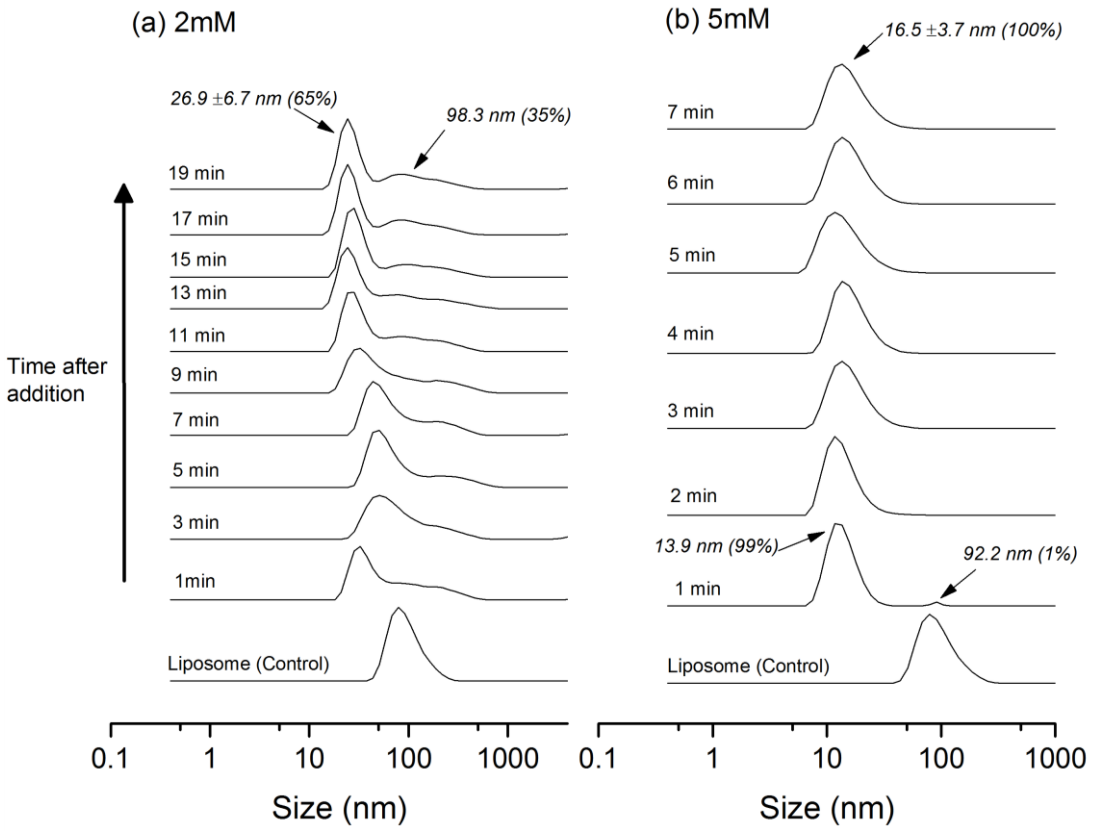


Fig 6.28 – Particle size distribution by volume for DOX-8 ternary surfactant system interaction with SUVs, before and after the addition of (a) 2 mM and (b) 5 mM total surfactant concentration over time. The arrows indicate the separate particle size populations.

The experiment with 5 mM total surfactant concentration shows a more rapid response with almost all SUVs being solubilised after 1 minute, producing mixed surfactant-

lipid micelles with an average size of ~14 nm and only 1 % by volume of the un-solubilised SUVs remain (~92 nm). After this point, complete solubilisation of SUVs takes place with average mixed micelles size between 14-16 nm. This response for 5 mM reaction is in agreement with the LCRA response for DOX-8, however there are some differences for the response at 2 mM concentration. The LCRA showed all the calcein was released and hence all SUVs solubilised at 2 mM total surfactant concentration for DOX-8 ternary system, whereas these DLS analysis shows some SUVs remain un-solubilised. This difference in concentration response between the two techniques was also observed for the binary systems (explained above), with LCRA showing greater solubilisation at the same concentration. Since the DLS experiments uses a larger volume of the reaction mixture, in a larger size cuvette, these differences are likely due to the scaling of the reaction mixtures.

To determine the influence of NI surfactant on the solubilisation mechanism of lipid bilayers, DOX-9 and 10 ternary systems were used which contained lower ratio of NI verses the other two anionic surfactants. Both these systems were tested at 2 mM total surfactant concentration to compare with the DOX-8 results. Fig 6.29 shows both the ternary systems to produced very similar particle size distribution curves to the DOX-8 reaction when added to the liposome solution. The main differences are the time taken for the reactions to settle and produce stable distribution curves, i.e. the rate of reaction. DOX-9 reaction, containing 0.2 mM NI, 0.4 mM LAS and AES, begins to settle after 13 minutes of addition, producing two particle sizes populations with average sizes of 30.4 ±4.75 nm (68.7 %) and 112.3 ±32.2 nm (31.3 %) at 21 minutes. The DOX-10 reaction, with further reduced ratio of NI (~0.11 mM NI, 0.44 mM LAS and AES), seems to settle after 17 minutes and ultimately creating two distributions with average particle sizes of 40.9 ±6.5 nm (63 %) and 102.6 ±24.9 nm (37 %).

As the ratio of NI is reduced in these ternary surfactant mixtures, the rate of reaction reduces as well. Also, the percent volume of the mixed surfactant-lipid micelles decreases and the percent volume of the SUVs increases. Therefore, these results further establish that less SUVs are solubilised as the NI concentration decrease in the ternary mixture, in agreement with the LCRA findings. Another noticeable difference between the three different ternary systems from the particle size analyses are the

average sizes of the mixed surfactant-lipid micelles. With reducing NI ratio in the mixture, the final mixed micelle size increases. The average diameter of the mixed surfactant-lipid micelles for the 1:1:1 ternary mixture (DOX-8) reaction at 2 mM total concentration is ~27 nm, which increases to ~30 nm and ~41 nm as the NI ratio is reduced by a factor of 2 and 4 respectively. This supports the principle that non-ionic surfactant produced smaller mixed micelles.[224, 226]

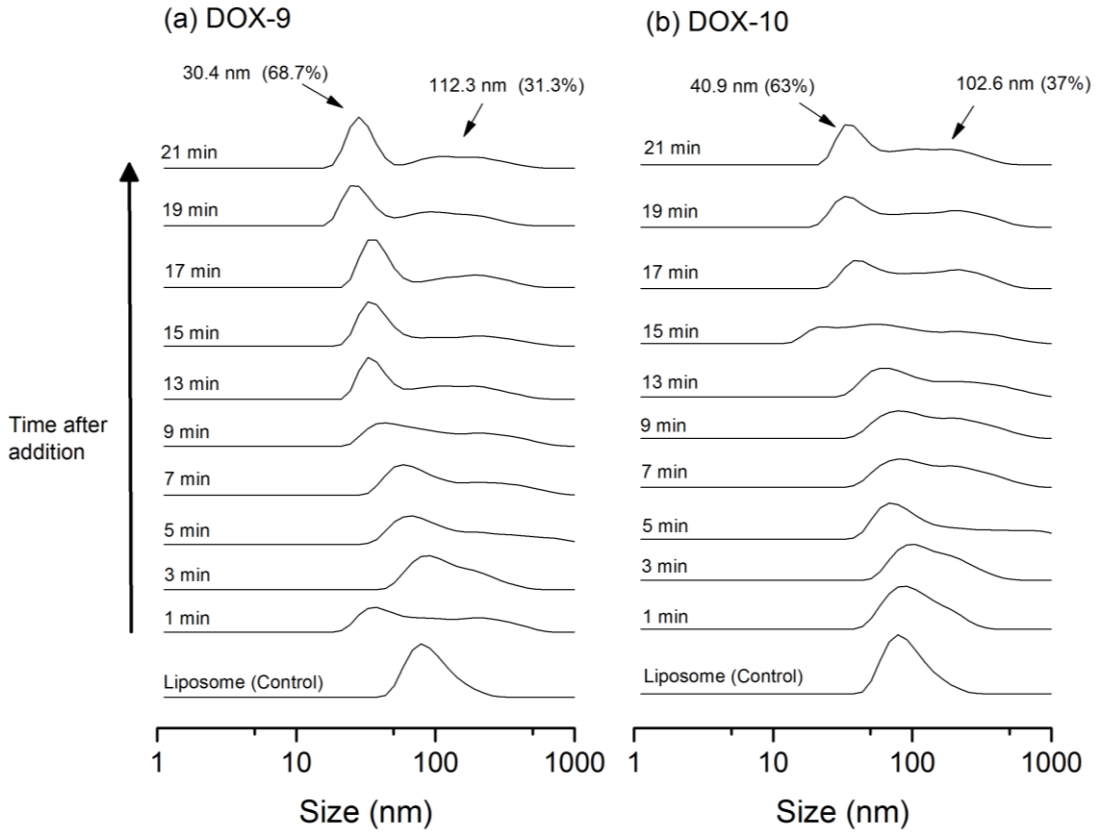


Fig 6.29 – Particle size distribution by volume for DOX ternary surfactant systems interaction with SUVs, before and after the addition of (a) DOX-9 and (b) DOX-10 at 5 mM. The arrows indicate the separate particle size populations.

6.4.4 Surfactant-lipid bilayer interactions

The results from both the techniques, LCRA and DLS real-time analysis, can be used to determine how these surfactant systems interact and solubilise the liposome in this project, representing the cornea epithelium lipid membrane composition. It was clearly gathered from both the experiments that the NI surfactant was driving the high rate of solubilisation in the all the systems and achieving complete solubilisation with small mixed micelles (~10 nm diameter size) by itself. This NI performance is very similar

to the control TX-100 experiments and therefore NI surfactant's time and concentration response can be related to its chemical structure. Fig 6.30 shows the annotated structure of the NI surfactant used in this project along with a schematic to illustrate its headgroup to tail ratio. The ethoxylated (EO) head group of NI contains on average between 7-9 ethylene oxide groups, similar to TX-100, creating a relatively large hydrophilic headgroup and hence involve a similar solubilisation mechanism. Upon insertion of NI into the lipid bilayer, the large headgroup is likely to create tension in the outer monolayer leading to curvature and budding off of the lipids with the surfactant, rapidly producing small mixed micelles. Like the TX-100, a low concentration of NI is required to onset the solubilisation process.

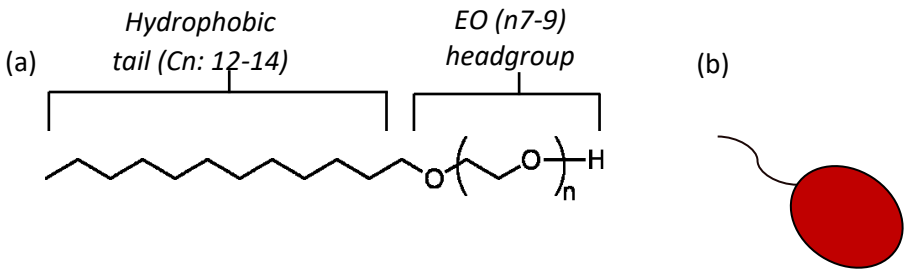


Fig 6.30 – Structure of the non-ionic (NI) ethoxylated surfactant used, showing (a) annotated chemical structure and (b) schematic structure to illustrate the headgroup to tail ratio.

The AES surfactant used also contains an ethoxylated headgroup (sulfonated to give the anionic charge), but only consist on average 2 to 4 ethylene oxide chains as shown in Fig 6.30(a). Therefore, AES not only has an anionic charge, its headgroup size is much smaller than the NI. This can explain the response of AES in the LCRA and DLS, showing a lower rate of solubilisation, but complete solubilisation above a certain concentration with larger mixed micelle size compared to NI. Due to the smaller headgroup to tail ratio, AES does not cause the rapid curvature in the outer monolayer of the lipid bilayer. The solubilisation mechanism with AES is likely to involve the flip-flop movement, where the AES monomers after getting incorporated in to the outer monolayer, transfer across to the inner monolayer via trans-membrane interchange and onset the solubilisation process after saturating the whole bilayer.

Comparing AES with the main anionic surfactant LAS, illustrated in Fig 6.31(b), show that LAS hydrophilic region only consist of a sulfonate group and a hydrophobic region containing a benzene attached to a hydrocarbon chain of varied lengths. Since benzene is usually typically attached at C_2 to C_4 position of the linear alky chain, a 'semi-branch' is created. Therefore LAS possesses a much smaller headgroup to tail ratio in comparison with the other two surfactants. This structural property of LAS seems to results in a very slow rate of solubilisations and incomplete solubilisation as shown from the LCRA and DLS experiments.

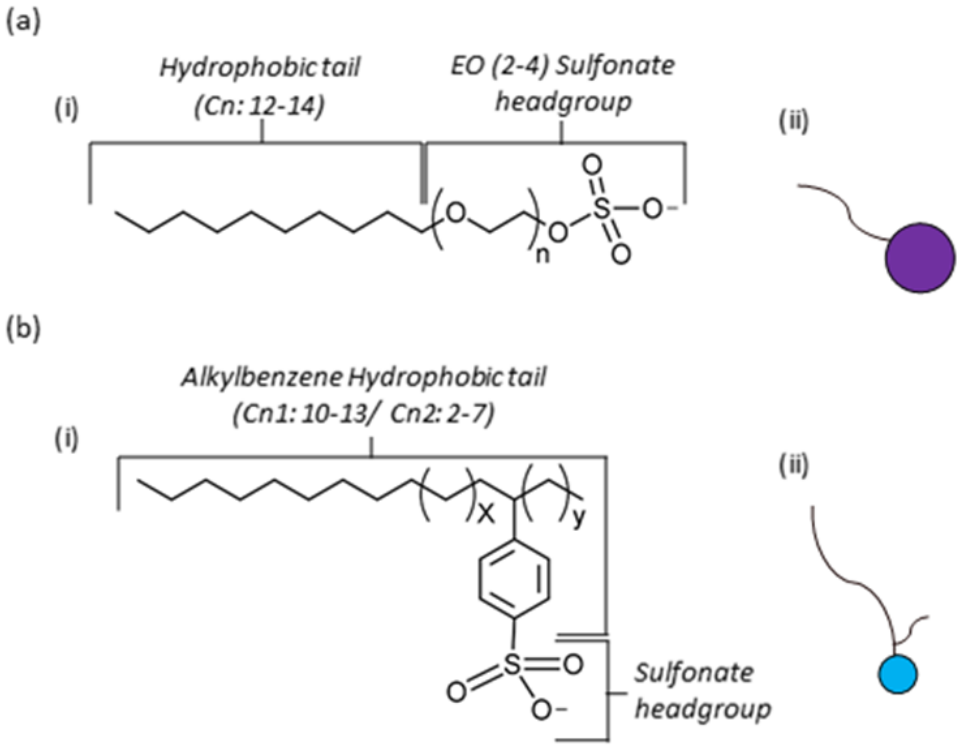


Fig 6.31 – Structures of (a) AES and (b) LAS surfactants, illustrating their (i) chemical structure and (ii) schematic to show the headgroup to tail ratio.

6.4.4.1 Solubilisation mechanism

After taking into account the structural properties of the three surfactants and the corresponding responses from both the techniques used, we can gather some decent understanding of the mechanisms of solubilisation for these particular liposomes. As explained previously, there are two potential mechanism by which lipid bilayers can be solubilised, through initial curvature of the outer monolayer or through flip-flop

movement. NI only surfactant systems or systems containing higher ratio of NI seem to follow the former mechanism, where the surfactant rapidly creates a localised curvature in the outer monolayer, producing mixed micelles. This leads to pores in the bilayer and eventually all liposomes are solubilised. This mechanism illustrated in Fig 6.32, alongside the flip-flop mechanism which is associated with other two anionic surfactants.

LAS response upon interacting with the liposomes, from both the LCRA and DLS experiments, revealed a very slow rate of solubilisation with un-solubilised SUVs remaining, even as the concentration of LAS is increased, resulting in three different sizes of aggregates. Therefore the partitioning of the lipid bilayer and creating a localised curvature seems to be time consuming for LAS. This is most likely due to LAS having a small headgroup to tail ratio, which allows LAS monomers to remain incorporated in the bilayer for longer periods without creating stress and curvature. As LAS gets inserted in to the outer monolayer (Fig 6.31, step 1b), its small headgroup to tail ratio would not allow for a rapid curvature to be created. LAS is also likely to follow the flip-flop mechanism of solubilisation, similar to AES, where the surfactant monomers get transferred across to the inner monolayer, saturating the vesicles with surfactants on both sides of the lipid bilayer (step 2b i). Real-time particle size analysis observed an initial increase in the SUVs size post the addition LAS only and LAS-AES binary systems. That observation could be representative of this vesicle saturation phase, where the liposome size increases as a result of surfactant remaining incorporated in the lipid bilayer. This increase in vesicle size upon saturation by surfactants has been reported by previous studies, where a range of individual surfactants were tested on several different liposome compositions, as well as by molecular dynamics studies on liposome solubilisation.[206, 230] Saturation of the whole bilayer with surfactants leads to disruption of parts of the vesicles, as the surfactant causes small changes in the localised curvature from both sides of the bilayer. This stage (step 2b ii) is the onset of solubilisation, producing pores in the vesicles and yielding surfactant-saturated vesicles and lipid-saturated mixed micelles. Although AES and LAS seem to follow the same flip-flop mechanism, AES has a higher rate of solubilisation and yields complete solubilisation of liposomes at higher concentrations. This suggest that the partitioning, flip-flop and saturation stages of the solubilisation mechanism is longer for LAS, which leads to delayed and slower onset.

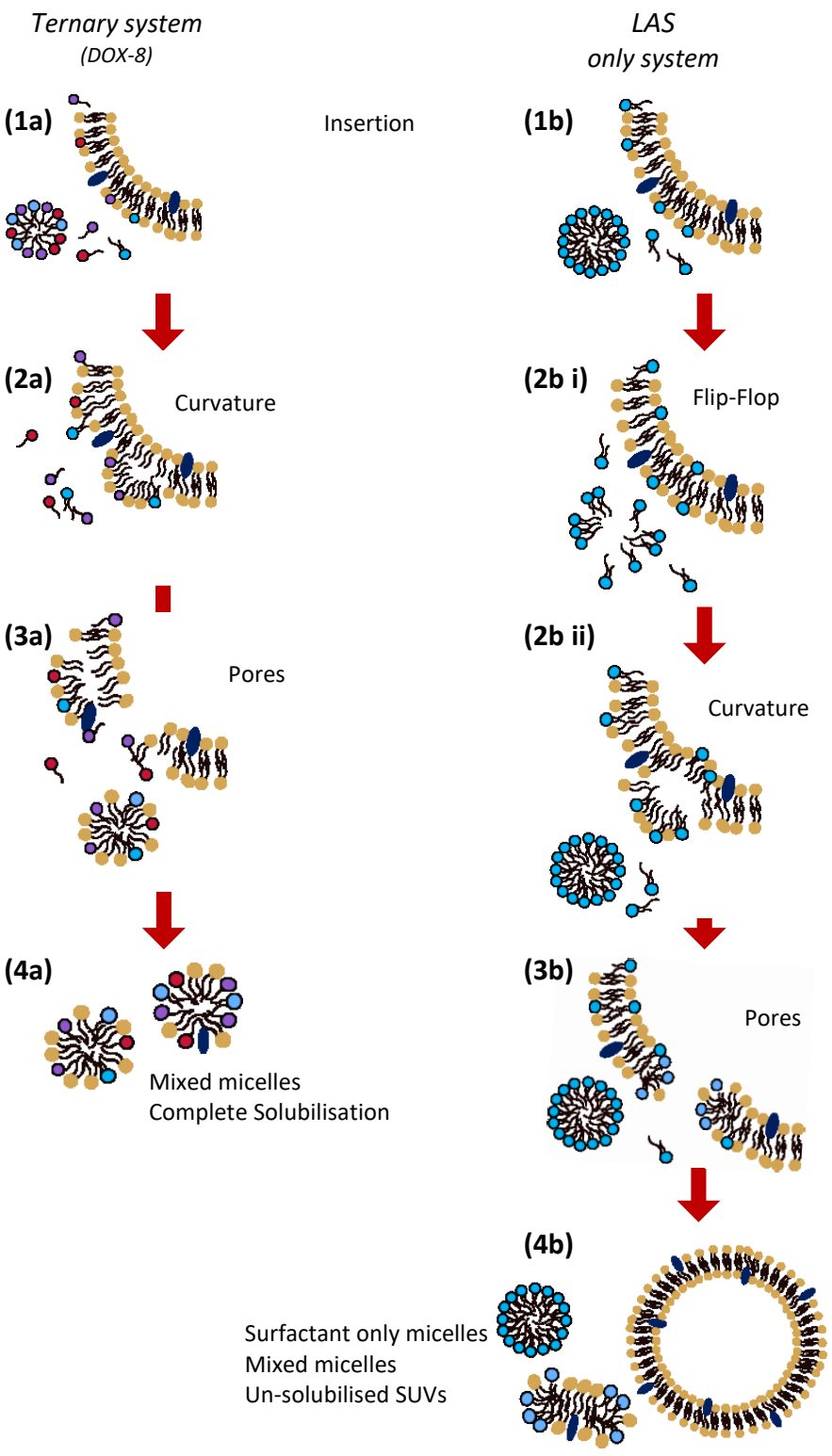


Fig 6.32 – Schematics of the likely mechanisms of interactions between the liposomes and (a) ternary surfactant system and (b) LAS only system. The mechanisms are categorised into four main steps; 1 – Insertion of the surfactant into the lipid bilayer, 2 – Flip-flop of surfactants between the monolayers and/or Curvature of the outer lipid monolayer, 3 – Formation of mixed micelles and pores in bilayer , 4 – Solubilisation process completed.

Previous studies have also shown this flip-flop stage to be the time-limiting factor depending on the type of detergent used. Since increasing the concentration of LAS does not produce higher rate nor complete solubilisation, the 'excess' surfactant being added is not being incorporated in to the bilayer, but instead prefers to self-assemble into surfactant only micelles, which was verified by the DLS analysis. Therefore, LAS only systems or LAS-AES (at low concentration) binary systems eventually produce; surfactant only micelles, mixed lipid-surfactant micelles and un-solubilised liposomes (step 4b).

6.4.4.2 Corneal swelling - % Calcein release relationship

Gaining an understanding of how the three surfactants are interacting individually as well as in binary/ternary systems with the liposomes designed to be representative of the chicken corneal epithetical membrane, enables me to better comprehend and understand the outcomes from the detergent ICE test-LCRA analysis (in chapter 5). When using a series of detergent samples (containing the three surfactants), a meaningful negative correlation was established between the ICE test- corneal swelling measurements and the calcein release data, showing that the detergent samples which gave slow and incomplete solubilisation, produced higher levels of corneal swelling. Since it has been established that the low rate of solubilisation and incomplete solubilisation is related to higher ratio of LAS (and lower ratio of NI) present in the detergent mixture, it is highly likely that corneal swelling is associated with the presence of LAS, with Fig 6.33 illustrating the proposed associations.

The slow insertion and flip-flop of LAS in the lipid bilayer, as well as the increase in vesicle size prior to solubilisation onset observed, suggest that detergent samples with higher ratio of LAS lead to surfactant monomers slowly partitioning and remaining in the corneal membrane bilayers for longer periods, likely causing the corneal swelling. Detergent samples which produced higher rate and level of calcein release (yielding rapid and complete solubilisation) showed less corneal swelling, indicate that surfactants which causes rapid solubilisation could be preventing/ lowering the level of corneal swelling. Hence, this further insinuates that a slow rate of flip-flop and a prolonged period of surfactant-saturation of the lipid bilayer is causing the corneal membranes to swell.

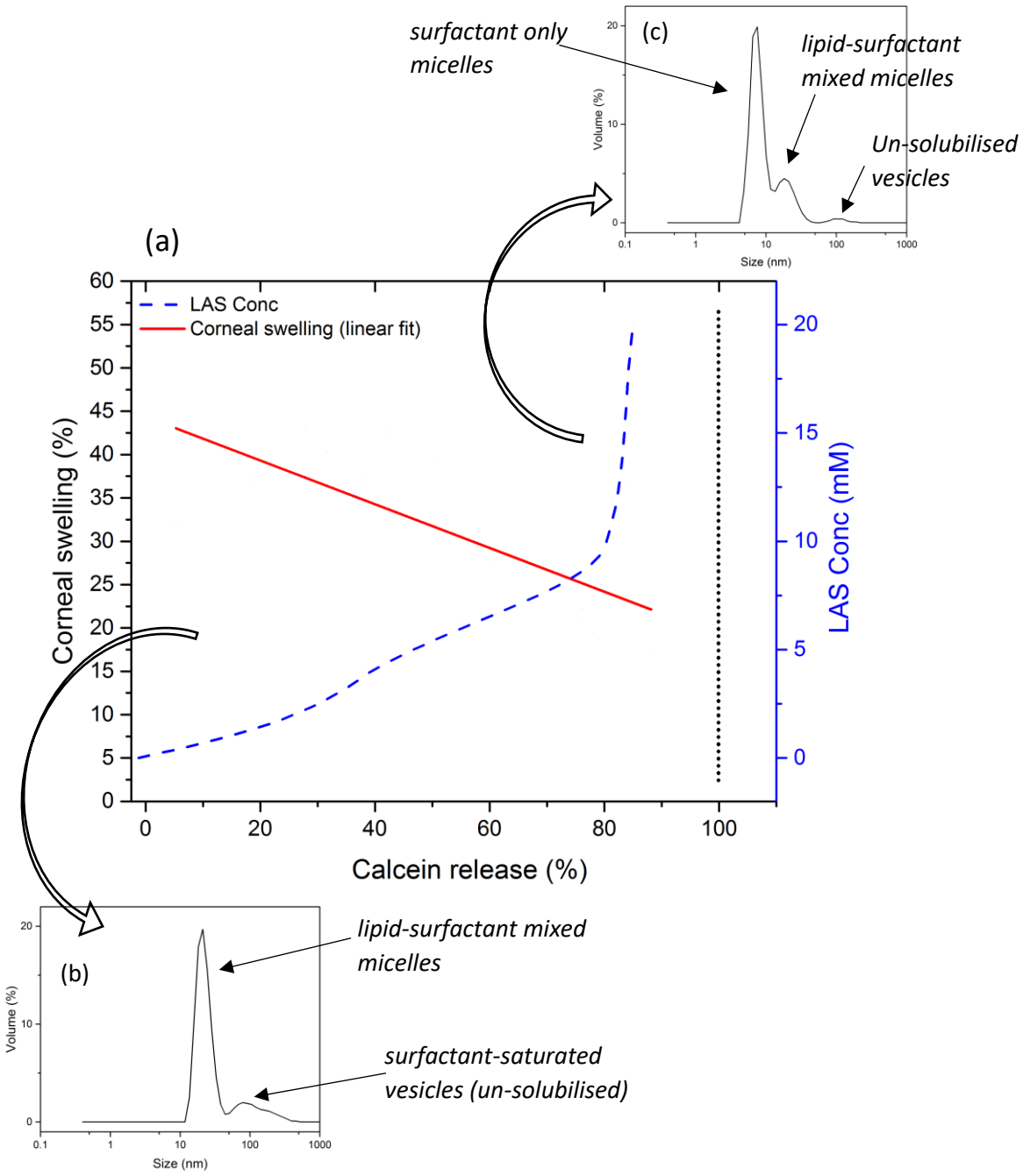


Fig 6.33 – Plots illustrating associations between (a) corneal swelling and LAS concentration via calcein release, along with (b) particle size distribution at low LAS concentration showing un-solubilised, larger vesicles and (c) particle size distribution at higher LAS concentration revealing LAS only micelles, mixed micelles and un-solubilised SUVS.

6.5 CHAPTER CONCLUSIONS

Using LCRA and real-time particle size analysis as complimentary techniques, provided me with some key learnings and a better understanding of how these particular surfactants interact with lipid bilayers and the mode of action involved in solubilising the liposomes representing the corneal epithelium membrane.

Non-ionic surfactant such as TX-100 and the alcohol ethoxylate (NI) used in this study delivers rapid and complete solubilisation of the SUVs due to its large headgroup to tail ratio. Since NI experiments gave very similar responses as the TX-100, it is highly suggested that NI's mode of action is along the lines of the conventional three-stage solubilisation mechanism. Due to its specific amphiphilic structural properties, NI induces a localised curvature in the outer monolayer at relatively low concentration, producing lipid-saturated mixed micelles. This creates an imbalance across the bilayer, which leads to the disruption and ultimately solubilisation of the entire lipid bilayer. Therefore, even if NI is present at a lower ratio in the detergent sample, the level of lipid bilayer permeation achieved will be high, although the rate of solubilisation will be lowered. The two anionic surfactants seem to follow the flip-flop mechanism, where the trans-membrane movement is slow and the surfactant-saturation of vesicles is prolonged, particularly for LAS.

These outcomes, especially from the LAS experiments, provide a potential explanation to the negative correlation between the calcein release data and ICE test corneal swelling measurements established in the previous chapter. The lengthened flip-flop step, an initial increase in vesicle size and a delayed onset of solubilisation observed for LAS could be why detergent samples which give low calcein release obtained higher corneal swelling results. Therefore, detergent samples with a higher ratio of LAS could be contributing to the irritancy through corneal swelling, whereas samples with NI levels above a certain concentration are causing damage through rapid permeation. Further investigation will be required to explore this theory, ideally using lipid bilayer models with increased complexity (e.g. Multilamellar vesicles or Stacked-Supported lipid bilayers).

Chapter 7
Conclusions and Further work

Surfactant have undergone extensive research over the decades, as there is an enormously diverse range of applications and disciplines within them to be explored, many of which are yet to be clearly understood. In this thesis, I have addressed the challenges encountered in developing concentrated liquid surfactant systems, particularly regarding the temperature stability and ocular safety.

7.1 SUMMARY OF FINDINGS

Through chapters 3 and 4 of this thesis, a better understanding has been gained on how altering the solvent quality affects the surfactant phase behaviour, specifically for SDS-water:glycerol systems. Chapter 3 establishes the robustness of the surface tension- pendant drop method, enabling the full range of the water-glycerol mixture to be explored and it was found that increasing the organic solvent content (i.e. decreasing the solvent polarity and the hydrogen bonding ability) causes the Krafft point to also increase towards higher CMCs and T_K. These changing Krafft point co-ordinated were determined with reasonable precision, enabling the SDS phase diagram to be mapped out to track these alterations in relation to the solubility boundary at low SDS concentrations. Although the efficiently of the pendant drop method in determining the T_K requires further investigation, this method provides a more effective, high-throughput alternative, particularly for systems with high organic solvent content, where other traditional methods like the conductivity technique has struggled. The validation and the robustness of the pendant drop method also allowed for the CMC of a large number of liquid detergent formulations to be analysed efficiently.

Expanding this study further in chapter 4, higher SDS concentrations in the range of 10-40 wt% were explored with the aid of DSC and X-ray scattering techniques to investigate the phase behaviour of SDS with changing solvent content. Both the techniques provided a complimentary insight in to the effect of organic solvent on the transformations of SDS hydrated crystals in to micelles/hexagonal phases and vice versa and also into the inter-conversions within the various SDS hydrate morphologies. Through DSC analysis, phase transition temperatures of SDS in 20, 40 and 60 wt% glycerol content were determined, including SDS hydrate nucleation temperatures. Finding these transition temperatures to be in good agreement with literature data, for SDS-water system, provided confidence in the results obtained from the different water-glycerol mixtures. From the DSC results, it was suggested that with increasing glycerol levels, the number of inter-conversions within the SDS hydrates also increase, through the observation of multiple, merged transition peaks. This was later confirmed by SAXS analysis, where the presence of multiple Bragg's lamellar peaks was found and used to identify the types SDS H_C formed.

Bringing together all the data and learnings from the Krafft point investigation, DSC phase transition temperatures studies and X-ray scattering structural analysis, SDS phase diagrams were established for 20, 40 and 60 wt% glycerol content, in up to 40 wt% SDS levels. These phase diagrams, focusing on the regions near the solubility boundary, can be used to determine the potential phase/ state resulting from a temperature condition and the solvent composition. This knowledge base now provides a platform of understanding the effects of changing solvent quality, allowing us to control the negative transformations encountered and hence the performance and stability of structured, surfactant-based formulations.

Chapters 5 and 6 in this thesis focuses on developing and determining the potential of model membranes as a tool for predicting eye irritancy and providing a complimentary method to the ICE test. Analysing the ICE test data in chapter 5 highlighted the subjectively of its scoring parameters, with only the corneal swelling measurements providing comparable data. Two different model lipid membranes, DIBs and liposomes (SUVs) were trialled initially, with the DIBs approach requiring extremely

diluted levels of detergent samples to slow down the interactions for observations to be made and hence proved to be a non-discriminatory tool. The liposome approached, using the calcein encapsulation technique (LCRA), with the vesicles developed to be representative of the chicken corneal membrane, showed differentiation between the various detergent formulations, leading to a meaningful negative correlation being established between the level of lipid bilayer permeation (calcein release) and the corneal swelling measurements. Therefore, based on this correlation, it is suggested that detergent formulations producing low levels of lipid bilayer permeation and slow interactions, induce a higher degree of corneal swelling.

Through further investigations in chapter 6, using LCRA and DLS real-time analysis for testing the three individual surfactants involved in the detergent formulations, it was determined that the NI surfactant, alcohol ethoxylate, is driving the rapid and complete solubilisation of the liposomes at low concentrations, whereas both the anionic surfactants, LAS and AES, gave much slower interactions with the lipid bilayer, even at higher concentrations. Due to the large headgroup to tail ratio of the NI surfactant, yielding results similar to that of the TX-100, it proves to be potent at permeating the lipid membrane and follows the widely recognised three-stage solubilisation mechanism. The LAS and AES surfactants however, are suggested to follow the flip-flop mechanism of interaction, showing slow trans-membrane movement of surfactants and hence a prolonged stage where the lipid bilayer is saturated with surfactant monomers, causing the vesicle size to increase before the onset of solubilisation. This mode of action seems to provide a plausible explanation for the relationship observed between the liposome permeation and corneal swelling measurements, where low rate of permeation and incomplete solubilisation corresponds to increased corneal swelling. These mechanisms need to be further explored, as it is likely that both the surfactant types are contributing to the eye irritation in different ways or in synergy, e.g. with NI rapidly permeating the lipid bilayer, allowing LAS to get incorporated deeper into the corneal membranes causing increased swelling and irritation.

The LCRA, together with the DLS analysis, proved to be a very efficient tool for investigating the interactions between surfactants and lipid bilayers, allowing for the different modes of solubilisation to be identified. Compared to other *in vitro* alternatives, this LCRA has established a high-throughput, reproducible and a less expensive approach for differentiating between the potential irritancy of surfactant-based systems, showing great promise for it to be developed further, yielding novel, complimentary tools for predicting UN GHS category 2 ocular irritants.

7.2 FURTHER WORK

The studies detailed in this thesis have opened up a range of opportunities for future investigations, some of which are already underway, using the results from this thesis and building on the knowledge gain over the course of this doctoral project.

To further investigate the phase behaviour of surfactant systems, microfluidics and simulation approaches will be interesting to explore, particularly using the SDS water-glycerol systems used in this thesis, looking into the effect of different temperature, pressure, mechanical vibrations, etc to mimic real environmental conditions (e,g, transportation) for gaining a better insight in to the nucleation of SDS hydrate in organic solvent.

The phase behaviour of surfactant systems investigated in this thesis was a binary system, in order to reduce the number of variables and provide a platform of understanding to build upon. These systems should be expanded in further studies, incorporating co-surfactants and polymers, gradually achieving a model system which is closer a functional product while developing a deeper insight in to the various transformation in stages. The success of X-ray scattering analysis, particularly with using the Linkam stage for providing a continuous cooling cycle, down to very low temperatures, should be carried forward, utilising this tool to investigate the effect different of cooling rates on nucleation, while gaining structure insights.

The future studies regarding ocular irritancy predictions can be separated into two categories. Since two different mode of actions are suggested in this thesis, the first set of investigations should be for developing a further understanding of the interactions between various surfactant types and lipid membranes, focusing on the mechanisms involved in the permeation and solubilisation of lipid bilayers. The second involves developing technologies and model membranes with increased complexity which are more representative of the corneal membrane as well as models which can better tolerate undiluted or more concentrated detergent levels, while showing differentiation for the degree of permeation.

Using the learning from the LCRA and DLS analysis, a study involving the use of Giant Unilamellar Vesicles (GUVs) in currently underway, to further understand the mechanisms of solubilisation through visual investigation, with the use of optical and fluorescence microscopy. Another approach that can be used is to development multi-layered/ tiered models, such as Multilamellar Vesicles (MLVs) or Stacked-Supported lipid bilayers (SSLBs), which may provide increased tolerance to concentrated surfactants as well as better differentiation through the different tiers of bilayer available for permeation. Also, it would be interesting to incorporate proteins into the lipid membrane composition to provide a closer representation of the corneal membrane and hence a better predictive *in vitro* method. It should be considered that eye irritancy models and assays may have to be customised according to the irritancy parameter of interest (e.g. swelling, opacity), to take into account that different mode of actions may contribute to irritancy in different way. This will allow us to determine, more accurately, the cause and the severity of potential damage that can occur.

References

1. H. Khan, J. M. Seddon, R. V. Law, N. J. Brooks, E. Robles, J. T. Cabral and O. Ces, *J Colloid Interf Sci*, 2019, **538**, 75-82.
2. K. Holmberg, B. Jönsson, B. Kronberg and B. Lindman, in *Surfactants and Polymers in Aqueous Solution*, John Wiley & Sons, Ltd, Chichester, 2003, DOI: 10.1002/0470856424.ch1, pp. 1-37.
3. M. M. Rieger and L. D. Rhein, in *Surfactants in Cosmetics*, ed. M. M. Rieger, Marcel Dekker INC, New York (NY), 2 edn., 1997, ch. 1, pp. 1-28.
4. C. Wibowo and K. M. Ng, *AIChE Journal*, 2001, **47**, 2746-2767.
5. E. Robles, personal communication.
6. A. J. Wicken and K. W. Knox, in *Chemistry and Biological Activities of Bacterial Surface Amphiphiles*, eds. G. D. Shockman and A. J. Wicken, Academic Press, 1981, DOI: https://doi.org/10.1016/B978-0-12-640380-0.50005-X, pp. 1-9.
7. E. Pramauro and E. Pelezetti, in *Comprehensive Analytical Chemistry*, Elsevier, Amsterdam, 1st edn., 1996, vol. 31, ch. 1, pp. 1-91.
8. I. W. Hamley, in *Introduction to Soft Matter*, John Wiley & Sons, Ltd, Chichester, 2007, DOI: 10.1002/9780470517338.ch4, pp. 161-220.
9. M. M. Rieger and L. D. Rhein, in *Surfactants in Cosmetics*, ed. M. M. Rieger, Marcel Dekker INC, New York (NY), 2 edn., 1997, ch. 2, pp. 29-82.
10. W. C. Griffin, *J. Cosmetic Sci.*, 1949, **1**, 311-326.
11. R. C Pasquali, N. Sacco and C. Bregni, *Latin American Journal of Pharmacy*, 2009, **28**.
12. W. C. Griffin, *J Soc Cosmet Chem*, 1954, **5**, 235-249.
13. A. C. Kogawa, B. G. Cernic, L. G. D. do Couto and H. R. N. Salgado, *Saudi Pharmaceutical Journal*, 2017, **25**, 934-938.
14. J. B. St. Laurent, F. de Buzzaccarini, K. De Clerck, H. Demeyere, R. Labeque, R. Lodewick and L. van Langenhove, in *Handbook for Cleaning/Decontamination of Surfaces*, eds. I. Johansson and P. Somasundaran, Elsevier Science B.V., Amsterdam, 2007, DOI: https://doi.org/10.1016/B978-044451664-0/50003-6, pp. 57-102.
15. B. E. Rapp, in *Microfluidics: Modelling, Mechanics and Mathematics*, ed. B. E. Rapp, Elsevier, Oxford, 2017, DOI: https://doi.org/10.1016/B978-1-4557-3141-1.50020-4, pp. 421-444.
16. J. N. Israelachvili, D. J. Mitchell and B. W. Ninham, *Journal of the Chemical Society, Faraday Transactions 2: Molecular and Chemical Physics*, 1976, **72**, 1525-1568.
17. K. Holmberg, B. Jönsson, B. Kronberg and B. Lindman, in *Surfactants and Polymers in Aqueous Solution*, John Wiley & Sons, Ltd, Chichester, 2003, DOI: 10.1002/0470856424.ch2, pp. 39-66.
18. P. Mukerjee and K. J. Mysels, *Critical micelle concentrations of aqueous surfactant systems*, National Bureau of Standard, Washington DC, 1971.
19. H. Wennerström and B. Lindman, *Physics Reports*, 1979, **52**, 1-86.
20. K. Gracie, D. Turner and R. Palepu, *Canadian Journal of Chemistry*, 1996, **74**, 1616-1625.
21. M. L. Moya, A. Rodriguez, M. D. Graciani and G. Fernandez, *J Colloid Interf Sci*, 2007, **316**, 787-795.
22. D. Lombardo, M. A. Kiselev, Magaz, Salvatore and P. Calandra, *Advances in Condensed Matter Physics*, 2015, **2015**, 22.

23. M. J. Rosen, in *Surfactants and Interfacial Phenomena*, John Wiley & Sons, Inc., 2004, DOI: 10.1002/0471670561.ch3, pp. 105-177.
24. R. Koynova and B. Tenchov, 2008, DOI: 10.1002/9780470048672.wecb287.
25. F. B. Rosevear, *Journal of the Society of Cosmetic Chemist*, 1968, **19**, 14.
26. G. J. T. Tiddy, *Physics Reports*, 1980, **57**, 1-46.
27. K. Holmberg, B. Jönsson, B. Kronberg and B. Lindman, in *Surfactants and Polymers in Aqueous Solution*, John Wiley & Sons, Ltd, Chichester, 2003, DOI: 10.1002/0470856424.ch3, ch. 3, pp. 67-96.
28. D. R. Karsa, R. M. Bailey, B. Shelmerdine and S. A. McCann, in *Industrial Applications of Surfactants IV*, ed. D. R. Karsa, Woodhead Publishing, 1999, DOI: https://doi.org/10.1533/9781845698614.1, pp. 1-22.
29. P. Kekicheff, *J Colloid Interf Sci*, 1989, **131**, 133-152.
30. P. Kékicheff, C. Grabielle-Madelmont and M. Ollivon, *J Colloid Interf Sci*, 1989, **131**, 112-132.
31. L. J. Magid, *The Journal of Physical Chemistry B*, 1998, **102**, 4064-4074.
32. L. A. Smith, A. Duncan, G. B. Thomson, K. J. Roberts, D. Machin and G. McLeod, *J Cryst Growth*, 2004, **263**, 480-490.
33. B. L. Bales, *J Phys Chem B*, 2001, **105**, 6798-6804.
34. K. Fontell, *Mol Cryst Liq Cryst*, 1981, **63**, 59-82.
35. Z. Huang, P. Qi, Y. Liu, C. Chai, Y. Wang, A. Song and J. Hao, *Physical Chemistry Chemical Physics*, 2019, **21**, 15256-15281.
36. K. Peddireddy, P. Kumar, S. Thutupalli, S. Herminghaus and C. Bahr, *Langmuir*, 2012, **28**, 12426-12431.
37. J. P. Marcolongo and M. Mirenda, *J Chem Educ*, 2011, **88**, 629-633.
38. E. Summerton, G. Zimbitas, M. Britton and S. Bakalis, *Trends in Food Science & Technology*, 2017, **60**, 23-30.
39. J. Gregory, *Particles in water: Properties and processes*, 2005.
40. H. Stechemesser and B. Dobiáš, *Coagulation and flocculation*, Taylor & Francis Group, New York, 2005.
41. K. Prajapati and S. Patel, *Archives of Applied Science Research*, 2012, **4**, 662-668.
42. R. M. Miller, O. Ces, N. J. Brooks, E. S. J. Robles and J. T. Cabral, *Cryst Growth Des*, 2017, **17**, 2428-2437.
43. S. VEDANTAM and V. V. RANADE, *Sadhana*, 2013, **38**, 1287-1337.
44. E. Summerton, G. Zimbitas, M. Britton and S. Bakalis, *J Cryst Growth*, 2016, **455**, 111-116.
45. P. Rajak, L. K. Nath and B. Bhuyan, *Indian J Pharm Sci*, 2019, **81**, 11-21.
46. J. M. Seddon, D. Demus, J. Goodby, G. W. Gray, H. Spiess and V. Vill, in *Handbook of Liquid Crystals Set*, John Wiley and Sons, 2008, vol. 1, pp. 635-679.
47. H. Bunjes and T. Unruh, *Advanced Drug Delivery Reviews*, 2007, **59**, 379-402.
48. A. I. I. Tyler, R. V. Law and J. M. Seddon, in *Methods in Membrane Lipids*, ed. D. M. Owen, Springer New York, New York, NY, 2015, DOI: 10.1007/978-1-4939-1752-5_16, pp. 199-225.
49. L. A. Feigin and D. I. Svergun, in *Structure Analysis by Small-Angle X-Ray and Neutron Scattering*, ed. G. W. Taylor, Princeton Resources, New Jersey, 1987, ch. 1, pp. 3-24.
50. H. P. Myers, *Introductory Solid State Physics*, Taylor and Francis, London, 2nd ed edn., 2009.
51. L. A. Feigin and D. I. Svergun, in *Structure Analysis by Small-Angle X-Ray and Neutron Scattering*, ed. G. W. Taylor, Princeton Resources, New Jersey, 1987, ch. 2, pp. 25-55.
52. M. Martínez-Ripoll, Crystallography; Scattering and diffraction, http://www.xtal.iqfr.csic.es/Cristalografia/parte_05-en.html, (accessed 12/02/2019, 2019).

53. K. Fukuyama and Y. Hatakeyama, in *Materials Science and Engineering of Carbon*, eds. M. Inagaki and F. Kang, Butterworth-Heinemann, 2016, DOI: https://doi.org/10.1016/B978-0-12-805256-3.00003-9, pp. 27-43.
54. K. J. Edler and D. T. Bowron, *Current Opinion in Colloid & Interface Science*, 2015, **20**, 227-234.
55. K. Frost, D. Kaminski, G. Kirwan, E. Lascaris and R. Shanks, *Carbohydrate Polymers*, 2009, **78**, 543-548.
56. E. Summerton, M. J. Hollamby, G. Zimbitas, T. Snow, A. J. Smith, J. Sommertune, J. Bettiol, C. Jones, M. M. Britton and S. Bakalis, *J Colloid Interf Sci*, 2018, **527**, 260-266.
57. M. Wagner, in *Thermal Analysis in Practice*, ed. M. Wagner, Hanser, 2018, DOI: https://doi.org/10.3139/9781569906446.007, ch. 7, pp. 66-143.
58. A. Raudino, M. G. Sarpietro and M. Pannuzzo, in *Drug-Biomembrane Interaction Studies*, ed. R. Pignatello, Woodhead Publishing, 2013, DOI: https://doi.org/10.1533/9781908818348.127, ch. 4, pp. 127-168.
59. S. V. Burylov and Y. L. Raikher, *Physical review. E, Statistical physics, plasmas, fluids, and related interdisciplinary topics*, 1994, **50**, 358-367.
60. E. Union, European Chemicals Agency (ECHA)- Overview, https://europa.eu/european-union/about-eu/agencies/echa_en, (accessed 14/04/2019, 2019).
61. E. Union, Understanding REACH, https://echa.europa.eu/regulations/reach/understanding-reach, (accessed 14/04/2019, 2019).
62. United Nations, *Globally Harmonized System of Classification and Labelling of Chemicals*, United Nations, New York and Geneva, 7 edn., 2017.
63. European Commission, Eye Irritation/Serious eye Damage, https://ec.europa.eu/jrc/en/eurl/ecvam/alternative-methods-toxicity-testing/validated-test-methods/eye-irritation, (accessed 14/04/2019, 2019).
64. R. Scazzola, G. Boeije, E. Bøtker Pedersen, W. Brenneman, B. Cagáňová, A. Celentano, E. De Coninck, H. Desel, N. Ebbehøj, E. Färber, F. Sesana and S. Zacharov, *Regul Toxicol Pharm*, 2019, **105**, 69-76.
65. M. Lee, J.-H. Hwang and K.-M. Lim, *Toxicological research*, 2017, **33**, 191-203.
66. R. D. Curren and J. W. Harbell, *Environmental health perspectives*, 1998, **106 Suppl 2**, 485-492.
67. K. R. Wilhelmus, *Surv Ophthalmol*, 2001, **45**, 493-515.
68. M. P. Vinardell and M. Mitjans, *J Pharm Sci*, 2008, **97**, 46-59.
69. J. H. Draize, G. Woodard and H. O. Calvery, *Journal of Pharmacology and Experimental Therapeutics*, 1944, **82**, 377.
70. C. Eskes, S. Bessou, L. Bruner, R. Curren, J. Harbell, P. Jones, R. Kreiling, M. Liebsch, P. McNamee, W. Pape, M. K. Prinsen, T. Seidle, P. Vanparys, A. Worth and V. Zuang, *Alternatives to laboratory animals : ATLA*, 2005, **33 Suppl 1**, 47-81.
71. M. K. Prinsen, *Toxicol in Vitro*, 2006, **20**, 78-81.
72. M. Balls, P. A. Botham, L. H. Bruner and H. Spielmann, *Toxicol in Vitro*, 1995, **9**, 871-929.
73. W. A. Chambers, S. Green, K. C. Gupta, R. N. Hill, K. Huntley, P. M. Hurley, L. A. Lambert, C. C. Lee, J. K. Lee and P. T. Liu, *Food and chemical toxicology : an international journal published for the British Industrial Biological Research Association*, 1993, **31**, 111-115.
74. OECD, *Test No. 438: Isolated Chicken Eye Test Method for Identifying i) Chemicals Inducing Serious Eye Damage and ii) Chemicals Not Requiring Classification for Eye Irritation or Serious Eye Damage*, 2018.

75. OECD, *Test No. 437: Bovine Corneal Opacity and Permeability Test Method for Identifying i) Chemicals Inducing Serious Eye Damage and ii) Chemicals Not Requiring Classification for Eye Irritation or Serious Eye Damage*, 2017.
76. N. P. Luepke, *Food Chem Toxicol*, 1985, **23**, 287-291.
77. E. Borenfreund and J. A. Puerner, *Toxicol Lett*, 1985, **24**, 119-124.
78. W. J. Pape, U. Pfannenbecker and U. Hoppe, *Mol Toxicol*, 1987, **1**, 525-536.
79. OECD, *Test No. 460: Fluorescein Leakage Test Method for Identifying Ocular Corrosives and Severe Irritants*, 2017.
80. U. Pfannenbecker, S. Bessou-Touya, C. Faller, J. Harbell, T. Jacob, H. Raabe, M. Tailhardat, N. Alepee, A. De Smedt, B. De Wever, P. Jones, Y. Kaluzhny, B. Le Varlet, P. McNamee, M. Marrec-Fairley and F. Van Goethem, *Toxicol in Vitro*, 2013, **27**, 619-626.
81. N. Alepee, S. Bessou-Touya, J. Cotovio, A. de Smedt, B. de Wever, C. Faller, P. Jones, B. Le Varlet, M. Marrec-Fairley, U. Pfannenbecker, M. Tailhardat, F. van Goethem and P. McNamee, *Toxicol in Vitro*, 2013, **27**, 1476-1488.
82. H. Abdelkader, B. Pierscionek, M. Carew, Z. Wu and R. G. Alany, *Brit Med Bull*, 2015, **113**, 59-71.
83. C. K. Mathews, K. E. Van Holde and K. G. Ahern, *Biochemistry*, Addison-Wesle, San Francisco, Calif, 3rd ed edn., 2000.
84. B. Alberts, A. Johnson, J. Lewis, M. Raff, K. Roberts and P. Walter, *Journal*, 2002.
85. B. Alberts, A. Johnson, J. Lewis, M. Raff, K. Roberts and P. Walter, *Journal*, 2002.
86. W. Shinoda, *Biochimica et Biophysica Acta (BBA) - Biomembranes*, 2016, **1858**, 2254-2265.
87. D. M. Small and D. J. Hanahan, *The physical chemistry of lipids*, Plenum Pr., New York, NY [u.a.], 1988.
88. L. J. Pike, *Journal of Lipid Research*, 2009, **50**, S323-S328.
89. H. Ohvo-Rekilä, B. Ramstedt, P. Leppimäki and J. Peter Slotte, *Progress in Lipid Research*, 2002, **41**, 66-97.
90. B. Mattei, R. B. Lira, K. R. Perez and K. A. Riske, *Chem Phys Lipids*, 2017, **202**, 28-37.
91. M. A. Kol, A. I. P. M. de Kroon, J. A. Killian and B. de Kruijff, *Biochemistry-Us*, 2004, **43**, 2673-2681.
92. F. X. Contreras, L. Sánchez-Magraner, A. Alonso and F. M. Goñi, *FEBS Letters*, 2010, **584**, 1779-1786.
93. S. R. Bushell, A. C. W. Pike, M. E. Falzone, N. J. G. Rorsman, C. M. Ta, R. A. Corey, T. D. Newport, J. C. Christianson, L. F. Scofano, C. A. Shintre, A. Tessitore, A. Chu, Q. Wang, L. Shrestha, S. M. M. Mukhopadhyay, J. D. Love, N. A. Burgess-Brown, R. Sitsapesan, P. J. Stansfeld, J. T. Huiskonen, P. Tammaro, A. Accardi and E. P. Carpenter, *Nat Commun*, 2019, **10**, 3956.
94. H. Bayley, B. Cronin, A. Heron, M. A. Holden, W. L. Hwang, R. Syeda, J. Thompson and M. Wallace, *Molecular bioSystems*, 2008, **4**, 1191-1208.
95. D. D. Lasic, *Liposomes : from physics to applications*, Elsevier, Amsterdam; New York, 1993.
96. R. P. Richter, R. Bérat and A. R. Brisson, *Langmuir*, 2006, **22**, 3497-3505.
97. S. Oiki, in *Patch Clamp Techniques: From Beginning to Advanced Protocols*, ed. Y. Okada, Springer Japan, Tokyo, 2012, DOI: 10.1007/978-4-431-53993-3_16, pp. 229-275.
98. Y. Elani, A. J. deMello, X. Z. Niu and O. Ces, *Lab Chip*, 2012, **12**, 3514-3520.
99. N. E. Barlow, G. Bolognesi, S. Haylock, A. J. Flemming, N. J. Brooks, L. M. C. Barter and O. Ces, *Sci Rep-Uk*, 2017, **7**, 17551.
100. N. E. Barlow, E. Smpokou, M. S. Friddin, R. Macey, I. R. Gould, C. Turnbull, A. J. Flemming, N. J. Brooks, O. Ces and L. M. C. Barter, *Biomicrofluidics*, 2017, **11**, 024107.

101. T. Trantidou, M. S. Friddin, A. Salehi-Reyhani, O. Ces and Y. Elani, *Lab Chip*, 2018, **18**, 2488-2509.
102. Y. Tsuji, R. Kawano, T. Osaki, K. Kamiya, N. Miki and S. Takeuchi, *Lab Chip*, 2013, **13**, 1476-1481.
103. A. Laouini, C. Jaafar-Maalej, I. Limayem-Blouza, S. Sfar, C. Charcosset and H. Fessi, *Journal of Colloid Science and Biotechnology*, 2012, **1**, 147-168.
104. S. B. Kulkarni, G. V. Betageri and M. Singh, *Journal of microencapsulation*, 1995, **12**, 229-246.
105. D. J. A. Crommelin and G. Storm, *Journal of Liposome Research*, 2003, **13**, 33-36.
106. S. G. Peisajovich and Y. Shai, in *Methods in Enzymology*, Academic Press, 2003, vol. 372, pp. 361-373.
107. A. L. Liu, *Advances in Planar Lipid Bilayers and Liposomes*, Elsevier Science, 2009.
108. S. Kato, H. Itagaki, I. Chiyoda, S. Hagino, T. Kobayashi, Y. Fujiyama, H. Kakoki and M. Yamaguchi, *Toxicol in Vitro*, 1988, **2**, 125-130.
109. K. Matsuzaki, S. Yoneyama, O. Murase and K. Miyajima, *Biochemistry-Us*, 1996, **35**, 8450-8456.
110. S. Burgess, Liposome Preparation, https://www.sigmaaldrich.com/technical-documents/articles/biology/liposome-preparation.html, (accessed 10/09/2018, 2018).
111. A. P. Lipids, Equipment - Avanti Mini-Extruder, https://avantilipids.com/divisions/equipment-products, (accessed 10/08/2018, 2018).
112. J. D. Berry, M. J. Neeson, R. R. Dagastine, D. Y. C. Chan and R. F. Tabor, *J Colloid Interf Sci*, 2015, **454**, 226-237.
113. PerkinElmer, *PYRIS Diamond DSC Instrument Technical Manual*, PerkinElmer Instruments, Shelton, 2001.
114. J. Filik, A. W. Ashton, P. C. Y. Chang, P. A. Chater, S. J. Day, M. Drakopoulos, M. W. Gerring, M. L. Hart, O. V. Magdysyuk, S. Michalik, A. Smith, C. C. Tang, N. J. Terrill, M. T. Wharmby and H. Wilhelm, *J Appl Crystallogr*, 2017, **50**, 959-966.
115. Olympus, *Research Inverted Systems Microscope 1X71/1X81*, Olympus, Japan, 2012.
116. A. P. Costa, X. Xu and D. J. Burgess, *Pharmaceutical research*, 2014, **31**, 97-103.
117. M. P. Taylor, A. E. Berger and J. Herzfeld, *Journal of Chemical Physics*, 1989, **91**, 528-538.
118. M. F. Ficheux, L. Bonakdar, F. Leal-Calderon and J. Bibette, *Langmuir*, 1998, **14**, 2702-2706.
119. V. M. Coiro, F. Mazza and G. Pochetti, *Acta Crystallographica Section C-Crystal Structure Communications*, 1986, **42**, 991-995.
120. D. J. Lee and W. H. Huang, *Colloid Polym Sci*, 1996, **274**, 160-165.
121. C. C. Ruiz, L. Diaz-Lopez and J. Aguiar, *J Disper Sci Technol*, 2008, **29**, 266-273.
122. A. Rodríguez, M. d. M. Graciani and M. L. Moyá, *Langmuir*, 2008, **24**, 12785-12792.
123. I. A. Sedov, M. A. Stolov and B. N. Solomonov, *Journal of Physical Organic Chemistry*, 2011, **24**, 1088-1094.
124. I. A. Sedov and B. N. Solomonov, *Fluid Phase Equilibria*, 2016, **425**, 9-14.
125. M. N. Rodnikova, *Journal of Molecular Liquids*, 2007, **136**, 211-213.
126. S. Dai and K. C. Tam, *The Journal of Physical Chemistry B*, 2006, **110**, 20794-20800.
127. I. A. Sedov, M. A. Stolov and B. N. Solomonov, *Fluid Phase Equilibria*, 2013, **354**, 95-101.
128. I. A. Sedov, M. A. Stolov and B. N. Solomonov, *The Journal of Chemical Thermodynamics*, 2013, **64**, 120-125.
129. R. Nagarajan and C. C. Wang, *Langmuir*, 2000, **16**, 5242-5251.
130. G. D'Errico, D. Ciccarelli and O. Ortona, *J Colloid Interf Sci*, 2005, **286**, 747-754.

131. R. A. Abdel-Rahem, *J Disper Sci Technol*, 2012, **34**, 932-940.
132. G. P. Association, *Physical Properties of Glycerine and Its Solutions*, Glycerine Producers' Association, 1963.
133. P. M. Meaney, C. J. Fox, S. D. Geimer and K. D. Paulsen, *IEEE transactions on microwave theory and techniques*, 2017, **65**, 1471-1478.
134. P. J. Missel, N. A. Mazer, G. B. Benedek, C. Y. Young and M. C. Carey, *J Phys Chem-Us*, 1980, **84**, 1044-1057.
135. S. Kumar, S. L. David, V. K. Aswal, P. S. Goyal and KabirudDin, *Langmuir*, 1997, **13**, 6461-6464.
136. L. J. Magid, Z. Li and P. D. Butler, *Langmuir*, 2000, **16**, 10028-10036.
137. Z. H. Ren, *Industrial & Engineering Chemistry Research*, 2015, **54**, 9683-9688.
138. S. G. Woolfrey, G. M. Banzon and M. J. Groves, *J Colloid Interf Sci*, 1986, **112**, 583-587.
139. E. Dutkiewicz and A. Jakubowska, *Colloid Polym Sci*, 2002, **280**, 1009-1014.
140. I. M. Umlong and K. Ismail, *Colloids and Surfaces A: Physicochemical and Engineering Aspects*, 2007, **299**, 8-14.
141. S. Hayashi and S. Ikeda, *The Journal of Physical Chemistry*, 1980, **84**, 744-751.
142. B. L. Bales, M. Benrraou and R. Zana, *J Phys Chem B*, 2002, **106**, 9033-9035.
143. C. Vautier-Giongo and B. L. Bales, *The Journal of Physical Chemistry B*, 2003, **107**, 5398-5403.
144. M. N. Islam, K. C. Sarker and G. Aktaruzzaman, *J Surfactants Deterg*, 2014, **17**, 525-530.
145. Z. Kokot, *Chemia Analityczna*, 2001, **46**, 823-829.
146. D. P. Acharya, D. Varade and K. Aramaki, *J Colloid Interf Sci*, 2007, **315**, 330-336.
147. L. J. Magid, *J Phys Chem B*, 1998, **102**, 4064-4074.
148. F. Leermakers, J. C. Eriksson and H. Lyklema, in *Fundamentals of Interface and Colloid Science*, ed. J. Lyklema, Academic Press, 2005, vol. 5, pp. 4.1-4.123.
149. W. Kunz, *Current Opinion in Colloid & Interface Science*, 2010, **15**, 34-39.
150. R. L. Sakaguchi and J. M. Powers, in *Craig's Restorative Dental Materials (Thirteenth Edition)*, eds. R. L. Sakaguchi and J. M. Powers, Mosby, Saint Louis, 2012, DOI: https://doi.org/10.1016/B978-0-323-08108-5.10004-0, pp. 33-81.
151. S. Ebnesajjad, in *Adhesives Technology Handbook (Second Edition)*, ed. S. Ebnesajjad, William Andrew Publishing, Norwich, NY, 2009, DOI: https://doi.org/10.1016/B978-0-8155-1533-3.50005-0, pp. 21-36.
152. S. Nordholm, J. Forsman, C. Woodward, B. Freasier and Z. Abbas, in *Generalized Van der Waals Theory of Molecular Fluids in Bulk and At Surfaces*, eds. S. Nordholm, J. Forsman, C. Woodward, B. Freasier and Z. Abbas, Elsevier, 2019, DOI: https://doi.org/10.1016/B978-0-12-811136-9.00009-5, pp. 135-170.
153. S. Ebnesajjad, in *Handbook of Adhesives and Surface Preparation*, ed. S. Ebnesajjad, William Andrew Publishing, Oxford, 2011, DOI: https://doi.org/10.1016/B978-1-4377-4461-3.10003-3, pp. 21-30.
154. B. E. Rapp, in *Microfluidics: Modelling, Mechanics and Mathematics*, ed. B. E. Rapp, Elsevier, Oxford, 2017, DOI: https://doi.org/10.1016/B978-1-4557-3141-1.50022-8, pp. 453-465.
155. P. L. du Noüy, *The Journal of general physiology*, 1919, **1**, 521-524.
156. L. Wilhelmy, *Annalen der Physik*, 1863, **195**, 177-217.
157. J. Campbell, *Journal of Physics D: Applied Physics*, 1970, **3**, 1499.
158. K. J. Mysels, *Colloid Surface*, 1990, **43**, 241-262.
159. K. J. Mysels, *Langmuir*, 1986, **2**, 428-432.
160. E. I. Franses, O. A. Basaran and C.-H. Chang, *Current Opinion in Colloid & Interface Science*, 1996, **1**, 296-303.

161. O. E. Yildirim, Q. Xu and O. A. Basaran, *Phys Fluids*, 2005, **17**, 062107.
162. A. Morita, D. Carastan and N. Demarquette, *Colloid Polym Sci*, 2002, **280**, 857-864.
163. D. K. Owens, *J Colloid Interf Sci*, 1969, **29**, 496-501.
164. G. J. Gittens, *J Colloid Interf Sci*, 1969, **30**, 406-412.
165. C. C. Addison and S. K. Hutchinson, *Journal of the Chemical Society (Resumed)*, 1948, DOI: 10.1039/JR9480000943, 943-948.
166. K. J. Mysels, *Langmuir*, 1986, **2**, 423-428.
167. M. J. Rosen, in *Surfactants and Interfacial Phenomena*, John Wiley & Sons, Inc., 2004, DOI: 10.1002/0471670561.ch2, pp. 34-104.
168. K. A. Wilk, B. Burczyk and H. Kubica, *Colloid Surface*, 1990, **50**, 363-371.
169. C. Vautier-Giongo and B. L. Bales, *J Phys Chem B*, 2003, **107**, 5398-5403.
170. J. L. Dashnau, N. V. Nucci, K. A. Sharp and J. M. Vanderkooi, *The Journal of Physical Chemistry B*, 2006, **110**, 13670-13677.
171. C. Chen, W. Z. Li, Y. C. Song and J. Yang, *Journal of Molecular Liquids*, 2009, **146**, 23-28.
172. R. J. Sengwa, R. Chaudhary and S. C. Mehrotra, *Mol Phys*, 2001, **99**, 1805-1812.
173. V. Coiro and F. Mazza, *Acta Crystallographica Section C-crystal Structure Communications - ACTA CRYSTALLOGR C-CRYST STR*, 1989, **45**, 1132-1136.
174. V. M. Coiro, F. Mazza and G. Pochetti, *Acta Crystallographica Section C*, 1986, **42**, 991-995.
175. L. A. Smith, R. B. Hammond, K. J. Roberts, D. Machin and G. McLeod, *Journal of Molecular Structure*, 2000, **554**, 173-182.
176. P. v. Mourik, B. Norder and S. J. Picken, *Liq Cryst*, 2012, **39**, 493-500.
177. M. Tariq, S. Hameed, I. H. Bechtold, A. J. Bortoluzzi and A. A. Merlo, *Journal of Materials Chemistry C*, 2013, **1**, 5583-5593.
178. A. G. Kikhney and D. I. Svergun, *FEBS Letters*, 2015, **589**, 2570-2577.
179. J. Li, A. Jiao, S. Chen, Z. Wu, E. Xu and Z. Jin, *Journal of Molecular Structure*, 2018, **1165**, 391-400.
180. H. Hirata, M. Sato, Y. Sakaiguchi and Y. Katsube, *Colloid Polym Sci*, 1988, **266**, 862-864.
181. V. K. Aswal, P. S. Goyal, S. De, S. Bhattacharya, H. Amenitsch and S. Bernstorff, *Chemical Physics Letters*, 2000, **329**, 336-340.
182. European Chemicals Agency, in *Encyclopedia of Toxicology (Third Edition)*, ed. P. Wexler, Academic Press, Oxford, 2014, DOI: https://doi.org/10.1016/B978-0-12-386454-3.00551-0, pp. 263-264.
183. European Chemicals Agency, REACH Roles, https://www.hse.gov.uk/reach/role.htm, (accessed 14/04/2019, 2019).
184. Health and Safety Executive, Background: Globally Harmonised System (GHS), http://www.hse.gov.uk/chemical-classification/legal/background-directives-ghs.htm, (accessed 14/04/2019, 2019).
185. S. L. Wilson, M. Ahearne and A. Hopkinson, *Toxicology*, 2015, **327**, 32-46.
186. H. Spielmann, *Altex-Altern Tierexp*, 1999, **16**, 171-172.
187. J. J. Scheibel, *J Surfactants Deterg*, 2004, **7**, 319-328.
188. Y. Yu, J. Zhao and A. E. Bayly, *Chinese Journal of Chemical Engineering*, 2008, **16**, 517-527.
189. K. Schutte, M. K. Prinsen, P. M. McNamee and R. Roggeband, *Regul Toxicol Pharm*, 2009, **54**, 272-281.
190. J. V. Forrester, A. Dick, P. G. McMenamin and W. R. Lee, in *The Eye: Basic Sciences in Practice*, eds. J. V. Forrester, A. D. Dick, P. G. McMenamin, F. Roberts and E. Pearlman, W.B. Saunders, 4th edn., 2016, ch. 1, pp. 1-102.
191. N. Ehlers and J. Hjortdal, *The Cornea. Epithelium and Stroma*, 2005.

192. J. Sowden and A. Streit, in *Kaufman's Atlas of Mouse Development Supplement*, eds. R. Baldock, J. Bard, D. R. Davidson and G. Morriss-Kay, Academic Press, Boston, 2016, DOI: https://doi.org/10.1016/B978-0-12-800043-4.00020-8, pp. 253-265.
193. J. M. Tiffany, *Dev Ophthalmol*, 2008, **41**, 1-20.
194. A. Jepsen, D. K. Maccallum and J. H. Lillie, *Exp Cell Res*, 1980, **125**, 141-152.
195. A. A. M. Torricelli, V. Singh, M. R. Santhiago and S. E. Wilson, *Invest Ophth Vis Sci*, 2013, **54**, 6390-6400.
196. A. B. G. Burton, M. York and R. S. Lawrence, *Food and Cosmetics Toxicology*, 1981, **19**, 471-480.
197. H. B. W. M. Koëter and M. K. Prinsen, *Comparison of in vivo and in vitro eye irritancy test systems: a study with 34 substances, alternative methods in toxicology, chapter A9*, Mary Ann Liebert, Inc, New Rochelle, NY, 1985.
198. M. K. Prinsen, C. F. M. Hendriksen, C. A. M. Krul and R. A. Woutersen, *Regul Toxicol Pharm*, 2017, **85**, 132-149.
199. M. Piehl, M. Carathers, R. Soda, D. Cerven and G. DeGeorge, *Porcine Corneal Ocular Reversibility Assay (PorCORA) predicts ocular damage and recovery for global regulatory agency hazard categories*, 2011.
200. P. Gautheron, M. Dukic, D. Alix and J. F. Sina, *Fund Appl Toxicol*, 1992, **18**, 442-449.
201. S. N. Kolle, A. Van Cott, B. van Ravenzwaay and R. Landsiedel, *Regul Toxicol Pharm*, 2017, **85**, 33-47.
202. C. Stanley, K. S. Elvira, X. Niu, A. Gee, O. Ces, J. Edel and A. J. deMello, *A microfluidic approach for high-throughput droplet interface bilayer (DIB) formation*, 2010.
203. E. J. Challita, J. S. Najem, R. Monroe, D. J. Leo and E. C. Freeman, *Sci Rep-Uk*, 2018, **8**, 6494.
204. B. Schlicht and M. Zagnoni, *Sci Rep-Uk*, 2015, **5**, 9951.
205. J. N. Weinstein, R. Blumenthal and R. D. Klausner, in *Methods in Enzymology*, Academic Press, 1986, vol. 128, pp. 657-668.
206. Y. Kapoor, B. A. Howell and A. Chauhan, *Invest Ophth Vis Sci*, 2009, **50**, 2727-2735.
207. A. M. Firsov, E. A. Kotova and Y. N. Antonenko, *Anal Biochem*, 2018, **552**, 19-23.
208. S. Hamann, J. Kiilgaard, T. Litman, F. Alvarez-Leefmans, B. R. Winther and T. Zeuthen, *Measurement of Cell Volume Changes by Fluorescence Self-Quenching*, 2002.
209. E. Tambutté, S. Tambutté, N. Segonds, D. Zoccola, A. Venn, J. Erez and D. Allemand, *Proceedings of the Royal Society B: Biological Sciences*, 2012, **279**, 19-27.
210. H. Patel, C. Tscheka and H. Heerklotz, *Soft Matter*, 2009, **5**, 2849-2851.
211. J. Sunamoto, K. Iwamoto, G. Imokawa and S. Tsuchiya, *Possible eye-irritant test using polysaccharide-coated liposomes as a corneal epithelium model*, 1987.
212. P. Zelenka, *Exp Eye Res*, 1978, **26**, 267-274.
213. D. A. Rintoul, R. D. Creed and G. W. Conrad, *Invest Ophth Vis Sci*, 1984, **25**, 1151-1155.
214. T. J. Hall-Manning, G. H. Holland, G. Rennie, P. Revell, J. Hines, M. D. Barratt and D. A. Basketter, *Food Chem Toxicol*, 1998, **36**, 233-238.
215. G. Y. Patlewicz, R. A. Rodford, G. Ellis and M. D. Barratt, *Toxicol in Vitro*, 2000, **14**, 79-84.
216. S. S. Ibrahim, *J Pharm Sci*, 2019, **108**, 1923-1933.
217. M. J. Rosen and J. T. Kunjappu, in *Surfactants and Interfacial Phenomena*, John Wiley & Sons, Inc., 2012, DOI: 10.1002/9781118228920.ch5, ch. 5, pp. 235-271.
218. C. Costagliola, V. Romano, E. Forbice, M. Angi, A. Pascotto, T. Boccia and F. Semeraro, *Clinical & experimental optometry*, 2013, **96**, 529-535.
219. S. K. Suri, M. S. Thakur and S. Bhardwaj, *Journal of the American Oil Chemists' Society*, 1993, **70**, 59-64.

220. I. Johansson, C. Strandberg, B. Karlsson, G. Karlsson and K. Hammarstrand, in *Industrial Applications of Surfactants IV*, ed. D. R. Karsa, Woodhead Publishing, 1999, DOI: https://doi.org/10.1533/9781845698614.88, pp. 88-107.
221. S. E. Belanger, P. B. Dorn, R. Toy, G. Boeije, S. J. Marshall, T. Wind, R. Van Compernolle and D. Zeller, *Ecotoxicology and Environmental Safety*, 2006, **64**, 85-99.
222. M. Giagnorio, A. Amelio, H. Grüttner and A. Tiraferri, *J Clean Prod*, 2017, **154**, 593-601.
223. E. Acosta, M. Bisceglia and D. H. Kurlat, *Physics and Chemistry of Liquids*, 2005, **43**, 269-275.
224. S. K. Hait and S. P. Moulik, *J Surfactants Deterg*, 2001, **4**, 303-309.
225. N. Li, H. Luo and S. Liu, *Spectrochimica Acta Part A: Molecular and Biomolecular Spectroscopy*, 2004, **60**, 1811-1815.
226. H. H. Paradies, *The Journal of Physical Chemistry*, 1980, **84**, 599-607.
227. A. Helenius and K. Simons, *Biochimica et Biophysica Acta (BBA) - Reviews on Biomembranes*, 1975, **415**, 29-79.
228. A. Pizzirusso, A. De Nicola, G. J. A. Sevink, A. Correa, M. Cascella, T. Kawakatsu, M. Rocco, Y. Zhao, M. Celino and G. Milano, *Physical Chemistry Chemical Physics*, 2017, **19**, 29780-29794.
229. D. Lichtenberg, H. Ahyayauch and Félix M. Goñi, *Biophysical Journal*, 2013, **105**, 289-299.
230. C.-M. Lin, G.-P. Chang, H.-K. Tsao and Y.-J. Sheng, *The Journal of Chemical Physics*, 2011, **135**, 045102.
231. H. Ahyayauch, M. I. Collado, A. Alonso and Felix M. Goñi, *Biophysical Journal*, 2012, **102**, 2510-2516.
232. C. Arnulphi, J. Sot, M. García-Pacios, J.-L. R. Arrondo, A. Alonso and F. M. Goñi, *Biophysical Journal*, 2007, **93**, 3504-3514.
233. H. Ahyayauch, M. Bennouna, A. Alonso and F. M. Goñi, *Langmuir*, 2010, **26**, 7307-7313.
234. H. Ahyayauch, B. Larijani, A. Alonso and F. M. Goñi, *Biochimica et Biophysica Acta (BBA) - Biomembranes*, 2006, **1758**, 190-196.
235. P. Goon, C. Manohar and V. V. Kumar, *J Colloid Interf Sci*, 1997, **189**, 177-180.
236. E. Samper, M. Rodríguez, M. De la Rubia and D. Rico, *Removal of metal ions at low concentration by micellar-enhanced ultrafiltration (MEUF) using sodium dodecyl sulfate (SDS) and linear alkylbenzene sulfonate (LAS)*, 2009.
237. M. T. García, E. Campos, M. Dalmau, I. Ribosa and J. Sánchez-Leal, *Chemosphere*, 2002, **49**, 279-286.
238. C. Genova, U. Schoenkaes, D. Smith and M. Stolz, *J Surfactants Deterg*, 2003, **6**, 365-372.
239. HERA, *Risk Assessment Alcohol Ethoxylates*, HERA, Belgium, 2009.
240. J.-L. Salager, A. M. Forgiarini and J. Bullón, *J Surfactants Deterg*, 2013, **16**, 449-472.
241. M. Asri, R. Daik and S. Ramli, *Study on the effect of oil phase and co-surfactant on microemulsion systems*, 2017.
242. H. Krüssmann and R. Bercovici, *Journal of Chemical Technology & Biotechnology*, 1991, **50**, 399-409.
243. M. Narenji, M. R. Talaee and H. R. Moghimi, *Iran J Pharm Res*, 2017, **16**, 423-431.
244. N. Efron, G. Young and N. A. Brennan, *Curr Eye Res*, 1989, **8**, 901-906.
245. A. Azeem, M. Rizwan, F. J. Ahmad, Z. Iqbal, R. K. Khar, M. Aqil and S. Talegaonkar, *AAPS PharmSciTech*, 2009, **10**, 69-76.

Appendix

Supplementary information is provided in this section that may be of further interest to the reader. This information is relevant but not fundamental to the understanding of the thesis.

SURFACE TENSION METHOD OPTIMISATION / VALIDATION.

Table 8.1 – Effect of droplet volume on the surface tension using 0.15 wt% SDS solution. Comparison of the mean surface tensions for 16.0 ul drop volume with 17, 18, 19 and 20 ul using two-tailed t-test, n=9). Difference of 2.0 µl drop size or more showed p-value < 0.05, i.e. a significantly different mean surface tension.

Drop volume (µl)	Surface tension (mN/m) Average	Standard Error	t-statistic	DF	*p*-value
16.0	47.07 ±0.767	-	-	-	-
17.0	47.71 ±1.023	0.422	1.516	16	0.1490
18.0	47.63 ±0.654	0.57	1.723	16	0.1042
19.0	48.33 ±0.823	0.37	3.402	16	0.0036
20.0	48.06 ±0.667	0.334	2.966	16	0.0091

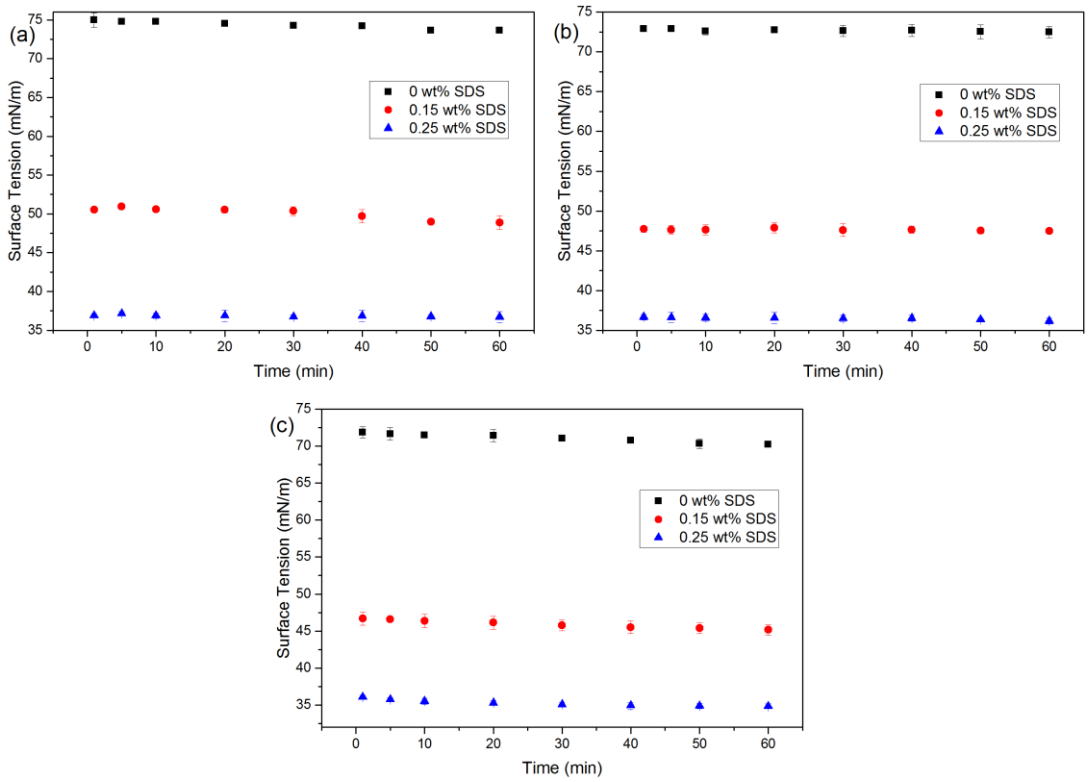


Fig 8.1 – Surface tension of a droplet over time for (a) 10°C (b) 20°C and (c) 40°C temperature at three different SDS concentrations. Used for equilibrium time validation.

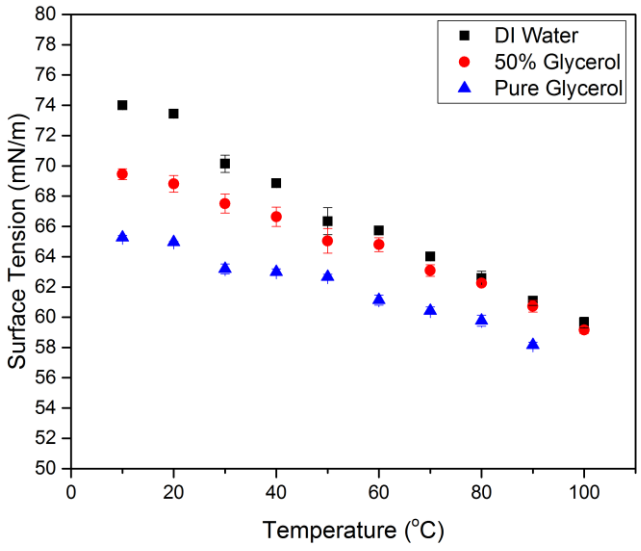


Fig 8.2 – Effect of temperature on the surface tension for DI water, 50% glycerol and pure glycerol. Carried out to determine the changes in the surface tension of water/glycerol solvent as the temperature is increased. These results were taken into account for the Krafft temperature experiments.

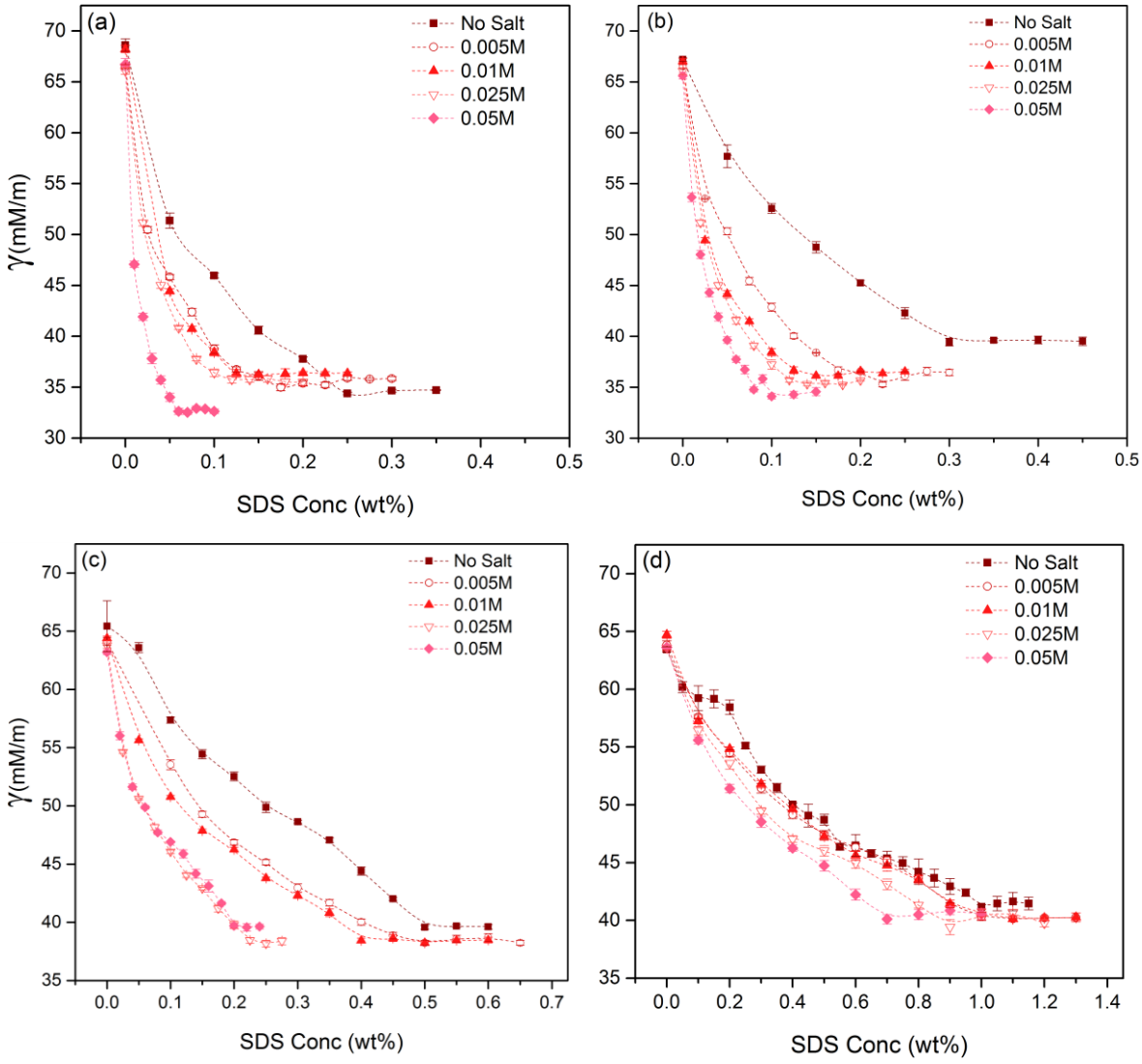


Fig 8.3 –Surface tension measurements to determine effect of NaCl concentration on the CMC for; (a) 40 % glycerol, (b) 60 % glycerol, (c) 80 % glycerol and (d) Pure glycerol solvent systems.

CONDUCTIVITY MEASUREMENTS

Table 8.2 – All Conductivity measurements for 0.005M NaCl solution in (a) pure DI water (b) 20 wt% glycerol (c) 40 wt% glycerol, (d) 60 wt% glycerol, (e) 80 wt% glycerol set 1 and (f) 80 wt% glycerol set 2.

(a)

SDS Conc (wt%)	Conductivity [uS/cm]				
	Repeat 1	Repeat 2	Repeat 3	Average	St.dev
0	633	638	637	636.00	2.65
0.05	732	728	731	730.33	2.08
0.075	795	794	792	793.67	1.53
0.1	848	850	848	848.67	1.15
0.125	890	896	893	893.00	3.00
0.15	956	952	954	954.00	2.00
0.175	1011	1010	1010	1010.33	0.58
0.2	1025	1026	1026	1025.67	0.58
0.225	1040	1038	1040	1039.33	1.15
0.25	1080	1085	1086	1083.67	3.21

(b)

SDS Conc (wt%)	Conductivity [uS/cm]				
	Repeat 1	Repeat 2	Repeat 3	Average	St.dev
0	452	455	455	454.00	1.73
0.05	545	546	546	545.67	0.58
0.075	586	585	587	586.00	1.00
0.1	630	632	634	632.00	2.00
0.11	652	655	654	653.67	1.53
0.12	669	672	670	670.33	1.53
0.14	686	685	683	684.67	1.53
0.15	698	697	695	696.67	1.53
0.16	708	706	705	706.33	1.53
0.17	714	712	714	713.33	1.15
0.18	722	720	719	720.33	1.53
0.19	730	732	729	730.33	1.53
0.2	740	740	742	740.67	1.15

(c)

SDS Conc (wt%)	Conductivity [uS/cm]				
	Repeat 1	Repeat 2	Repeat 3	Average	St.dev
0	265	268	265	266.00	1.73
0.025	292	293	293	292.67	0.58
0.05	315	312	313	313.33	1.53
0.075	341	342	341	341.33	0.58
0.1	358	357	358	357.67	0.58
0.125	378	377	378	377.67	0.58
0.15	410	412	412	411.33	1.15
0.175	423	422	423	422.67	0.58
0.2	431	432	429	430.67	1.53
0.225	445	445	446	445.33	0.58
0.25	459	458	459	458.67	0.58
0.275	470	471	471	470.67	0.58
0.3	485	481	483	483.00	2.00

(d)

SDS Conc (wt%)	Conductivity [uS/cm]				
	Repeat 1	Repeat 2	Repeat 3	Average	St.dev
0	113	113	113	112.80	0.20
0.025	128	130	130	129.30	0.87
0.05	136	137	137	136.60	0.20
0.075	144	145	145	144.57	0.35
0.1	155	154	155	154.60	0.20
0.15	176	176	175	175.57	0.21
0.2	199	199	199	198.77	0.15
0.275	214	215	214	214.33	0.58
0.325	218	219	218	218.33	0.58
0.35	221	222	221	221.33	0.58
0.4	224	225	224	224.33	0.58

(e)

SDS Conc (wt%)	Conductivity [uS/cm]				
	Repeat 1	Repeat 2	Repeat 3	Average	St.dev
0	23.3	23.5	23.6	23.47	0.15
0.1	30.8	30.9	30.6	30.77	0.15
0.15	34.4	34.6	34.8	34.60	0.20
0.2	40.2	40.3	40.6	40.37	0.21
0.25	44.1	44.5	44.6	44.40	0.26
0.3	51.5	51.8	51.3	51.53	0.25
0.35	56.8	57.2	56.9	56.97	0.21
0.4	63.2	63.4	63.5	63.37	0.15
0.45	66.3	66.8	67.1	66.73	0.40
0.5	70.5	70.8	70.3	70.53	0.25
0.55	73.2	73.3	73.5	73.33	0.15
0.6	78.1	78.3	78.6	78.33	0.25
0.65	81.4	81.8	81.5	81.57	0.21

(f)

SDS Conc (wt%)	Conductivity [uS/cm]				
	Repeat 1	Repeat 2	Repeat 3	Average	St.dev
0	24.1	23.9	23.8	23.93	0.15
0.1	35.3	35.5	35.7	35.50	0.20
0.15	39.4	39.6	40.2	39.73	0.42
0.2	46.4	47.6	47.4	47.13	0.64
0.25	50.9	50.8	50.1	50.60	0.44
0.3	58.5	58.7	58.4	58.53	0.15
0.35	62.4	62.6	62.6	62.53	0.12
0.4	66.2	66.5	67.5	66.73	0.68
0.45	73.3	73.6	73.5	73.47	0.15
0.5	77.5	77.7	77.3	77.50	0.20
0.55	80.2	80.5	80.3	80.33	0.15
0.6	85.3	85.6	86.4	85.77	0.57
0.65	89.9	90.7	89.2	89.93	0.75

Table 8.3 – All Conductivity measurements for 0.01M NaCl solution in (a) pure DI water (b) 20 wt% glycerol (c) 40 wt% glycerol, (d) 60 wt% glycerol, (e) 80 wt% glycerol set 1 and (f) 80 wt% glycerol set 2.

(a)

SDS Conc (wt%)	Conductivity [uS/cm]				
	Repeat 1	Repeat 2	Repeat 3	Average	St.dev
0	1470.00	1472.00	1470.00	1470.67	1.15
0.025	1500.00	1498.00	1496.00	1498.00	2.00
0.05	1527.00	1528.00	1528.00	1527.67	0.58
0.075	1570.00	1568.00	1570.00	1569.33	1.15
0.1	1610.00	1609.00	1610.00	1609.67	0.58
0.11	1642.00	1643.00	1643.00	1642.67	0.58
0.12	1670.00	1673.00	1674.00	1672.33	2.08
0.13	1698.00	1695.00	1695.00	1696.00	1.73
0.14	1706.00	1707.00	1707.00	1706.67	0.58
0.15	1712.00	1712.00	1711.00	1711.67	0.58
0.16	1720.00	1718.00	1720.00	1719.33	1.15

(b)

SDS Conc (wt%)	Conductivity [uS/cm]				
	Repeat 1	Repeat 2	Repeat 3	Average	St.dev
0	700.00	698.00	696.00	698.00	2.00
0.05	782.00	780.00	778.00	780.00	2.00
0.06	803.00	800.00	798.00	800.33	2.52
0.07	812.00	814.00	811.00	812.33	1.53
0.08	836.00	830.00	838.00	834.67	4.16
0.09	850.00	848.00	849.00	849.00	1.00
0.1	862.00	860.00	860.00	860.67	1.15
0.11	874.00	875.00	875.00	874.67	0.58
0.12	892.00	890.00	893.00	891.67	1.53
0.13	900.00	898.00	902.00	900.00	2.00
0.14	908.00	905.00	902.00	905.00	3.00
0.15	915.00	918.00	916.00	916.33	1.53

(c)

SDS Conc (wt%)	Conductivity [uS/cm]				
	Repeat 1	Repeat 2	Repeat 3	Average	St.dev
0	414.00	416.00	414.00	414.67	1.15
0.025	448.00	447.00	447.00	447.33	0.58
0.05	498.00	500.00	498.00	498.67	1.15
0.06	522.00	520.00	523.00	521.67	1.53
0.07	544.00	542.00	544.00	543.33	1.15
0.08	565.00	566.00	566.00	565.67	0.58
0.09	584.00	584.00	582.00	583.33	1.15
0.1	603.00	602.00	602.00	602.33	0.58
0.11	620.00	620.00	622.00	620.67	1.15
0.12	639.00	641.00	641.00	640.33	1.15
0.13	646.00	648.00	648.00	647.33	1.15
0.14	655.00	654.00	654.00	654.33	0.58
0.15	663.00	662.00	662.00	662.33	0.58

(d)

SDS Conc (wt%)	Conductivity [uS/cm]				
	Repeat 1	Repeat 2	Repeat 3	Average	St.dev
0	201.00	202.00	201.00	201.33	0.58
0.025	218.00	217.00	218.00	217.67	0.58
0.05	227.00	228.00	229.00	228.00	1.00
0.075	240.00	237.00	239.00	238.67	1.53
0.1	250.00	251.00	250.00	250.33	0.58
0.125	257.00	257.00	258.00	257.33	0.58
0.15	264.00	262.00	260.00	262.00	2.00
0.175	269.00	268.00	268.00	268.33	0.58
0.2	274.00	273.00	274.00	273.67	0.58
0.225	280.00	278.00	279.00	279.00	1.00
0.25	284.00	286.00	284.00	284.67	1.15

(e)

SDS Conc (wt%)	Conductivity [uS/cm]				
	Repeat 1	Repeat 2	Repeat 3	Average	St.dev
0	55.00	52.00	53.00	53.33	1.53
0.1	62.10	61.60	61.00	61.57	0.55
0.15	69.5	70.2	69.8	69.83	0.35
0.2	71.00	71.10	71.10	71.07	0.06
0.25	73.2	73.5	73.8	73.50	0.30
0.3	78.20	78.30	78.30	78.27	0.06
0.35	82.5	83.3	83.1	82.97	0.42
0.4	101.2	101.1	101.15	101.15	0.05
0.45	106.30	106.50	106.80	106.53	0.25
0.5	107.8	107.8	107.9	107.83	0.06
0.55	109.30	109.50	109.30	109.37	0.12
0.6	116.3	116.8	117.4	116.83	0.55
0.65	122.6	122	122.3	122.30	0.30

(f)

SDS Conc (wt%)	Conductivity [uS/cm]				
	Repeat 1	Repeat 2	Repeat 3	Average	St.dev
0	56.00	55.00	56.80	55.93	0.90
0.1	66.30	66.60	66.80	66.57	0.25
0.15	71.9	72.3	72.5	72.23	0.31
0.2	76.00	75.70	76.90	76.20	0.62
0.25	80.9	78.6	79.8	79.77	1.15
0.3	84.20	83.50	84.60	84.10	0.56
0.35	86.5	87.2	87.8	87.17	0.65
0.4	93.2	93.1	93.6	93.30	0.26
0.45	102.60	103.60	103.90	103.37	0.68
0.5	110.6	109.8	109.5	109.97	0.57
0.55	116.00	116.90	115.90	116.27	0.55
0.6	117.2	117.5	116.3	117.00	0.62
0.65	119.8	120.3	120.6	120.23	0.40

Table 8.4 – All Conductivity measurements for 0.025M NaCl solution in (a) pure DI water (b) 20 wt% glycerol (c) 40 wt% glycerol, (d) 60 wt% glycerol, (e) 80 wt% glycerol set 1 and (f) 80 wt% glycerol set 2.

(a)

SDS Conc (wt%)	Conductivity [uS/cm]				
	Repeat 1	Repeat 2	Repeat 3	Average	St.dev
0	2460.00	2455.00	2458.00	2457.67	2.52
0.05	2686.00	2688.00	2683.00	2685.67	2.52
0.055	2748.00	2745.00	2750.00	2747.67	2.52
0.06	2804.00	2797.00	2798.00	2799.67	3.79
0.065	2917.00	2927.00	2926.00	2923.33	5.51
0.07	2950.00	2947.00	2956.00	2951.00	4.58
0.075	2960.00	2955.00	2960.00	2958.33	2.89
0.08	2980.00	2983.00	2976.00	2979.67	3.51
0.085	2990.00	2988.00	2985.00	2987.67	2.52
0.09	3027.00	3025.00	3030.00	3027.33	2.52
0.095	3062.00	3057.00	3060.00	3059.67	2.52

(b)

SDS Conc (wt%)	Conductivity [uS/cm]				
	Repeat 1	Repeat 2	Repeat 3	Average	St.dev
0	1690.00	1692.00	1690.00	1690.67	1.15
0.01	1708.00	1709.00	1710.00	1709.00	1.00
0.02	1720.00	1718.00	1720.00	1719.33	1.15
0.03	1731.00	1730.00	1731.00	1730.67	0.58
0.04	1739.00	1742.00	1742.00	1741.00	1.73
0.05	1749.00	1749.00	1751.00	1749.67	1.15
0.06	1762.00	1763.00	1763.00	1762.67	0.58
0.07	1776.00	1776.00	1778.00	1776.67	1.15
0.08	1785.00	1786.00	1783.00	1784.67	1.53
0.09	1792.00	1792.00	1794.00	1792.67	1.15
0.1	1799.00	1800.00	1800.00	1799.67	0.58
0.11	1808.00	1805.00	1806.00	1806.33	1.53

(c)

SDS Conc (wt%)	Conductivity [uS/cm]				
	Repeat 1	Repeat 2	Repeat 3	Average	St.dev
0	1166.00	1165.00	1166.00	1165.67	0.58
0.01	1230.00	1220.00	1235.00	1228.33	7.64
0.02	1290.00	1292.00	1290.00	1290.67	1.15
0.03	1321.00	1320.00	1322.00	1321.00	1.00
0.04	1358.00	1357.00	1358.00	1357.67	0.58
0.05	1382.00	1381.00	1381.00	1381.33	0.58
0.06	1398.00	1398.00	1397.00	1397.67	0.58
0.07	1426.00	1427.00	1425.00	1426.00	1.00
0.08	1440.00	1442.00	1440.00	1440.67	1.15
0.09	1455.00	1454.00	1456.00	1455.00	1.00
0.1	1460.00	1459.00	1460.00	1459.67	0.58
0.11	1468.00	1468.00	1470.00	1468.67	1.15
0.12	1476.00	1475.00	1476.00	1475.67	0.58
0.13	1485.00	1485.00	1487.00	1485.67	1.15

(d)

SDS Conc (wt%)	Conductivity [uS/cm]				
	Repeat 1	Repeat 2	Repeat 3	Average	St.dev
0	470.00	470.00	470.00	470.00	0.00
0.02	474.00	475.00	475.00	474.67	0.58
0.04	483.00	482.00	482.00	482.33	0.58
0.06	490.00	492.00	492.00	491.33	1.15
0.08	506.00	506.00	508.00	506.67	1.15
0.1	521.00	520.00	520.00	520.33	0.58
0.12	523.00	524.00	523.00	523.33	0.58
0.14	527.00	528.00	528.00	527.67	0.58
0.16	533.00	533.00	532.00	532.67	0.58
0.18	538.00	537.00	537.00	537.33	0.58
0.2	542.00	541.00	542.00	541.67	0.58

(e)

SDS Conc (wt%)	Conductivity [uS/cm]				
	Repeat 1	Repeat 2	Repeat 3	Average	St.dev
0	119.80	119.50	120.40	119.90	0.46
0.02	128.50	128.60	128.20	128.43	0.21
0.05	137.30	137.30	137.50	137.37	0.12
0.075	136.3	135.4	136.8	136.17	0.71
0.1	139.5	140	139.6	139.70	0.26
0.125	143.7	144.3	144.5	144.17	0.42
0.15	146.5	146.3	146.8	146.53	0.25
0.175	151.5	151.8	152.3	151.87	0.40
0.2	160.1	160.3	160.5	160.30	0.20
0.225	167.5	168.3	168.2	168.00	0.44
0.25	173.7	172.8	173.5	173.33	0.47
0.3	178.6	179.7	178.3	178.87	0.74
0.325	183.3	184.1	183.8	183.73	0.40

(f)

SDS Conc (wt%)	Conductivity [uS/cm]				
	Repeat 1	Repeat 2	Repeat 3	Average	St.dev
0	121.50	122.80	122.60	122.30	0.70
0.02	130.50	130.90	130.10	130.50	0.40
0.05	134.60	135.20	134.90	134.90	0.30
0.075	138.9	137.5	138.3	138.23	0.70
0.1	143.6	143.5	143.7	143.60	0.10
0.125	146.8	147.4	146.4	146.87	0.50
0.15	149.6	149.4	149.3	149.43	0.15
0.175	152.6	153.6	153.7	153.30	0.61
0.2	156.3	156.7	156.2	156.40	0.26
0.225	160.3	160.8	161.9	161.00	0.82
0.25	165.4	165.1	164.5	165.00	0.46
0.3	171.2	170.6	171.5	171.10	0.46
0.325	176.2	177.1	177.5	176.93	0.67

Table 8.5 – All Conductivity measurements for 0.05M NaCl solution in (a) pure DI water (b) 20 wt% glycerol (c) 40 wt% glycerol, (d) 60 wt% glycerol, (e) 80 wt% glycerol set 1 and (f) 80 wt% glycerol set 2.

(a)

SDS Conc (wt%)	Conductivity [uS/cm]				
	Repeat 1	Repeat 2	Repeat 3	Average	St.dev
0	5220.00	5220.00	5220.00	5220.00	0.00
0.005	5240	5240	5240	5240.00	0.00
0.01	5290	5290	5280	5286.67	5.77
0.02	5380	5390	5380	5383.33	5.77
0.03	5490	5480	5490	5486.67	5.77
0.035	5500.00	5500.00	5510.00	5503.33	5.77
0.04	5560.00	5570.00	5560.00	5563.33	5.77
0.045	5560.00	5570.00	5570.00	5566.67	5.77
0.05	5590.00	5600.00	5600.00	5596.67	5.77
0.055	5600.00	5610.00	5610.00	5606.67	5.77
0.06	5620.00	5630.00	5630.00	5626.67	5.77
0.07	5650.00	5640.00	5640.00	5643.33	5.77
0.08	5660.00	5650.00	5650.00	5653.33	5.77
0.09	5660.00	5670.00	5670.00	5666.67	5.77
0.1	5670.00	5680.00	5670.00	5673.33	5.77
0.11	5670.00	5680.00	5680.00	5676.67	5.77
0.12	5680.00	5680.00	5680.00	5680.00	0.00
0.13	5680.00	5690.00	5680.00	5683.33	5.77

(b)

SDS Conc (wt%)	Conductivity [uS/cm]				
	Repeat 1	Repeat 2	Repeat 3	Average	St.dev
0	3440.00	3438.00	3436.00	3438.00	2.00
0.01	3460.00	3461.00	3458.00	3459.67	1.53
0.02	3478.00	3478.00	3476.00	3477.33	1.15
0.03	3499.00	3500.00	3499.00	3499.33	0.58
0.04	3518.00	3520.00	3516.00	3518.00	2.00
0.05	3535.00	3538.00	3538.00	3537.00	1.73
0.06	3545.00	3544.00	3546.00	3545.00	1.00
0.07	3554.00	3552.00	3552.00	3552.67	1.15
0.08	3562.00	3560.00	3562.00	3561.33	1.15
0.09	3570.00	3572.00	3571.00	3571.00	1.00
0.1	3579.00	3582.00	3582.00	3581.00	1.73

(c)

SDS Conc (wt%)	Conductivity [uS/cm]				
	Repeat 1	Repeat 2	Repeat 3	Average	St.dev
0	2033.00	2038.00	2037.00	2036.00	2.65
0.01	2089.00	2088.00	2090.00	2089.00	1.00
0.02	2121.00	2122.00	2125.00	2122.67	2.08
0.03	2157.00	2160.00	2158.00	2158.33	1.53
0.04	2190.00	2193.00	2194.00	2192.33	2.08
0.05	2235.00	2233.00	2232.00	2233.33	1.53
0.06	2250.00	2250.00	2253.00	2251.00	1.73
0.07	2264.00	2268.00	2267.00	2266.33	2.08
0.08	2280.00	2282.00	2281.00	2281.00	1.00
0.09	2293.00	2292.00	2290.00	2291.67	1.53
0.1	2304.00	2301.00	2305.00	2303.33	2.08

(d)

SDS Conc (wt%)	Conductivity [uS/cm]				
	Repeat 1	Repeat 2	Repeat 3	Average	St.dev
0	983.00	982.00	983.00	982.67	0.58
0.02	986.00	985.00	984.00	985.00	1.00
0.035	1000.00	1000.00	1000.00	1000.00	0.00
0.04	1010.00	1010.00	1009.00	1009.67	0.58
0.05	1018.00	1020.00	1020.00	1019.33	1.15
0.06	1028.00	1027.00	1028.00	1027.67	0.58
0.07	1032.00	1033.00	1033.00	1032.67	0.58
0.08	1040.00	1038.00	1037.00	1038.33	1.53
0.09	1043.00	1044.00	1045.00	1044.00	1.00
0.1	1050.00	1050.00	1052.00	1050.67	1.15

(e)

SDS Conc (wt%)	Conductivity [uS/cm]				
	Repeat 1	Repeat 2	Repeat 3	Average	St.dev
0	200.30	200.70	200.80	200.60	0.26
0.02	210.20	211.50	211.60	211.10	0.78
0.04	218.30	218.50	218.80	218.53	0.25
0.06	224.30	225.00	224.60	224.63	0.35
0.08	229.60	229.80	230.70	230.03	0.59
0.1	230.30	230.60	230.70	230.53	0.21
0.12	234.5	234.8	234.7	234.67	0.15
0.14	236.0	236.3	236.5	236.27	0.25
0.16	237.5	237.3	237.6	237.47	0.15
0.18	239.3	239.4	239.1	239.27	0.15
0.2	239.8	240.0	239.1	239.63	0.47
0.22	241.0	240.0	241.0	240.67	0.58
0.24	242.1	241.5	241.8	241.80	0.30

(f)

SDS Conc (wt%)	Conductivity [uS/cm]				
	Repeat 1	Repeat 2	Repeat 3	Average	St.dev
0	199.60	200.60	199.70	199.97	0.55
0.02	206.50	206.90	207.20	206.87	0.35
0.04	215.80	215.80	215.90	215.83	0.06
0.06	224.10	223.50	224.90	224.17	0.70
0.08	233.40	233.80	233.60	233.60	0.20
0.1	239.80	239.70	238.60	239.37	0.67
0.12	244.6	245.1	244.6	244.77	0.29
0.14	249.2	248.7	248.9	248.93	0.25
0.16	253.5	254.6	254.1	254.07	0.55
0.18	258.9	258.5	258.7	258.70	0.20
0.2	263.2	263.5	263.9	263.53	0.35
0.22	267.9	267.6	268.1	267.87	0.25
0.24	271.5	270.8	271.3	271.20	0.36

Table 8.6 – All Conductivity measurements for Pure Glycerol in (a) No NaCl and (b) 0.05M NaCl solution.

(a)

SDS Conc (wt%)	Conductivity [uS/cm]				
	Repeat 1	Repeat 2	Repeat 3	Average	St.dev
0	9.92	10.24	9.65	9.94	0.30
0.1	10.9	11.0	10.5	10.77	0.28
0.2	10.84	11.42	9.95	10.74	0.74
0.3	11.8	11.9	10.1	11.24	1.03
0.4	12.76	12.30	9.85	11.64	1.56
0.5	13.7	12.4	10.3	12.14	1.75
0.6	13.68	13.48	11.45	12.87	1.23
0.7	13.9	13.6	12.3	13.27	0.90
0.8	14.06	13.66	13.05	13.59	0.51
0.9	14.2	13.9	13.9	13.97	0.19
1	16.52	14.84	13.65	15.00	1.44
1.1	16.5	15.4	14.5	15.44	1.02
1.2	16.94	15.82	14.45	15.74	1.25

(b)

SDS Conc (wt%)	Conductivity [uS/cm]				
	Repeat 1	Repeat 2	Repeat 3	Avg	StDev
0	65.02	65.42	66.96	65.80	1.02
0.1	65.9	66.0	65.5	65.77	0.28
0.2	65.84	65.42	65.95	65.74	0.28
0.3	66.40	66.60	66.11	66.37	0.25
0.4	66.8	65.84	65.6	66.08	0.64
0.5	67.22	67.08	65.10	66.47	1.19
0.6	67.63	67.32	66.6	67.18	0.53
0.7	68.0	67.56	67.09	67.56	0.48
0.8	67.45	66.80	68.6	67.61	0.90
0.9	68.86	67.04	69.08	68.33	1.12
1	68.3	67.28	69.6	68.37	1.15
1.1	69.68	67.62	71.07	69.46	1.74
1.2	71.09	67.76	72.6	70.47	2.46

LIPOSOME-CALCEIN RELEASE ASSAY

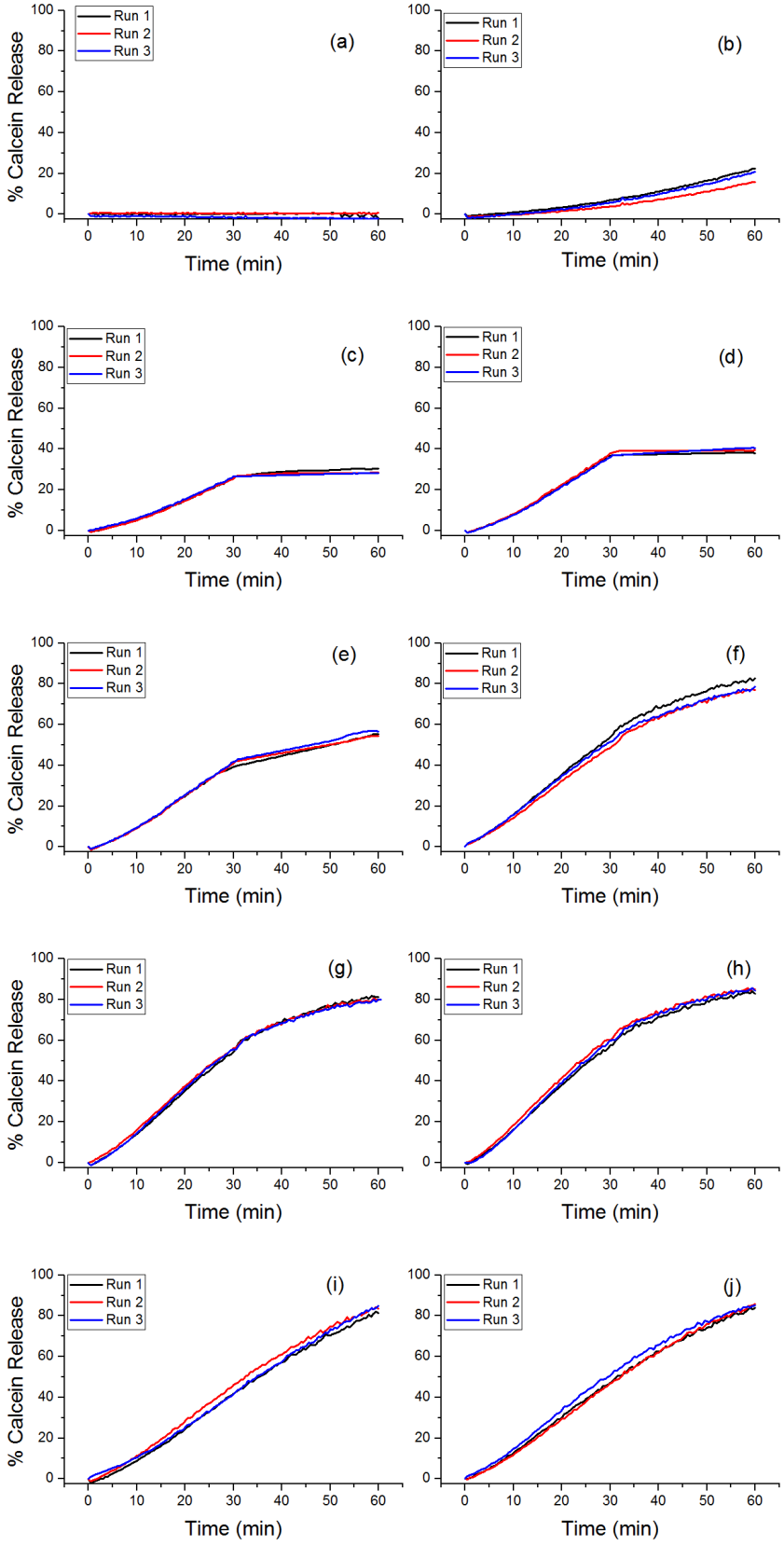


Fig 8.4 – All % Calcein Release time response for LAS surfactant at (a) 0 (b) 1.2 (c) 2 (d) 4 (e) 6.4 (f) 8 (g) 10 (h) 12.8 (i) 16 and (j) 20 mM.

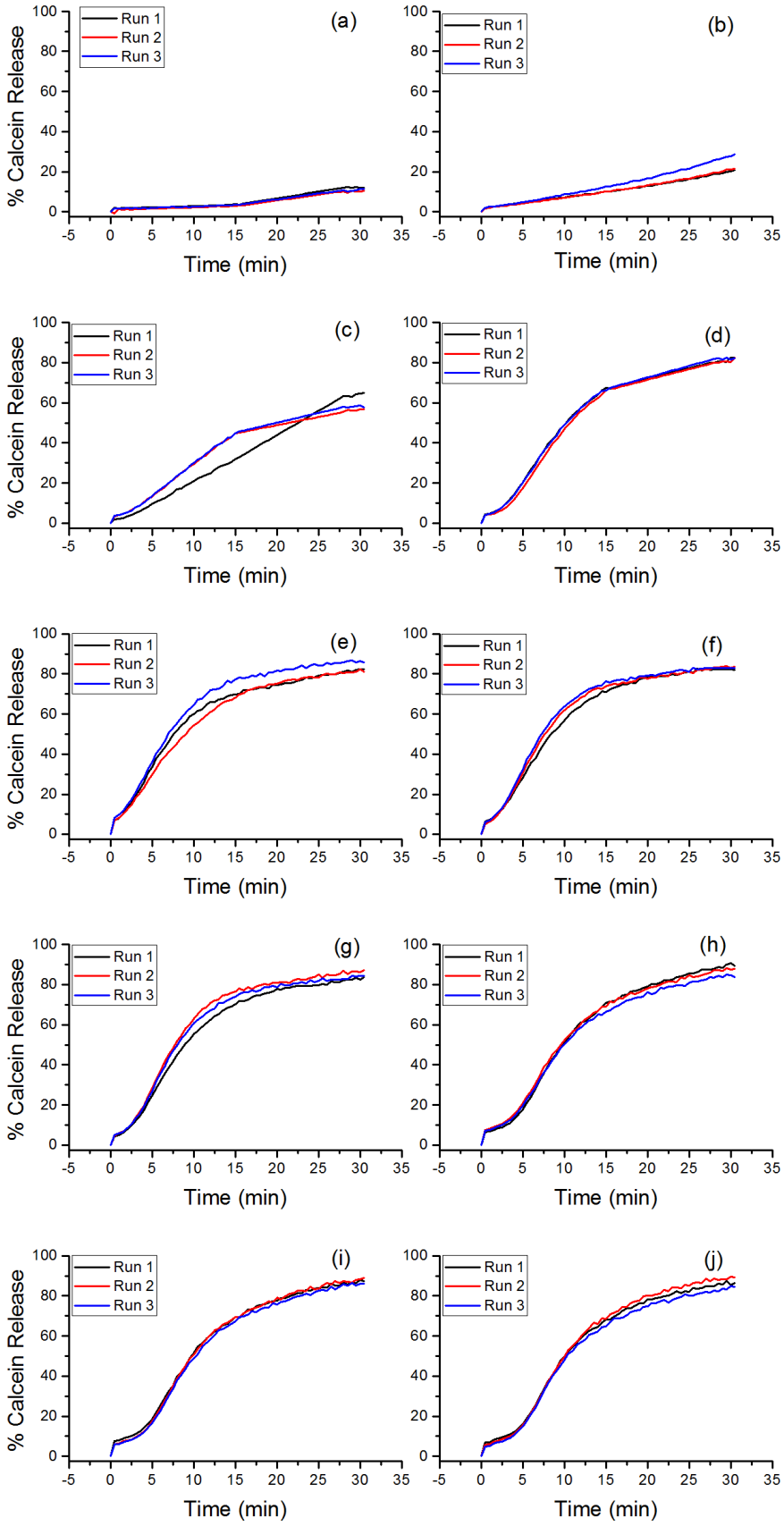


Fig 8.5 – All % Calcein Release time response for AES surfactant at (a) 0.8 (b) 1.2 (c) 2 (d)4 (e) 5.2 (f) 6.4 (g) 8 (h) 12.8 (i) 16 and (j) 20 mM.

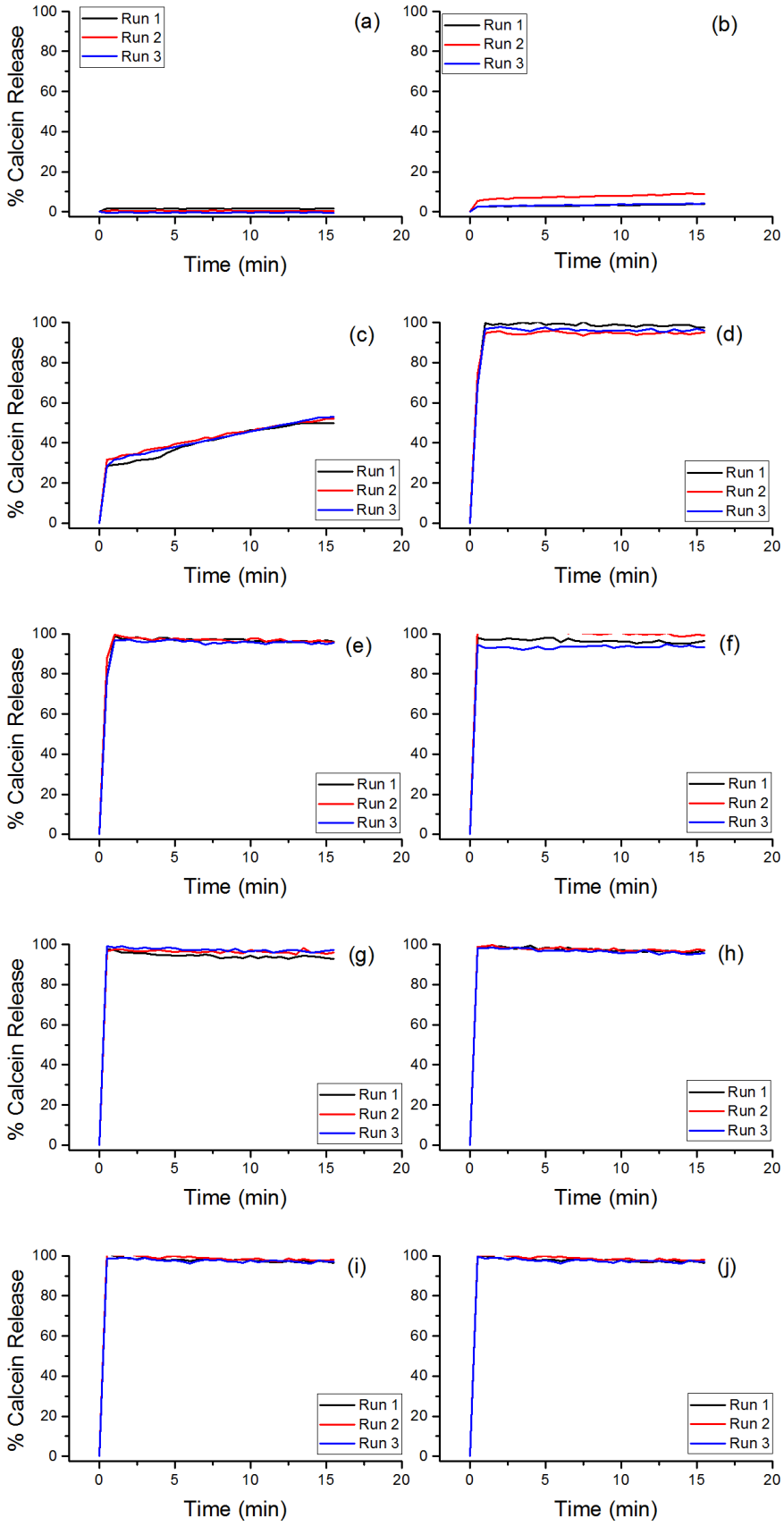


Fig 8.6 – All % Calcein Release time response for NI surfactant at (a) 0 (b) 0.025 (c) 0.05 (d)0.1 (e) 0.2 (f) 0.4 (g) 0.8 (h) 1.6 (i) 2 and (j) 4 mM.